

Photovoltaic and Gas Sensing Applications of Transitional Metal Nanocomposites of Poly(3-Hexylthiophene)-Titanium Dioxide



**UNIVERSITY of the
WESTERN CAPE**

POPOTI JACQUELINE MAAKE (BSc Hons)

A thesis submitted in fulfillment of the requirements for the

degree of

MAGISTER SCIENTIAE (CHEMISTRY)

In the

**Faculty of Science, University of the Western Cape,
Bellville, Cape Town, South Africa**

Supervisor: Prof Emmanuel Iwuoha

Co-supervisor: Prof David E. Motaung

APRIL 2021

ABSTRACT

This thesis starts with the reviewing of studies on the loading of noble metals and nanostructured metal oxides into bulk heterojunction organic solar cell device architectures. The reviews focused on the innovative developments in the use of various fullerene derivatives as electron acceptors in organic solar cells. It additionally reflected on the effect of metallic nanoparticles (NPs), such as gold (Au) and silver (Ag), on the performance of organic solar cells. Besides the metallic NPs, the effect of metal oxide nanoparticle loading, e.g. CuO, ZnO and TiO₂, on the organic solar cell performance, and the use of noble metals doped TiO₂ on the gas sensing application were reviewed. Though a significant amount of work has been done in this area of study, much work still needs to be done on how to reduce the doping temperature in order to minimize power consumption. The present challenge is how the properties of nanostructured materials could be tweaked to make them function as highly efficient light-harvesting materials for high performance organic solar application, or as highly sensitive and selective layer for gas sensing application. This forms the focus of the current study. Undoped and Au-, Ag- and Cu-doped TiO₂ nanoparticles were hydrothermally synthesised and incorporated into poly(3-hexylthiophene-2,5-diyl) (P3HT) matrix. The solar cells derived from P3HT:TiO₂ (loaded with Au, Ag or Cu NPs) were tested under 100 mW/cm² (AM 1.5 G) irradiation. The findings showed that the solar cell performance and V_{oc} were dependent on the dopant and the doping level. Higher performance and superior V_{oc} of 3.88 % and 0.69V were observed for 0.5 mol. % Ag doped TiO₂ blended in P3HT. Furthermore, the 0.5 mol. % Ag doped TiO₂ blended in P3HT displayed internal series resistance (R_s) and shunt resistance (R_{sh}) values of 11.44 and 266.40 Ω cm²,

respectively. Consequently, based on the performance of the 0.5 mol. % doping of Ag and Cu, the bimetallic Ag/Cu doped TiO₂ nanoparticles were prepared and used in gas sensing and solar cells applications. For gas sensing, the p-type bimetallic Ag/Cu doped TiO₂ nanoparticles-based sensor displayed a timely selective detection of xylene vapour among the BTEX (benzene, toluene, ethylene-benzene and xylene) and acetone vapours at low operating temperature. It was observed that the bimetallic Ag/Cu doped TiO₂ nanoparticles transformed from n-type to p-type at the higher bimetallic Ag/Cu loading. Among the bimetallic Ag/Cu doped TiO₂ nanoparticles, the p-type 0.5% Ag/Cu doped TiO₂ displayed a remarkable response (i.e. sensor resistance in gas/sensor resistance in air, $R_g/R_a \approx 33.2$) towards xylene vapour at 150 °C. The sensor disclosed a greater selectivity, prompt response/recovery speed and good repeatability and stability towards xylene vapour. The heightened xylene gas sensing characteristics could be justified by the catalytic activity and point defects induced by the loading of the bimetallic Ag/Cu in the p-type TiO₂. Besides, the incorporation of bimetallic Ag/Cu doped TiO₂ and ZnO in the poly(3-hexylthiophene) (P3HT) surface, was a promising approach for improving the light-harvesting features of inorganic-organic P3HT:TiO₂-Ag/Cu:ZnO for improved performance. As a result, the higher plasmonic Ag/Cu loading -TiO₂ in P3HT:ZnO displayed a superior open circuit voltage (V_{oc}) of 0.74 V., which resulted to a higher power conversion efficiency of 4.1%. Therefore, the power conversion efficiency (PCE) of bimetallic improved, compared to 3.88% efficiency observed for a single metal loading in TiO₂. The underlying mechanism to the rationalization of the improved PCE for the bimetallic materials can be predominantly ascribed to the strong synergistic influence of larger light scattering, light harvesting and charge

generation and separation efficiency capability, and the plasmonic-enhanced effect induced by the loading of p-type Ag/Cu-TiO₂ nanoparticles



UNIVERSITY *of the*
WESTERN CAPE

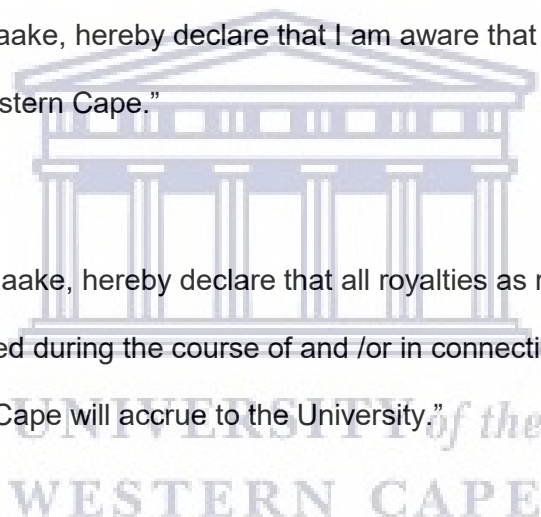
DECLARATION

“Photovoltaic and gas sensing applications of transitional metal nanocomposites of poly(3-hexylthiophene)-titanium dioxide”

(i) “I, Popoti Jacqueline Maake, declare that the Master of Sciences Degree research thesis or interrelated, publishable manuscripts/published articles, or coursework Masters degree thesis that I herewith submit for the Master of Sciences Degree qualification at the University of the Western Cape is my independent work, and that I have not previously submitted it for a qualification at another institution of higher education.”

(ii) “I, Popoti Jacqueline Maake, hereby declare that I am aware that the copyright is vested in the University of the Western Cape.”

(iii) “I, Popoti Jacqueline Maake, hereby declare that all royalties as regards to intellectual property that was developed during the course of and /or in connection with the study at the University of the Western Cape will accrue to the University.”



In the event of a written agreement between the University and the student, the written agreement must be submitted in Lieu of the declaration by the student.

Signature:

Date:


.....

...22 April 2021

DEDICATION

I dedicate this work to my Daughter, Mpho Lauren Maake and to God Almighty.



UNIVERSITY *of the*
WESTERN CAPE

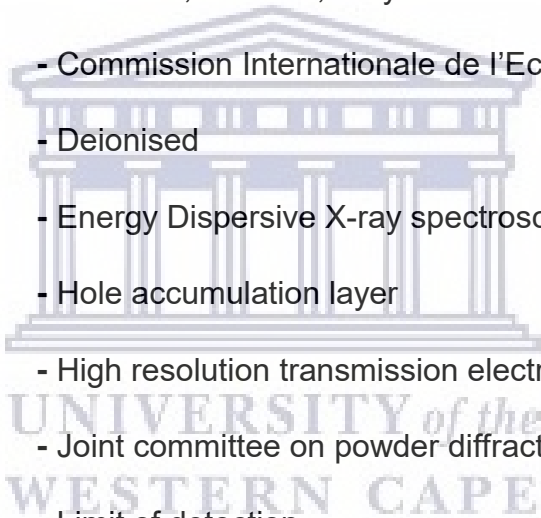
ACKNOWLEDGEMENTS

- I acknowledge the relationship, the fellowship and the communion with the Holy Spirit in my life. I Thank God Almighty for His endless love and the grace of the Lord Jesus Christ for making all things possible.
- I Thank Man of God, Pastor Chris Oyakhilome for the online teaching on the Word of God throughout the COVID-19 pandemic not to faint and being steadfast in my prayer life.
- My outmost gratitude to my supervisor Prof. D.E Motaung (University of Limpopo and Affiliated Professor, University of the Free State) for his advice on my career path and for his support, guidance, commitment, belief and encouragement throughout the work.
- Sincere gratitude to my supervisor Prof. E. Iwuoha (University of the Western Cape) for his support, guidance, commitment throughout the work.
- I am grateful to Dr. A.S. Bolokang (CSIR), Prof. C.J. Arendse (UWC) and Prof. V. Vohra (University of Electro-Communications, Japan) for proof reading and language editing on my review article.
- I am grateful to Dr. Teboho Mokoena and Dr. Ioannis Kortidis for discussions and advices with no complaints.
- Sincere gratitude to Dr. Vincent Ojijo, Mr. Rakgoshi Lekalakala and Mr. Sifiso Skosana for their discussions and advices throughout my Honors degree.
- I am grateful to Ms. Margaret Ward and Prof. Suprakas Sinha Ray for their advice on my career growth.
- Sincere gratitude to CENAM Staff (CSIR) and best team Material Characterization, Testing and Analytical Facility (CSIR) for their support. XPS analyses from University of the Free State are also acknowledged.
- I am profoundly grateful to my siblings for their fervent prayers and support throughout the years.
- Finally, I acknowledge the financial support of the DSI/CSIR HCD studentship and National Research Foundation (NRF).

KEYWORDS

Heterojunction organic solar cell; n-type and p-type semiconductors; plasmonic materials; poly(3-hexylthiophene-2,5-diyl) (P3HT); titanium dioxide gas sensors; volatile organic compounds.

ACRONYMS



BET	- Brunauer-Emmett-Teller
BTEX	- Benzene, Toluene, Ethylenebenzene, Xylene
CIE	- Commission Internationale de l'Eclairage
DI	- Deionised
EDS	- Energy Dispersive X-ray spectroscopy
HAL	- Hole accumulation layer
HRTEM	- High resolution transmission electron microscopy
JCPDS	- Joint committee on powder diffraction standards
LOD	- Limit of detection
MOX	- Metal oxides
PL	- Photoluminescence
P3HT	- Poly(3-hexylthiophene – 2,5 – diyl)
RH	- Relative humidity
SAED	- Selected area electron diffraction
SEM	- Scanning electron microscopy
SMO	- Semiconducting metal oxides
TGA	- Thermo gravimetric analysis

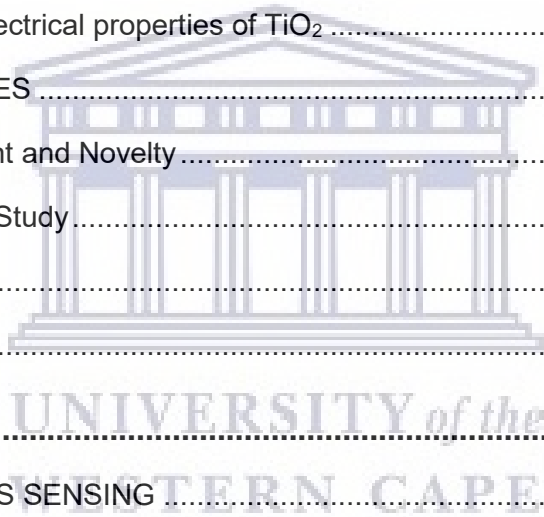
UV	- Ultraviolet
VOCs	- Volatile organic compounds
XPS	- X-ray photoelectron spectroscopy
XRD	- X-ray diffractometer



UNIVERSITY *of the*
WESTERN CAPE

TABLE OF CONTENTS

ABSTRACT	ii
List of Figures and Schemes.....	xiv
List of Tables	xviii
List of Publications.....	xix
National conferences.....	xix
CHAPTER ONE	20
1. INTRODUCTION.....	20
1.2. BULK PROPERTIES OF TiO ₂	20
1.2.1. Structural and Optical Properties of TiO ₂	21
1.2.2. Surface and electrical properties of TiO ₂	23
1.3 AIMS AND OUTLINES.....	27
1.3.1. Problem statement and Novelty.....	27
1.3.2. Objectives of the Study.....	28
1.3.3 Thesis Outline.....	29
1.4. REFERENCES	31
CHAPTER TWO	33
BACKGROUND OF GAS SENSING	33
2.1 BRIEF HISTORY ON GAS SENSING	33
2.2 EXAMPLES OF GASES OF CONCERN	33
2.3 GLOBAL DEMAND FOR SENSORS.....	34
2.4 CLASSIFICATION OF GAS SENSORS	34
2.5 CHARACTERISTICS OF A SENSOR.....	35
2.6. SEMICONDUCTING METAL OXIDE GAS SENSORS	36
2.6.1 Size and Dimension.....	37
2.6.2 Surface Modification by Additives	38
2.6.3. Sensing Mechanism	39
2.7 APPLICATION OF TiO ₂ NANOMATERIALS IN GAS SENSING	40



REFERENCES	46
CHAPTER THREE	51
3.1. INTRODUCTION	51
3.2. INFLUENCE OF NOBLE METALS ON P3HT: PCBM.....	53
3.2.1. Effect of Au on P3HT: PCBM Solar Cell Performance	54
3.2.1.1 Metallic Au NPs embedded the buffer layer	54
3.2.1.2 Metallic Au NPs integrated in active layer of the OPV devices	59
3.2.1.3. Effect of Au on P3HT: PCBM optical and structural properties	63
3.2.2. Effect of Ag on P3HT: PCBM solar cell performance	65
3.2.2.1 Ag NPs embedded in the buffer layer	65
3.2.2.2 Ag NPs embedded in the active layer	69
3.2.2.3. Effect of Ag on P3HT: PCBM optical and structural properties	73
3.3. INFLUENCE OF TiO ₂ METAL OXIDE.....	74
3.3.1. Effect of TiO ₂ on P3HT: PCBM solar cell performance.....	74
3.3.1.1 TiO ₂ embedded in the buffer layer	74
3.3.1.2. TiO ₂ embedded in the active layer	79
3.3.1.3. Effect of TiO ₂ on P3HT: PCBM optical and structural properties	85
3.2.2. Effect of ZnO on P3HT: PCBM performance	86
3.3.2.1. ZnO embedded in the buffer layer	86
3.3.2.2. ZnO embedded in the active layer	90
3.2.2. Effect of ZnO on P3HT: PCBM optical and structural.....	93
3.3.3 Effect of CuO on P3HT: PCBM solar cell performance	97
3.3.1.2 CuO NPs embedded in the active layer	100
3.3.3.3. Effect of CuO on P3HT: PCBM optical and structural properties	103
3.3.4. Influence of bimetallic metal oxide on polymer: PCBM solar cell performance	105
3.3.5. The role of noble metals and metal oxides in organic solar cell stability	105
3.4. CONCLUSION AND REMARKS	107
REFERENCES	109

CHAPTER FOUR	131
CHARACTERIZATION TECHNIQUES	131
4.1 INTRODUCTION	131
4.2 X-RAY DIFFRACTION.....	131
4.3. ELECTRON MICROSCOPE.....	133
4.3.1 Scanning Electron Microscope	133
4.3.2 Transmission Electron Microscope	135
4.4 PHOTOLUMINESCENCE SPECTROSCOPY	136
4.5 X-RAY PHOTOELECTRON SPECTROSCOPY (XPS).....	137
4.6. BRUNAUER-EMMETT-TELLER.....	139
4.7. ELECTRON PARAMAGNETIC RESONANCE (EPR).....	140
4.8. GAS SENSING STATION	142
REFERENCES.....	144
CHAPTER FIVE	146
Superior Open Circuit Voltage Induced by Metals Doping in TiO₂ as a Non-Fullerene Material Towards Organic Solar Cells Performance	146
5.1. INTRODUCTION	146
5.2. EXPERIMENTAL.....	148
5.2.1. Materials.....	148
5.2.2. Synthesis of undoped and doped TiO ₂ nanoparticles.....	148
5.2.3 Characterization	149
5.2.4. Fabrication of Photovoltaic Solar Cell devices	149
5.3. RESULTS AND DISCUSSION.....	150
5.3.1. Structural properties of Au, Ag and Cu doped TiO ₂ nanoparticles.....	150
5.3.2. Morphology analyses of Au, Ag and Cu doped TiO ₂ nanoparticles	152
5.3.3. Chemical state analyses of Au, Ag and Cu doped TiO ₂ nanoparticles	156
5.3.4. Paramagnetic properties of Au, Ag and Cu doped TiO ₂ nanoparticles	160
5.3.5. Incorporation of Au, Ag and Cu TiO ₂ blended in P3HT.....	163
3.5.1. Thermo-gravimetric analyses of Au, Ag and Cu doped TiO ₂ blended in P3HT	163

5.3.6. UV-VIS absorbance spectra of Au, Ag and Cu doped TiO ₂ blended in P3HT.....	164
3.7. Photovoltaic Solar Cells Devices	165
5.4. CONCLUSION.....	170
REFERENCES.....	172
CHAPTER SIX.....	176
Fabrication of P-type Bimetallic Ag/Cu doped TiO₂ Nanoparticles for Dual Application for Selective Detection of Xylene Vapour and Their use in Organic Solar as Non-Fullerene.....	176
6.1. INTRODUCTION.....	176
6.2. EXPERIMENTAL PROCEDURE	179
6.2.1 Materials.....	179
6.2.2. Synthesis of TiO ₂ nanoparticles.....	179
6.2.3. Synthesis of bimetallic Ag/Cu doped TiO ₂ nanoparticles.....	180
6.2.4. Characterization	180
6.2.5. Fabrication of Photovoltaic Devices and Characterization.....	181
6.2.6. Fabrication of Gas Sensor Devices and Characterization	182
6.3. RESULTS AND DISCUSSION.....	182
6.3.1. Structural properties and surface morphology	182
6.3.1.1. Incorporation of bimetallic of Cu and Ag nanoparticles doped TiO ₂	182
6.3.2. Xylene gas sensing mechanism.....	194
6.3.3. Characterization of Solar Cells Devices	203
6.4. CONCLUSION AND REMARKS.....	207
REFERENCES.....	209
CHAPTER SEVEN	216
SUMMARY/CONCLUSION AND FUTURE WORK.....	216
FUTURE WORK.....	217
APPENDIX SECTION	217

LIST OF FIGURES AND SCHEMES

Fig. 1. 1: Crystal structures of TiO ₂ (a) anatase, (b) rutile, and (c) brookite phases [21]. Ball-and-stick model of the rutile (110) - (1×1) surface. The large light balls correspond to O ₂ , while the small black balls are associated to titanium. Vacancies in bridging oxygen rows are common on vacuum-annealed surfaces. The figure also displays two kinds of surface defects, i.e. O ₂ vacancies and Ti interstitials which can influence the surface chemistry.	22
Fig. 1. 2: SEM micrographs of TiO ₂ nanostructures (a) P25-Degussa, (b) P25-Degussa annealed at 700 °C, (c) as-synthesized TiO ₂ washed with 0.5 M HCl (d) 0.5 M HCl annealed at 700 °C, (e) as-synthesized TiO ₂ washed with 1.0 M HCl, (f) 1.0 M HCl annealed at 700 °C.	25
Fig. 1. 3: Selectivity histogram plots of the (a) as-synthesized and (b) annealed at 700 °C TiO ₂ tested towards 40 ppm CH ₄	26
Fig. 2. 1: Schematic diagram of sensing strip [12].	35
Fig. 2. 2: Research studies on MOX for gas sensors [21].	37
Fig. 2. 3: Schematic model on the sensitivity of metal oxide gas sensors [25].	38
Fig. 2. 4: The sensing performance comparison of TiO ₂ , MoS ₂ and Pd-TiO ₂ /MoS ₂ [5].	42
Fig. 3. 1: a) LSP confined in the spherical metallic NP(s) with diameter (a). The SP(s) are excited with the incident photon energy, <i>hν</i> . (b) Architecture of OPV with small spherical NP(s) embedded inside organic active layer. (Reprinted with permission from [14] Copyright 2016: Elsevier).	52
Fig. 3. 2: Schematic diagram displaying the plasmonic materials performance where the light is scattered at different angles as to improve the effective optical path length and absorbing light. a) Light trapping by scattering from metal nanoparticles at surface of the solar cell. b) Light trapping by the excitation of LSPs in metal nanoparticles embedded in semiconductor. c) Light trapping by excitation of surface plasmon polaritons at metal/ semiconductor interface. A corrugated metal back surface couples light to surface plasmon polariton or photonic modes that propagate in the plane of the semiconductor. (Reprinted with permission from [20] Copyright 2010: Nature Materials).	54
Fig. 3. 3: Device characteristics and spectral responses of plasmonic OSCs. Current density-voltage (<i>J-V</i>) characteristics of control device (black squares) and the best plasmonic OSCs with AuNPs (red circles) and Au@AgNCs (blue up triangles) embedded. The filled and open symbols denote the PCDTBT:PC ₇₀ BM (Type II) and PTB ₇ :PC ₇₀ BM devices, respectively. (Reprinted with permission from [35] Copyright 2014: ACS publications).	57

Fig. 3. 4: <i>J-V</i> characteristics of the under AM 1.5G irradiation. (Reprinted with permission from [41] Copyright 2015: Elsevier).....	61
Fig. 3. 5: UV-vis absorption spectrum of Au (a) NSt(s), b) NR(s) and (c) NS(s). Insert shows the SEM image of the nanostructure. (Reprinted with permission from Ref. [50]. Copyright 2016: Elsevier).....	64
Fig. 3. 6: The <i>J-V</i> characteristics and spectral responses of plasmonic OPVs with various size of AnNPs. (a) The <i>J-V</i> curves of the plasmonic OPV (red circles) and the OPV (black squares). The filled and open symbols denote the PDCTBT:PC ₇₀ BM and PTB7:PC ₇₀ BM devices, respectively. The plasmonic devices were optimized in terms of size and concentration. (Reprinted with permission from [56] Copyright 2013: Springer Nature).	66
Fig. 3. 7: (a) <i>J-V</i> characteristics of inverted P3HT:PC ₆₁ BM OSCs and PBCTTT-C-T:PC ₇₁ BM OSCs using TiO ₂ and Au Nps-TiO ₂ as ELTs under solar illumination (AM1.5G) (b) <i>J-V</i> characteristics of the inverted P3HT:PC ₆₁ BM OSCs and PBCTTT-C-T:PC ₇₁ BM OSCs using TiO ₂ and Ag NPs-TiO ₂ as ETLs under solar illumination (AM1.5G).	77
Fig. 3. 8: (a) Under 1 sun illumination and (b) in dark. Forward (-0.1 V → 1.2 V) and backward (1.2 V → -0.1 V) scans are indicated as solid and dashed lines, respectively. (c) <i>J-V</i> curve and (d) EQE spectrum of the best solar cells with TiO _x (thickness ~8 nm)/brookite TiO ₂ electron collector stored in dry air for 2 days. (e) Cross-sectional SEM image of CH ₃ NH ₃ PbI ₃ perovskite solar cells with TiO _x (thickness ~8 nm)/brookite TiO ₂ electron collector. (Reprinted with permission from [92] copyright 2018: ACS Publications).....	83
Fig. 3. 9: <i>J-V</i> characteristics under AM 1.5 G illuminations for different device architecture. (Reprinted with permission from [106] Copyright 2013: ACS Publications).	87
Fig. 3. 10: The structure of the hybrid solar cell based on electrospun ZnO nanofibers and P3HT. (Reprinted with permission from [121] Copyright 2010: ACS Publications).	90
Fig. 3. 11: The <i>J-V</i> characteristic ZnO: P3HT: PCBM thin films with PEDOT: PSS and DMF-modulated PEDOT: PSS. (Reprinted with permission from [123] Copyright 2013: ACS Publications).	91
Fig. 3. 12: Schematic structure of an ITO/ZnO seed layer/ZnO nanorod/P3HT:PCBM/MoO ₃ /Ag photovoltaic device. (Reprinted with permission from [132] Copyright 2011: Elsevier).....	94
Fig. 3. 13: (a) The current-voltage characteristics of the photovoltaic devices under 100 mW/cm ² AM 1.5G irradiation. Inserts: Device A represents the hybrid solar cells with the solution processed fullerene interlayer. Device B denotes the hybrid solar cells without the fullerene interlayer. (b) Energy band diagram for P3HT: PCBM/ZnO nanorod arrays hybrid solar cells. (Reprinted with permission from [139] Copyright 2010: Elsevier).	96
Fig. 3. 14: <i>J-V</i> characteristics of single and double layer polymer solar cells. (Reprinted with permission from [147] Copyright 2013: ACS publications.	98

Fig. 3. 15: <i>J-V</i> characteristics of single and double junction solar cells [158]. Reproduced with permission from [157] Copyright 2015: JETNSR publication).	101
Fig. 4. 1: Schematic diagrams based on conditions for Bragg's law (cited from wikipedia).	132
Fig. 4. 2: The schematic diagram for the XRD set-up [3].	133
Fig. 4. 3: Schematic diagram of SEM [6].	134
Fig. 4. 4: Schematic diagram displaying the TEM set-up [7].	136
Fig. 4. 5: Schematic representation of Nanolog [9].	137
Fig. 4. 6: Schematic diagram of XPS technique [12].	139
Fig. 4. 7: Schematic diagram of BET system [15].	140
Fig. 4. 8: Energy level for an electron spin in applied magnetic field B [16].	141
Fig. 4. 9: Schematic diagram of electron paramagnetic resonance [17].	142
Fig. 4. 10: KENOSISTEC KSGAS6S Italy gas sensing station. (Reprinted with permission from Ref. [19]. Copyright 2019: Elsevier).....	143
Fig. 5. 1: XRD patterns of (a) Au doped TiO ₂ , (b) Ag doped TiO ₂ and (c) Cu doped TiO ₂ . Note (d-f) corresponds to insets of Fig. 5.1a-c, respectively.	151
Fig. 5. 2: SEM images of various concentration of Ag, Au, Cu and pure TiO ₂	153
Fig. 5. 3: TEM micrographs of (a-b) 0.5 mol.% Au, (d-e) 0.5 mol. % Ag and (g-h) 0.5 mol.% Cu doped TiO ₂ samples. Note: (c, f and i) correspond to SAED patterns of 0.5 mol.% Au, Ag and Cu doped TiO ₂ , respectively.....	154
Fig. 5. 4: N ₂ -adsorption-desorption isotherms of the pure and doped TiO ₂ nanoparticles.	155
Fig. 5. 5: The XPS analyses of (a-c) 0.1, 0.5 and 2.0 mol.% Au, (d-f) 0.1, 0.5 and 2.0 mol.% Ag and (g-i) 0.1, 0.5 and 2.0 mol.% Cu doped TiO ₂ samples.	158
Fig. 5. 6: The XPS O 1s core levels of (a-c) 0.1, 0.5 and 2 mol.% Au, (d-f) 0.1, 0.5 and 2 mol.% Ag and (g-i) 0.1, 0.5 and 2 mol.% Cu doped TiO ₂ samples.	159
Fig. 5. 7: EPR measurement of TiO ₂ doped with various concentration (0.1, 0.5, 1 and 2 mol.%) of (a) Au, (b) Ag and (c) taken at room temperature with microwave power of 5mW.	161
Fig. 5. 8: TGA graphs of Au, Ag, Cu doped TiO ₂	163
Fig. 5. 9: UV/vis absorbance spectra of (a) P3HT blended with various concentrations of (a) Au, (b) Ag and (c) doped in TiO ₂ . The blended materials are prepared in a 1:1 wt. ratio of P3HT:TiO ₂ -dopants (i.e Au, Ag and Cu).....	165
Fig. 5. 10: <i>J-V</i> curves of the doped TiO ₂ blended in P3HT solar cells.....	167
Fig. 5. 11: PCE and V _{OC} as a function of doping level of metals in TiO ₂ blended in P3HT solar cells.....	168
Fig. 6. 1: (a) XRD patterns of bimetallic Ag/Cu doped TiO ₂ nanoparticles and (b) magnified patterns showing (101) and (110) peaks.	183

Fig. 6. 2: SEM micrographs of the (a) pure TiO ₂ , bimetallic Ag/Cu doped TiO ₂ nanoparticles (b) 0.1 % mol. Ag/Cu, (c) 0.5 mol.% Ag/Cu, (d) 0.1 mol.% Ag /0.5 mol.% Cu and (e) 0.5 mol.% Ag/ 0.1 mol.% Cu.	185
Fig. 6. 3: (a) Resistance in air of various bimetallic Ag/Cu doped TiO ₂ nanoparticless ensors at various operational temperature, (b) benzene, (c) toluene, (d) ethylene-enzene, (e) xylene and (f) acetone.....	188
Fig. 6. 4: Real-time resistance plot of various sensors tested to xylene vapour at (a) 100 and (b) 150 °C.	189
Fig. 6. 5: Response curves for pure TiO ₂ and bimetalic Ag/Cu nanopartlces based sensors tested towards (a) benzene, (b) toluene, (ethlyene-enzene, (d) xylene and (e) acetone. Note (f) corresponds to real-time response curve of bimetallic 0.5 mol.% AgCu doped TiO ₂ based sensor towards xylene.	190
Fig. 6. 6: (a) Radar selectivity plot (a-b) repeatability and stability plot of bimetallic 0.5 mol.% Ag/Cu doped TiO ₂ nanoparticle based sensor towards 80 and 100 ppm xylene over seven days at 150 °C and (c) Response versus number of days (i.e. stability) plot of bimetallic 0.5 mol.% Ag/Cu doped TiO ₂ nanoparticle based sensor towards 100 ppm xylene vapour at 150 °C. Note letters A correspond to acetone, while others are BTEX in radar plot, i.e Fig. 6.6a.	192
Fig. 6. 7: Room temperature PL spectra of (a) undoped and bimetallic AgCu doped TiO ₂ nanoparticles, and (b-e) In-situ PL spectra of bimetallic AgCu doped TiO ₂ nanoparticles conducted from 25 to 150 °C.....	196
Fig. 6. 8: In-situ PL fitted spectra of at different temperatures (a-c) 0.1 % mol. Ag/Cu (d-f) 0.1% mol. Ag/0.5 mol.% Cu, (g-i) 0.5 mol.% Ag /0.1 mol.% Cu and (j-l) 0.5 mol.% Ag/Cu of at 25, 100 and 150 °C, respectively.....	197
Fig. 6. 9: Ti2p XPS spectra of (a) 0.1 mol.% Ag/Cu, (b) 0.1 mol.% Ag/0.5 mol.% Cu, (c) 0.5 mol.% Ag/ 0.1 mol.% Cu ad (d) 0.5 mol.% Ag/Cu. Note (e-h) correspond to O 1s spectra of (e) 0.1 mol. % Ag/Cu, (f) 0.1 mol.% Ag /0.5 mol.% Cu, (g) 0.5 mol.% Ag/ 0.1 mol.% Cu and 0.5 mol.% Ag/Cu bimetallic doped TiO ₂ nanoparticles.....	199
Fig. 6. 10: (a-d) Cu2p (a) 0.1 mol.%. Ag/Cu, (b) 0.1 mol.% Ag/0.5 mol.%Cu, (c) 0.5 mol.% Ag /0.1 mol.% Cu and (d) 0.5 mol.% Ag/Cu, and (e-h) Ag 3d of (e) 0.1 mol.% Ag/Cu, (f) 0.1 mol.% Ag/0.5 mol.%Cu, (g) 0.5 mol.% Ag /0.1 mol.% Cu and (h) 0.5 mol.% of the bimetallic Ag/Cu doped TiO ₂ nanoparticles.	201
Fig. 6. 11: N ₂ adsorption-desorption isotherms of the (a) 0.1 mol. % AgCu, 0.1 mol.% Ag0.5 mol.%Cu, (c) 0.5 mol.% Ag /0.1 mol.% Cu and (d) 0.5 mol.% Ag/Cu of the bimetallic Ag/Cu doped TiO ₂ nanoparticles.....	203
Fig. 6. 12: I-V characteristics of the P3HT blended with 0.1 mol. % Ag/0.5 mol.%Cu, (c) 0.5 mol.% Ag /0.1 mol.% Cu and (d) 0.5 mol.% Ag/Cu of the bimetallic Ag/Cu doped TiO ₂	

nanoparticles recorded under illumination (AM1.5G), (b) I_{sc} and V_{oc} as a function of Ag and Cu contents, and (c) UV-Vis spectra of P3HT incorporated with TiO_2 doped with Ag/Cu concentrations..... 206

LIST OF TABLES

Table 1.1: Summary of the elementary characteristics of TiO_2 phases [7, 8].	23
Table 2. 1: Xylene sensing properties of SMO sensor.	43
Table 2. 2: Comparison study based on TiO_2 gas sensors for CO, C_7H_8 and C_8H_{10} .	45
Table 3. 1: Device characterization data of OPV with metallic AuNPs in buffer layer	58
Table 3. 2: Device characterization data of OPV with metallic AuNPs in active layer	62
Table 3. 3: Device characterization data of OPV with metallic AgNPs in buffer layer	68
Table 3. 4: Device characterization data of OPV with metallic AgNPs in active layer	71
Table 3. 5: Device characterization data of OPV with TiO_2 in buffer layer	78
Table 3. 6: Summary of device characterization data of OPV with using TiO_2 in the active layer	84
Table 3. 7: Device characterization data of OSCs with ZnO in the buffer layer.	89
Table 3. 8: Device characterization data of OPV with ZnO in the active layer.	93
Table 3. 9: Device characterization data of OPV with metallic CuO in buffer layer.	100
Table 3. 10: Device characterization data of OPV with metallic CuO in active layer.	103
Table 5. 1: Crystallite size and crystal lattice of Au, Ag and Cu doped TiO_2	152
Table 5. 2: Summary of EPR data related to number of spins, g-factor and assignments of the peaks for the Au, Ag and Cu doped TiO_2 nanoparticles [39-41].	162
Table 5. 3: Summary of solar cells parameters.	170
Table 6. 1: Summary of the crystallite size and lattice strain of bimetallic Ag/Cu doped TiO_2	183
Table 6. 2: Summary of pure, doped and heterostructure derived from TiO_2 sensors for detection of xylene vapour.	193
Table 6. 3: Summary of photovoltaic properties extracted under illumination (AM1.5G).	207

LIST OF PUBLICATIONS

1. **Popoti J. Maake**, Amogelang S. Bolokang, Christopher J. Arendse, Varun Vohra, Emmanuel I. Iwuoha, David E. Motaung.
Metal Oxides and Noble Metals Application in Organic Solar Cells”
Solar Energy 207 (2020) 347–366.
2. **Popoti J. Maake**, Teboho P. Mokoena, Amogelang S. Bolokang, Hendrik C. Swart, Emmanuel I. Iwuoha, David E. Motaung.
Fabrication of P-type Bimetallic Ag/Cu doped TiO₂ Nanoparticles for Dual Application for Selective Detection of Xylene Vapour and Their use in Organic Solar as None Fullerene
ACS Applied Material and Interfaces (2021) Submitted

NATIONAL CONFERENCES

1. **Popoti P. Maake**, E. Iwuoha, D.E. Motaung, Incorporation of Transitional and Noble Metals Nanostructures in P3HT:TiO₂ Blends and their Applications in Photovoltaics and Gas Sensing, The 56th Congress of the Microscopy Society of Southern Africa.



CHAPTER ONE

BACKGROUND OF THE STUDY

1. INTRODUCTION

Semiconductor metal oxide titanium dioxide (TiO_2) material has been considered as a vital material because of its striking features, with respect to economic point of view, like affordability, enormous availability and ecology, e.g. non-toxic, and comprehensive physical and chemical possibilities. In the recent years, the advancement of nanoscience and nanotechnology presented innovative prospects, not only in an academic perception, nonetheless also with a vision to countless applications. Thus, this chapter provides an overview on the application of TiO_2 on gas sensing and organic photovoltaic solar cells. Where in gas sensing, the TiO_2 is used as a sensing layer and while in solar cells is used as an electron acceptor or donor when prepared as an n-type or p-type material, respectively. Thorough discussion based on the structure, optical, surface and electrical characteristics of TiO_2 are also discussed.

1.2. BULK PROPERTIES OF TiO_2

TiO_2 is extremely imperative in research due to its very remarkable electronic structures and wide band gap of approximately 3.2 eV that maybe tailored in various synthesis methods. It possesses extensive range of industrial and high-tech applications as photo catalyst, pigment, and ultra-violet absorption. Therefore, TiO_2 is a vital material, which is very appropriate for fuel cells, solar cells, sensors, etc. The properties such as nontoxicity, chemical stability, high refractive index, etc. contribute strongly to its practical application.

1.2.1. Structural and Optical Properties of TiO₂

TiO₂ is a certainly occurring mineral which occurs in three crystal structures, like anatase, rutile and brookite (see Fig. 1.1) depending on the synthesis conditions [1-3]. At low temperature, the anatase phase is stable. The brookite phase is metastable and at high temperatures it changes to rutile. The anatase and rutile phases possess P4₂/mnm tetragonal structure. Brookite possesses the orthorhombic structure [4]. While at higher temperatures, it changes to rutile. Studies have shown that anatase TiO₂ reveals improved photocatalytic behaviour, leading in enormous photocatalytic applications [5]. Furthermore, due to its stability, rutile phase is extensively employed for high temperature applications in mining industries for detection of methane gas. The rutile phase is the thermodynamically utmost stable. The (110) face contains the lowest surface energy and is the most strongly investigated surface. The (1×1) surface bulk-terminated is presented in Fig. 1.1d. One noticeable instance of the effect of bulk defects on the surface structure is the look of crystallographic shear planes on the surface. On very diminished, dark samples, they evident themselves as half-height steps running alongside definite crystallographic directions [6]. Only comparatively bright samples display entirely the (1×1) surface structure, see Fig. 1.1. Diebold [6] presented a detailed discussion related to the structure and reconstructions of other pertinent low-index rutile surfaces is are deliberated elsewhere [7, 8]. Alongside the direction of the [001], rows of six-fold-coordinated Ti atoms (as in the bulk) alternating with five-fold-coordinated Ti atoms with one 'dangling bond' that is perpendicular to the surface. The two types of oxygen (O₂) atoms exist. The O₂ that exists in the main surface plane are three-fold-coordinated as in the bulk. The supposed bridging oxygen

atoms are two-fold coordinated. Table 1.1 lists the crystal structure, lattice parameters, band gap values and associated parameters of various TiO₂ phases.

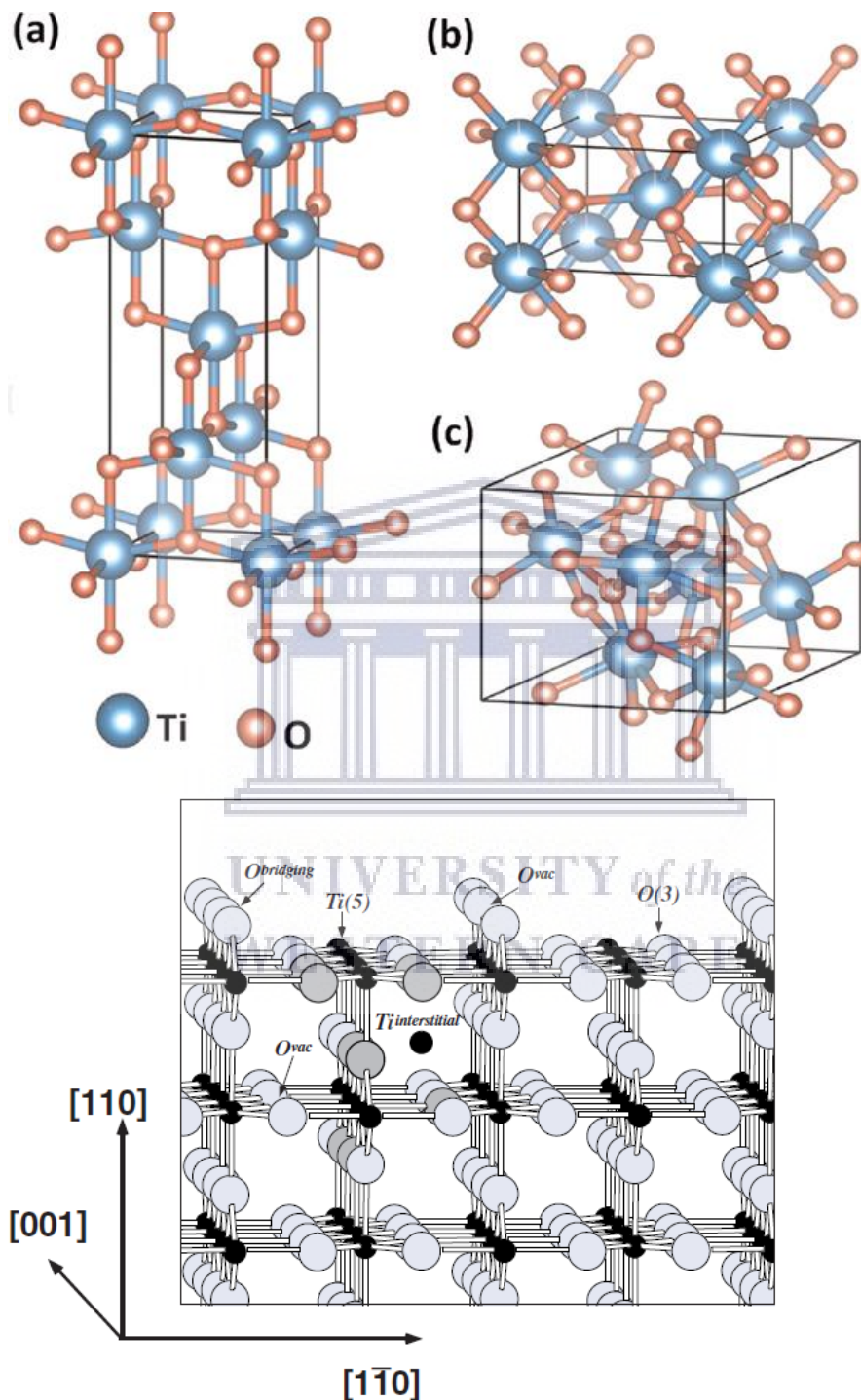


Fig. 1. 1: Crystal structures of TiO₂ (a) anatase, (b) rutile, and (c) brookite phases [21]. (d) Ball and stick model of the rutile (110) - (1x1) surface. The large light balls correspond to O₂, while the small black balls are associated to titanium. Vacancies in bridging oxygen rows are common on vacuum-annealed surfaces. The figure also displays two kinds of surface defects, i.e. O₂ vacancies and Ti interstitials which can influence the surface chemistry [6].

Table 1.1: The the elementary characteristics of TiO₂ phases summary [7, 8].

Properties	Anatase	Rutile	Brookite
Crystal structure	Tetragonal	Tetragonal	Orthorhombic
Atoms per unit cell (Z)	4	2	8
Lattice parameters (nm)	a= 0.3785 c= 0.9514	a= 0.4594 c= 2.9587	a=9.184 b=5.447 c=5.145
Point group	4/mmm	4/mmm	mmm
Space group	I4 ₁ /amd	P4 ₂ /mnm	Pbca
Density (kg. m ⁻³)	3894	4250	4110
Hardness (Mohs)	5.5 - 6	6 -6.5	5.5-6
Bulk Modulus (GPa)	183	206	245
Theoretical band gap (eV)	3.23	3.0	4.1

1.2.2. Surface and electrical properties of TiO₂

The surface plays an important role in nanomaterials, since it enables interaction between reagents and the material. The surface chemistry of TiO₂ is swayed by the circumstance that it contains a combination of ionic and covalent bonding. By manipulating the surface characteristics of the TiO₂, the material's performance or behaviour can be enhanced. Studies have shown that incorporation of impurities or either by doping of introducing another semiconductor metal oxide structure can strongly influence the properties of the TiO₂ on the surface [5], by sensitizing [9],

and by controlling the size at the nanoscale. Usually, infiltration of impurities results to a distortion of the lattice, which further lead to further defect states by replacing the Ti^{4+} ions in the lattice. Studies have conveyed that the TiO_2 nanomaterials display considerably various physical and chemical characteristics in comparison to bulk materials [10, 11]. This is due to the nanostructured grains are virtually depleted of charge carries ever since utmost are trapped on the surface. Once they are exposed to the tested target gases they display pronounced conductivity in comparison to air [12]. The porosity of the manipulated nanomaterial is also considered as a prompting factor, since it promotes the adsorption-desorption of target gas. Moreover, the nanomaterials size and dimensions also play a vital important part on the performance of both gas sensing and solar devices. Studies have reported that small particle sizes or tailored structure are advantageous to TiO_2 -based devices [9]. The quantum confinement influence directs the phonons and photons transport features and consequently electrons and holes transport within the nanostructures. For instance, the scanning electron microscopy (SEM) micrographs displayed in Fig. 1.2 denote that the morphology of the TiO_2 nanostructures changes with annealing conditions [13]. Such changes played a vital role on the gas sensing performance towards CH_4 gas is depicted in sensing responses of the TiO_2 sensors in Fig. 1.3. Tshabalala et al. [13] observed that samples annealed at higher operating temperature, illustrated higher sensing performance in comparison to those prepared at low temperature due to transformed morphology, which further resulted to higher surface area [13]. Detailed discussion on the TiO_2 for gas sensing application is given chapter 2 of this thesis.

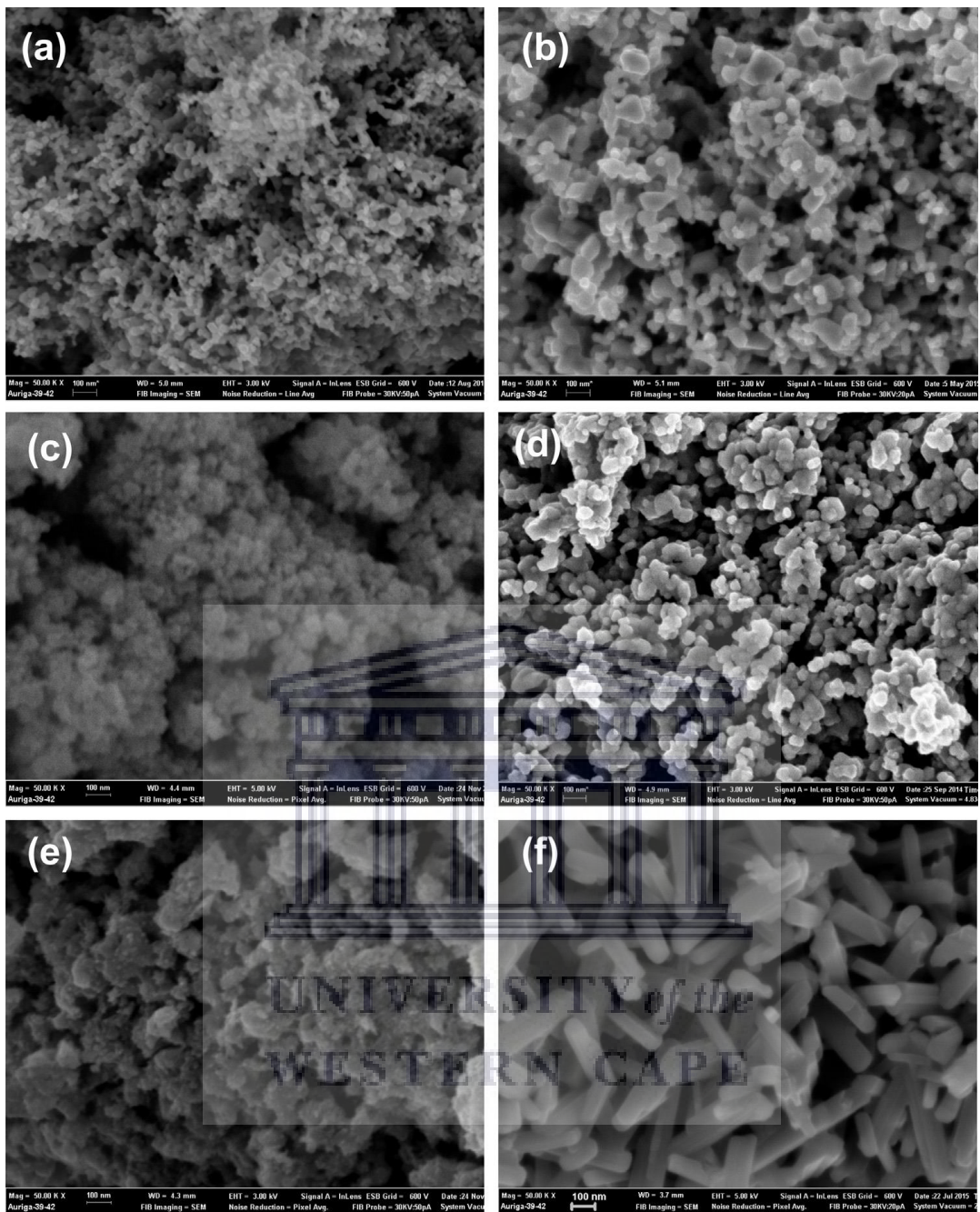


Fig. 1. 2: SEM micrographs of TiO₂ nanostructures (a) P25-Degussa, (b) P25-Degussa annealed at 700 °C, (c) as-synthesized TiO₂ washed with 0.5 M HCl (d) 0.5 M HCl annealed at 700 °C, (e) as-synthesized TiO₂ washed with 1.0 M HCl, (f) 1.0 M HCl annealed at 700 °C.

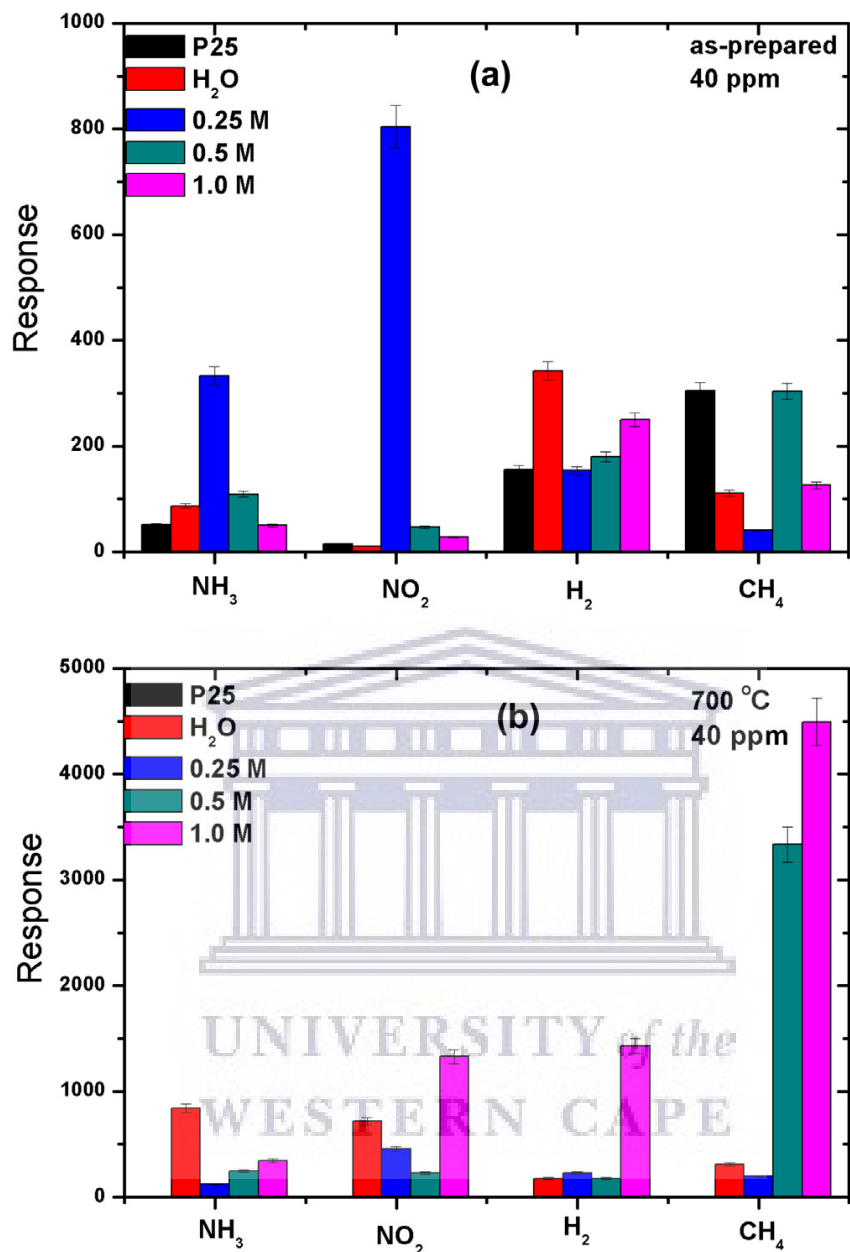


Fig. 1. 3: Selectivity histogram plots of the (a) as-synthesized and (b) annealed at 700 °C TiO₂ tested towards 40 ppm CH₄.

Additionally, with respect to photovoltaic (PV) application, studies have also noted that the TiO₂ physical and chemical characteristics are not only influenced by the intrinsic electronic structure, nevertheless also by their size, shape, surface features, etc. [14]. Various morphologies have been developed and applied in PV devices. Commonly, it is critical to exploit the TiO₂ specific surface area in order to enable the

reaction at the TiO₂ interface and the interrelating media. In addition to superior surface area, the nanostructures ought also to possess superior electron mobility in a way that the ejected electrons in the TiO₂ may be collected efficiently. Since the defects in TiO₂ tends to behave as electron traps and occur in grain boundaries at the contacts between nanoparticles, the utilization of a network structure entailing of TiO₂ single nanocrystal, such as nanowires rather than nanoparticles are anticipated to persuade a pronounced enhancement for prompt electron transportation. Nonetheless, such proposal has not been established thus far and the TiO₂ nanostructure endures to deliver optimised findings in PVs, in spite of the existence disorder. In addition, the TiO₂ characteristics intensely convey on the alterations of the nanomaterial host, such as organic molecules, ions, and inorganic materials) and on the interfaces of TiO₂ nanomaterials with the surroundings. The surface alteration does not only influence the interfacial energy offset, nonetheless it also contains substantial influence on the charge separation and transport, and as well as the recombination processes [15]. Our recent review article has shown that when the TiO₂ is used as either buffer or an active layer it improved the solar cell performance. Detailed discussion related to the use of TiO₂ in photovoltaic solar cells can be found in our published review article, which falls under chapter three [14] and ref. [15].

1.3 AIMS AND OUTLINES

1.3.1. Problem statement and Novelty

Though fabrication of semiconductor metal oxide (SMO) nanomaterials with various properties has been realized in the past, nonetheless the fabrication of SMO possessing multi-functional active structure properties that can be utilized in gas sensing application and photovoltaic solar cells and still display superior sensing

performances (such as superior sensitivity, quick response-recovery rates) and photovoltaic performances (e.g. best light harvesting, rapid charge separation and transport, etc.) still present significant scientific challenges. The on-going research interest in the fabrication of such materials is motivated by the augmented emission of toxic gases in the industrial processes that lead into detrimental threat to public health and environmental sustainability. Thus, the current research aims to fabricate the TiO₂ nanomaterials that are doped with noble and transitional metals, such as silver, gold and copper and also the fabrication of an n-type and p-type bimetallic Ag/Cu doped TiO₂ nanoparticles. The individual and bimetallic Ag/Cu doped TiO₂ will be used for solar cell application and gas sensing for selective detection of xylene vapour among the BTEX (benzene, toluene, ethylene-benzene and xylene) and acetone vapours at low operating temperature.

1.3.2. Objectives of the Study

Objective of this dissertation:

- Synthesis and optimization of pure and Au, Ag and Cu doped TiO₂ by microwave assisted hydrothermal method.
- Study the structural properties of the materials using X-ray diffraction, X-ray photo-electron spectroscopy and transmission electron microscope.
- Study the morphological and optical properties of the material by scanning electron microscope and photoluminescence.
- Investigate the application undoped and doped TiO₂ in solar cells and gas sensors
- Design, optimization and fabrication of TiO₂ based sensor by introducing the bimetallic Ag/Cu and their testing towards BTEX, i.e. benzene, toluene,

ethylene-benzene and xylene and acetone for selective detection of xylene in the presence of other interference gases, such as BTE and acetone and study the electrical resistivity and gas response.

1.3.3 Thesis Outline

Chapter One: Structural, morphological and optical Properties of TiO₂

- This chapter discusses the structural, morphological and optical properties of TiO₂ and their effect on the gas sensing and solar cell applications.

Chapter Two: Background and Literature Review on Gas Sensing

- Chapter two focuses on the literature review of TiO₂. The characteristics, different properties, structure and particle morphology that can be achieved and their effect on the gas sensing properties

Chapter Three: Background and Literature review on Solar Cells

- Chapter three focuses on the background and literature review of TiO₂ on solar cells applications. We discuss the effect of the noble metals and transional metals doping on the TiO₂ solar cells application and the use of TiO₂ as buffer layer and active layer.

Chapter Four: Characterization Techniques

- Chapter four deals with the theoretical background of analytical techniques used in this thesis.

Chapter Five:

- Synthesis of pure TiO₂ oxide the Cu, Ag and Au nanoparticles

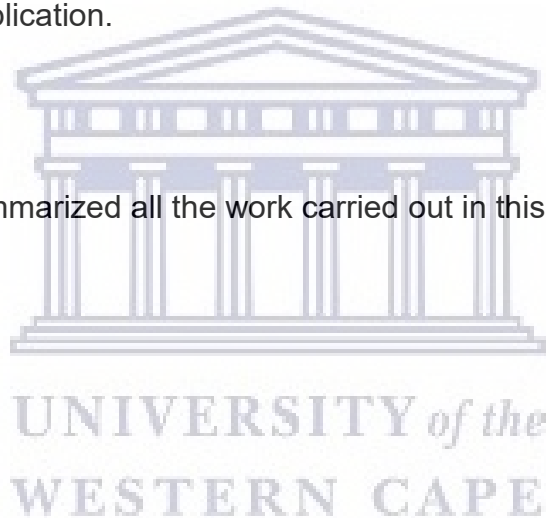
- Study the optical, morphological, and structural properties of the synthesized doped TiO₂ nanoparticles using Cu, Ag and Au and their optimization in photovoltaic solar cell application.

Chapter Six:

- Chapter six deals with the optimized and synthesis of bimetallic Ag/Cu doped TiO₂ nanoparticles.
- Study the effect of optimized bimetallic Ag/Cu doped on the structure, crystallite size, morphological properties and their performance in gas sensing and solar cell application.

Chapter Seven

- This chapter summarized all the work carried out in this thesis.



1.4. REFERENCES

1. Diebold, U., 2003. The surface of titanium dioxide, *Surf. Sci. Rep.* 48, pp.53-229.
2. Hanaor, D.A.H., Sorrell, C.C., 2011. Review of the anatase to rutile phase transformation, *J. Mater. Sci.* 46, 855-874.
3. Chen, X., Mao, S.S., 2007. Titanium dioxide nanomaterials: synthesis, properties, modifications, and applications, *Chem. Rev.* 107, pp.2891-2959.
4. Fujishima, K., 1972. Honda, Electrochemical photolysis of water at a semiconductor Electrode, *Nature* 23, pp.37-38.
5. De Angelis, F., Di Valentin, C., Fantacci, S., Vittadini, A., Selloni, A., 2014. Theoretical studies on anatase and less common TiO₂ Phases: Bulk, surfaces, and nanomaterials, *Chem. Rev.* 114, 9708–9753.
6. U. Diebold, 2003. Structure and properties of TiO₂ surfaces: a brief review, *Appl. Phys. A* 76, pp.681–687.
7. Gong, X.-Q., Selloni, A., Batzill M., Diebold, U., 2006. Steps on anatase TiO₂(101), *Nature Materials*, 5, pp.665–670
8. Diebold, U., In: *The chemical physics of solid surfaces*, Vol. 9, ed. By D.P. Woodruff (Elsevier, Amsterdam 2001) pp. 443
9. Ito, S., Zakeeruddin, S.M., Humphry-Baker, R., Liska, P., Charvet, R., Comte, P., Nazeeruddin, M.K., Penchy, P., Takata, M., Miura, H., Uchida, S., Gratzel, M., 2006. High-Efficiency organic-dye-Ssensitized solar cells controlled by Nanocrystalline-TiO₂ Electrode Thickness, *Adv. Mater.* 18, pp.1202-1205.
10. Zhou, W., Liu, H., Boughton, R.I., Du, G., Lin, J., Wang, J., Liu, D., 2010. One-dimensional single-crystalline Ti–O based nanostructures: properties, synthesis, modifications and applications, *J. Mater. Chem.* 20, pp.5993-6008.
11. Yamazoe, N., New approaches for improving semiconductor gas sensors, 1991. *Sens. Actuators, B* 5, pp.7-19.
12. Huang, J., Wan, Q., 2009. Gas Sensors Based on Semiconducting Metal Oxide One-Dimensional Nanostructures, *Sensors* 9, pp.9903-9924.
13. Tshabalala, Z.P., Shingange, K., Dhonge, B.P., Ntwaeaborwa, O.M., Mhlongo, G.H., Motaung, D.E., 2017. Fabrication of ultra-high sensitive and selective CH₄ room temperature gas sensing of TiO₂ nanorods: Detailed study on the annealing temperature, *Sensors and Actuators B: Chemical* 238, pp.402–419.
14. Maake, P.J., Bolokang, A.S., Arendse, C.J., Vohra, V., Iwuoha, E.I., Motaung, D.E., 2020. Metal Oxides and Noble Metals Application in Organic Solar Cells, *Solar Energy* 207, pp. 347–366.

15. Bai, Y., Iván M.-S., De Angelis F., Bisquert, J., Wang, P., 2014. Titanium Dioxide Nanomaterials for Photovoltaic Applications, *Chem. Rev.*, 114, 19, pp.10095–10130



UNIVERSITY *of the*
WESTERN CAPE

CHAPTER TWO

BACKGROUND OF GAS SENSING

2.1 BRIEF HISTORY ON GAS SENSING

Chemical sensor is a device that alters chemical data ranging from concentration of a particular sample component to total composition analysis into useful analytical signal according to the International Union of Pure and Applied Chemistry (IUPAC) [1]. Gas sensors monitor and detect leakages and fires. Suitable gas detector is of utmost important requirement in various sectors such as food industries, which uses gas sensor to detect volatile organic compounds released from rotten food [2]. The environmental sector detects the toxicity and pollutants released in the environment such as carbon. Safety of employees in industrial sector is extremely important hence the use of gas detector during and after production in gas production, laboratory activities, fermentation, and mining [3, 4]. Health sector also use breath analyzer for early detection of condition such as cancer and diabetes. Recent applications in mobile phones are providing a platform that allows integrating sensors and identifying harmful threads in personal environment [5].

2.2 EXAMPLES OF GASES OF CONCERN

Global warming is the main concern nowadays because of gas pollutants in the air resulting in health hazards. Longer period inhalation of gases such as carbon monoxide (CO), carbon dioxide (CO₂), ammonium, nitrous oxide (N₂O), sulphur dioxide (SO₂) and Hydrogen sulfide (H₂S) can result in fatality. Hence, monitoring such gases is important to assist in prevent occurrence of fatal accidents such is fire

and explosions. Industrial emission is the main cause of pollutants mostly in road transport and maritime which results in nitrogen oxide (NO_x) and carbon dioxide. Wherefore, NO_x contribute to depletion of ozone in stratosphere. Moreover, NO_x and SO₂ results in formation of acid rain [6]. The burning of carbon in coal industries result in the by-product of carbon dioxide wherein excess can result in suffocation and contribute to global warming. Also burning of coal oxidizes to yield CO, which hinders supply of oxygen into body tissue causing seizures and death [7, 8] in humanity. The Hydrogen sulfide (H₂S) naturally in human body occurs as a waste product. However, exposure to H₂S greater than 10 ppm is poisonous to human organ and can result in death [9].

2.3 GLOBAL DEMAND FOR SENSORS

European Union estimated 400 000 premature deaths due to urban air pollution effect in European Union. Hence, European Commission adopted an edict in December 2013 that determines the air objectives until 2030 that strictly permit national emission for six pollutants [10]. Moreover, the industrial market in United States of America has reported in 2009 the demand for sensors with annual average increment rate of 4.6% since 2004. Occupational health and safety standard implementation is becoming compulsory in many countries this positively influence the demand of gas sensors. In 2013, the market report estimated \$1.782 million for gas sensors with a compound annual growth rate of 5.1% expected in 2020 [11].

2.4 CLASSIFICATION OF GAS SENSORS

Usually, a gas sensor comprises of electrode, substrate, heater and sensitive layer. The sensitive layer is a made of material that is placed on the substrate. This

sensitive layer interacts with target gas to measure the change in chemical or physical properties. Whereas, the electrode measure the changes caused by analyte present shown as analytical signal to give interpreted data. While, heater control the temperature of sensor. A schematic diagram below shows gas sensor in Fig. 2.1.

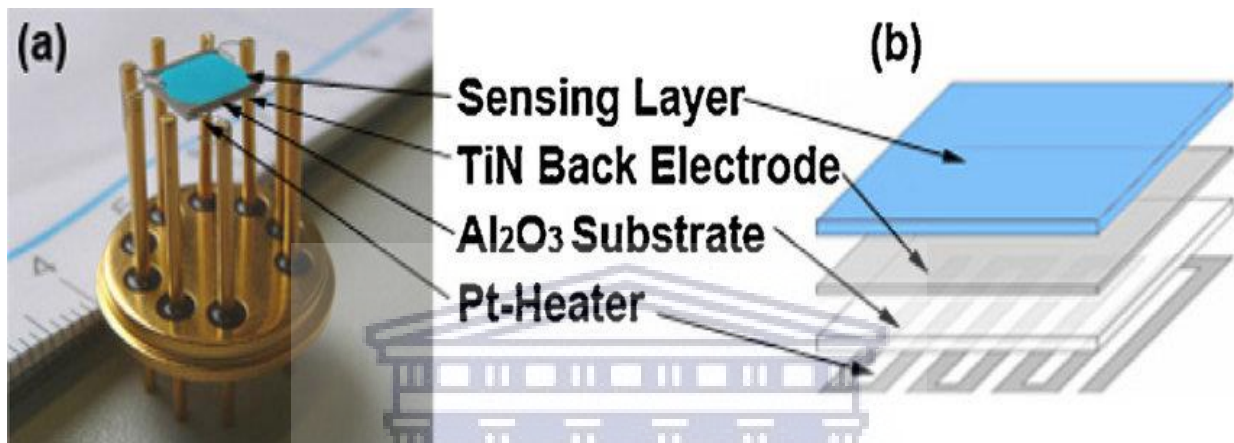


Fig. 2. 1: Schematic diagram of sensing strip [12].

There are different types of gas sensors in terms of sensitive such as semiconductor metal oxide that measures the electrical conductivity properties, Optical sensors that measure luminescence, absorbance and refractive index properties, calorimetric for temperature measurement, Piezoelectric sensor that measure mass properties and Electrochemical sensor that measure the electromotive force properties among the many list of gas sensors classification [13].

2.5 CHARACTERISTICS OF A SENSOR

The aim of research in gas sensing devices is overcoming the challenges of sensitivity, selectivity, fast response time and recovery time, stability and low working

temperature. Characteristic that governs the performance of sensing devices are as follow [14, 15]

- Sensitivity (S) is a measured signal change per analyte concentration unit given by the relationship: $S = [(R_{air} - R_{gas})/R_{gas}]$
- Whereas the detection limit is the analyte smallest concentration that the sensor can detect at a particular given temperature calculated as:

$$LOD = 3 [Noise_{rms}/S]$$

- Selectivity refers to the sensor's capability to respond to selective group analytes or specific analyte.
- Response time is required time for sensor to react to certain gas group.
- Recovery time is time recovered by sensor signal back to initial state after removal of target gas.
- Working temperature is the temperature needed to heat sensor to its maximum sensitivity.
- Stability in sensor is the ability to generate reproducible results for a certain period.
- Lifetime is the period at which sensor will constantly operate.

2.6. SEMICONDUCTING METAL OXIDE GAS SENSORS

Semiconductors metal oxides (SMO) got attention ever since Brattain et al. in 1952 established a change in resistivity of germanium exposed in mixture of gases [16]. Subsequently, Seiyama et al. [17] in 1962 reported that ZnO thin films change electrical conductivity when exposed to propane at 485 °C. Moreover, Shaver in 1967 explain the effect of enhancing selectivity and sensitivity of noble metals on

electrical properties of SMO [18]. Taguchi [19] became the first to develop chemoresistive gas sensing devices using SnO₂ as sensitive material.

Today advancement in material science and fabrication process allows improved sensitivity and reliability that are cost effective [20]. The diverse applications of metal oxide semiconductors in gas sensing, solar cells and photo-catalysis is due to good thermal stability and high temperature operation. Most nanostructure SMO i.e., SnO₂, ZnO, TiO₂, WO and CuO are advancing owing to their practical sensitivity to various gases such as NO₂, NH₃, CO, H₂ and CH₄, H₂S. The most used MOX as sensing materials are SnO₂, ZnO and TiO₂ as shown in fig 2.2 on the flow chart below.

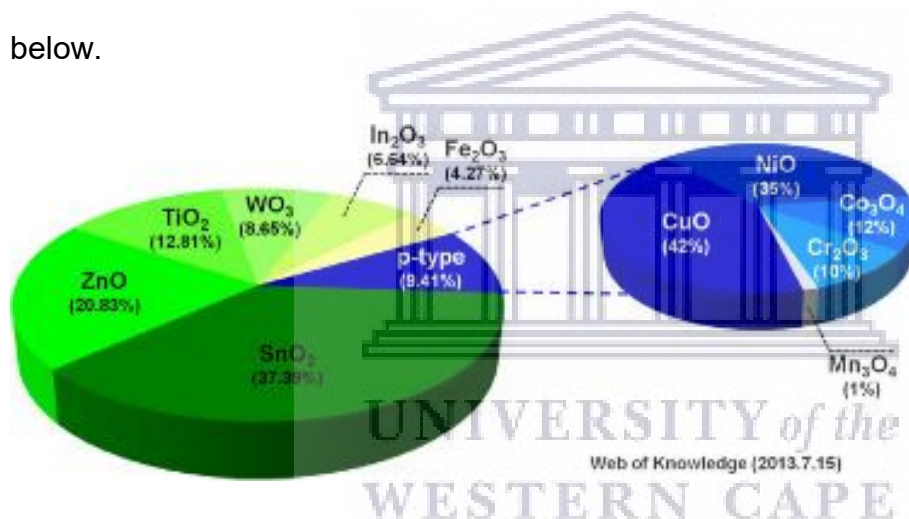


Fig. 2. 2: Research studies on SMO for gas sensors [21].

2.6.1 Size and Dimension

Tuning of material grain size during synthesis enhance sensitivity of SMO [22, 23]. Semi-quantitative model of high response material is obtaining with grain size (D) greater than two times the thickness (L) of surface charge layer ($D \gg 2L$). The model suggests that when $D \gg 2L$, the sensitivity is independent of D and the structure is not sensitive. Nonetheless, when $D \geq 2L$ influence the sensing material conductivity and define size dependence of gas sensitivity. Extensive research in development of

new material to improve gas-sensing performance is due of this model [24, 25, 26].

Figure 2.3 below shows a schematic model.

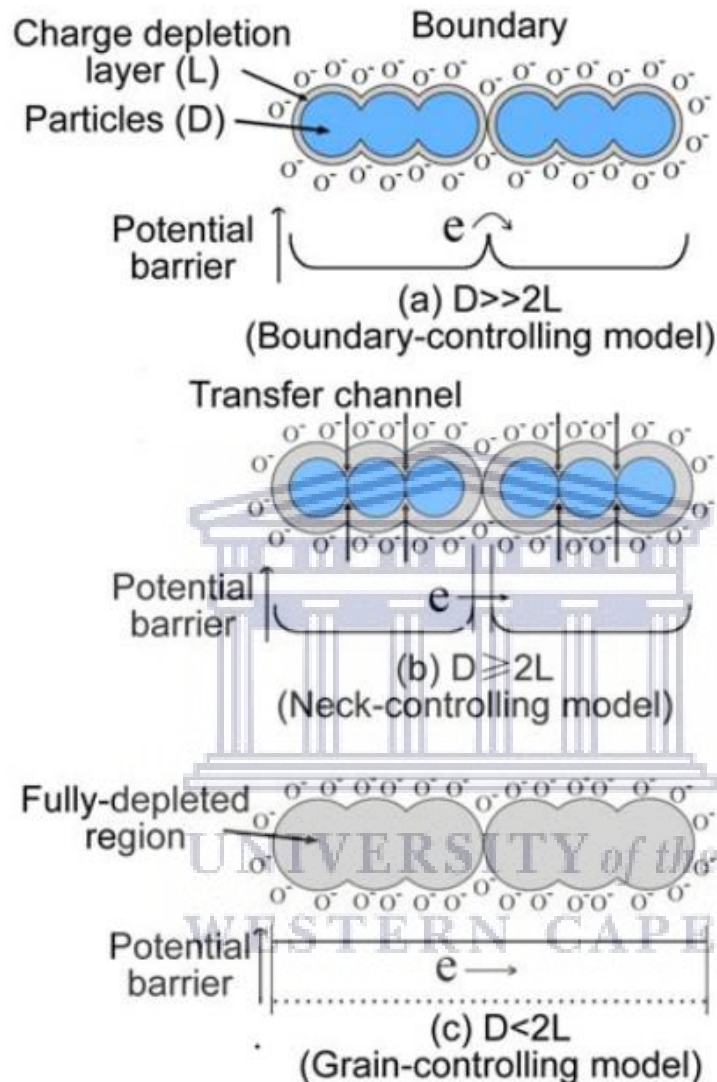


Fig 2. 3: Schematic model on the sensitivity of metal oxide gas sensors [25].

2.6.2 Surface Modification by Additives

Diverse researches have used mixture of metal oxide as composite material to enhanced properties of SMO sensors in order to attain higher sensitivity and selectivity compared to the individual constituent of MOX [27, 28]. Application such as light transistors and sensors use metal oxide dopants to advance dilute magnetic semiconductors. Moreover, the application of solar cell narrows their band gap by

introducing metal oxide such as ZnO and TiO₂. Wherefore, new energy state forbidden band are introduced that enable wide band range absorption of electromagnetic spectrum resulting in enhanced efficiency of material.

Performances of sensor are influence by factors such as crystallite size, oxidation state, dopant distribution and homogeneity [29, 30]. However, metal oxides are not catalytically active enough hence the incorporation of noble metals (Ag, Au and Pt) and transition metals (Cr, Mn, Fe and Cu) to enhanced their properties [31-35]. Joshi et al [36] upon incorporating gold dopant on ZnO nanowires observed an enhanced catalytic activity compared to the undoped ZnO nanowires. Furthermore, Ahmed et al [37] observed that incorporation of Mn doped ZnO nanaorods in oxygen gas sensing at room temperature results in high sensitivity compared to the undoped ZnO nanaorods. The enhanced sensitivity was owing to the decrease in rod diameter and greater surface to volume ratio.

2.6.3. Sensing Mechanism

Wolkestein et al [38] was the first to report the mechanism of metal oxide gas sensors based on electron theory of chemisorption and catalysis in 1961. Later, Morrison explores conditions for electric charge transportation of semiconductor when exposed to target gases [39]. Hence, Yamazoe et al [40] elaborate the gas sensing mechanism in semiconductor metal oxides in connection to their theories. Two types of semiconductors are n-type and p-type. The n-type semiconductors (SnO₂, ZnO and TiO₂) are electrons carrier charges while the p-type (CuO, TeO₂) are holes' charge carriers. Both n-type and p-type semiconductor when exposed to reducing or oxidizing target gas an alteration in resistance is witnessed which is a result of REDOX reaction [41].

By exposing n-type to reducing gas causes adsorption of gas molecule on surface to react with chemisorbed oxygen ions resulting in donor of electron in metal oxide. Electron concentration increases with depletion layer becoming thin causing charge flow repair, resulting in decrease electric resistance and the opposite happens in oxidizing agent. In the event of p-type when exposed to reducing gas an increase in electrical resistance is observe while in oxidizing gas a decrease in electrical resistance occur. Gas sensors depend on geometry and size of crystallites including their interconnection. Thin space region increase charge flow over small period causing quick response time resulting in enhanced sensitivity and response of the sensor [42].

2.7 APPLICATION OF TiO₂ NANOMATERIALS IN GAS SENSING

Toxic gases such as carbon monoxide (CO), benzene (C₆H₆), toluene (C₇H₈) and xylene (C₈H₁₀) have far reaching health effect which can lead to death due to explosive and combustible effect they portray. The occupational safety and health administration has set limit exposure of 35 ppm for an 8-hour shift. Thus, semiconductor metal oxide (SMO) based sensors have capable properties such as alteration in conduction resistance in the existence of analyte gas. Amongst the SMOs, titanium dioxide (TiO₂) has unique characteristic such as large band gap, chemical stability and potential technological applications in gas sensor and solar cells [43]. Mabrook and Hawkins et al. [44] reported sensing performance of undoped TiO₂ based benzene sensor at room temperature with high detection range of 150 ppm with moderately slow response and recovery times of 1 min and 5 min. The single semiconductor oxide is weakly sensitive due to low chemical reactivity thus limit their application and development.

Dutta et al. [45] modified synthesis nanoporous p-titania thin film using sol gel method towards detecting low concentration of benzene, toluene and xylene (BTX) sensor at low temperature. The results indicated fast response and recovery rate to be ~24 s/12 s, ~14 s/20 s and ~20 s/14 s for benzene, toluene and xylene respectively at lowest concentration of 0.1 ppm with optimum operating temperature of 75 °C. Hsu et al. [46] used the electrochemical method to synthesis TiO₂ nanotubes whereas LSCNO perovskite film was prepared using sol gel method process. Then both were fabricated together into p-n junction and measured in CO gas sensor. The testing results indicated moderate response of 38.41% at 200°C with concentration of CO at 400 ppm. Whereas, benzene gas sensor based on Pd-decorated TiO₂/MoS₂ ternary nanocomposite upon exposure to 50 ppm concentration, the response time was about 13s and the recovery time was about 10s which was ascribed to synergistic effect of the ternary nanostructures. The response recovery time are 15s/13s and 17s/18s for MoS₂ and TiO₂ respectively [47]. Fig. 1 below is the sensing performance comparison of TiO₂, MoS₂ and Pd-TiO₂/MoS₂. Nonetheless, TiO₂-doped ZnO sensors showed a great sensitivity to benzene and acetone with lower concentration of 100ppm at 370°C. The sensors showed the respond and recovery time was around 10 and 5s respectively. While the operating temperature for alcohol at 240°C still observed rapid response and recovery [48]. Zhang et al. [49] successfully prepared the silver (Ag) loaded hedgehog-like TiO₂ architectures using hydrothermal method. The response of the Ag loaded hedgehog like TiO₂ to 100 ppm xylene measured at 375°C to be 5s and recovery time of 2s.

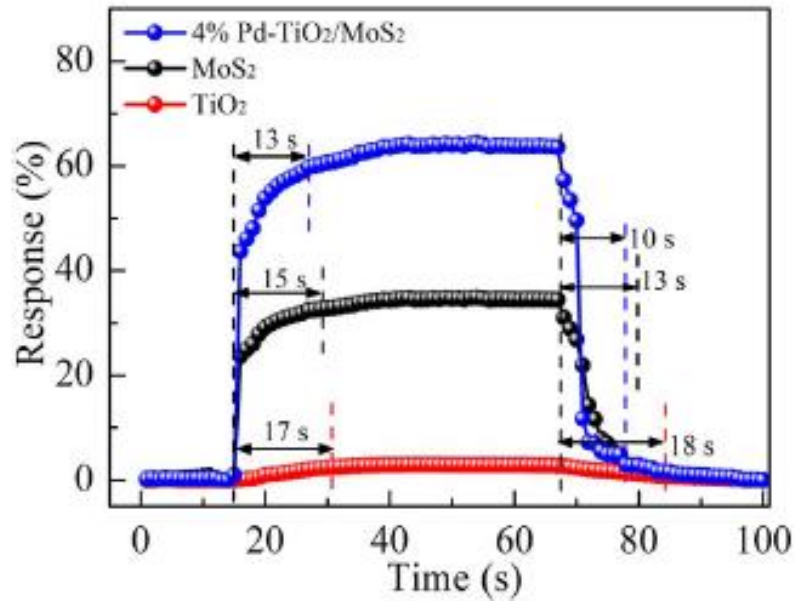


Fig. 2. 4: The sensing performance comparison of TiO₂, MoS₂ and Pd-TiO₂/MoS₂ [47].

The Ag loaded hedgehog like TiO₂ exhibited better properties compared to the response of other sensors to xylene. Compared to Shen synthesizing the hierarchical ZnO rose architecture using hydrothermal method combined with calcination process and fabricated the gas sensors. The gas sensing results showed the response of the fabricated sensors to 20 ppm xylene at operating temperature of 206 °C is 2s and the recovery time is 24 s [50]. Whereas, ZnO nanoflower with high concentration of 200 ppm xylene at 206 °C, showed response rate of 9s and recovery time of 38s [51]. The response time for 5 wt% Fe-doped MoO₃ and α-MoO₃/α-Fe₂O₃ at optimum temperature of 206 °C with moderate concentration of 100 ppm xylene results 20 s and 87s with recovery time at about 75s and 190s respectively [52,53]. The sensing performance of the Ag-loaded TiO₂ sensors evidently showed the response of sensor to xylene was better compared to all tested VOCs. As shown below in Table 2,1, the xylene sensing properties for various SMO sensor.

Table 2. 1: Xylene sensing properties of SMO sensor.

Sensing materials	Xylene (ppm)	Operating T. (°C)	Response (s)	Recovery (s)	Refs.
0.5 at.% Ag/TiO ₂	100	375	5	2	[49]
Au-ZnO rose-like	20	206	2	4	[50]
ZnO nanoflower	200	200	9	38	[51]
5 wt.% Fe-doped MoO ₃	100	206	20	75	[52]
α-MoO ₃ /α-Fe ₂ O ₃	100	206	87	190	[53]
2 at.% W-doped NiO	200	75	178	152	[54]
3 at.% Sn-doped NiO	100	225	298	223	[55]

Wisitorsaat et al. [56] presented the progress of NiO_x doped TiO₂ thin films prepared by ion-assisted electron beam evaporator. The results showed the differences in gas sensing response between the n-type and p-type NiO_x doped TiO₂. The n-type response increases with operating temperature and the p-type response decreases with temperature. The p-type response showed significant enhancement on acetone and ethanol gas at 300 °C. Fig. 2.5 below shows resistance of 1% TiO₂ thin film and 0% NiO_x are reduced when exposed to reducing gas. The 1% NiO_x behavior shows no significant difference from the undoped one. While the 10% NiO_x and pure NiO_x thin film increased upon exposure to reducing gas.

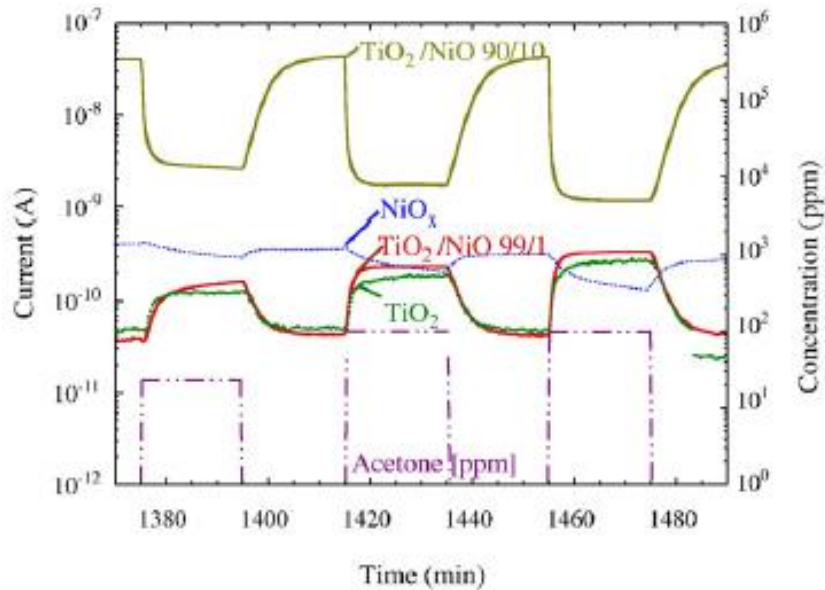


Fig. 2.5. Variation of the current flowing through NiO_x-TiO₂ films for acetone gas.

However, modified TiO₂ nanowires and sea-urchin-like hierarchically arranged TiO₂ nanostructures (HHC) among the many structures were synthesized using hydrothermal method resulting in high surface area with diameter ranging from meso to macropores. The sensing performances of the fabricated sensors were measured towards toluene and xylene gases at low operating temperature of 25 °C. The HHC sensor display potential selectivity towards CO with response 2.38, while TNW sensor showed a greater response of 6.57 and selective towards C₇H₈ at low temperature. A more noticeable response toward 20 ppm CO was obtainable by HHC with response and recovery times of 85 and 124 s due to active sites and available surface area presented by structural morphology. The results showed that the HHC sensor upon exposure to CO gas decrease as temperature increases. While, the opposite behavior upon exposure to C₈H₁₀ was observed wherefore response increased with operating temperature. They further observed that TNW sensor showed greater response towards C₈H₁₀ followed by TNP sensor even though it has smaller surface area compared to HHC [57]. Pozos et al. [58]

synthesized TiO₂ thin films using ultrasonic spray pyrolysis and obtained response of 300 towards 300 ppm at operating temperature of 300 °C. Seekaw et al. [61] fabricated the graphene carbon nanotubes loaded with TiO₂ nanoparticles using chemical vapor deposition and sparking methods. The results showed enhanced response for 42.9% towards 500ppm toluene vapor at room temperature. Table 2.2 below presents TiO₂ gas sensor on various VOCs gases.

Table 2. 2: Comparison study based on TiO₂ gas sensors for CO, C₇H₈ and C₈H₁₀.

Gas	Sensors	Conc. (ppm)	Operating T. (°C)	Response	Refs.
CO	TiO ₂ /perovskite	400	200	38.41%	[46]
	TiO ₂ thin film	300	300	300	[58]
	Pd-TiO ₂	800	400	4.25	[59]
	TiO ₂ hierarchical	20	25	2.46	[57]
C ₇ H ₈	TiO ₂	400	50	12.5%	[50]
	Pt@ZnO-TiO ₂	5	300	11.1	[60]
	3D TiO ₂ /G-CNT	500	25	42%	[61]
	Au-loaded TiO ₂	100	375	7.3	[62]
	TiO ₂ Nanowires	60	25	7.65	[57]
	TiO ₂ nanotubes	400	50	16%	[50]
C ₈ H ₁₀	Hedgehog-like Ag-TiO ₂	100	375	6.49	[62]
	Co ₃ O ₄ /TiO ₂	100	120	11.17	[63]
	TiO ₂ Nanowires	100	125	36.26	[57]

Note: Conc. (ppm) and Operating T. (°C) correspond to concentration and operating temperature, respectively.

REFERENCES

1. Bochenkov, V.E. and Sergeev, G.B., 2010. Sensitivity, selectivity, and stability of gas-sensitive metal-oxide nanostructures. *Metal oxide nanostructures and their applications*, 3, pp.31-52.
2. Capone, S., Forleo, A., Francioso, L., Rella, R., Siciliano, P., Spadavecchia, J., Presicce, D.S. and Taurino, A.M., 2003. Solid state gas sensors: state of the art and future activities. *Journal of Optoelectronics and Advanced Materials*, 5(5), pp.1335-1348.
3. Neri, G., 2015. First fifty years of chemoresistive gas sensors. *Chemosensors*, 3(1), pp.1-20.
4. Cottineau, T., Pronkin, S.N., Acosta, M., Mény, C., Spitzer, D. and Keller, V., 2013. Synthesis of vertically aligned titanium dioxide nanotubes on microcantilevers for new nanostructured micromechanical sensors for explosive detection. *Sensors and Actuators B: Chemical*, 182, pp.489-497.
5. Avila Rodríguez, M.I., Rodríguez Barroso, L.G. and Sánchez, M.L., 2018. Collagen: A review on its sources and potential cosmetic applications. *Journal of Cosmetic Dermatology*, 17(1), pp.20-26.
6. World Health Organization, WHO Air quality guidelines for particulate matter, ozone, nitrogen dioxide and sulfur dioxide: global update 2005: summary of risk assessment, Geneva World Heal. Organ. (2006) 1–22.
7. Brunekreef, B., Künzli, N., Pekkanen, J., Annesi-Maesano, I., Forsberg, B., Sigsgaard, T., Keuken, M., Forastiere, F., Barry, M., Querol, X. and Harrison, R.M., 2015. Clean air in Europe: beyond the horizon
8. Gorguner, M. and Akgun, M., 2010. Acute inhalation injury. *The Eurasian journal of medicine*, 42(1), p.28.
9. Ruiz, A., Arbiol, J., Cirera, A., Cornet, A. and Morante, J.R., 2002. Surface activation by Pt-nanoclusters on titania for gas sensing applications. *Materials Science and Engineering: C*, 19(1-2), pp.105-109.
10. Kaur, M., Jain, N., Sharma, K., Bhattacharya, S., Roy, M., Tyagi, A.K., Gupta, S.K. and Yakhmi, J.V., 2008. Room-temperature H₂S gas sensing at ppb level by single crystal In₂O₃ whiskers. *Sensors and Actuators B: Chemical*, 133(2), pp.456-461.
11. EC-European Commission, 2016. Directive (EU) 2016/2284 of the European Parliament and of the Council of 14 December 2016 on the reduction of national emissions of certain atmospheric pollutants, amending Directive 2003/35/EC and repealing Directive 2001/81/EC. *OJL*, 344, pp.1-31.

12. Davydovskaya, P., Pohle, R., Tawil, A. and Fleischer, M., 2013. Work function based gas sensing with Cu-BTC metal-organic framework for selective aldehyde detection. *Sensors and Actuators B: Chemical*, 187, pp.142-146.
13. Liu, X., Cheng, S., Liu, H., Hu, S., Zhang, D. and Ning, H., 2012. A survey on gas sensing technology. *Sensors*, 12(7), pp.9635-9665.
14. Wang, C., Yin, L., Zhang, L., Xiang, D. and Gao, R., 2010. Metal oxide gas sensors: sensitivity and influencing factors. *Sensors*, 10(3), pp.2088-2106.
15. Choi, K.J. and Jang, H.W., 2010. One-dimensional oxide nanostructures as gas-sensing materials: review and issues. *Sensors*, 10(4), pp.4083-4099.
16. Brattain, W.H. and Bardeen, J., 1953. Surface properties of germanium. *The Bell System Technical Journal*, 32(1), pp.1-41.
17. Seiyama, T., Kato, A., Fujiishi, K. and Nagatani, M., 1962. A new detector for gaseous components using semiconductive thin films. *Analytical Chemistry*, 34(11), pp.1502-1503.
18. Shaver, P.J., 1967. Activated tungsten oxide gas detectors. *Applied Physics Letters*, 11(8), pp.255-257.
19. Taguchi, N., 1971. Gas-detecting device. U.S. Patent 3,631,436.
20. Gubpta, B.L., 2004. GB-200N industrial sensor technologies and markets.
21. Fine, G.F., Cavanagh, L.M., Afonja, A. and Binions, R., 2010. Metal oxide semiconductor gas sensors in environmental monitoring. *sensors*, 10(6), pp.5469-5502.
22. Tshabalala, Z.P., 2016. Room temperature gas sensing characteristics of titanium dioxide nanostructures: effects of hydrochloric acid on the structure and magnetic properties (Doctoral dissertation, University of the Free State).
23. Yang, X., Salles, V., Kaneti, Y.V., Liu, M., Maillard, M., Journet, C., Jiang, X. and Brioude, A., 2015. Fabrication of highly sensitive gas sensor based on Au functionalized WO₃ composite nanofibers by electrospinning. *Sensors and actuators B: chemical*, 220, pp.1112-1119.
24. Sadek, A.Z., 2007. S. Member, S. Choopun, W. Wlodarski, SJ Ippolito, and K. Kalantar-zadeh. *IEEE Sens. J*, 7, p.919.
25. Han, N., Wu, X., Chai, L., Liu, H. and Chen, Y., 2010. Counterintuitive sensing mechanism of ZnO nanoparticle based gas sensors. *sensors and actuators B: chemical*, 150(1), pp.230-238.
26. Sun, Y.F., Liu, S.B., Meng, F.L., Liu, J.Y., Jin, Z., Kong, L.T. and Liu, J.H., 2012. Metal oxide nanostructures and their gas sensing properties: a review. *Sensors*, 12(3), pp.2610-2631.
27. Rothschild, Y. *Komem, J.Appl.Sci.*, 95 (2004) 6374-6380

28. Mondal, B., Basumatari, B., Das, J., Roychaudhury, C., Saha, H. and Mukherjee, N., 2014. ZnO–SnO₂ based composite type gas sensor for selective hydrogen sensing. *Sensors and Actuators B: Chemical*, 194, pp.389-396.
29. Zhang, L., Jing, X., Liu, J., Wang, J. and Sun, Y., 2015. Facile synthesis of mesoporous ZnO/Co₃O₄ microspheres with enhanced gas-sensing for ethanol. *Sensors and Actuators B: Chemical*, 221, pp.1492-1498.
30. Pearton, S.J., Norton, D.P., Ivill, M.P., Hebard, A.F., Zavada, J.M., Chen, W.M. and Buyanova, I.A., 2007. ZnO doped with transition metal ions. *IEEE Transactions on electron devices*, 54(5), pp.1040-1048.
31. Deng, Q.R., Xia, X.H., Guo, M.L., Gao, Y. and Shao, G., 2011. Mn-doped TiO₂ nanopowders with remarkable visible light photocatalytic activity. *Materials Letters*, 65(13), pp.2051-2054.
32. Choi, S.W. and Kim, S.S., 2012. Room temperature CO sensing of selectively grown networked ZnO nanowires by Pd nanodot functionalization. *Sensors and Actuators B: Chemical*, 168, pp.8-13.
33. Ramgir, N.S., Sharma, P.K., Datta, N., Kaur, M., Debnath, A.K., Aswal, D.K. and Gupta, S.K., 2013. Room temperature H₂S sensor based on Au modified ZnO nanowires. *Sensors and Actuators B: Chemical*, 186, pp.718-726.
34. Abdullah, Q.N., Yam, F.K., Hassan, Z. and Bououdina, M., 2015. Pt-decorated GaN nanowires with significant improvement in H₂ gas-sensing performance at room temperature. *Journal of colloid and interface science*, 460, pp.135-145.
35. Xiang, Q., Meng, G.F., Zhao, H.B., Zhang, Y., Li, H., Ma, W.J. and Xu, J.Q., 2010. Au nanoparticle modified WO₃ nanorods with their enhanced properties for photocatalysis and gas sensing. *The Journal of Physical Chemistry C*, 114(5), pp.2049-2055.
36. Joshi, R.K., Hu, Q., Alvi, F., Joshi, N. and Kumar, A., 2009. Au decorated zinc oxide nanowires for CO sensing. *The Journal of Physical Chemistry C*, 113(36), pp.16199-16202.
37. Ahmed, F., Arshi, N., Anwar, M.S., Danish, R. and Koo, B.H., 2014. Morphological evolution of ZnO nanostructures and their aspect ratio-induced enhancement in photocatalytic properties. *RSC advances*, 4(55), pp.29249-29263.
38. Wolkenstein, T., 1961. Effect of ionizing radiation on the adsorptive and catalytic properties of semiconductors. *Discussions of the Faraday Society*, 31, pp.209-218.
39. Morrison, S.R., 1981. Semiconductor gas sensors. *Sensors and Actuators*, 2, pp.329-341.
40. Yamazoe, N., Kurokawa, Y. and Seiyama, T., 1983. Effects of additives on semiconductor gas sensors. *Sensors and Actuators*, 4, pp.283-289.

41. Huang, J. and Wan, Q., 2009. Gas sensors based on semiconducting metal oxide one-dimensional nanostructures. *Sensors*, 9(12), pp.9903-9924.
42. Shankar, P. and Rayappan, J.B.B., 2015. Gas sensing mechanism of metal oxides: The role of ambient atmosphere, type of semiconductor and gases-A review. *Sci. Lett. J*, 4(4), p.126.
43. Abdul-Wahab, S.A., En, S.C.F., Elkamel, A., Ahmadi, L. and Yetilmezsoy, K., 2015. A review of standards and guidelines set by international bodies for the parameters of indoor air quality. *Atmospheric Pollution Research*, 6(5), pp.751-767.
44. Mabrook, M. and Hawkins, P., 2002. Benzene sensing using thin films of titanium dioxide operating at room temperature. *Sensors*, 2(9), pp.374-382
45. Dutta, K., Bhowmik, B., Hazra, A., Chattopadhyay, P.P. and Bhattacharyya, P., 2015. An efficient BTX sensor based on p-type nanoporous titania thin films. *Microelectronics Reliability*, 55(3-4), pp.558-564.
46. Hsu, K.C., Fang, T.H., Hsiao, Y.J. and Wu, P.C., 2019. Response and characteristics of TiO₂/perovskite heterojunctions for CO gas sensors. *Journal of Alloys and Compounds*, 794, pp.576-584.
47. Zhang, D., Jiang, C. and Zhou, X., 2018. Fabrication of Pd-decorated TiO₂/MoS₂ ternary nanocomposite for enhanced benzene gas sensing performance at room temperature. *Talanta*, 182, pp.324-332.
48. Zhu, B.L., Xie, C.S., Wang, W.Y., Huang, K.J. and Hu, J.H., 2004. Improvement in gas sensitivity of ZnO thick film to volatile organic compounds (VOCs) by adding TiO₂. *Materials Letters*, 58(5), pp.624-629.
49. Zhang, Y., Bai, J., Zhou, L., Liu, D., Liu, F., Liang, X., Gao, Y., Liu, F., Yan, X. and Lu, G., 2019. Preparation of silver-loaded titanium dioxide hedgehog-like architecture composed of hundreds of nanorods and its fast response to xylene. *Journal of colloid and interface science*, 536, pp.215-223.
50. Shen, Z., Zhang, X., Ma, X., Mi, R., Chen, Y. and Ruan, S., 2018. The significant improvement for BTX (benzene, toluene and xylene) sensing performance based on Au-decorated hierarchical ZnO porous rose-like architectures. *Sensors and Actuators B: Chemical*, 262, pp.86-94.
51. Wang, L., Wang, S., Xu, M., Hu, X., Zhang, H., Wang, Y. and Huang, W., 2013. A Au-functionalized ZnO nanowire gas sensor for detection of benzene and toluene. *Physical Chemistry Chemical Physics*, 15(40), pp.17179-17186.
52. Xu, R., Zhang, N., Sun, L., Chen, C., Chen, Y., Li, C. and Ruan, S., 2016. One-step synthesis and the enhanced xylene-sensing properties of Fe-doped MoO₃ nanobelts. *RSC advances*, 6(108), pp.106364-106369.

53. Jiang, D., Wei, W., Li, F., Li, Y., Liu, C., Sun, D., Feng, C. and Ruan, S., 2015. Xylene gas sensor based on α - MoO_3/α - Fe_2O_3 heterostructure with high response and low operating temperature. *RSC Advances*, 5(49), pp.39442-39448.
54. Feng, C., Wang, C., Zhang, H., Li, X., Wang, C., Cheng, P., Ma, J., Sun, P., Gao, Y., Zhang, H. and Sun, Y., 2015. Enhanced sensitive and selective xylene sensors using W-doped NiO nanotubes. *Sensors and actuators B: Chemical*, 221, pp.1475-1482.
55. Gao, H., Wei, D., Lin, P., Liu, C., Sun, P., Shimano, K., Yamazoe, N. and Lu, G., 2017. The design of excellent xylene gas sensor using Sn-doped NiO hierarchical nanostructure. *Sensors and Actuators B: Chemical*, 253, pp.1152-1162.
56. Wisitsoraat, A., Tuantranont, A., Comini, E., Sberveglieri, G. and Wlodarski, W., 2009. Characterization of n-type and p-type semiconductor gas sensors based on NiOx doped TiO_2 thin films. *Thin Solid Films*, 517(8), pp.2775-2780.
57. Tshabalala, Z.P., Mokoena, T.P., Jozela, M., Tshilongo, J., Hillie, T.K., Swart, H.C. and Motaung, D.E., 2020. TiO_2 Nanowires for Humidity-Stable Gas Sensors for Toluene and Xylene. *ACS Applied Nano Materials*.
58. Pozos, H.G., Krishna, K.T.V., Amador, M.D.L.L.O., Kudriavtsev, Y. and Alvarez, A.M., 2018. TiO_2 thin film based gas sensors for CO-detection. *Journal of Materials Science: Materials in Electronics*, 29(18), pp.15829-15837.
59. Pan, F.; Lin, H.; Zhai, H.; Miao, Z.; Zhang, Y.; Xu, K.; Guan, B.; Huang, H.; Zhang, H. P-doped TiO_2 film sensors prepared by premixed stagnation flames for CO and NH_3 gas sensing. *Sens. Actuator. B* 2018, 261, 451-459.
60. Dutta, K.; Chattopadhyay, P.P.; Lu, C.-W.; Ho, M.-S.; Bhattacharyya, P. A highly sensitive BTX sensor based on electrochemically derived wall connected TiO_2 nanotubes, *Applied Surface Science* 2015, 354, 353–361.
61. Seekaew, Y.; Wisitsoraat, A.; Phokharatkul, D.; Wongchoosuk, C.; Room Temperature Toluene Gas Sensor Based on TiO_2 Nanoparticles Decorated 3D Graphene-Carbon Nanotube Nanostructures. *Sens. Actuators, B* 2019, 279, 69-78.
62. Liu, W.; Xu, L.; Sheng, K.; Zhou, X.; Zhang, X.; Chen, C.; Dong, B.; Bai, X.; Lu, G.; Song, H. Facile synthesis of controllable TiO_2 composite nanotubes via templating route: Highly sensitive detection of toluene by double driving from Pt @ZnO NPs. *Sens. Actuator. B* 2018, 273, 1676-1686.
63. Bai, S.; Tian, Y.; Guo, J.; Feng, Y.; Luo, R.; Li, D.; Chen, A.; Liu, C.C. Synthesis of $\text{Co}_3\text{O}_4/\text{TiO}_2$ composite by pyrolyzing ZIF-67 for detection of xylene. *Appl. Surf. Sci.* 2018, 435, 384–392.

CHAPTER THREE

Metal Oxides and Noble Metals Application in Organic Solar Cells*

3.1. INTRODUCTION

Photovoltaic (PV) technology plays a major role in resolving the global energy crisis in an eco-friendly and sustainable way. Currently, the mass production of 90% worldwide market is silicon (Si) based PVs as opposed to the polymer solar cells (PSCs) [1]. However, PSCs have been intensively researched due to their cost effectiveness, flexible tuning properties, and appropriateness for mass production in addition; they are not generating toxic substance or greenhouse gases and necessitating little maintenance during operation [2-4]. The current efficiency recorded to date of OPV cells is over 16.5%, owing to concurrently improved short circuit current density and open-circuit voltage, as opposed to the state of the art Si based solar cells [5]. Nonetheless, much attention is given to organic solar cells over the single solar cell due to loss thermalization and narrow absorption spectra in single solar cell PSCs. They are based on the synthesis of donor and acceptor materials with different designs of interconnection layers [6]. Polymer: fullerene blends showed that they can produce PCEs over 10% and integration of nanostructures into their devices architecture for light manipulation can further enhance these performances. Stabilization is established in this charge separated state of fullerene based material as a prerequisite in artificial electron transfer structures [7, 8]. Organic PSCs may also be enhanced by the integration of noble

*The contents of this chapter have been published in **Solar Energy 207 (2020) 347–366**

metal nanoparticles (NPs), which display strong localized surface plasmon resonance (LSPR) effect [9]. Excitation of LSPR within the noble metallic NPs arises due to induced collective oscillation of the conductive electrons by the electromagnetic radiation in the individual nanoparticle. The effect of the LSPR is dependent on the geometry, dielectrically properties, size and spacing of the metallic NPs [10]. Inclusion of metallic NPs in the charge transporting layer is favoured, which extend the LSPR effect as opposed to the active layer that generates exciton quenching [11]. Hence, the incorporation of noble metallic NPs that induces LSPR has been reported to enhance optical absorption properties [12,13]; consequently, matching the frequency of the incident photon to the frequency of the oscillation excited electron in metal NPs that actuates the LSP as shown in Fig. 3.1.

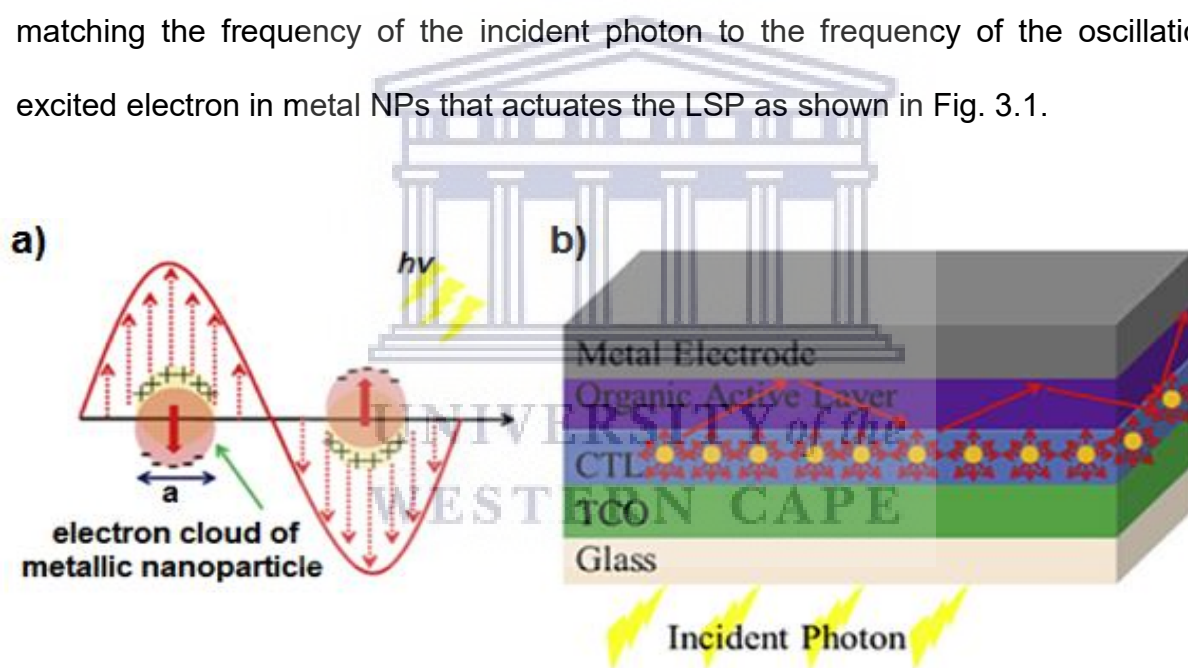
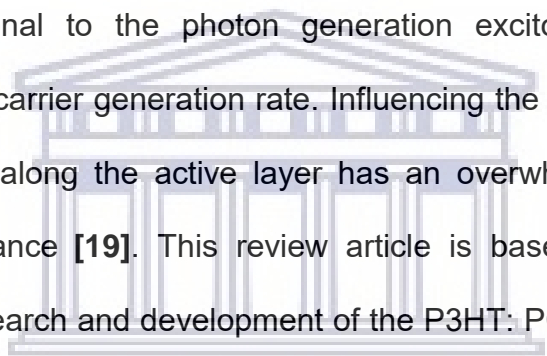


Fig. 3. 1: a) LSPR confined in the spherical metallic NP(s) with diameter (a). The SP(s) are excited with the incident photon energy, $h\nu$. (b) Architecture of OPV with small spherical NP(s) embedded on the CTL. (Reprinted with permission from [14] Copyright 2016: Elsevier).

These LSPR enhanced solar devices have stimulated much recognition as an alternative renewable energy source. Major studies have now focused on using noble metal NPs with spherical morphologies. Nanostructures such as stars and

rods result in a strong LSPR owing to their sharp structures, thereby elevating the effectiveness of the cells [15-17]. Amongst studied NPs morphologies, the utmost contributor of power conversion efficiency (PCE) were the usage of Au star-shaped NPs. This was due to the superior optical properties of Au nanostars over nanorods/sphere; according to surface enhanced Raman spectroscopy studies [18]. Nonetheless, optical engineering techniques using optical spacers such as TiO₂ or ZnO were reported to enhance photon absorption. This report was ascribed to the maximum light intensity within the active layer caused by the spatial redistribution of the optical electric field energy dissipation. The optical electric field energy dissipation is proportional to the photon generation exciton, which in turn is proportional to the free carrier generation rate. Influencing the local value of the free carrier generation rate along the active layer has an overwhelming effect on the overall device performance [19]. This review article is based on the theoretical interpretation of the research and development of the P3HT: PCBM based solar cell.



UNIVERSITY of the
WESTERN CAPE

3.2. INFLUENCE OF NOBLE METALS ON P3HT: PCBM

The noble metals of interest in this article are metallic NPs of Au and Ag. It is well known that the incorporation of the above mentioned metallic NPs in polymeric materials, such as the P3HT: PCBM based solar cell, can trigger the surface plasmon effect. Generally, a substantial quantity of light is lost in most organic solar cells, due to the excessively thin film thickness of roughly 100 nm, which in turn results in abundant incident light passing through the active layer and reaching the cathode. Therefore, the effective approach to overcome this loss of light is through the incorporation of noble metals that can enhance the light absorption capabilities of the P3HT: PCBM solar within a broad wavelength range. Light absorption can be

enhanced in three mechanisms; i.e. by light scattering, localized surface plasmon resonance, and through surface plasmon polariton (see Fig. 3.2). These mechanisms depend on the particular geometry and different structures of metal NPs in the OPV: firstly, by entrenching metallic NP(s) in the active layer, secondly on the outside of the active layer and thirdly, by back grating contact from the side of active layer.

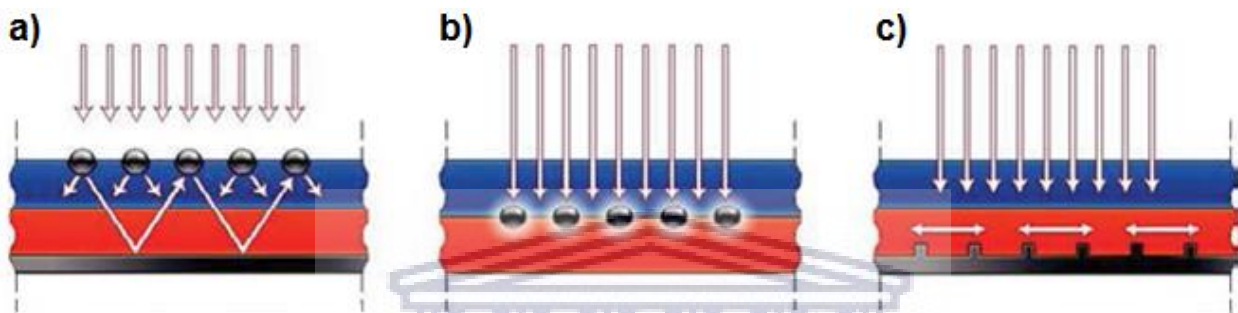


Fig. 3. 2: Schematic diagram displaying the plasmonic materials performance where the light is scattered at different angles as to improve the effective optical path length and absorbing light. a) Light trapping by scattering from metal nanoparticles at surface of the solar cell. b) Light trapping by the excitation of LSPs in metal nanoparticles embedded in semiconductor. c) Light trapping by excitation of surface plasmon polaritons at metal/semiconductor interface. A corrugated metal back surface couples light to surface plasmon polariton or photonic modes that propagate in the plane of the semiconductor. (Reprinted with permission from [20] Copyright 2010: Nature Materials).

3.2.1. Effect of Au on P3HT: PCBM Solar Cell Performance

3.2.1.1 Metallic Au NPs embedded the buffer layer

The geometry of metallic nanostructures is another important factor that affects the efficiency of the solar devices. Hence, inclusion of plasmonic nanostructures in the buffer layer has been reported by various researchers to induce an optical effect, which elevates light absorption in the active layer that results in actuating the rate of exciton generation. This resulted in an elevation of exciton dissociation at the

donor/acceptor interface, with an enhanced device photocurrent [21-23]. Previous studies have shown that the integration of these plasmonic NPs induced the electrical effect that increased the conductivity and surface roughness of the buffer layer [24,25] and was attributed to the lateral distribution of light along the buffer layer that induce field enhancement near the metallic NPs [26]. Inclusion of Au nanocubes in the buffer layer of PTB7: PCBM based devices showed a PCE of approximately 8.2% according to Ng et al., which was assigned to the forward optical properties [27]. Otieno et al. highlighted a PCE of approximately 3.23% with an increment of 32.4% on the cells, which was ascribed to greater charge injection of AuNPs in a buffer layer [28]. Using laser generated NPs in PCPDTBT: C₇₀-PCBM based devices, an enhancement in the PCE to approximately 6.28 % was achieved, which was ascribed to the scattering effect of the transmitted photons back to active layer by the NPs [29]. Liu et al. reported a PCE of approximately 7.1% with 8.1% increment, which was due to an improved exciton dissociation rate at the interface of the buffer layer and light absorption enhancement of the active layer [30]. The hygroscopic and acidic nature of the PEDOT: PSS layer caused degradation of the solar device. Hence, replacement of PEDOT: PSS by self-assembled of 2-Thenylmercaptan on Au has demonstrated a significant advancement of 2.5% efficiency, which Zhang et al. assigned to the design of 2-Thenylmercaptan on gold that inhibits charge recombination and decreases the contact resistance, which increases PCE [31]. Qiao et al. showed that the coalescence of different diameters of Au nanospheres (NS) in the buffer layer enhanced the efficiency of the solar device showing PCE of 2.36%, while showing a 20% improvement and this was attributed to strong SPR effect by larger AuNS [32]. The use of seed mediated growth to synthesise Au nanorods (NRs) according to the processes from Nikoobalth

et al. was employed, to assemble interfacial Au NRs through thermal transformed nanodots (ND) on ITO substrate, which was found to elevate the PCE to 3.65 % [33]. Lee et al. assigned the increment to the strong coupling of Au plasmon effect and organic exciton causing effective charge transfer of the solar device [34]. The use of Au NPs in solar cells is due to a broader LSPR effect in longer visible spectrum as compared to Ag NPs, whereas Ag NPs have a high scattering effect as compared to Au NPs. Hence, combination of Au@Ag core shell nanocubes (NC) in the buffer layer was found to enhance the PCE of various devices. Baek et al. reported a PCE of 6.08 % in Au@Ag core shell NC as compared to PCE of 5.57% in AuNPs of PCDTBT: PC₇₀BM active layer [35]. They further displayed in the active layer of PTB7:PC₇₀BM an enhanced PCE of 8.74% in Au@Ag core shell NC as compared to 8.14% in AuNPs, which was accredited to the high scattering efficiency and broader LSPR, especially at longer wavelength in the visible spectra. The *J-V* characteristics in Fig. 3.3 shows the enhanced J_{sc} in Au@Ag core shell NC integrated devices compared to AuNP integrated devices; owing to their superior scattering effect displaying the highest PCE. The authors observed low enhanced EQE and absorption of the OSCs with the AuNPs incorporated in comparison to AgNP embedded devices in spite of the enhanced incorporating concentration. The low EQE and absorption improvement are related to the inferior scattering efficiency of the AuNPs in comparison to the AgNPs. The scattering power of AgNPs is greater than the absorption power, whereas the AuNPs display inferior scattering efficiency and solid self-absorption power in spite of the broadband scattering response at the visible range of the extended wavelength. Consequently, the improvement factor of the absorption by active materials is restricted because of the intrinsically inferior AuNPs scattering efficiency. Thus, the metal-metal core-shell construction

overwhelmed the intrinsically weak scattering efficiency of AuNPs due to constructed hybrid plasmonic structure consisting of both gold and silver, where a thin Ag shell covered the Au core and acted as a scattering enhancer. Baek et al. showed that the appropriate shell thickness should be less than 15nm Ag shell (blue region) to minimize the blue shift of LSPR though maximizing the scattering effect throughout the visible range. Thus, the PCE was enhanced due to improved J_{sc} and fill factor and they noted that the charge collection efficiency was enhanced due to charge enhanced mobility. Hence, Ag@Au NC showed a 2.2 fold higher external quantum efficiency enhancement compared to AuNPs devices at wavelength of 450-700nm in PCDTBT: PC-based organic cells.

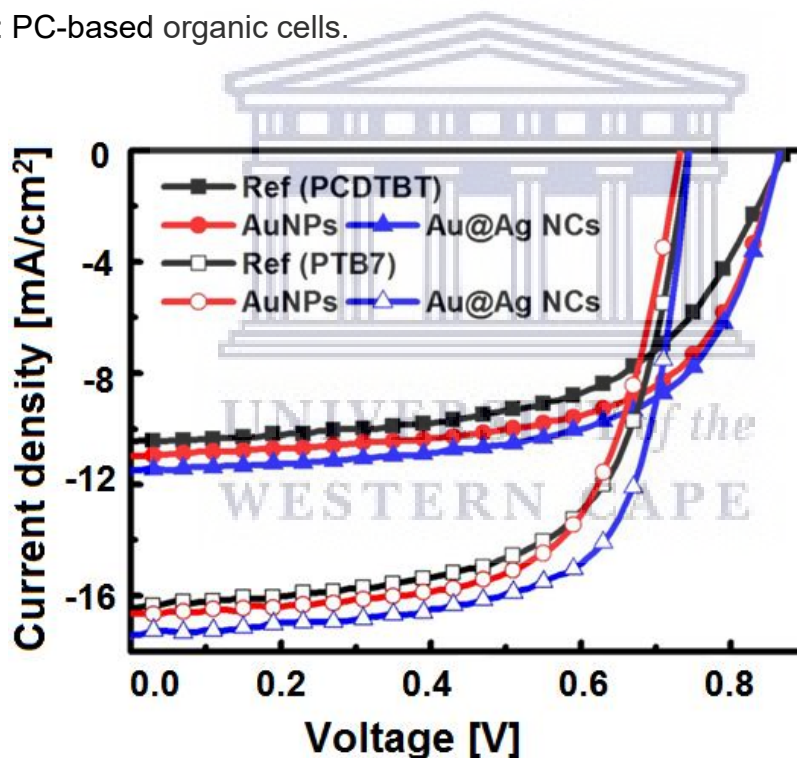


Fig. 3. 3: Device characteristics and spectral responses of plasmonic OSCs. Current density-voltage (J - V) characteristics of control device (black squares) and the best plasmonic OSCs with AuNPs (red circles) and Au@AgNCs (blue up triangles) embedded. The filled and open symbols denote the PCDTBT:PC₇₀BM (Type II) and PTB7:PC₇₀BM devices, respectively. (Reprinted with permission from [35] Copyright 2014: ACS publications).

Xu et al. used small molecular solar cells to integrate concurrently the Au silica NRs in the active layer and Au nanospheres in the buffer layer, resulting in an efficiency of 8.54% that was attributed to improved hole transport in the buffer layer and broader optical absorption in the active layer. For the inclusion of Au nanospheres in the buffer layer, an efficiency of 7.41% was reported [36]. The highest efficiency was observed with the incorporation of Au@Ag in the buffer layer of PT₇B:PC₇₀BM compared to buffer layer of PCDTBT: PC₇₁BM [35]. Table 3.1 lists the device characterization data of OSCs with AuNP(s) embedded into buffer layer.

Table 3. 1: Device characterization data of OPV with metallic AuNPs in buffer layer

ARCHITECTURE	PCE (%)	V _{oc}	J _{sc}	FF (%)	Refs.
Glass/ITO/PEDOT:PSS:AuNPs/PTB7:PC ₇₁ BM/Ca/Al	8.2	0.73	16.7	68	[27]
Glass/ITO/PEDOT:PSS+Au/P3HT:PCBM/Al	3.32	0.61	9.94	53.3	[28]
Glass/ITO/PEDOT:PSS:/PCDTBT:PC ₇₀ BM/Al	6.28	0.88	11.47	62	[29]
Glass/ITO/PEDOT: PSS/AuAgNPprism/PTB7:PC ₇₀ BM/ZnO/Al	7.1	0.75	15	64	[30]
Glass/ITO/Au:PEDOT:PSS/P3HT:PC ₆₁ BM/LiF/Al	2.2	0.54	8.1	50	[31]
ITO glass/Au:2-Thenylmercaptan/P3HT:PC ₆₁ BM/LiF/Al	2.5	0.56	7.1	65	[31]
Glass/ITO/PEDOT:PSS:AuNS(5nm)/MEH-PPV:PCBM/Al	1.99	0.76	0.66	39.2	[32]
Glass/ITO/PEDOT:PSS:AuNS(15nm)/MEH-PPV:PCBM/Al	2.36	0.78	0.74	44.8	[32]
Glass/ITO/AuND (LD): PEDOT: PSS/P3HT:PCBM/LiF/Al	3.65	0.58	11.13	57	[33]
Glass/ITO/PEDOT:PSS:AuNPs/PCDTBT:PC ₇₀ BM/TiO _x /Al	5.87	0.87	10.71	63	[35]
Glass/ITO/PEDOT:PSS:Au@AgNCs/PCDTB	6.08	0.87	11.1	63	[35]

T:PC₇₀BM/TiO_x/Al				0	
Glass/ITO/PEDOT:PSS: AuNP/PTB7:PC₇₀BM /TiO_x/Al	8.14	0.73	16.6	67	[35]
			4		
Glass/ITO/PEDOT:PSS: Au@AgNCs/PTB7: PC₇₀BM/TiO_x/Al	8.74	0.74	17.3	68	[35]
			8		
Glass/ITO/PEDOT:PSS: Au-SiO₂/ p-DTS(FBTTh₂):PC₇₀BM: Au/Ag/Ca	8.54	0.77	15.5	71.5	[36]
			6		
Glass/ITO/PEDOT:PSS: Au-SiO₂/p-DTS(FBTTh₂):PC₇₀BM/Ag/Ca	7.41	0.77	13.5	71.2	[36]
			3		

3.2.1.2 Metallic Au NPs integrated in active layer of the OPV devices

Wang et al. demonstrated various polymer solar cells embedded with octahedral AuNPs in the active layer that reduced the exciton quenching and cell resistance [37]. The diverse solar devices of P3HT: PCBM, PCDTBT: PCBM and Si-PCPDTBT: PCBM embedded with octahedral Au NPs resulted in a PCE of 4.36%, 6.45% and 4.54%, respectively. The enhanced PCE was assigned to the longer optical path caused by the multiple light scattering of Au NPs in the active layer of these solar cells. The emphasis was on the optimized thickness of the devices with Au NPs, showing an increased PCE as compared to the optimised thickness of the devices without AuNPs. Xu et al. integrated Au-silica NRs of various thicknesses in both active layers of P3HT:PC₇₁BM and a low bandgap polymer PCPDTBT:PC₇₁BM, which resulted in an increased PCE of 3.58% and 4.40%, respectively [39]. The elevated PCEs were ascribed to light scattering of Au-silica NRs in the active layer of both solar cells and was more pronounced in low bandgap polymer devices. Hence, further studies were carried out to reduce the shell thickness of Au-silica to effectively enhance both localized field and light scattering with reference to an experimental study of Brown et al., using Au-silica nanosphere (NS) of 3-8 nm shell thickness [40]. Xu et al. further reports that integration of Au-silica NS in active layer of p-DTS (FBTTh₂):PC₇₀BM increased the J_{sc} from 12.04 to 12.69 mA/cm² without

any change in the V_{oc} and FF [41]. Whereas, inclusion of Au-silica NR in the active layer of p-DTS (FBTTh₂):PC₇₀BM improved the J_{sc} to 15.14mA/cm² with no change in V_{oc} and FF. The pronounced J_{sc} was attributed to the enhanced absorption in Au-silica NR as compared to Au-silica NS. The integration bare Au NR in the active layer of p-DTS (FBTTh₂):PC₇₀BM resulted in PCE of 6.9%, whereas the one integrated with Au-silica NR reached PCE of 8.2%, showing a significant improvement due to the presence of a reduced shell thickness of Au-silica NR. The enhanced absorption in both devices was accredited to the scattering and LSPR effects. The small molecule BHJ of p-DTS (FBTTh₂):PC₇₀BM based solar cell integrated with Au-SiO₂ NR in the active layer yielded the highest PCE with a shell thickness of 5 nm. They observed that a further reduction in the shell thickness increases recombination, while a greater shell thickness decreases the electric field intensity. The inclusion of nanostructured Au-SiO₂ NR improved the J_{sc} significantly in comparison to Au-SiO₂ NS, as displayed in Fig. 3.4. They further revealed absorption peaks at 520 nm and 680 nm for Au-SiO₂ NR in chlorobenzene solvent compared to single peak at 528 nm for Au-SiO₂ NS. A high quality factor for LSPR in Au-SiO₂ NR ranging from 550 - 1000 nm was also observed, which matches the absorption spectrum of the donor p-DTS (FBTTh₂). The use of low band gap polymer PCPDTBT: PC₇₁BM and p-DTS (FBTTh₂):PC₇₀BM by Xu et al. yielded efficiency of 4.4% and 8.2%, respectively, showing a more pronounced efficiency in the low band gap polymer of p-DTS (FBTTh₂):PC₇₀BM based solar cells [41].

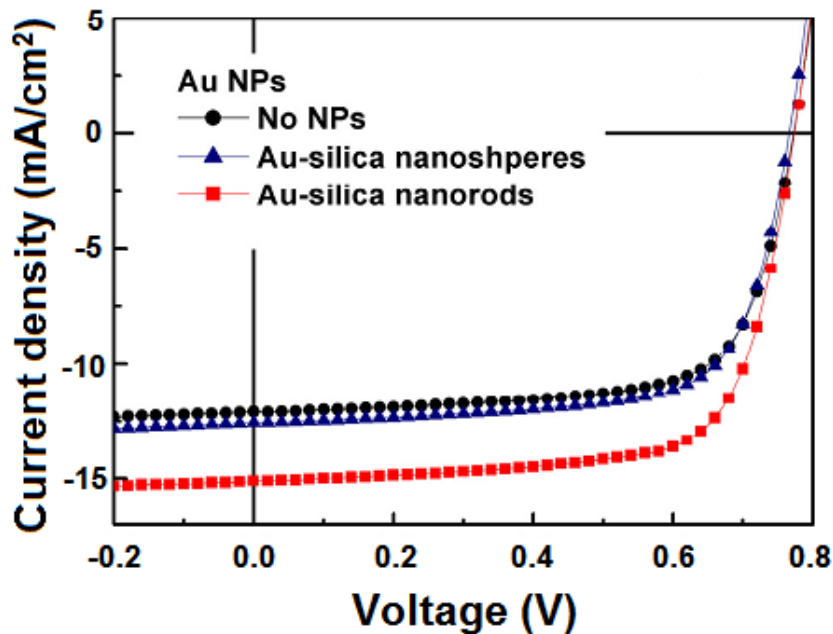


Fig. 3. 4: *J-V* characteristics of the under AM 1.5G irradiation. (Reprinted with permission from [41] Copyright 2015: Elsevier).

Tseng et al. reported various shapes of Au NP embedded in the active layer of solar devices, which included cubes, rhombic dodecahedra (RD), edge- and corner-truncated octahedral (ECTO), and triangular plates [42]. The absorption spectra of the active layer remained the same after doping with these NPs. However, the absorption intensity increased significantly, with the RD absorbance being the highest, resulting to a PCE of 4.14% compared to the rest with ECTO, followed by cubes and triangle NPs displaying efficiencies of 3.76%, 3.75% and 3.62%, respectively. The increased absorbance in these various AuNPs was assigned to the light scattering and LSPR effect. The use of P3HT-PC₆₀BM-Au as sensitizer in the dye sensitizer solar cells displayed an increased in efficiency as compared to none sensitizer solar cells and this was accredited to the plasmon induced effect by Au NPs and the reduced charge recombination in PC₆₀BM. Hence, de Freitas et al. observed an increase in the absorption and exciton generation in the device showing

a further increased when combined with N719 dye [43]. Xie et al. showed that coalescing of AuNPs in both P3HT: PCBM layer and PEDOT: PSS layer further increased the PCE to 3.85% compared to an increase of 3.41% in only the active layer or an increase of 3.61% in only the buffer layer [44]. This further increment was attributed to the added NPs into the individual layers. Spyropoulos et al. reported on the concatenation of surfactant-free AuNPs in the active layer, inclining the PCE to 3.71%, which was allotted to reduction in exciton quenching through recombination process in the capped AuNP layer. The LPSR is induced by small sized AuNPs, while multiple scattering is induced by larger sized AuNPs [45]. Table 2 shows the device characterization data of OPVs with AuNP(s) incorporated into active layer.

Table 3. 2: Device characterization data of OPV with metallic AuNPs in active layer

ARCHITECTURE	PCE (%)	V _{oc}	J _{sc}	FF (%)	Refs.
Glass/ITO/PEDOT:PSS/P3HT:PC ₇₀ BM: Au/TiO _x /Al cathode	4.36	0.63	11.18	61.0	[37]
Glass/ITO/PEDOT:PSS/PCDTBT:PC ₇₀ BM: Au/TiO _x /Al cathode	6.45	0.89	11.16	65.0	[37]
ITO glass/PEDOT:PSS/Si-PCPDTBT:PC ₇₀ BM: Au/TiO _x /Al cathode	4.54	0.57	13.13	61.0	[37]
Glass/ITO/PEDOT:PSS/P3HT:PC ₇₀ BM: Au-SiO ₂ /Ca/Al	3.58	0.62	8.73	66	[39]
Glass/ITO/PEDOT:PSS/PCPDTBT:PC ₇₀ BM: Au-SiO ₂ /Ca/Al	4.40	0.59	12.70	58.1	[39]
Glass/ITO/PEDOT:PSS/p-DTS(FBTTh2) ₂ : PC ₇₀ BM: AuNR/ Ca/Ag	6.90	0.78	12.58	70.2	[41]
Glass/ITO/PEOT:PSS/p-DTS(FBTTh2) ₂ :PC ₇₀ BM: Au-SiO ₂ NS/ Ca/Ag	6.80	0.77	12.69	70.2	[41]
Glass/ITO/PEOT:PSS/p-DTS(FBTTh2) ₂ :PC ₇₀ BM: Au-	8.20	0.77	15.40	70.4	[41]

SiO ₂ NR/Ca/Ag						
Glass/ITO/ZnO/P3HT:PC ₆₁ BM: AuRD/MoO _x /Ag	4.14	0.61	10.39	65.3		[42]
Glass/ITO/ZnO/P3HT:PC ₆₁ BM: AuECTO/MoO _x /Ag	3.76	0.60	9.94	63.0		[42]
Glass/ITO/ZnO/P3HT:PC ₆₁ BM: Aucube/MoO _x /Ag	3.75	0.60	9.95	62.8		[42]
ITO/ZnO/P3HT:PC ₆₁ BM: Atriangle/MoO _x /Ag	3.62	0.60	9.57	63.1		[42]
FTO glass/TiO ₂ :N719/P3HT: Au/Pt	3.51	0.71	9.22	54.0		[43]
FTO glass/TiO ₂ :N719/P3HT:PC ₆₀ BM/Pt	4.90	0.72	11.57	59.0		[43]
FTO glass/TiO ₂ :N719/P3HT:PC ₆₀ BM: Au/Pt	5.94	0.74	14.24	56.0		[43]
Glass/ITO/PEDOT:PSS/P3HT:PC ₆₁ BM :Au/LiF	3.41	0.61	8.85	63.5		[44]
Glass/ITO/PEDOT:PSS: Au/P3HT: PC ₆₁ M: Au/LiF	3.85	0.61	9.74	65.0		[44]
Glass/ITO/PEDOT:PSS/P3HT:PC ₆₁ BM : AuNPs/Al	3.71	0.6	9.77	63.3		[45]

UNIVERSITY of the

3.2.1.3. Effect of Au on P3HT: PCBM optical and structural properties

Wang et al. revealed that a 2 nm Au NP film incorporated in the P3HT: PCBM boost the optical absorption in the spectral range of 350-1000 nm, attributed to photon scattering and trapping in the Au NPs by their surface plasmon effect [46].

Namboothiry et al. also reported improved optical absorption within the spectral range of 320 nm - 750 nm when Au NPs is at the ITO/MoO₃ interface [47].

Park et al. reported that the integration of Au NPs of 5 nm - 10 nm in P3HT does not greatly enhanced the solar cell, due to their close absorption spectra [48].

The optical properties of metal NPs depend on its size and the shape, as shown by Chen et al.

where a red shift was observed with the increase in the spherical Au NPs size [49].

Kozanoglu et al. observed in diverse metallic nanosphere, NRs and nanostars that the PCE is greatly enhanced, especially in the morphology of the Nanostars [50]. They assigned the PCE improvement to the substantial light scattering and enhanced electromagnetic field induced, due to the plasmonic effect. Scanning electron microscope (SEM) micrographs (Fig. 3.5, insets) present an asymmetrical branched structure of nanostars with UV-VIS showing absorption spectral range within 600 nm- 900 nm. The NRs peaks appeared at 540 nm and 800 nm and that of the NS at 525 nm. Hence, the nanostars showed a significant improvement in the J-V characteristics with lower series resistance as compared to the NRs and NS.

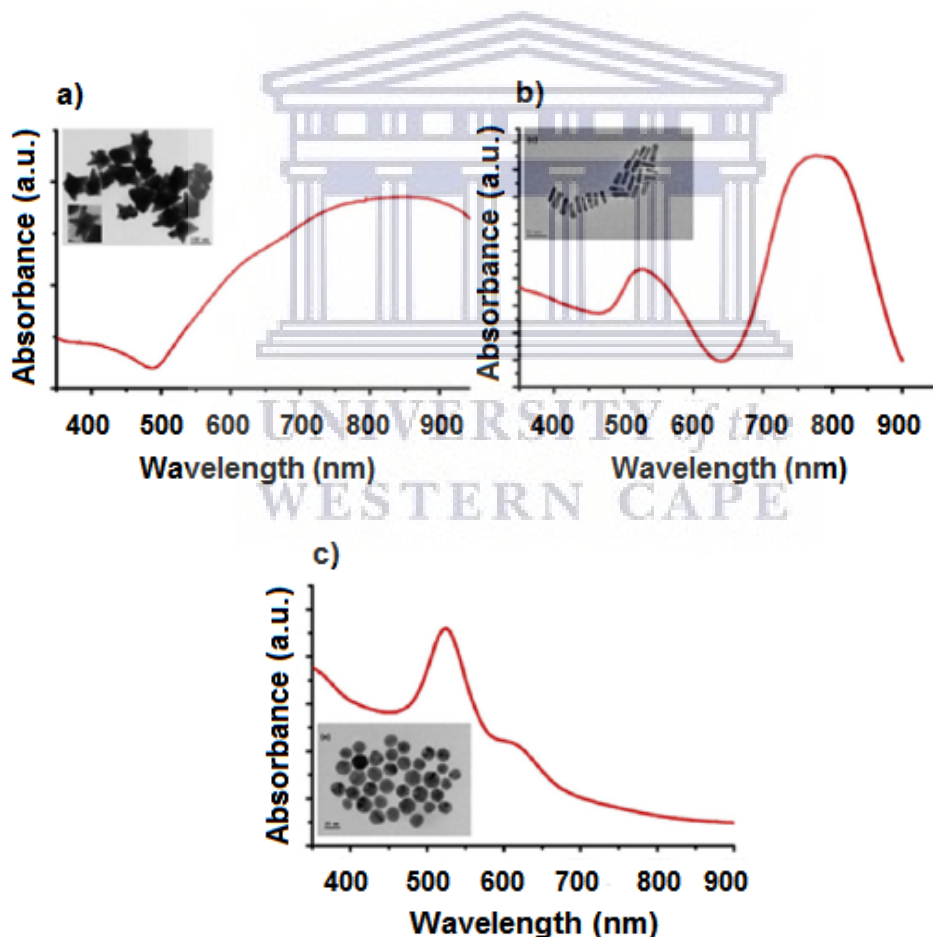


Fig. 3. 5: UV-vis absorption spectrum of Au (a) NSt(s), b) NR(s) and (c) NS(s). Insert shows the SEM image of the nanostructure. (Reprinted with permission from Ref. [50]. Copyright 2016: Elsevier).

3.2.2. Effect of Ag on P3HT: PCBM solar cell performance

3.2.2.1 Ag NPs embedded in the buffer layer

Studies have shown that the incorporation of silver nanostructures into solar cells enhanced the device efficiency, owing to their higher degree of order of the enhanced local field and the ease of altering the absorption spectrum in the near infrared and visible spectral range [51, 52]. Hence, Noh et al. reported on the plasmonic effect of Ag shaped nanoprism (NPSs), which coalesced in the buffer layer of P3HT: PCBM device to enhance the efficiency of the bulk heterojunction organic solar cells (BHJ-OSCS) [53]. The modified seed mediated growth method was used to synthesis AgNPSs through the addition of aqueous AgNO₃ to a mixture of poly sodium styrene sulfonate, aqueous trisodium citrate and aqueous NaBH₄. The use of AgNPSs displayed an increased PCE of 5.21% in the absence of PEDOT layer as compared to the reference with PCE of 4.66%, while an increase in the inter-distance by addition of buffer layer decreased the PCE to 4.91%. However, the J_{sc} and FF in the presence of the PEDOT layer improved, which was attributed to the enhanced near field of LSPR from AgNPSs. Wang et al. disclosed that the integration of Ag nanowire (NW) mesh transparent electrode on polyethylene terephthalate (PET) substrate with an acrylic resin buffer layer on the P3HT:PC₆₀BM solar devices improved the efficiency to 4.45%, as opposed to ITO on glass substrate device with efficiency of 3.37% [54]. For PTB7:PC₇₀BM devices, the incorporation of the AgNW mesh transparent electrode on polyethylene terephthalate (PET) substrate with an acrylic resin buffer layer exhibited a PCE of 7.58%, compared to device with ITO on glass substrate, displaying an efficiency of 7.12%. The higher efficiency was interrelated with the trapping effect and light scattering induced by AgNW mesh. Hao et al. denoted that the inclusion of Ag@SiO₂ NPs in

the buffer layer increased the efficiency of solar devices to 3.35% compared to its pristine with PCE of 2.81% [55]. The enhanced efficiency was correlated with the large size Ag@SiO₂NP due to LSPR by the near and far field scattering effect. Further studies by Baek et al. concurred that the size of the AgNPs influences the scattering efficiency, which affects the performance of the device, exhibiting an efficiency of 7.6% in the PCDTBT:PCBM device, compared to the pristine device with a 6.4% efficiency [56]. An efficiency of 8.6% for the PTB7:PCBM device was further realized, compared to its reference with a PCE of 7.9%. Their method revealed the best J-V characteristics displayed in Fig. 3.6 with improved J_{sc} and FF, due to the improved optical properties.

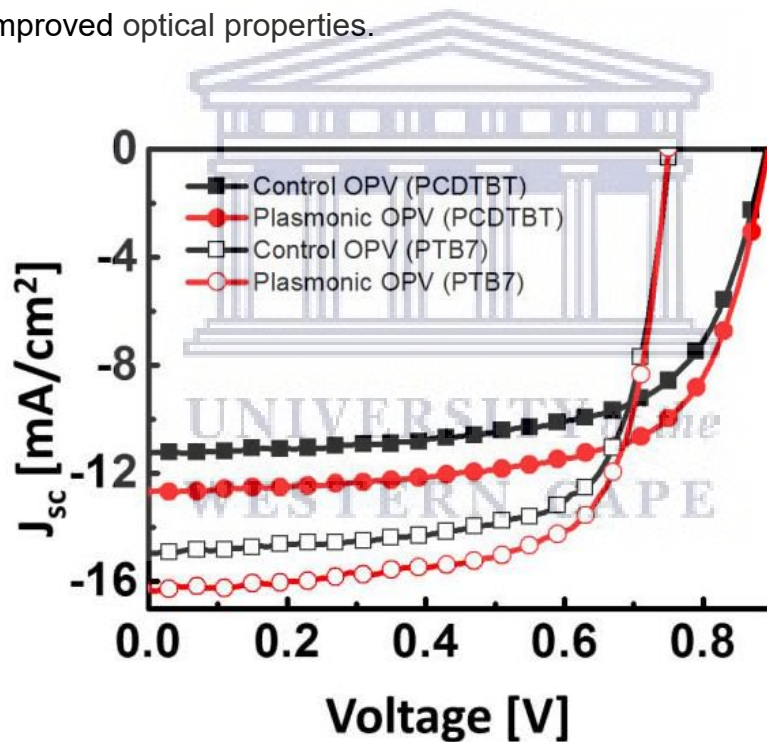


Fig. 3. 6: The J-V characteristics and spectral responses of plasmonic OPVs with various size of AnNPs. (a) The J-V curves of the plasmonic OPV (red circles) and the OPV (black squares). The filled and open symbols denote the PDCTBT:PC₇₀BM and PTB7:PC₇₀BM devices, respectively. The plasmonic devices were optimized in terms of size and concentration. (Reprinted with permission from [56] Copyright 2013: Springer Nature).

Jägeler-Hoheisel et al. articulated the spacer layer introduction to adjust the distance between AgNPs and the active layer [57], thereby divulging an efficiency of 2.65% compared to reference of 1.93% on ZnPc:C₆₀ device. They further pronounced an efficiency of 3.4% in comparison to that of pristine (i.e. 2.7%) in the device of F₄-ZnPc:C₆₀. Xu et al. corroborated the AgNPs in the buffer layer to better improve the efficiency compared to the AuNPS on the PTB7:PC₇₀BM device [58]. The efficiency reached 7.52% in the AgNP doped TiO₂ compared to the 7.02% in the AuNP doped TiO₂. The high efficiency for the AgNP doped TiO₂ was ascribed to exciton dissociation increment, which reduces the recombination rate. Thin film evaporation was used to integrate the Ag nanoisland on the buffer layer of P3HT:PCBM, thereby extending the PCE from 1.3% to 2.2%, which was credited to the enhanced optical absorption by the LSPR of the AgNPs [59]. Thermal deposition of silver on the buffer layer of the P3HT:ICBA device was used to attain the nanostructured rear electrode, which Chen et al. publicised to enhance the efficiency of the inverted polymer solar cells to 7.21%, compared to the flat electrode cell with efficiency of 6.26% [60]. This was imputed to the light trapping of AgNps in the MoO₃ rear electrode by surface plasmonic and backscattering effects, owing to the fact that the Ag nanostructured rear electrode is on top of the active layer compared to flat electrode cell. Jung et al. reported on the assembly of nanobumps (NBA) on MoO₃ buffer layer concealing the AgNPs to further intensify the PCDTBT:PC₇₀BM device's performance to 6.07%, compared to the device with a flat PEDOT:PSS buffer layer with efficiency of 5.63% [61], while both of their reference cells without AgNPs presents similar efficiency of ≈ 5.20%. The enhanced performance was assigned to the multi-reflection and strong forward scattering effect in the NBA structure and further inhibits recombination losses due to the fully covered AgNPs by MoO₃, which makes it isolated from the

active layer. However, in the flat PEDOT:PSS layer; due to its hygroscopic and acidic nature; it leads to instability of the device and moreover exposed AgNPs, which were directly in contact with active layer promote recombination losses and exciton quenching thereby deteriorating the performance of the device. Table 3.3 shows the device characterization data of Os with AgNP(s) incorporated into buffer layer.

Table 3. 3: Device characterization data of OPV with metallic AgNPs in buffer layer

ARCHITECTURE	PCE (%)	V _{oc}	J _{sc}	FF (%)	Refs.
ITO glass/PEDOT:PSS:AgNPs/P3HT:PC ₆₁ B M/AI	4.91	0.53	1.59	60.9	[53]
PET substrate/Acrylic resin/AgNW:PEDOT:PSS/P3HT: PC ₆₀ BM/LiF/AI	4.45	0.60	12.1 5	60	[54]
Glass/ITO/PEDOT: PSS/P3HT: PC ₆₀ BM/LiF/AI	3.37	0.61	8.79	61	[54]
PET substrate/Acrylic resin/PEDOT:PSS/PTB7:PC ₇₀ BM:AgNW/ LiF/AI	7.58	0.68	19.1 6	58	[54]
ITO/PEDOT: PSS/PTB7HT: PC ₇₀ BM/Ag/LiF/AI	7.12	0.75	16.3 5	59	[54]
Glass/ITO/PEDOT:PSS:Ag@SiO ₂ /P3HT: PC ₆₀ BM/LiF/A	3.35	0.59	9.67	58.3	[55]
Glass/ITO/PEDOT:PSS:AgNP- 67/PCDTBT: PC ₇₀ BM/TiO _x /AI	7.6	0.89	12.6 7	67	[56]
Glass/ITO/PEDOT:PSS:AgNP- 67/PTB7:PC ₇₀ BM/TiO _x /AI	8.6	0.75	16.3 3	70	[56]
Glass/ITO/W2 (hpp) 4/C ₆₀ (hpp) 4/ C ₆₀ /ZnPc: C ₆₀ / ZnPc/ BF-DPB: F6-TCNNQ/ V ₂ O ₅ /Ag: BF-DPB: F6-TCNNQ/AI	2.65	0.50	9.4	55.7	[57]
Glass/ITO/W2 (hpp) 4/C60(hpp)4/ C60/F4- ZnPc:C60/ F ₄ -ZnPc/ BF-DPB: F6-TCNNQ/	3.4	0.67	9.3	53.9	[57]

V2O5/Ag: BF-DPB: F6-TCNNQ/Al					
Glass/ITO/TiO ₂ : Ag (or Au) NPs/PTB7:PC ₇₀ BM/MoO ₃ (8 nm)/Al	7.52	0.71	16.8 0	63.0	[58]
Glass/ITO/ZnO/P3HT: ICBA/AgNPs:MoO ₃ /Al	7.21	0.85	12.8 6	66.0	[60]
Glass:ITO/Ag NPs-MoO ₃ (NBA)/PCDTBT: PC ₇₀ BM/LiF/Al	6.07	0.88	10.4 8	65.0	[61]
Glass/ITO/PEDOT:PSS:AgNP/PCDTBT:P C ₇₀ BM/LiF/Al	5.63	0.89	10.2 4	62.0	[61]

3.2.2.2 Ag NPs embedded in the active layer

Various shapes of Ag nanostructures yield different properties such as its absorbance and reflective effect. Diverse research works have authenticated that Ag nanomaterials have an effective light scattering effect compared to Au nanomaterials. Hence, a comparative study of Ag nanoplates and AgNPs displayed different levels of optical reflectance and absorption spectra in the active layer of various devices [62]. Wang et al. revealed an efficiency of 4.4% for P3HT:PC₇₁BM device integrated with Ag nanoplates compared to its pristine cell with an efficiency of 3.3% and the one with AgNPS reaching 4.0%. The improved performance was due to effective light scattering of the Ag nanoplates, which increased the optical path length thereby hindering recombination losses. They further detailed an enhanced efficiency of 6.6% in the PCDTBT:PC₇₁BM layer of the Ag nanoplate-based device as compared to the AgNPs based device and reference with efficiency of \approx 5.9% and 6.4% respectively. This affirms the Ag nanoplates positive effect in the OSC devices. Kim et al. presented a relative study of AgNPs and AgNWs in the active layer of P3HT: PCBM to elevate the performance of the device to efficiency of 3.56% and 3.91% respectively, owing to the electron/hole carrier mobility in AgNWs

based devices, which are 1.5 times larger than AgNPs based devices [63]. This results in an increased electrical conductivity with an increase in J_{sc} and PCE. Chen et al. synthesised various ratios of AuAg alloy NPs with several stabilizing ligands to intermingle with P3HT:PC₆₁BM layer exhibiting PCE of 4.73% and 3.53% compared to AgNPs based device with 4.60% efficiency [64]. Li et al. corroborated the seed mediated growth method to synthesis AgNPs from previous studies to enhance the performance of the devices [65]. The blends of different nanostructured material, i.e. AgNPs and AgNPs gave rise to different LSPR peaks resulting in broader absorption enhancement. The mixed nanostructured based device presented a higher performance of ~ 4.30% compared to the cell with AgNPs only and AgNPs only displaying efficiency of 4.07% and 3.99%, respectively. The improved performance of the device was assigned to the simultaneously excitation of high order and low order resonance, resulting in the observed broadband resonance. Jang et al. employed sol gel method to synthesis the Ag@SiO₂, which entails a mixture of aqueous silver nitrate added to aqueous CTAB solution and aqueous ascorbic acid [66]. This is followed by accelerating the reaction with addition of sodium hydroxide and controlling the thickness of the SiO₂ by adding tetraethoxysilane and finally washing and centrifuge with ethanol and acetone. The use of core/ shell in the Ag@SiO₂ was to hinder the recombination losses. The inverted solar devices with blends of P3HT: PCBM and Ag@SiO₂ in the active layer reached a PCE of up to 3.94% compared to Ag@SiO₂ placed on top of the buffer layer or active layer displaying efficiency of 3.66% and 3.38%, respectively. They ascribed the fine tune performance to the LSP and scattering effect by Ag core and SiO₂ respectively, resulting in D/A electron-hole carrier in the active layer. Yao et al. exploited the AgNPs owing to the strong optical effect with large local field and

scattering enhancement effect compared to NS [67]. Photo induced (PNP) and thermal induced (TNP) method to synthesis AgNPs were used and integrated in different locations of the PIDTT-DFBT: PCBM devices to enhance its performance. The front type device with TNP AgNPs in the PEDOT: PSS layer improved up to 8.35% and the PNP AgNPs in the buffer layer reached up to 8.50% efficiency. The higher efficiency in the PNP was attributed to the sharper triangular geometry and the consistence size distribution. The rear type device with TNP AgNPs in C₆₀-bis was enhanced to a PCE of about 8.30%. The dual type devices resulted in a much improved efficiency of around 9.02%, which is in agreement with several research reports. This enhanced efficiency was ascribed to the combination of dual doped interfacial layer and the tuning of AgNPs. They further substantiated their flexible approach with different polymer based devices leading to efficiency of ≈7.06% in the dual type of PCDTBT: PC71BM based devices, while in PIDT-PhanQ device the efficiency reached 7.85%. Table 3.4 illustrates the device characterization data of OPVs with AgNP(s) incorporated into active layer.

Table 3. 4: Device characterization data of OPV with metallic AgNPs in active layer

ARCHITECTURE	PCE	V _{oc}	J _{sc}	FF	Refs.
Glass/ITO/PEDOT:PSS/P3HT:PC ₇₁ BM:Agnanoplates/TiO _x /Al cathode	4.4	0.61	13.58	52	[62]
Glass/ITO/PEDOT:PSS/P3HT:PC ₇₁ BM:AgNPs/TiO _x /Al cathode	4.0	0.62	12.95	50	[62]
Glass/ITO/PEDOT:PSS/PCDTBT:PC ₇₁ BM:Agnanoplates/TiO _x /Al cathode	6.6	0.87	13.19	57	[62]
Glass/ITO/PEDOT:PSS/PCDTBT:PC ₇₁ BM:AgNPs/TiO _x /Al	6.4	0.87	12.12	61	[62]
Glass/ITO/PEDOT:PSS/P3HT:PC ₆₁ BM:AgNWs/Al	3.91	0.66	9.32	63.9	[63]

Glass/ITO/PEDOT:PSS/P3HT:PC ₆₁ BM:AgNPs/A I	3.56	0.65	9.28	59.1	[63]
Glass/ITO/PEDOT:PSS/P3HT:PC ₆₁ BM:Ag ₁₁ Au ₈₉ /Ca/Al	4.73	0.63	12.21	61.5	[64]
Glass/ITO/PEDOT:PSS/P3HT:PC ₆₁ BM:Ag ₂₈ Au ₇₂ /Ca/Al	3.53	0.60	11.38	51.7	[64]
Glass/ITO/PEDOT:PSS/P3HT:PC ₆₁ BM:Ag/Ca/Al	4.60	0.64	11.96	60.1	[64]
Glass/ITO/PEDOT:PSS/P3HT:PC ₆₁ BM: Agblends/Ca/Al	4.30	0.64	10.61	63.3	[65]
Glass/ITO/PEDOT:PSS/P3HT:PC ₆₁ BM: Agnanoprisms/ Ca/Al	4.07	0.64	9.93	64.1	[65]
Glass/ITO/PEDOT:PSS/P3HT:PCB ₆₁ M:AgNPs/ Ca/Al	3.99	0.64	9.80	63.5	[65]
Glass/ITO/P3HT:PCBM:Ag@SiO ₂ /MoO ₃ /Ag	3.94	0.61	9.72	66.5	[66]
Glass/ITO/P3HT:PCBM/Ag@SiO ₂ /MoO ₃ /Ag	3.38	0.58	9.54	60.5	[66]
Glass/ITO/ZnO/Ag@SiO ₂ /P3HT:PCBM /MoO ₃ /Ag	3.66	0.58	9.63	65.8	[66]
Glass/ITO/PEDOT:PSS/TNP-535 (front)/PIDTT- DFBT:PC ₇₁ BM/C ₆₀ -bis/Ag	8.35	0.96	13.5	62	[67]
Glass/ITO/PEDOT:PSS/PNP-535(front)/PIDTT- DFBT:PC ₇₁ BM/C ₆₀ -bis/Ag	8.50	0.96	13.72	62	[67]
Glass/ITO/PEDOT:PSS /PIDTT-DFBT:PC ₇₁ BMC ₆₀ -bis/ TNP-450 (rear)/Ag	8.30	0.96	13.47	62	[67]
Glass/ITO/PEDOT:PSS/PNP-535(front)/PIDTT- DFBT:PC ₇₁ BM/C ₆₀ -bis/ TNP-450(rear)/Ag	9.02	0.96	14.36	63	[67]
Glass/ITO/PEDOT:PSS/PNP- 535(front)/PCDTBT:PC ₇₁ BM/C ₆₀ -bis/ TNP-450 (rear)/Ag	7.06	0.90	12.21	62	[67]
Glass/ITO/PEDOT:PSS/PNP-535(front) /PIDT- PhanQ:PC ₇₁ BM/C ₆₀ -bis/ TNP-450(rear)/Ag	7.58	0.88	13.18	67	[67]

3.2.2.3. Effect of Ag on P3HT: PCBM optical and structural properties

Shen et al. introduced the core shell Ag@SiO₂ and Ag nanoplates (Ag-nP1) to avoid electron quenching, due to direct contact with active layer of PBDTTT:PCBM cell [68]. They reiterated that blends of different Ag nanostructures can harvest light in different wavelength regions to elevate the performance of the devices. Inclusion of encapsulated Ag@SiO₂ to active layer and bare Ag-nP1 on ITO substrate was demonstrated to enhance the cell. The Ag-nP1 was widely distributed, revealing a strong absorption peak at 750 nm that was accredited to the AgnP1 in plane dipole resonance. The Ag@SiO₂ were homogenously dispersed with an absorption peak at 425 nm. The blend of these Ag nanostructures therefore covers the full wavelength range in the visible spectra. Li et al. employed a room temperature vacuum assisted nanoimprinting method in the inverted solar devices [69], by reiterating the use of dual metallic nanostructures involving back reflector of Ag nanograting electrode and the AuNPs located under the PBDTTT-C-T:PC₇₁BM active layer. They noted that mask grating that occurred during nanoprinting revealed a Rayleigh anomaly peak of 750 nm that is red-shifted to around 800 nm. They ascribed the red-shift to the Ag nanoprinting by the surface plasmonic resonance (SPR) effect, which contributed to the absorption enhancement of the cell. The absorption enhancement in the AuNPs was in the region of 400-600 nm and was accredited to the localised plasmonic resonance (LSPR) of AuNPs. Xue et al. demonstrated a P3HT: PCBM based devices incorporated with AgNPs to enhance the device, resulting in absorption of 350- 600nm, which was accredited to the LSPR within the AgNPs [70]. Yoon et al. displayed the self-assemble layer of Ag nanosphere uniformly distributed in the P3HT: PCBM layer enhancing the absorption within the spectral range of 350- 650nm, which was ascribed to the electric field accumulating in the active layer

around the Ag nanosphere by LSP [71]. However, Pei et al. integrated the Ag nanodisks synthesised by a solution processed method, where control of the size and shape was used to fine-tune the LSPR within the entire visible range [72]. Their approach displayed enhanced absorption within the spectral range of 400-650 nm, which was assigned to the matched spectral overlap among the plasmon resonance of Ag nanodisks and the P3HT. Wang et al. demonstrated that AgNPs clusters that are randomly dispersed in the active layer of PCDTBT/PC₇₀BM, can effectively increase the optical absorbance within a spectral range of around 350 nm - 550 nm [73]. This is due to the scattering effect of the incident light by the plasmon resonance of AgNPs clusters in the active layer and the electron-hole pair generated around the excited field of AgNPs clusters.

3.3. INFLUENCE OF TiO₂ METAL OXIDE

3.3.1. Effect of TiO₂ on P3HT: PCBM solar cell performance

3.3.1.1 TiO₂ embedded in the buffer layer

Metal oxides such as ZnO and TiO₂ are used mostly as electron transport layers, whereas hole transport layer are commonly MoO₃, WO₃ and V₂O₅ [74]. The use of metal oxides, such as TiO₂ and ZnO in various applications is due to their superlative optical translucency across the whole visible spectral range and their wide band gap with easy doping ability to active ions [75, 76]. Hence, the extensive investigation of TiO₂ as interlayer in the inverted organic solar cell has been widely reported. Hadipour et al. disclosed that the use of temperature solution processed TiO_x as a low work function in the inverted solar cell to function as a buffer layer yield higher performances with processable advantages as compared to the evaporated buffer

layer such as Ca [77]. Baek et al. replaced the buffer layer of PEDOT:PSS due to its instable, hygroscopic and acidic nature, which had a negative impact on the performance of the solar cells [78]. The method of nanoimprinting lithography with PMMA nanopoles was used to fabricate nanoporous TiO₂ that was integrated into the buffer layer of P3HT:PCBM based devices. The efficiency of 1.49% for nanoporous TiO₂ compared to 1.19% for flat TiO₂ was attributed to the increased interface area of P3HT-TiO₂ from its effective charge separation and reduced series resistance. Gopinath et al. synthesized cost effective NPs of TiO₂, Au and Pt from plant extraction of Terminalia arjuna bark [79]. The T. Arjuna bark functions as a reducing and capping agent, due to its rich bioactive components showing a homogenous distribution of particles. The innocuous synthesised NPs were employed using the doctor blade technique in the application to enhance the performance of the devices. A pristine TiO₂ displayed an efficiency of approximately 2.79%, whereas in the presence of AuNPs, the efficiency reached 3.44% and in the presence of Pt it reached 3.14%. The increased V_{oc} in Au and Pt doped-TiO₂ was attributed to the reduced recombination rate by the metallic NPs. Örnek et al. explored the interfacial layer of Eu doped-TiO₂ in the P3HT: PCBM based inverted solar cell, reporting an efficiency of ~ 2.47%, compared to the pure TiO₂ reaching to an efficiency of 1.16% [80]. The enhanced performance was credited to the accumulation of electron transport of doped Eu in TiO₂ as compared to pure TiO₂. Xie et al. applied several NP doped-TiO₂ in various active layers of solar cells to display that charge accumulation is the reason for enhanced electron extraction; and as a result, the performance of both P3HT and PBDTTT-C-T based solar devices improved [81]. They further displayed that plasmonic resonance of the small NPs showed no significant improvement in the optical absorption. They projected

improved PCE of $\approx 4.26\%$ in Au-TiO₂ and $\approx 4.01\%$ in Ag-TiO₂ of P3HT active layer. They substantiated the improvement with low bandgap polymer of PBDTTT-C-T reporting efficiency of ≈ 8.20 in Au-TiO₂ and ≈ 7.87 in Ag-TiO₂. The J_{sc} and FF were improved in the presence of either AuNPs or AgNPs incorporated in the TiO₂ in the active layer of P3HT inverted solar cells. However, a significant improvement was noticed in the J_{sc} and FF of the low bandgap polymer in both Au-TiO₂ and in Ag-TiO₂ of PBDTTT-CT active layer. The J-V characteristic of the inverted solar cells under AM 1.5 G illumination is displayed in Fig 3.7. Lin et al. presented the method of polymer assisted deposition (PAD) method to produce metal-organic films [82].

The PAD method involves binding of polymer to metal ions simultaneously controlling the viscosity to yield a homogenous distribution of metal precursor and forming uniform metal-organic films. Hence, different processes for metal oxide films preparation were reported [83, 84]. They divulged that the polymer assisted deposition (PAD) method produces smooth and uniform high quality thin films, displaying the versatility of PAD method in TiO₂ and ZnO films as buffer layer and MoO₃ film as anode buffer to yield a relative high efficiency compared to those synthesised through other methods. Table 3.5 shows the device characterization data of OPVs with TiO₂ incorporated in the buffer layer.

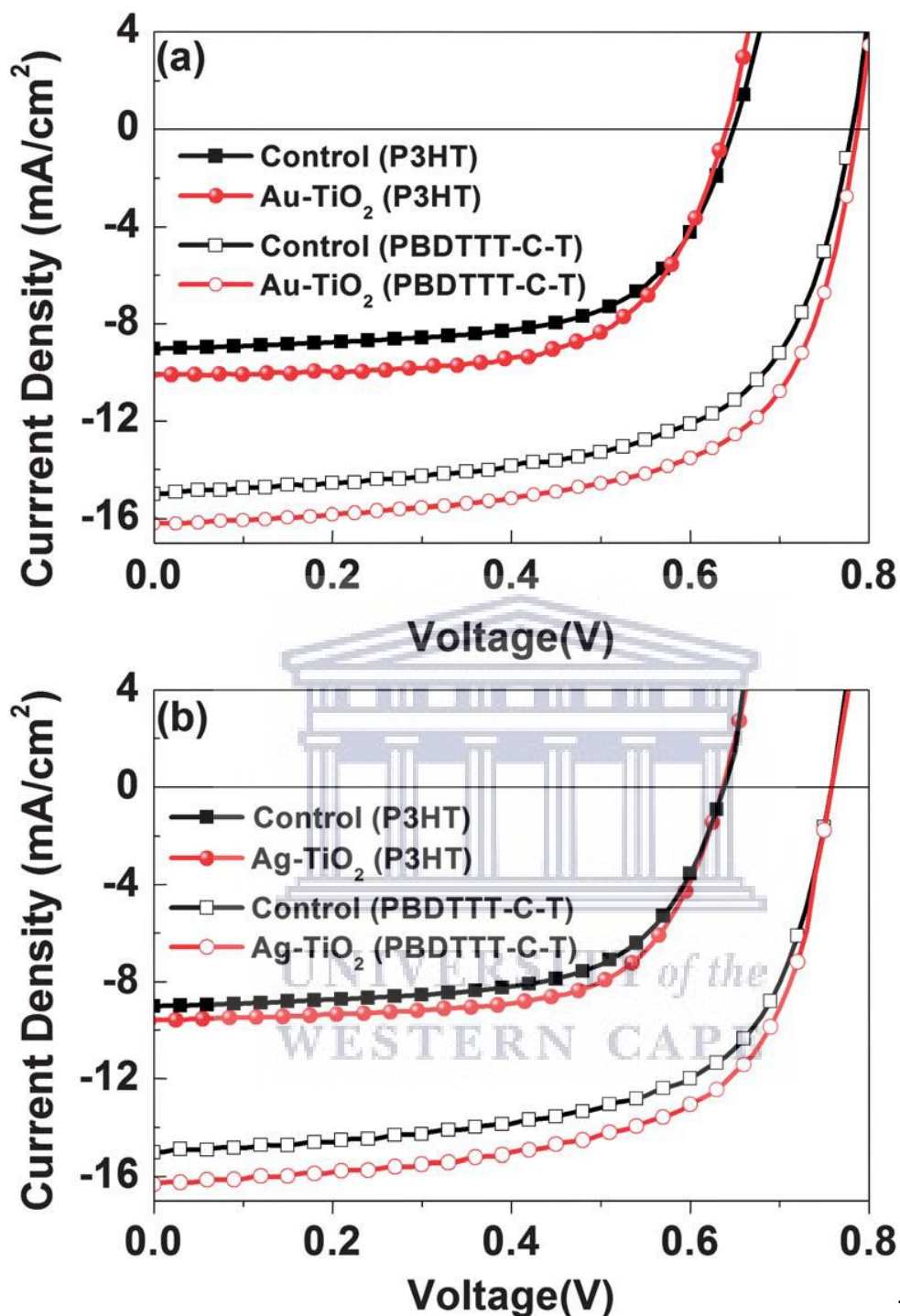


Fig. -C-T:PC₇₁BM
 OSCs using TiO₂ and Au Nps-TiO₂ as ELTs under solar illumination (AM1.5G) (b) J-V characteristics of the inverted P3HT:PC₆₁BM OSCs and PBCTTT-C-T:PC₇₁BM OSCs using TiO₂ and Ag NPs-TiO₂ as ETLs under solar illumination (AM1.5G).

Table 3. 5: Device characterization data of OPV with TiO₂ in buffer layer

ARCHITECTURE	PCE	V _{oc}	J _{sc}	FF	Refs.
Glass/ITO/ flat TiO ₂ /P3HT:PC ₆₁ BM/Au	1.19	0.44	6.80	39.6	[78]
Glass/ITO/ nanoporous TiO ₂ /P3HT:PC ₆₁ BM/Au	1.49	0.45	7.71	43.1	[78]
Glass/ITO/ZnO/ZnO/CuO/P3HT:PC ₇₁ BM/MoO ₃ /Al	5.13	0.73	14.0	57.0	[79]
Glass/ITO/Eu: TiO ₂ /P3HT:PC ₆₁ BM/Ag	2.47	0.58	9.47	44	[80]
Glass/ITO/TiO ₂ /P3HT:PC ₆₁ BM/MoO ₃ /Ag	3.64	0.64	9.03	62.9	[81]
Glass/ITO/Au:TiO ₂ /P3HT:PC ₆₁ BM/MoO ₃ /Ag	4.26	0.63	10.35	65.1	[81]
Glass/ITO/Ag:TiO ₂ /P3HT:PC ₆₁ BM/MoO ₃ /Ag	4.01	0.63	9.59	65.3	[81]
Glass/ITO/TiO ₂ /PBDTTT-C-T:PC ₇₁ BM/MoO ₃ /Ag	7.31	0.77	15	62.8	[81]
Glass/ITO/Au:TiO ₂ / PBDTTT-C-T:PC ₇₁ BM/MoO ₃	8.20	0.78	16.21	64.3	[81]
Glass/ITO/Ag:TiO ₂ / PBDTTT-C-T:PC ₇₁ BM/MoO ₃ / Ag	7.87	0.76	16.32	63.4	[81]
Glass/ITO/STO/P3HT:PC ₆₁ BM/MoO ₃ /Al PAD	2.96	0.61	8.99	53	[83]
Glass/FTO//D149-TiO ₂ ND/P3HT/PEDOT:PSS/Au	3.12	0.63	8.12	61	[84]
Glass/ITO/ZnO-TiO ₂ /P3HT:PCBM/Ag	3.32	0.64	9.95	51.6	[85]
Glass/ITO/ZnOTiO ₂ /P3HT/Au Sol-gel	0.76	0.46	3.48	47	[86]

3.3.1.2. TiO₂ embedded in the active layer

Yang et al. concurred with the hypothesis of TiO₂ nanotubes aggregates to decrease the device's absorbance, nonetheless collection and transportation of charges increases with impeded recombination rate [87]. The presence of TiO₂ nanotubes aggregates yielded efficiency of about 3.2% as a result of electron transport enhancement. Mcgehee et al. reported that the side chains of P3HT effect π stacking in the conjugated backbone due to their regular arrangement results in high carrier mobility [88]. Hence, the study of different molecular weight in solar devices by Wu et al. showed that a distinct molecular weight of P3HT can be formed by changing the ratio of Ni(dppp)Cl₂ and as a result; the high the molecular weight the high the carrier mobility [89]. Thus, incorporation of TiO₂ in high molecular weight of P3HT (66kDa) resulted in efficiency of around 0.60%, whereas the lower molecular weight of P3HT (10kDa) was around 0.56% efficiency. The difference in PCE was accredited to dissimilar conformation and packing manner, which influences the electrical and optical properties. Tai et al. employed electrospinning technique to fabricate the nanofibrous films of TiO₂ blending with active layer of P3HT based hybrid solar cells [90]. They observed that the designed electrospun nanofibers with controllable alignment and size increase the electrical contact between the cathode electrode and the TiO₂ NPs, owing to their continuous carrier pathway and large interfacial area. They further enhanced the performance by co-modification of 3-phenylphronic acid (PPA) and ruthenium dye (N719) on the surface of TiO₂ nanofibres, which influenced the ordered backbone of P3HT layer. They spin coated the sol gel solution of a TiO₂ compact layer onto a ITO substrate to intensify the adhesion of the electrospun TiO₂ nanofibres and infiltrated the P3HT layer in each cross aligned TiO₂ nanofibrous film by spin coating it with P3HT solution.

Modification of ruthenium dye could not cover the whole TiO₂ nanofibrous films due to the steric effect and hence PPA was added for better surface coverage. The co-modification increased the performance of the hybrid solar cell from PCE of around 0.59% to 1.09%, which was assigned to the enhanced coupling of electrons among the TiO₂ and absorbed dye and to the hindered recombination rate of carriers that reduce the trap density at the interface. Tu et al. promulgated that a stable P3HT:TiO₂ based solar cell with its lower efficiency can be enhanced by doping with boron to increase electron mobility or doped with Bismuth to increase electron density of the anatase TiO₂ [91]. The sol gel method was used to synthesise three types of TiO₂ NRs from hydrolysis of TTIP, boron and bismuth named as TiO₂ (as-synthesised), TiO₂ (B-doped) and TiO₂ (Bi-doped), respectively. The W4-dye modified TiO₂ for B-doped and Bi-doped TiO₂ displayed a PCE of around 0.87% and 0.89%, respectively. The improved performances in the B-doped TiO₂ was ascribed to the higher electron mobility and the improved crystallinity due to smaller ionic radius of B³⁺ compared to Ti⁴⁺. However, in the Bi-doped TiO₂, the highest V_{oc} and J_{sc} was due to improved electron density due to the Bi electron lone pairs. Kogo et al. created the amorphous TiO_x combined with brookite TiO₂ at a low process temperature to enhance the performance of the CH₃NH₃PbI₃ perovskite solar cell [92]. The synthesised TiO_x was spin coated on ITO substrate as a blocking layer, followed by spin coating the brookite TiO₂ as an electron collector. Subsequently the CH₃NH₃PbI₃ was spin coated. They reported an efficiency of about 20.2% in backward scan mode, which was ascribed to superior alignment of the electron band of TiO_x in reference to brookite TiO₂. The device with the brookite TiO₂ only displayed a PCE of around 13.0%. The reduced efficiency was attributed to the higher recombination rate of the carriers in the interface. The device with blocking

layer of TiO_x only exhibited an efficiency of around 13.2%, which was attributed to the inefficient collection of the electron by the TiO_x layer. They further demonstrated that $\text{TiO}_x/\text{brookite TiO}_2$ based devices resulted in a higher efficiency compared to $\text{SnO}_x/\text{brookite TiO}_2$ based devices. The higher efficiency in the $\text{TiO}_x/\text{brookite TiO}_2$ is due to the superior band alignment for electron collection compared to the $\text{SnO}_x/\text{brookite TiO}_2$. The amorphous SnO_x layer's inability to collect electron, results in a higher recombination rate, thereby deteriorating the cell performance. The J-V characteristic of solar cells under illumination and in the dark is displayed in Fig 3.8, including the forward and backward scans. According to Fig. 3.8, perovskite solar cells employing the amorphous TiO_x layer yield a higher V_{oc} than the Brookite TiO_2 only ones. In fact, Table 1 and Fig. 2 from the work of Kogo et al. exhibit similar V_{oc} for solar cells employing TiO_x only and $\text{TiO}_x/\text{Brookite TiO}_2$ bilayers. V_{oc} in solar cells are complex parameters that can be influenced by several factors, such as an increase in R_s or the intrinsic energy levels of the charge collecting layers. Here, upon insertion of a thin 8 nm amorphous TiO_x layer between the ITO electrode and the Brookite TiO_2 porous layer, the series resistance decreases (Fig. 3.2 and Fig. S2 in the referenced paper).

Using photoelectron yield spectroscopy and the optical bandgap of the hole blocking layers, the authors estimated that compared to the frontier energy levels of Brookite TiO_2 (3.9 eV and 7.3 eV), those of TiO_x are downshifted by 0.2 eV. However, such shift is inconsistent with the higher V_{oc} observed when employing the amorphous TiO_x layers. In fact, the authors ascribe the higher V_{oc} to a better hole blocking capacity of the amorphous TiO_x layer which would reduce the leak current in the devices. Despite the fact that shunt resistance values were not provided by the authors, this seems to be a reasonable explanation when carefully analysing the

data presented in Fig. 3.2(c). From a theoretical point of view (see equation 3.1) [93], in the equivalent circuit model of solar cells suggests that V_{OC} is associated with $\ln(1/I_0)$, where I_0 is the reverse saturation current of the devices.

$$V_{OC} = \frac{nk_B T}{q} \ln\left(\frac{J_{ph}}{J_0} + 1\right) \quad (3.1)$$

where k_B is the Boltzmann constant, T is the temperature, J_0 is the reverse saturation current density, J_{ph} is photo-current density and n is the ideality factor of the diode. Less leak current (and a lower reverse saturation current) is thus consistent with the increase in V_{OC} observed upon insertion of the thin TiO_x as hole blocking layer. The V_{OC} may also be influenced by J_{sc} , but in this case we can consider that the minor changes in J_{sc} have a relatively low impact on the V_{oc} . We should also mention here that the authors did not provide any other experimental data that would allow us to further analyse their results and thus additional discussion would only be based on speculations. Table 3.6 shows the device characterization data of OPVs with TiO_2 incorporated in the active layer.

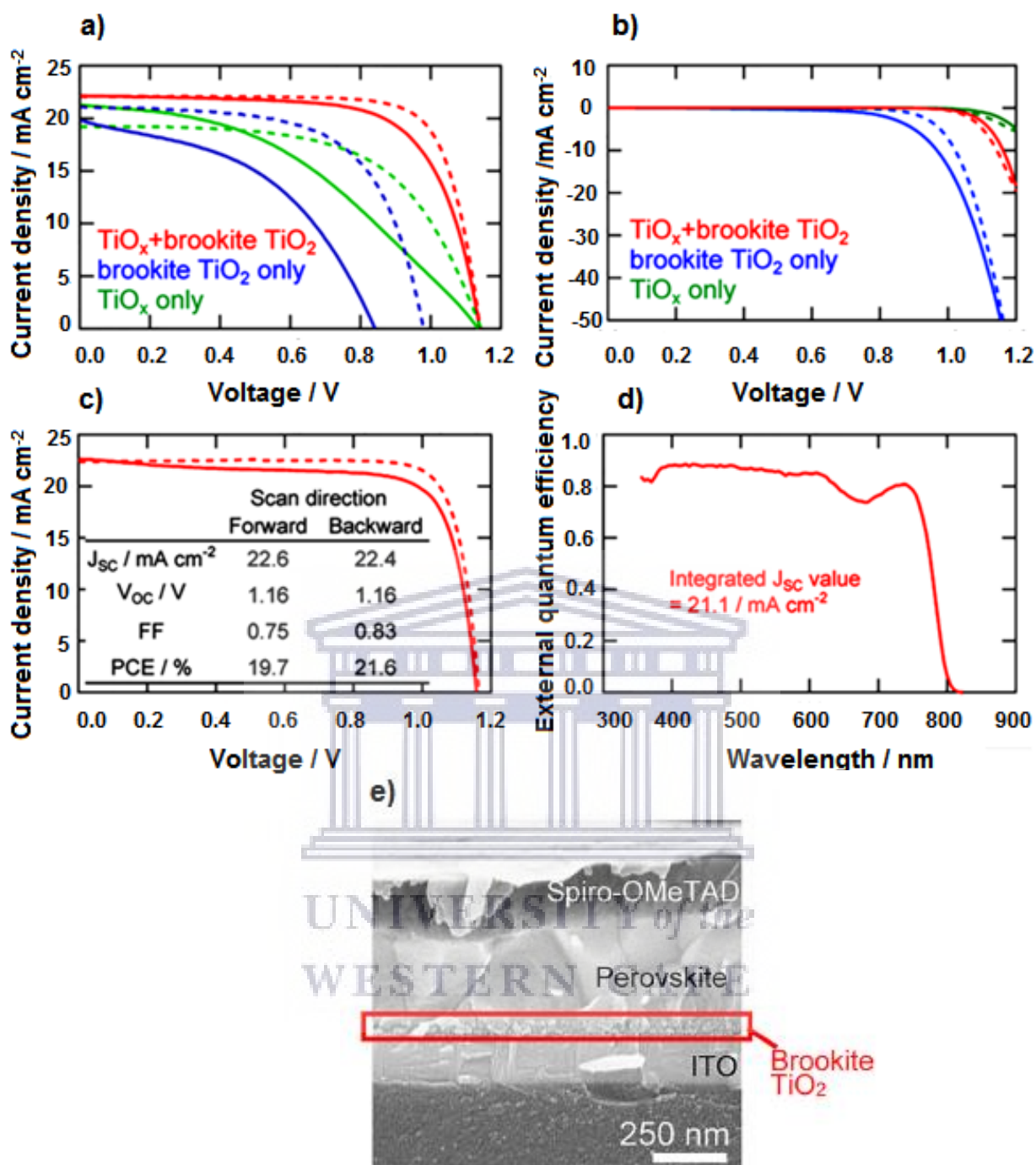


Fig. 3. 8: (a) Under 1 sun illumination and (b) in dark. Forward ($-0.1 \text{ V} \rightarrow 1.2 \text{ V}$) and backward ($1.2 \text{ V} \rightarrow -0.1 \text{ V}$) scans are indicated as solid and dashed lines, respectively. (c) J-V curve and (d) EQE spectrum of the best solar cells with TiO_x (thickness $\sim 8 \text{ nm}$)/brookite TiO_2 electron collector stored in dry air for 2 days. (e) Cross-sectional SEM image of $\text{CH}_3\text{NH}_3\text{PbI}_3$ perovskite solar cells with TiO_x (thickness $\sim 8 \text{ nm}$)/brookite TiO_2 electron collector. (Reprinted with permission from [92] copyright 2018: ACS Publications).

Table 3. 6: Summary of device characterization data of OPV with using TiO₂ in the active layer

ARCHITECTURE	PCE	V _{oc}	J _{sc}	FF	Refs.
Glass/ITO/ZnO/PSiF-DBT:PC ₆₁ BM/MoO ₃ /Au	3.8	0.90	5.03	60	[87]
Glass/ITO/PEDOT:PSS/P3HT(66kDa):TiO ₂ /Al	0.61	0.60	2.8	36.5	[89]
Glass/ITO/PEDOT:PSS/P3HT(10kDa):TiO ₂ /Al	0.20	0.56	1.2	29.3	[89]
Glass/ITO/TiO ₂ / P3HT /Au	0.59	0.62	1.89	50	[90]
Glass/ITO/TiO ₂ / N719/P3HT /Au	0.90	0.67	2.53	53	[90]
Glass/ITO/TiO ₂ /N719+PPA/ P3HT /Au	1.09	0.69	2.92	54	[90]
ITO/PEDOT:PSS/as-TiO ₂ :P3HT/TiO ₂ NRs/Al.	0.67	0.86	1.80	42	[91]
ITO/PEDOT:PSS/(B-doped)-TiO ₂ :P3HT/TiO ₂ NRs/Al	0.87	0.83	2.67	39.2	[91]
ITO/PEDOT:PSS/(Bi-doped)-TiO ₂ :P3HT/TiO ₂ NRs/Al	0.89	0.89	2.81	35.5	[91]
Glass/ITO/TiO _x /brookite TiO ₂ /CH ₃ NH ₃ Pbl ₃ /spiro-OMeTAD/Au	20.2	1.14	22.5	79	[92]
Glass/ITO/TiO _x /CH ₃ NH ₃ Pbl ₃ /spiro-OMeTAD/Au	13.2	1.14	19.2	60	[92]
Glass/ITO/brookite TiO ₂ /CH ₃ NH ₃ Pbl ₃ /spiro-OMeTAD/Au	13.0	0.98	21.1	63	[92]
Glass/ITO/SnO _x /brookite TiO ₂ /CH ₃ NH ₃ Pbl ₃ /spiro-OMeTAD/Au	18.1	1.14	21.7	73	[92]
Glass/FTO/compact TiO ₂ / nanoparticle TiO ₂ :N 719:P3HT/Au	0.35	0.26	8.47	16	[94]
Glass/FTO/compact TiO ₂ /nanofiber ATiO ₂ : N 719:P3HT/Au	0.15	0.17	3.26	28	[94]

Boroomandnia et al. demonstrated that anatase crystalline TiO₂ is highly conductive compared to the rutile crystalline phase and further displayed that TiO₂ NPs exhibit an enhanced interface area compared to TiO₂ nanofibres [94]. Hence, modifications of N719 dye on anatase crystalline TiO₂ NPs increased the efficiency to $\approx 0.353\%$,

due to improved electronic coupling among the TiO_2 and absorbed dye and the reduced density of trap states of $\text{TiO}_2/\text{P3HT}$ interface area that hinders the recombination effect.

3.3.1.3. Effect of TiO_2 on P3HT: PCBM optical and structural properties

Lin et al. uncovered the 3D nanostructured solar cell based on thicker ZnO NRs that developed perpendicularly to the substrate with thinner TiO_2 NRs integrated in the P3HT active layer of the device [95]. TEM analyses showed the growth direction of the synthesised TiO_2 nanorods was in the longitudinal direction. The UV-vis absorption spectra of pristine P3HT ranged from 350 nm-650 nm with weaker vibronic structure and a blue shift of P3HT band, which was due to infiltration of P3HT/ TiO_2 hybrid into ZnO nanorods array. Lim et al. observed that ordered TiO_2 nanotubes arrays when infiltrated with P3HT polymer, using the dip coating method, shows well aligned tubes with absorption spectrum around 500 nm for P3HT/ TiO_2 nanotubes. This was ascribed to the fact that the pores of the TiO_2 nanotube array are entrenched with the polymer [96]. However, Bartholomew et al observed a low infiltration of 0.5% of the polymer in the random nanocrystalline TiO_2 networks (RNTNs), which is contrary to Lim's observation [97]. The degree of polymer infiltration was increased using heat treatment, but resulted in a low 3% infiltration of the polymer and this was attributed to the thick RNTNs with internal voids that were not easily accessible. However, it was revealed that pores of mesoporous TiO_2 network were accessible with a uniform pore size, from SEM imaging, and that infiltration of the polymer volume into film is dependent on the temperature [98]. They noted a red-shift of the absorption, attributed to the crystallised polymer chains. Hence, they emphasised that the effective charge carrier mobility and electron

transfer originate in the stacking of polymer chains into the TiO₂ film. Diverse research on vertical oriented TiO₂ nanotubes array has been established by numerous researchers owing to its continuous electron-accepting network. Therefore, Shankar et al developed a double heterojunction solar cell through a blend of P3HT: PCBM infiltrated into a transparent and non-transparent TiO₂ nanotube array that can be illuminated either on the front- or back side [99]. They demonstrated an enhanced performance in the front side illumination, which was ascribed to the lower photonic losses as compared to the backside illumination.

3.2.2. Effect of ZnO on P3HT: PCBM performance

3.3.2.1. ZnO embedded in the buffer layer

ZnO is an n-type semiconductor with a bandgap and conduction band position similar to TiO₂. However, the carrier mobility of ZnO is higher than that of anatase TiO₂ [100]. Doping ZnO with aluminium at low temperature can increase its carrier density and different ways of ZnO film preparation make it an attractive selection choice to enhanced efficiency better in the organic solar devices [101-103]. Chen et al. fabricated P3HT:PC₆₁BM and PBDTTBO: PC71BM based solar devices using the sol gel method by incorporating PEI-blend ZnO in the buffer layer, perpendicularly aligned to the ITO substrate, to enhance the efficiency of the devices [104]. They observed an increase in both devices that where integrated with ZnO:PEI layer as compared to ZnO/PEI layer and the one without PEI. The enhanced performances in the ZnO:PEI was assigned to the distribution of the N atoms on the surface of the buffer layer, which increased the carrier mobility, band alignment and the surface smoothness of the interfacial layer. Their results concurred with the hypothesis of Woo et al. concerning the distribution of N moieties on the buffer layer surface [105].

They witnessed an increased in the short-current density of the devices. Tan et al. established the performance of P3HT: PCBM layer integrated with crystalline ZnO NP in the buffer layer of heterojunction solar cell through the sol gel method (Tan et al., 2013). They accomplished an increased efficiency of $\approx 3.72\%$ in the inverted cell of ZnO NP buffer layer as compared to normal 1 of MoO₃ buffer layer and normal 2 of PEDOT:PSS buffer layers with efficiency around 2.07% and 3.04%, respectively. The improved efficiency was attributed to the improved matching of the energy level of the ZnO NP to the PCBM, whereas in the absence of ZnO buffer layer resulted in an S curve shape accompanied with decreased V_{oc} . Fig. 3.9 displays the J–V characteristics and device data for different device architecture.

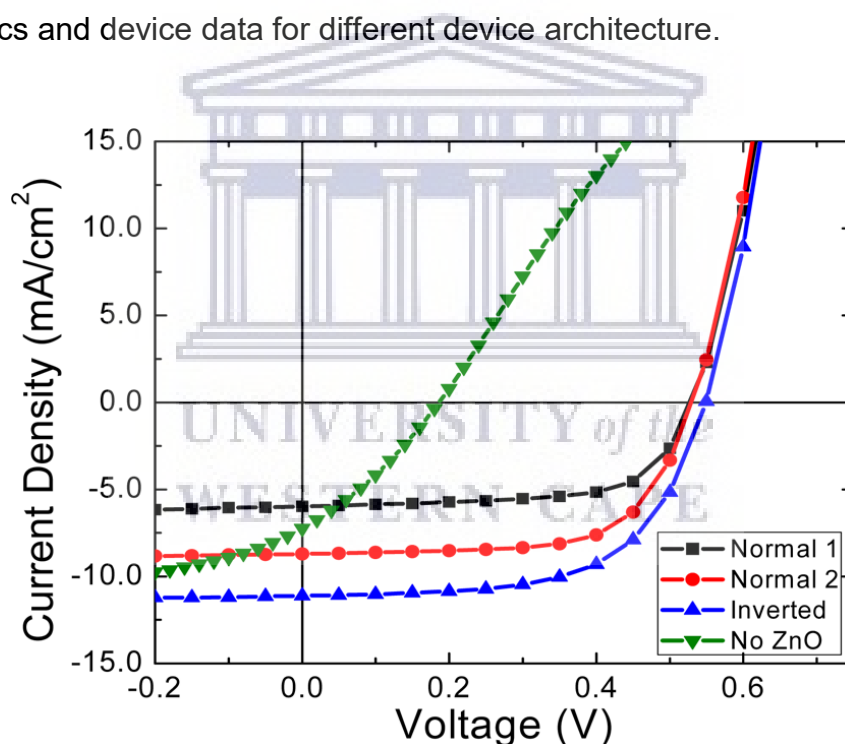


Fig. 3. 9: *J–V* characteristics under AM 1.5 G illuminations for different device architecture. (Reprinted with permission from [106] Copyright 2013: ACS Publications).

Ambade et al. explored both the P3HT:PCBM and PTB7-Th:PCBM based solar devices incorporated with thiophene-S doped planar Zn NRs (Thio-S Zn NRs) as an electron transport layer to improve the performance of the inverted solar devices

[107]. The increased efficiency was around 3.68% and 8.15%, respectively, which was assigned to the improved alignment of the energy level and the induced doping effect, which resulted in four-fold increase of electrical conductivity as compared to the undoped planar Zn NRs devices with PCE of around 2.38% and 6.5%. Mohan et al. compared the influence of the sol gel method and mixed solvent on ZnO buffer layer of both P3HT and PTB7 based solar devices [108]. The mixed solvent method on both active layer of P3HT:PC₇₁BM and PTB7: PC₇₁BM displayed an improved efficiency of 5.6% and 9.1% respectively. However, the sol gel method at high temperature on both P3HT:PC₇₁BM and PTB7: PC₇₁BM based solar cells resulted in PCE of around 4.1% and 6.5%, respectively. The enhanced *J-V* characteristic in the mixed solvent method is attributed to enhanced charge extraction and free carrier transport as a result of the high fill factor (FF) with enhanced charge collection, resulting from the low sheet resistance [109,110]. The high ordering as a result of well blending in mixed solvent has been observed in the AFM images, which contributed to the enhanced performance and influenced the longevity and carrier mobility of the cells in both P3HT:PC₇₁BM and PTB7: PC₇₁BM active layer, as opposed to the sol gel method. Sharma et al. explored the PffBT4T-2OD:PC₇₀BM based solar devices modified with a buffer layer of Ga-doped ZnO (GZO) using sol gel method [111]. They observed an enhanced V_{oc} , despite the low process temperature prior to the spin coating of the active layer, which is contrary to previous studies. They further displayed an increase in the FF due to the highly ordered crystalline PffBT4T-2OD with efficiency reaching $\approx 9.74\%$, owing to GZO's increased transport properties as opposed to pristine ZnO. Table 3.7 reveals the device characterization data of OSCs with ZnO incorporated in the buffer layer.

Table 3. 7: Device characterization data of OSCs with ZnO in the buffer layer.

ARCHITECTURE	PCE	V _{oc}	J _{sc}	FF	Refs.
Glass/ITO/ZnO:PEI(7%)/P3HT:PC ₆₁ BM/MoO ₃ /Ag	4.6	0.60	11.4	67	[104]
Glass/ITO/ZnO:PEI(3%)/P3HT:PC ₆₁ BM/MoO ₃ /Ag	4.3	0.60	10.9	66	[104]
Glass/ITO/ZnO:PEI(7%)/ PBDTTBO: PC ₇₁ BM/MoO ₃ /Ag	8.7	0.85	14.7	70	[104]
Glass/ITO/ZnO/PEI(2nm)/ PBDTTBO: PC ₇₁ BM/MoO ₃ /Ag	8.1	0.86	13.7	68	[104]
Glass/ITO/nc-ZnO/P3HT:PCBM/MoO ₃ /Ag	3.72	0.55	11.0	61.5	[106]
Glass/ITO/PEDOT:PSS/P3HT:PCBM/nc-ZnO/Al	3.04	0.53	8.7	66	[106]
Glass/ITO/MoO ₃ /P3HT:PCBM/nc-ZnO/Al	2.07	0.52	6.0	66.3	[106]
Glass/ITO/Thi-S-PZnRs/P3HT:PC ₆₀ BM/MoO ₃ /Ag	3.86	0.61	10.8	55	[107]
Glass/ITO/Thi-S-PZnRs/PTB7-Th:PC ₆₀ BM/MoO ₃ /Ag	8.15	0.79	14.9	69	[107]
Glass/ITO/PZnRs/P3HT:PC ₆₀ BM/MoO ₃ /Ag	2.38	0.55	8.01	54	[107]
Glass/ITO/PZnRs/PTB7-Th:PC ₆₀ BM/MoO ₃ /Ag	6.5	0.78	13.7	61	[107]
Glass/ITO/ZnO (mixed solvent)/P3HT:PC ₇₁ BM/MoO ₃ /Ag	5.6	0.63	14.7	60.5	[108]
Glass/ITO/ZnO (mixed solvent)/PTB7:PC ₇₁ BM/MoO ₃ /Ag	9.1	0.73	19.5	63.5	[108]
Glass/ITO/ZnO (sol gel)/P3HT:PC ₇₁ BM/MoO ₃ /Ag	4.1	0.5	13.2	54.7	[108]
Glass/ITO/ZnO (sol gel)/PT7B:PC ₇₁ BM/MoO ₃ /Ag	6.5	0.72	18.3	49.4	[108]
Glass/ITO/ZnO/PffBT4T-2OD:PC ₇₀ BM/MoO _x /Al	8.72	0.76	17.3	65.9	[111]
Glass/ITO/GZO-ZnO/PffBT4T- 2OD:PC ₇₀ BM/MoO _x /Al	9.74	0.77	18.6	67.6	[111]

3.3.2.2. ZnO embedded in the active layer

The ability of ZnO to crystallize at low temperature has attracted much attention as opposed to high crystallization temperature of TiO₂. However, ZnO with its wide bandgap absorb only in the UV light [112-114] and therefore the modification of ZnO is required to absorb in the visible region [115-118]. Kim et al. and Zhang et al. explored the electrospinning of ZnO nanofibres in dye sensitized solar cells, reaching efficiency of 3.02% [119-120]. Hence, the use of this electrospun ZnO nanofiber by enhancing the performance of hybrid solar devices was studied [121]. They observed that ZnO nanofibers with no surface treatment displayed a performance of 0.51%. Fig. 3.10 shows the fabrication of electrospun ZnO nanofibers in the P3HT hybrid solar device.

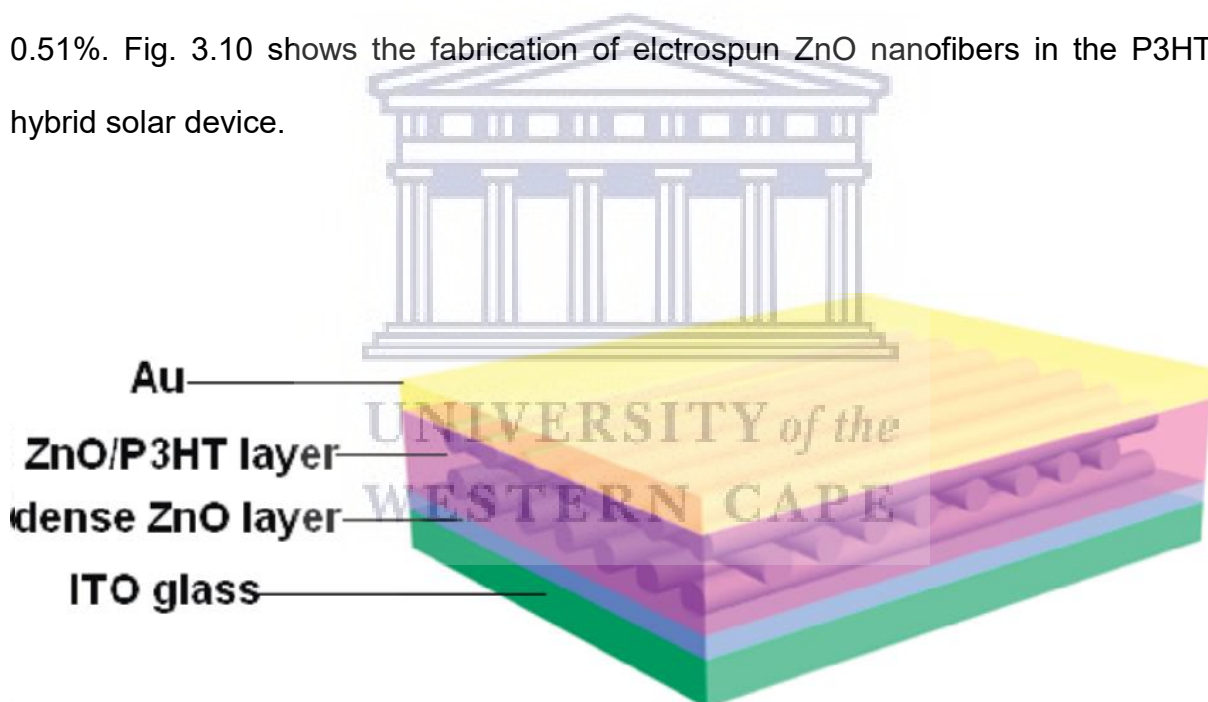


Fig. 3. 10: The structure of the hybrid solar cell based on electrospun ZnO nanofibers and P3HT. (Reprinted with permission from [121] Copyright 2010: ACS Publications).

Later, Spoerke et al. employed the method of CdS modified electrospun ZnO nanofibers on ITO substrate of the P3HT based solar cell [122]. They demonstrated an efficiency of around 0.65% in the presence of a three-layered modified CdS, in contrast with the 0.3% efficiency for devices without CdS. This was assigned to the

elevated CdS absorption in the visible region and its inhibited recombination effect. Oh et al. studied the performance of P3HT: PCMB based devices by inclusion of ZnO in the active layer by reducing the resistivity of PEDOT: PSS buffer layer with N,N-dimethyl formamide (DMF) (Oh et al., 2013). The reduced resistivity elevated the J-V characteristics of the cells resulting in an efficiency of around 3.39% as opposed to the cell without ZnO or DMF with an efficiency of 2.79% and 1.91%, respectively. The improved efficiency was attributed to increase in conductivity, which increases the diffusion length of the carriers with a reduced recombination (see Fig. 3.11).

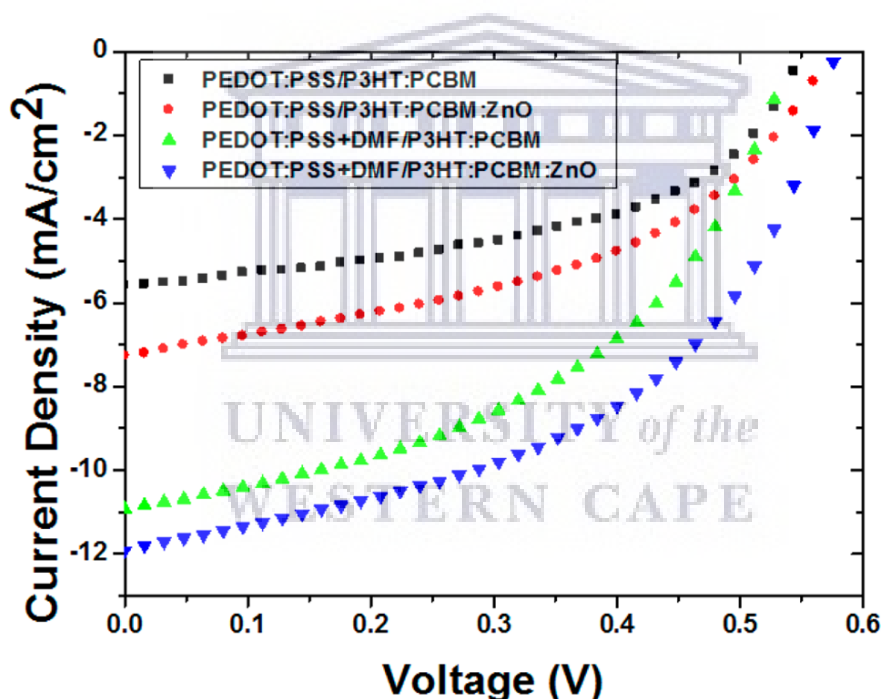


Fig. 3. 11: The J-V characteristic ZnO: P3HT: PCBM thin films with PEDOT: PSS and DMF-modulated PEDOT: PSS. (Reprinted with permission from [123] Copyright 2013: ACS Publications).

Ajuria et al. exploited the effect of synthesised ZnO NPs that were spin coated on the ZnO nanowire arrays in the active layer of P3HT: PCBM solar devices [124]. The SEM imaging the observed a poor blending on the infiltration of different ZnO nanostructures on P3HT: PCBM surface, yielding low efficiency of 3.63%. This was

accredited to the fact that ZnO nanostructure was covered by P3HT: PCBM only, on the top surface resulting in potential loss of optoelectronic properties of the photovoltaic cell. However, good infiltration of P3HT: PCBM ensued an efficiency of $\approx 4.1\%$, owing to the smooth coverage of the nanowire array by the blended P3HT: PCBM that enlarged the dissociation area, resulting in an increased exciton splitting as alternated to planar structured. The approach of infiltrating the mesoporous ZnO network with conjugated polymers displayed a limited efficiency owing to its interface quality [125-128]. Hence, Olson et al. investigated the effect of vertically aligned ZnO nanofibres infiltrated with conjugated polymers in the P3HT: PCBM solar devices [129]. They observed a fourfold increase in the J_{sc} of the modified ZnO contrary to the planar structures, which was ascribed to the increased interfacial area with efficiency reaching to 0.61%. Sung et al. assembled the combination of vertical and single crystalline ZnO nanosheets (NS) with petite branches, using chemical bath deposition at room temperature, by infiltrating with P3HT to improve the efficiency of the hybrid solar cells [130]. They noted an increase in J-V characteristics as opposed to the ZnO NRs array. They attributed the improved performance of 0.88% to the fast transport rate of the electrons and the significant absorption peak owing to the suitable free space within the ZnO NS as opposed to 0.76% efficiency of ZnO NRs array owing to insufficient interfacial area. Lin et al. evaluated the fabrication of ZnO NS coated with TiO₂ NPs in dye sensitized solar cells (DSSC) using chemical deposition method in contrast with ZnO NPs or ZnO NS electrodes [131]. They observed in the SEM imaging that ZnO-NS are uniformly distributed and perpendicularly aligned to the FTO substrate with the efficiency reaching up to 6.06% as opposed to efficiency in ZnO NPs amounting to 2.92%. They further displayed enhanced performance in TiO₂-NP/ZnO-NS film reaching to 7.07%

efficiency, which was ascribed to increased surface area induced by TiO₂ loading.

Table 3.8 demonstrates the device characterization data of OSCs with ZnO incorporated in the active layer.

Table 3. 8: Device characterization data of OPV with ZnO in the active layer.

ARCHITECTURE	PCE	Voc	Jsc	FF	Refs.
Glass/ITO/ZnO/ZnOnanofiber: P3HT/Au	0.23	0.66	0.64	38	[112]
Glass/ITO/ZnO/ ZnO nanofiber/P3HT/Au	0.3	0.39	1.91	39.4	[112]
Glass/ITO/PEDOT: PSS/P3HT: PC ₆₁ BM:ZnO/LiF/Al	1.91	0.57	7.27	45.9	[123]
Glass/ITO/PEDOT:PSS(DMF)/P3HT:PC ₆₁ BM/LiF/Al	2.78	0.54	10.9	47.1	[123]
Glass/ITO/PEDOT:PSS(DMF)/P3HT:PCBM:ZnO/LiF/Al	3.39	0.57	11.9	49.2	[123]
ITO/ZnONW+NP: P3HT:PCBM (poor blend)/MoO ₃ /Ag	3.63	0.57	11.8	57	[124]
ITO/ZnONW+NP: P3HT: PCBM(good blend)/MoO ₃ /Ag	4.1	0.57	13.7	52	[124]
Glass/ITO/ZnO fibres: P3HT/Ag	0.53	0.44	2.2	56	[125]
Glass/ITO/ZnO NS62-P3HT/PEDOT: PSS/Au	0.88	0.42	3.85	54	[130]
Glass/ITO/ZnO NR-P3HT/PEDOT: PSS/Au	0.50	0.33	2.84	53	[130]
Glass/FTO/ZnO-NP:D-149/Pt	2.92	0.48	13.8	43.3	[131]
Glass/FTO/ZnO-NS:D-149/Pt	6.06	0.53	18.0	63.4	[131]
Glass/FTO/TiO ₂ -NP/ZnO-NS: D-149/Pt	7.07	0.57	19.5	62.8	[131]

3.2.2. Effect of ZnO on P3HT: PCBM optical and structural

The simple solution process of ZnO at low temperature and its higher transparency and effective electron mobility has attracted much attention for its application in solar

cells. As a result, Yun et al. examined the effect of low density ZnO NRAs infiltrated with P3HT through solution process in the inverted hybrid solar cell as shown in Fig. 3.12 [132]. Motaung et al. synthesized ZnO nanorods using hydrothermal method, and they observed that incorporation of ZnO nanorods on the surface of P3HT and blended films result to complete PL quenching justifying a charge transfer along the ZnO/P3HT and ZnO/P3HT:fullerenes. The nanorods worked as an effective electron collectors by reducing the average electron diffusion distance in the P3HT and fullerenes network [133].

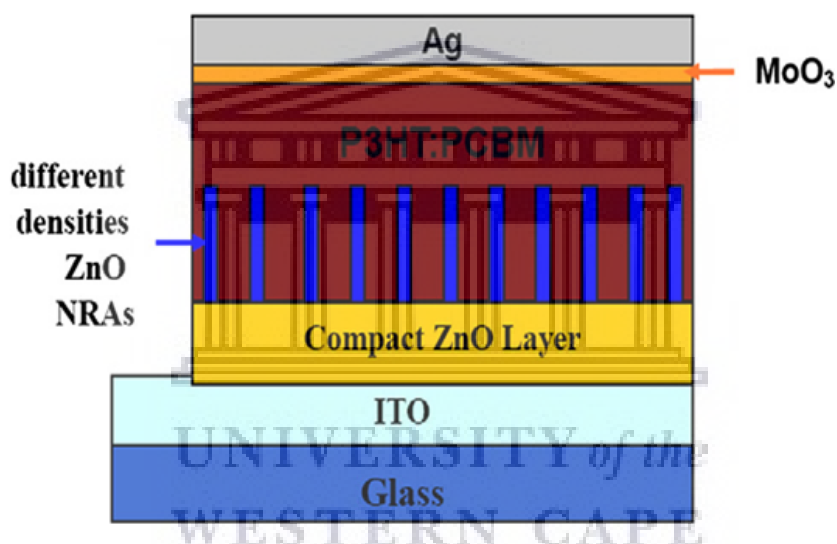


Fig. 3. 12: Schematic structure of an ITO/ZnO seed layer/ZnO nanorod/P3HT:PCBM/MoO₃/Ag photovoltaic device. (Reprinted with permission from [132] Copyright 2011: Elsevier).

The SEM imaging displayed vertically aligned ZnO NRAs on the ZnO seed layer with the polymer fully infiltrated in the low density ZnO NRAs. The well-arranged morphology of low density ZnO NRAs resulted in an improved interfacial interaction that induces efficient charge transport. The UV absorption spectra of PCBM and P3HT were displayed at 386 nm and 510 nm, respectively, with ZnO NRAs shoulder peak blue-shifted to around 360 nm. Ibrahim et al. employed a method of wet

grinding using ethylene glycol solvent to synthesise ZnO NPs that were spin coated on the ITO substrate of the P3HT: PCBM based device [134]. The grinding method induces stability in the ZnO NPs with a well-organized morphology. Below a wavelength of 400 nm, they observed a peak reduction in the IPCE with a slight improvement in UV region. Wang et al. examined the method of electrochemical deposition using DMSO to synthesise mesoporous ZnO films, which were infiltrated with P3HT to improve the performance of the solar cells [135]. They observed from the SEM imaging a smooth film surface of closed packed pores with high crystallinity. The optical transmittance of the porous ZnO film and reference ranged from 300-900 nm. Chou et al. introduced a prolonged drying method to study the effect it has on the polymer and its inclusion in the spacing of ZnO NRs of the hybrid solar cells [136]. The slowly dried films were reported to have a high molecular weight polymer due to the reduced spin rate. They reported a 4.7 times increase in absorption of the slowly dried films as opposed to fast dried films owing to the high polymer density. The absorption peak of the slowly dried films red shifted to 513 nm, which was attributed to the high degree of crystallinity of the polymer [137,138]. The prolonged dried method displayed the full infiltration of the polymer in the ZnO NRs spacing with an increased interfacial layer. AFM imaging revealed a rough surface morphology. Thus, an increase in hole mobility was observed resulting in an improved FF. Huang et al. reconnoitred the infiltration of ZnO NRAs with PCBM interlayer in dichloromethane solvent to enhance the hybrid solar devices [139]. SEM imaging confirms the vertical aligned ordered ZnO NRAs that were fully infiltrated with the PCBM interlayer. The AFM imaging revealed a rough surface in the presence of PCBM interlayer as a result of the highly ordered polymer. They observed an absorption peak of P3HT molecule at 515 nm from both devices with

and without the interlayer, which was ascribed to the highly crystalline polymer chain of P3HT. Fig. 3.13 presents an improved J-V characteristic of device A with a fullerene interlayer, as opposed to device B without the fullerene interlayer. The contact area was minimized by the presence of the interlayer among the ZnO NRAs and P3HT; resulting in anticipated increased V_{oc} .

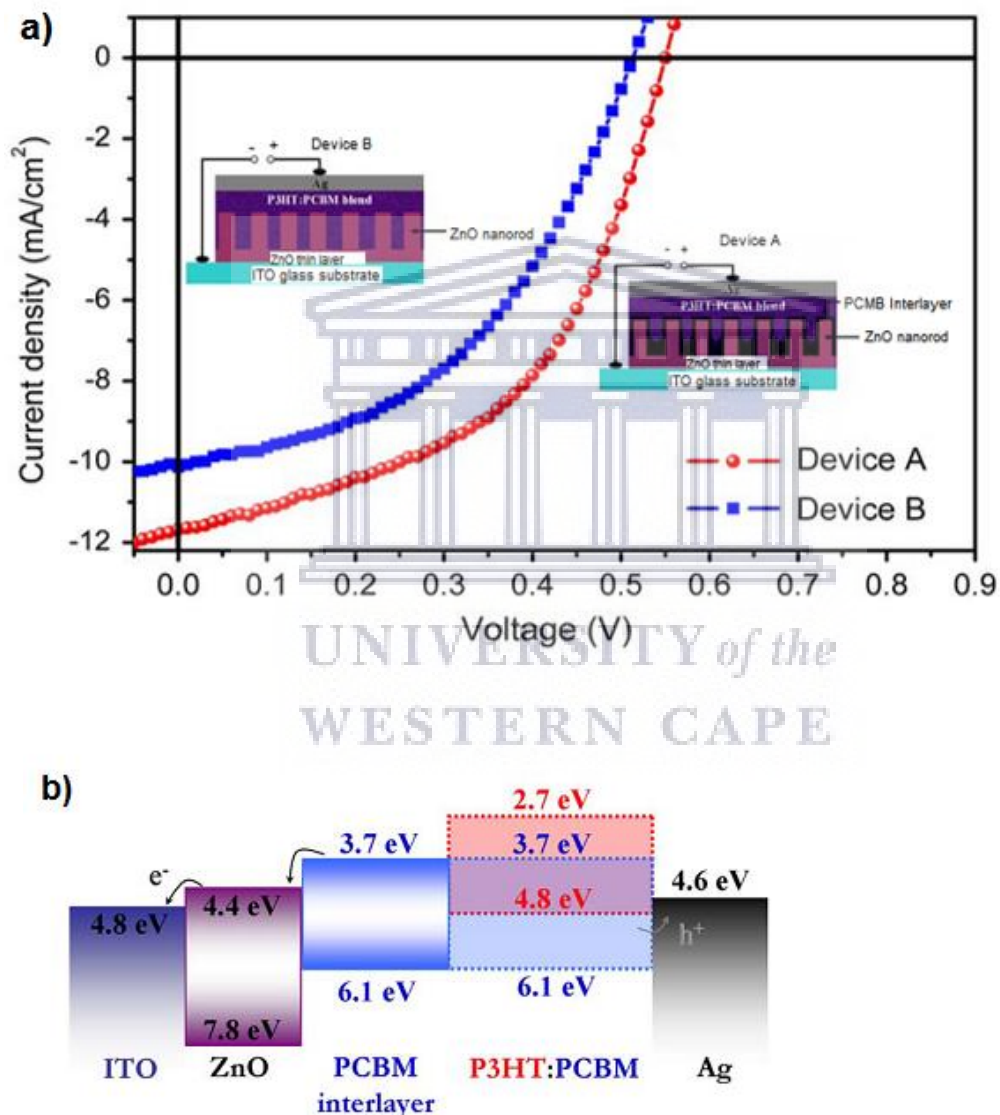


Fig. 3. 13: (a) The current-voltage characteristics of the photovoltaic devices under 100 mW/cm^2 AM 1.5G irradiation. Inserts: Device A represents the hybrid solar cells with the solution processed fullerene interlayer. Device B denotes the hybrid solar cells without the fullerene interlayer. (b) Energy band diagram for P3HT: PCBM/ZnO nanorod arrays hybrid solar cells. (Reprinted with permission from [139] Copyright 2010: Elsevier).

3.3.3 Effect of CuO on P3HT: PCBM solar cell performance

3.3.3.1 CuO NPs embedded in the buffer layer

The use of a PEDOT: PSS buffer layer has been reported to cause instability in the solar cells due to their acidic and hygroscopic nature. Substitution of PEDOT:PSS with p-type semiconductor CuO NPs was explored owing to its innocuous nature, low-cost and its influence on the optoelectronic properties of the photovoltaic cells [140-145]. Xu et al. corroborated the effect of CuO buffer layer in the conjugated polymers of P3HT and PBDTTT-C based solar devices with interchangeable acceptors [147]. They observed an increment in the open-circuit voltage (V_{oc}) and short-circuit current density (J_{sc}) of the PSCs in diverse solar cells containing a CuO buffer layer compared to the PEDOT: PSS buffer layer. The increased J-V characteristics in the active layer of P3HT: PCBM interfaced with CuO NPs in Fig 3.14 was attributed to hole collection increase, which impedes the recombination rate, thereby resulting in an efficiency of around 4.10% as opposed to the buffer layer of PEDOT: PSS with efficiency reaching 3.70 %. The consistency of the interlayering CuO NPs in the solar cells was further substantiated with the low band gap PBDTTT-C copolymer and displayed an efficiency of up to 7.14%. They also reported an enhanced performance in substituting PCBM with ICBA owing to its high LUMO level. They exhibited an increased efficiency of $\approx 6.72\%$ in the P3HT: ICBA based solar cells containing CuO buffer layer, contrary to the PEDOT: PSS buffer layer with a PCE of around 6.29%. The enhancement was credited to greater visible absorption of ICBA material. The buffer layers remediate the stability of solar devices significantly as opposed to cells without buffer layers in the active layer of P3HT:PCBM, P3HT:ICBA and PBDTTT-C, which were reported to have an efficiency of around 2.80%, 4.49% and 5.83%, respectively.

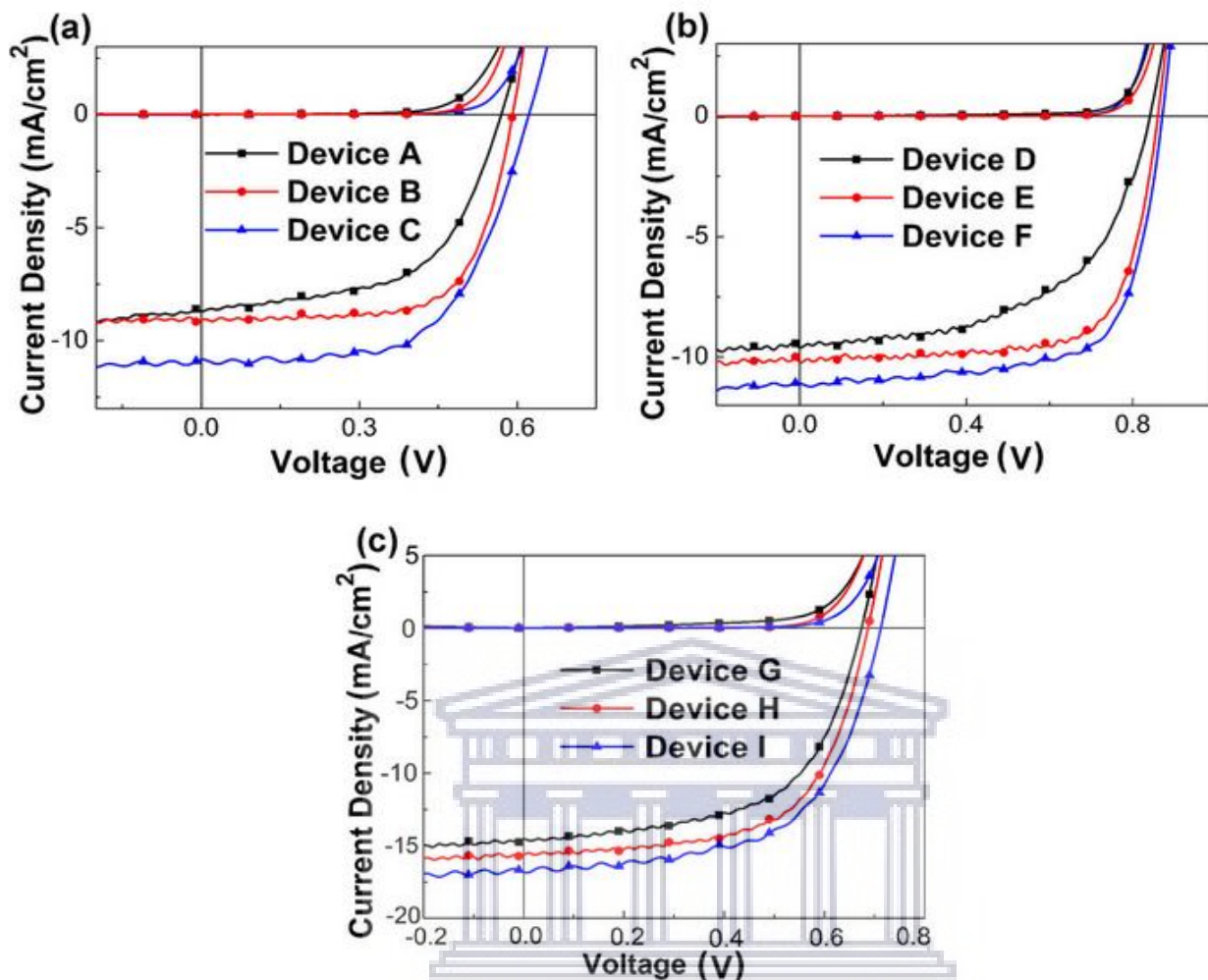


Fig. 3. 14: *J-V* characteristics of single and double layer polymer solar cells. (Reprinted with permission from [147] Copyright 2013: ACS publications.

Kim et al. indicated that the gap state near the Fermi level can be influenced by the distinct oxidation state of CuO [148]. Other researchers explored the solution processing treatment for improved quality and smooth surface for CuO films to better the performance of solar cells [149,150]. Hence, Lien et al. perused the oxidation state of copper oxide using vacuum thermal evaporation in the active layer of P3HT:PCBM solar cells [151]. They displayed from the normalized UV-vis absorption that the band gap of CuO and Cu₂O are 1.50 eV and 2.58 eV, respectively. An increase

in the J-V characteristic of CuO buffer layer was reported with an efficiency reaching up to 4.06% as compared to PEDOT: PSS and Cu₂O buffer layer with a PCE value of 3.29% and 2.52%, respectively. The increase in efficiency was ascribed to the correct band alignment of CuO to the active layer of P3HT, which induced easy transport of holes to the anode electrode.

However, a low valence band of Cu₂O was observed compared to the Ag anode band edge, which resulted in carrier transport inhibition. Shen et al. reconnoitred the effect of the integrated CuO_x buffer layer in the solar cell of P3HT and PBDDTTT-C polymers [152]. They used the sol gel method for the synthesis of the CuO films and spin coated it on the ITO glass, which revealed a high film transparency in contrast with the reference of PEDOT: PSS buffer layer. The J_{sc} improved significantly in the CuO_x buffer layer of P3HT device, which was assigned to the desirable band alignment and high film transparency as opposed to the PEDOT: PSS buffer layer. The processing solution therefore plays a significant role in the stability of the solar devices. Table 3.9 reveals the device characterization data of OPVs with CuO incorporated in the buffer layer.

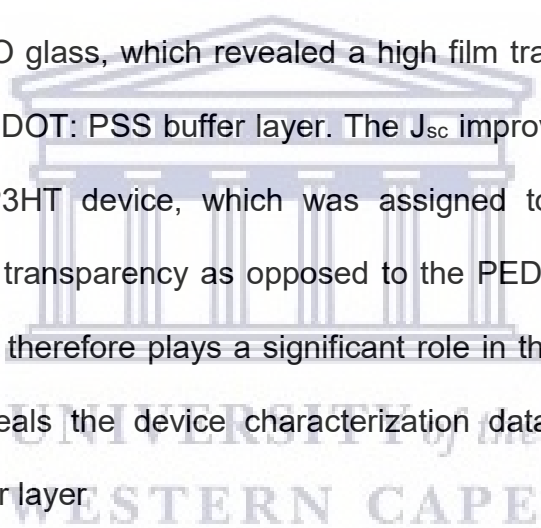


Table 3. 9: Device characterization data of OPV with metallic CuO in buffer layer.

ARCHITECTURE	PCE (%)	V _{oc}	J _{sc}	FF (%)	Refs.
Glass/ITO/ZnO/P3HT: PC61BM:CTSe NCs/Ag	1.35	0.48	6.95	41	[146]
Glass/ITO/PEDOT: PSS/P3HT: ICBA/Ca/Al	3.70	0.59	9.11	68.9	[147]
Glass/ITO/CuO-NPs/PBDTTT-C:PC ₇₀ BM/Ca/Al	4.10	0.62	10.81	61.2	[147]
Glass/ITO/PEDOT: PSS/P3HT: ICBA/Ca/Al	6.29	0.86	10.27	71.3	[147]
Glass/ITO/CuO-NPs/PBDTTT-C:PC ₇₀ BM/Ca/Al	6.72	0.87	11.08	69.7	[147]
Glass/ITO/PEDOT: PSS/PBDTTT-C: PCBM/Ca/Al	6.70	0.69	15.67	62.0	[147]
Glass/ITO/CuO-NPs/PBDTTT-C: PCBM/Ca/Al	7.14	0.71	16.86	59.7	[147]
Glass/ITO/ZnO/ P3HT: PCBM/CuO/Ag	4.06	0.63	10.98	57.9	[151]
Glass/ITO/ZnO/ P3HT: PCBM/PEDOT: PSS/Ag	3.29	0.61	10.27	49.9	[151]
Glass/ITO/ZnO/ P3HT: PCBM/Cu ₂ O/Ag	2.52	0.50	8.96	55.8	[151]
Glass/ITO/CuO _x /P3HT: PC61BM/Ca/Al	4.14	0.63	10.10	64.7	[152]
Glass/ITO/PEDOT: PSS/P3HT: PCBM/Ca/Al	3.63	0.62	8.67	67.3	[152]
Glass/ITO/CuO/PBDTTT-C: PCBM/Ca/Al	5.84	0.71	15.03	54.8	[152]
Glass/ITO/PEDOT: PSS/ PBDTTT-C: PCBM/Ca/Al	5.90	0.72	14.41	56.7	[152]

3.3.1.2 CuO NPs embedded in the active layer

The inclusion of CuO NPs was extensively studied owing to their intrinsic electrical properties and ideal energy gap, which influenced the performance of the solar cells [153-155]. Wanninayake et al. probe the effect of CuO NPs in the active layer of P3HT: PCBM hybrid solar cells [156]. They reported an increase in the J-V

characteristics of cells containing CuO NPs with an efficiency of $\approx 2.96\%$ as opposed to the cell without CuO NPs displaying a PCE value of 2.10% . The enhanced performance was ascribed to the potent charge injection of CuO NPs, resulting in higher optical absorption. Wanninayake et al. advanced his analyses by including the Au NPs in the PEDOT: PSS buffer layer to further enhance the performance [157]. They obtained a PCE value of approximately 3.51% with increased J_{sc} owing to free charge collection from the absorbed light. From their SEM analyses, they observed a homogenous distribution of CuO NPs that induced charge collection and photon absorption. Wanninayake et al. further explored the performance in contrast to single and double junction PSC, by incorporating CuO NPs in the P3HT:PC₇₀BM active layer [158]. They reported an efficiency of approximately 2.93% and 1.10% in the single and double junction cell, respectively, and by annealing the device the efficiency increased to 3.70% and 1.46% in single and double junction, respectively.

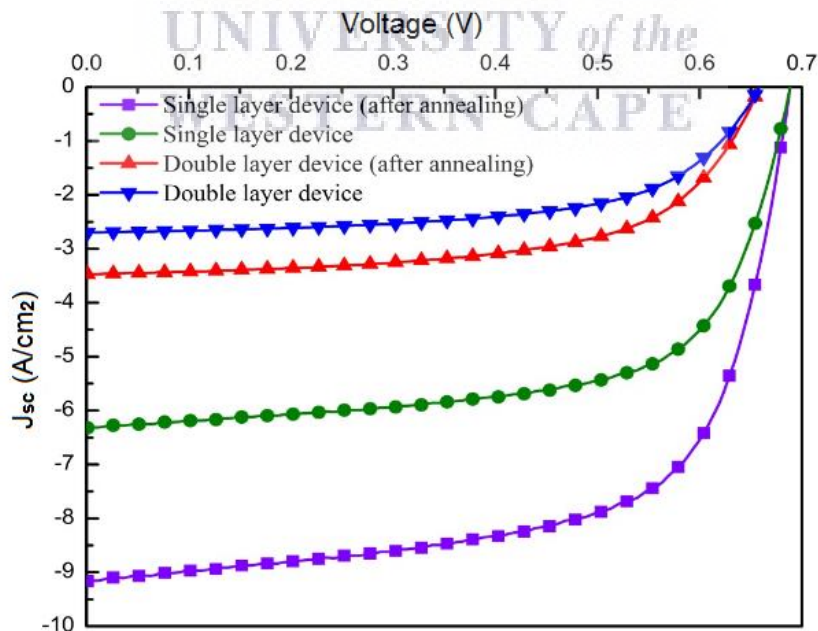


Fig. 3. 15: J - V characteristics of single and double junction solar cells [158]. Reproduced with permission from [157] Copyright 2015: JETNSR publication).

The low efficiency in the double junction cell is due to the high photocurrent in the front sub cell instead of the back sub cell, which hindered current flow that resulted in the poor J-V characteristics. The use of a low band gap in the front cell also has a negative effect, resulting in a high resistivity that decreases the fill factor, thereby deteriorating the optoelectronic properties. The use of a high band gap material in front sub cell and a low band gap material in the back sub cell were recommended to maximize performance of the PSC. Iqbal et al. studied the effect of Fe doped CuO nanotubes (NT) synthesised from copper acetate, NaOH and a ferric chloride solution, to enhance the performance of the hybrid solar cells [159]. A significant change in the Fe doped CuO morphology was observed as opposed to undoped CuO, which they assigned it to the ionic radius of Fe^{3+} in contrast with Cu^{2+} ion. They reported an efficiency of approximately 0.47% in undoped CuO, whereas for the Fe doped CuO the efficiency decreased to roughly 0.41%. The reduction in efficiency was due to photo-induced hindrance of the charge carrier, which triggered charge recombination. Lee et al. employed a sol gel synthesis method, because of its low cost and low temperature usage for modification of Cu_xO film in enhancing the efficiency of the P3HT: PCBM inverted devices [160]. They observed an increment PCE in the Cu_xO films formed from Cu (II) acetate solution at 250 °C annealing, which was attributed to higher optical absorption. A PCE value of up to 1.45% was achieved, as opposed to the Cu_xO films formed from Cu (I) acetate solution. Ikram et al. demonstrated the integration of CuO NPs in the P3HT: PCBM based solar devices to effectively improve the optical properties of the devices [161]. They revealed from SEM studies the non-linear dispersion that increased charge carrier transport, while the AFM analyses exhibited an increased surface roughness due to doped CuO active layer. The highest efficiency of 3.7% was reported with an

increment in the J-V characteristics. Table 10 reveals the device characterization data of OPVs with CuO incorporated in the active layer.

Table 3. 10: Device characterization data of OPV with metallic CuO in active layer.

ARCHITECTURE	PCE (%)	Voc	J _{sc}	FF (%)	Refs.
ITO/PEDOT: PSS/P3HT/PCBM/CuONP/AI	2.96	0.67	6.48	68	[156]
ITO/PEDOT:PSS/Au/ P3HT:PCBM/CuONP/AI	3.51	0.67	7.49	69.2	[157]
P3HT:PC ₇₀ BM/CuONP/AI (single)	2.96	0.67	6.48	68	[158]
P3HT:PC ₇₀ BM/CuONP/AI (double)	1.10	0.65	2.70	63.3	[158]
P3HT:PC ₇₀ BM/CuONP/AI (single/annealing)	3.70	0.61	9.14	67.3	[158]
P3HT:PC ₇₀ BM/CuONP/AI (double/annealing)	1.43	0.66	3.47	64.7	[158]
ITO/PEDOT: PSS/P3HT-CuO/AI	0.47	0.39	2.18	54.0	[159]
ITO/PEDOT: PSS/P3HT-CuO: Fe/AI	0.41	0.36	2.01	56.0	[159]
ITO/P3HT: PCBM/Cu _x O/Ag	1.45	0.51	6.82	42.0	[129]
ITO/ZnO/P3HT: CuO:PCBM/MoO ₃ /Ag	3.7	0.60	11.9	51.7	[161]

3.3.3.3. Effect of CuO on P3HT: PCBM optical and structural properties

Savva et al. explored the incorporation of CuO NPs as a buffer layer in the CH₃NH₃PbI₃ perovskite solar cell, showing enhanced light absorption compared to PEDOT: PSS layer [162]. Light absorption was found to be enhanced by the increased grain size of the perovskite, which facilitated a large surface area, thereby reducing the recombination rate. They demonstrated that the external quantum

efficiency increased in the wavelength range of 400-800 nm in the CuO NPs based devices compared to PEDOT-PSS devices. In addition, an increase in transmittance in the range of 600-800 nm was observed, which was ascribed to the light scattering effect in the CuO NPs. Yu et al. reconnoitred the integration of Cu₂O as a buffer layer in the P3HT: PCBM solar devices displaying an enhanced efficiency and stability of the devices [163]. They observed high optical transparency in Cu₂O thin films that allowed for improved absorption in the active layer, leading to an increased cell efficiency. An increase in Cu₂O concentration caused agglomeration, which led to low optical transparency, thereby resulting in a poor performance of the cell. Sabri et al. investigated ZnO/P3HT: PCBM based hybrid devices with CuO nanoparticles integrated as a buffer layer using solution dispersed method [164]. They observed an increase in cell efficiency for CuO based devices, irrespective of the solvent. In the CuO based devices the IPCE spectra were reported to reach a peak maximum of roughly 84% at 515 nm, whereas without CuO, the peak reached approximately 56%. The hole collection improved in the presence of CuO, which in turn blocked the reverse flow of electron towards the Ag. This in turn results in an increased shunt resistance and a reduced series resistance. Shun et al. observed that the combination of graphene oxide doped with CuCl₂ (GO:CuCl₂) as a hole transport layer in PTB7:PC₇₁BM solar devices enhances its efficiency [165]. They reported an enhanced EQE of GO: CuCl₂ in the range 400-800 nm, owing to improved hole injection that led to an increased PCE. The GO: CuCl₂ based cells displayed a superior interfacial contact, which was ascribed to the enhanced interaction of Cu²⁺ and GO. A significant PL quenching, indicative of improved charge transfer, was noted for the GO: CuCl₂ based cells GO: as opposed to GO and PEDOT: PSS based devices.

3.3.4. Influence of bimetallic metal oxide on polymer: PCBM solar cell performance

Bimetallic usage of nanostructured doping in the matrix of TiO_2 have been reported to evince improved properties and interaction as opposed to their monometallic counterparts. Their interaction brings a diversity of properties related to two individual metals and to new properties owing to their coordination [166-168]. Tonui et al. conveyed that the integration of Ag/Cu NPs using polyvinyl pyrrolidone (PVP) as a capping agent in the P3HT: PCBM based cell expand the range of the optical absorption [169]. They showed TEM images with core-shell Cu@Ag excited by LSPR in small NPs, while that in the photoactive layer is due to multiple light scattering, resulting in an efficiency of 4.7%. Dlamini et al. explored the bimetallic of Ag@Cu₂O incorporated in the P3HT: PCBM devices using PVP surfactant, which displayed an enhanced PCE of 3.87% that was accredited to the near field on the site of metal NPs and the hole mobility effect [170]. Sah et al. displayed the integration of different size bimetallic Ag-Au-Ag NRs in P3HT:PC₇₁BM and PTB7:PC₇₁BM based solar cell devices [171]. They disclosed an increased efficiency of 7.36% in the PTB7 based cell and 4.34% in the P3HT based cell device, which was attributed to scattering absorption effect in the active layer and the broad absorption range by the LSPR. Arbab et al. reported the bimetallic Ag/Zn NPs coalesced in the P3HT: PCBM cell using the chemical reduction method to increase the PCE to 5% efficiency [172].

3.3.5. The role of noble metals and metal oxides in organic solar cell stability

The stability and efficiency of organic solar cell are important aspect of the device to perform at is best. Hence it is important to have a compatible energy level of interfacial layer and successful morphological modification. The efficiency of the cell,

the hole/electron mobility and its resistance to humidity must be aligned in order to slowdown the process of photo degradation to obtain a long-term stable device. The use of P3HT in various studies have been reported, owing to its cost effectiveness and high hole mobility notwithstanding its HOMO energy level, which hinder maximum effectiveness of the device [173-177]. Jeong et al. substantiated the stability problem of solar cells using the deep HOMO energy level of fluorinated polythiophene derivative (FEH) that displays additional effective charge-extraction capability at the interface of the perovskite/HTL in comparison to P3HT. This is associated to the electron-withdrawing behaviour of the fluorine atoms in FEH and its capability to create further even films on the perovskite layer [178]. They proved that FEH hole layer under water contact has a more hydrophobic surface, which enhanced the stability compared to P3HT hole layer. Exposure of FEH based cell to over 500 hrs in their studies, resulted in the FEH based cell preserving more than 80% of its initial efficiency. They reported a PCE of 18.0% in the FEH fabricated cell compared to 10.8% in P3HT based cell. Yang et al. interrogated the addition of high boiling point solvents 1,8-diiodooctane and o-chlorobenzaldehyde in the presence of PT7B-Th:PCBM solar devices yielding a PCE of greater than 10% compared to no solvent solar cells with PCE of 3.8% [179]. Jayan et al. probed the nc-TiO₂-P3HT cell fabricated with various kind of positive electrode of Cu, Ag and Au for light harvesting [180]. The stability and efficiency of an inexpensive Cu based cell were better enhanced compared to expensive Ag and Au based electrode, owing to chemical bond formation of copper-sulphur complex in nc-TiO₂-P3HT cell. They revealed that copper-sulphur complex acts as a scavenger of free electrons in the absence of oxygen hindering the decaying of TiO₂, which results in the slowing down of the decomposition of the nc-TiO₂-P3HT solar cell. Kadem et al. scrutinized the

integration of PEDOT: PSS treated with ammonium hydroxide (NH_4OH) in the P3HT: PCBM based cell compared to pristine PEDOT: PSS based cell [181]. They reported better stability showing only about 43% reduction in efficiency after 58 days in comparison to 66% decrease in efficiency observed in the pristine PEDOT: PSS based device. Recent study [182] have shown that the devices using the $\text{ZnO}:\text{ZnWO}_4$ layer also displays an excellent long-term stability in air retaining roughly 95% of their PCE original value after being stored for 500h that is associated with the reduction of zinc interstitial defect density in the $\text{ZnO}:\text{ZnWO}_4$ film.

3.4. CONCLUSION AND REMARKS

This review paper was centred around the fundamental aspects of incorporating noble metals and metal oxides nanostructures in the BHJ PSCs, with the emphasis on the solar cell performance, structural and optical properties. The use of noble metals and metal oxides reported in this review displayed emancipated possibilities of enhancing the photo absorption among BHJ PSCs relative to its stability, efficiency and cost effectiveness. Light harvesting was enhanced owing to single/dual plasmonic effect of multiple light scattering and/or LSPR effect, without cell thickness increased and irrespective of the position of integration. A comparison of the effect of metallic NPs of Au, Ag based devices according to the theoretical interpretation were highlighted and the influence of metal oxide of CuO, ZnO and TiO_2 on the performance of the solar cells. Though the noble metals are readily incorporated into OSCs irrespective of their position inside. Nonetheless, incorporation of the noble metals in the photoactive layer is a vital space arrangement for creating the greatest of plasmonic near-field effects which result maximum improvement of IPCE% and enhanced PCE. It also enhances the photo

absorption by whichever enhancing the light scattering process or near-field improvement without increasing the thickness of the active layer. Additionally, embedded plasmonic nanomaterials at various layers/dual interface instead of a single layer for each device as to trigger dual plasmonic properties, i.e. stronger scattering efficiency has been considered as effective way for OSCs. Though, misalignment at the conduction and valence band of plasmonic NPs that result to charge trapping region and degradation in V_{OC} should be avoided. It was further observed that the control and prepared size of the noble metals have significant influence on the scattering efficiency that affects the device performance. However, the limitation exists with several studies is the consistency in variation of noble metals and metals oxides and size incorporated in OSCs. Finally, in OSC, the plasmonic-aided architecture has proven to be promising alternative to significantly enhance the device performance, more specifically if they are applied in low band gap polymer OSCs, which the low band gap polymer absorption could be extended to infrared region. Nonetheless, careful fabrication and optimization of noble nanostructures is compulsory to achieve a significant influence on the PCE in OSCs. Moreover, this review highlighted on the important aspects of photo degradation, hole/ electron mobility effectiveness and misalignment of the energy levels to obtain a long term stable device. With the recent breakthrough of an efficiency of >16% by Cui et al. and the current research effort on the long-term stability and cost effective fabrications, an enthusiastic near future can be anticipated for the commercialization of PSCs.

REFERENCES

1. Xu, X., 2015. Plasmonic organic solar cells with gold nanoparticles (Doctoral dissertation).
2. Sariciftci, N.S., Smilowitz, L., Heeger, A.J. and Wudl, F., 1992. Photoinduced electron transfer from a conducting polymer to buckminsterfullerene. *Science*, 258(5087), pp.1474-1476.
3. Motaung, D.E., Malgas, G.F. Nkosi, S.S., Mhlongo, G.H., Mwakikunga, B.W., Malwela, T., Arendse, C.J., Muller, T.FG., Cummings, F.R., 2013. Comparative study: the effect of annealing conditions on the properties of P3HT: PCBM blends, *Journal of materials Science* 1763-1778.
4. Motaung, D.E., Malgas, G.F. and Arendse, C.J., 2010. Correlation between the morphology and photo-physical properties of P3HT: fullerene blends. *Journal of materials science*, 45(12), pp.3276-3283.
5. Cui, Y., Yao, H., Zhang, J., Zhang, T., Wang, Y., Hong, L., Xian, K., Xu, B., Zhang, S., Peng, J. and Wei, Z., 2019. Over 16% efficiency organic photovoltaic cells enabled by a chlorinated acceptor with increased open-circuit voltages. *Nature communications*, 10(1), p.2515
6. Yu, J., Zheng, Y. and Huang, J., 2014. Towards high performance organic photovoltaic cells: A review of recent development in organic photovoltaics. *Polymers*, 6(9), pp.2473-2509
7. Vohra, V., Kawashima, K., Kakara, T., Koganezawa, T., Osaka, I., Takimiya, K. and Murata, H., 2015. Efficient inverted polymer solar cells employing favourable molecular orientation. *Nature Photonics*, 9(6), p.403.
8. Segura, J.L., Martín, N. and Guldi, D.M., 2005. Materials for organic solar cells: The C₆₀/π-conjugated oligomer approach. *Chemical Society Reviews*, 34(1), pp.31-47.

9. A. Srivastava, D.P. Samajdar, D. Sharma, 2018. Plasmonic effect of different nanoarchitectures in the efficiency enhancement of polymer based solar cells: A review, *Solar Energy* 173, 905–919
10. You, J., Takahashi, Y., Leonard, K., Yonemura, H. and Yamada, S., 2017. Influence of space arrangement of silver nanoparticles in organic photoelectric conversion devices. *Journal of Photochemistry and Photobiology A: Chemistry*, 332, pp.586-594.
11. Islam, M., Wahid, S., Chowdhury, M.M., Hakim, F. and Alam, M.K., 2017. Effect of spatial distribution of generation rate on bulk heterojunction organic solar cell performance: A novel semi-analytical approach. *Organic Electronics*, 46, pp.226-241.
12. Park, K.M., Lee, M.B. and Choi, S.Y., 2015. Investigation of surface features for 17.2% efficiency multi-crystalline silicon solar cells. *Solar Energy Materials and Solar Cells*, 132, pp.356-362.
13. Chen, B., Liu, C., Ge, L. and Hayashi, K., 2017. Electrical conduction and gas sensing characteristics of P3HT/Au nano-islands composite. *Sensors and Actuators B: Chemical*, 241, pp.1099-1105.
14. Lim, E.L., Yap, C.C., Teridi, M.A.M., Teh, C.H., bin Mohd Yusoff, A.R. and Jumali, M.H.H., 2016. A review of recent plasmonic nanoparticles incorporated P3HT: PCBM organic thin film solar cells. *Organic Electronics*, 36, pp.12-28.
15. Chen, F.C., Wu, J.L., Lee, C.L., Hong, Y., Kuo, C.H. and Huang, M.H., 2009. Plasmonic-enhanced polymer photovoltaic devices incorporating solution-processable metal nanoparticles. *Applied Physics Letters*, 95(1), p.182.
16. Kim, S.S., Na, S.I., Jo, J., Kim, D.Y. and Nah, Y.C., 2008. Plasmon enhanced performance of organic solar cells using electrodeposited Ag nanoparticles. *Applied Physics Letters*, 93(7), p.305.
17. Morfa, A.J., Rowlen, K.L., Reilly III, T.H., Romero, M.J. and van de Lagemaat, J., 2008. Plasmon-enhanced solar energy conversion in organic bulk heterojunction photovoltaics. *Applied Physics Letters*, 92(1), p.013504.

18. Kim, K. and Carroll, D.L., 2005. Roles of Au and Ag nanoparticles in efficiency enhancement of poly (3-octylthiophene)/C₆₀ bulk heterojunction photovoltaic devices. *Applied Physics Letters*, 87(20), p.203113.
19. Ahn, S., Rourke, D. and Park, W., 2016. Plasmonic nanostructures for organic photovoltaic devices. *Journal of Optics*, 18(3), p.033001.
20. Atwater, H.A. and Polman, A., 2010. Plasmonics for improved photovoltaic devices. *Nature materials*, 9(3), p.205.
21. Wu, J.L., Chen, F.C., Hsiao, Y.S., Chien, F.C., Chen, P., Kuo, C.H., Huang, M.H. and Hsu, C.S., 2011. Surface plasmonic effects of metallic nanoparticles on the performance of polymer bulk heterojunction solar cells. *ACS nano*, 5(2), pp.959-967.
22. Tan, K.S., Chuang, M.K., Chen, F.C. and Hsu, C.S., 2013. Solution-processed nanocomposites containing molybdenum oxide and gold nanoparticles as anode buffer layers in plasmonic-enhanced organic photovoltaic devices. *ACS applied materials & interfaces*, 5(23), pp.12419-12424.
23. Kao, C.S., Chen, F.C., Liao, C.W., Huang, M.H. and Hsu, C.S., 2012. Plasmonic-enhanced performance for polymer solar cells prepared with inverted structures. *Applied Physics Letters*, 101(19), p.193902.
24. N'Konou, K., Many, V., Ruiz, C.M., Treguer-Delapierre, M. and Torchio, P., 2018. Effect of shell thickness of gold-silica core-shell nanospheres embedded in an organic buffer matrix for plasmonic solar cells. *Journal of Applied Physics*, 123(6), p.063102.
25. Woo, S., Jeong, J.H., Lyu, H.K., Han, Y.S. and Kim, Y., 2012. In situ-prepared composite materials of PEDOT: PSS buffer layer-metal nanoparticles and their application to organic solar cells. *Nanoscale research letters*, 7(1), p.641.
26. Li, X., Deng, Z., Yin, Y., Zhu, L., Xu, D., Wang, Y. and Teng, F., 2014. Efficiency enhancement of polymer solar cells with Ag nanoparticles incorporated into PEDOT: PSS layer. *Journal of Materials Science: Materials in Electronics*, 25(1), pp.140-145.

27. Ng, A., Yiu, W.K., Foo, Y., Shen, Q., Bejaoui, A., Zhao, Y., Gokkaya, H.C., Djurišić, A.B., Zapien, J.A., Chan, W.K. and Surya, C., 2014. Enhanced performance of PTB7: PC71BM solar cells via different morphologies of gold nanoparticles. *ACS applied materials & interfaces*, 6(23), pp.20676-20684.
28. Otieno, F., Shumbula, N.P., Airo, M., Mbuso, M., Moloto, N., Erasmus, R.M., Quandt, A. and Wamwangi, D., 2017. Improved efficiency of organic solar cells using Au NPs incorporated into PEDOT: PSS buffer layer. *AIP Advances*, 7(8), p.085302.
29. Petridis, C., Savva, K., Kymakis, E. and Stratakis, E., 2017. Laser generated nanoparticles based photovoltaics. *Journal of colloid and interface science*, 489, pp.28-37.
30. Liu, D., Liang, Q., Li, G., Gao, X., Wang, W., Zhan, Q., Ji, T., Hao, Y. and Cui, Y., 2017. Improved Efficiency of Organic Photovoltaic Cells by Incorporation of AuAg-Alloyed Nanoprisms. *IEEE Journal of Photovoltaics*, 7(4), pp.1036-1041.
31. Zhang, S., Chen, Z., Xiao, L., Qu, B. and Gong, Q., 2011. Organic solar cells with 2-Thenylmercaptan/AU self-assembly film as buffer layer. *Solar Energy Materials and Solar Cells*, 95(3), pp.917-920.
32. Qiao, L., Wang, D., Zuo, L., Ye, Y., Qian, J., Chen, H. and He, S., 2011. Localized surface plasmon resonance enhanced organic solar cell with gold nanospheres. *Applied Energy*, 88(3), pp.848-852.
33. Nikoobakht, B. and El-Sayed, M.A., 2003. Surface-enhanced Raman scattering studies on aggregated gold nanorods. *The Journal of Physical Chemistry A*, 107(18), pp.3372-3378.
34. Lee, J.H., Park, J.H., Kim, J.S., Lee, D.Y. and Cho, K., 2009. High efficiency polymer solar cells with wet deposited plasmonic gold nanodots. *Organic Electronics*, 10(3), pp.416-420.
35. Baek, S.W., Park, G., Noh, J., Cho, C., Lee, C.H., Seo, M.K., Song, H. and Lee, J.Y., 2014. Au@ Ag core-shell nanocubes for efficient plasmonic light scattering effect in low bandgap organic solar cells. *ACS nano*, 8(4), pp.3302-3312.

36. Xu, X. (2015). Plasmonic organic solar cells with gold nanoparticles. Doctoral thesis, Nanyang Technological University, Singapore
37. Wang, D.H., Kim, D.Y., Choi, K.W., Seo, J.H., Im, S.H., Park, J.H., Park, O.O. and Heeger, A.J., 2011. Enhancement of donor–acceptor polymer bulk heterojunction solar cell power conversion efficiencies by addition of Au nanoparticles. *Angewandte Chemie*, 123(24), pp.5633-5637.
38. Shailendra Kumar Dwivedia, D.C. Tiwari, Santosh K. Tripathi, Prabhat K. Dwivedi, P. Dipak, Tarun Chandel, N. Eswara Prasad, Fabrication and properties of P3HT: PCBM/Cu₂SnSe₃ (CTSe) nanocrystals based inverted hybrid solar cells, *Solar Energy* 187 (2019) 167–174
39. Xu, X., Kyaw, A.K.K., Peng, B., Zhao, D., Wong, T.K., Xiong, Q., Sun, X.W. and Heeger, A.J., 2013. A plasmonically enhanced polymer solar cell with gold–silica core–shell nanorods. *Organic electronics*, 14(9), pp.2360-2368.
40. Brown, M.D., Suteewong, T., Kumar, R.S.S., D’Innocenzo, V., Petrozza, A., Lee, M.M., Wiesner, U. and Snaith, H.J., 2010. Plasmonic dye-sensitized solar cells using core– shell metal– insulator nanoparticles. *Nano letters*, 11(2), pp.438-445.
41. Xu, X., Kyaw, A.K.K., Peng, B., Xiong, Q., Demir, H.V., Wang, Y., Wong, T.K. and Sun, X.W., 2015. Influence of gold-silica nanoparticles on the performance of small-molecule bulk heterojunction solar cells. *Organic Electronics*, 22, pp.20-28.
42. Tseng, W.H., Chiu, C.Y., Chou, S.W., Chen, H.C., Tsai, M.L., Kuo, Y.C., Lien, D.H., Tsao, Y.C., Huang, K.Y., Yeh, C.T. and He, J.H., 2015. Shape-dependent light harvesting of 3D gold nanocrystals on bulk heterojunction solar cells: plasmonic or optical scattering effect?. *The Journal of Physical Chemistry C*, 119(14), pp.7554-7564.
43. de Freitas, J.N., Mamo, M.A., Maubane, M., van Otterlo, W.A., Coville, N.J. and Nogueira, A.F., 2012. Nanocomposites of gold and poly (3-hexylthiophene) containing fullerene moieties: Synthesis, characterization and application in solar cells. *Journal of Power Sources*, 215, pp.99-108.

44. Xie, F.X., Choy, W.C., Wang, C.C., Sha, W.E. and Fung, D.D., 2011. Improving the efficiency of polymer solar cells by incorporating gold nanoparticles into all polymer layers. *Applied Physics Letters*, 99(15), p.219.
45. Spyropoulos, G.D., Stylianakis, M.M., Stratakis, E. and Kymakis, E., 2012. Organic bulk heterojunction photovoltaic devices with surfactant-free Au nanoparticles embedded in the active layer. *Applied Physics Letters*, 100(21), p.213904.
46. Wang, L.D., Zhang, T., Zhu, S.Q., Zhang, X.Y., Wang, Q.L., Liu, X. and Li, R.Z., 2012. Two-dimensional ultrathin gold film composed of steadily linked dense nanoparticle with surface plasmon resonance. *Nanoscale research letters*, 7(1), p.683.
47. Namboothiry, M.A., Zimmerman, T., Coldren, F.M., Liu, J., Kim, K. and Carroll, D.L., 2007. Electrochromic properties of conducting polymer metal nanoparticles composites. *Synthetic Metals*, 157(13-15), pp.580-584.
48. Park, M., Chin, B.D., Yu, J.W., Chun, M.S. and Han, S.H., 2008. Enhanced photocurrent and efficiency of poly (3-hexylthiophene)/fullerene photovoltaic devices by the incorporation of gold nanoparticles. *Journal of Industrial and Engineering Chemistry*, 14(3), pp.382-386.
49. Chen, X., Yang, X., Fu, W., Xu, M. and Chen, H., 2013. Enhanced performance of polymer solar cells with a monolayer of assembled gold nanoparticle films fabricated by Langmuir–Blodgett technique. *Materials Science and Engineering: B*, 178(1), pp.53-59.
50. Kozanoglu, D., Apaydin, D.H., Cirpan, A. and Esenturk, E.N., 2013. Power conversion efficiency enhancement of organic solar cells by addition of gold nanostars, nanorods, and nanospheres. *Organic Electronics*, 14(7), pp.1720-1727.
51. Liang, H., 2014. Controlling the synthesis of silver nanostructures for plasmonic applications (Doctoral dissertation, Université du Québec, Institut national de la recherche scientifique).

52. Erwin, W.R., Zarick, H.F., Talbert, E.M. and Bardhan, R., 2016. Light trapping in mesoporous solar cells with plasmonic nanostructures. *Energy & Environmental Science*, 9(5), pp.1577-1601.
53. Noh, H.S., Cho, E.H., Kim, H.M., Han, Y.D. and Joo, J., 2013. Organic solar cells using plasmonics of Ag nanoprisms. *Organic Electronics*, 14(1), pp.278-285.
54. Wang, B.Y., Yoo, T.H., Lim, J.W., Sang, B.I., Lim, D.S., Choi, W.K., Hwang, D.K. and Oh, Y.J., 2015. Enhanced light scattering and trapping effect of Ag nanowire mesh electrode for high efficient flexible organic solar cell. *Small*, 11(16), pp.1905-1911.
55. Hao, Y., Song, J., Yang, F., Hao, Y., Sun, Q., Guo, J., Cui, Y., Wang, H. and Zhu, F., 2015. Improved performance of organic solar cells by incorporating silica-coated silver nanoparticles in the buffer layer. *Journal of Materials Chemistry C*, 3(5), pp.1082-1090.
56. Baek, S.W., Noh, J., Lee, C.H., Kim, B., Seo, M.K. and Lee, J.Y., 2013. Plasmonic forward scattering effect in organic solar cells: a powerful optical engineering method. *Scientific reports*, 3, p.1726.
57. Jägeler-Hoheisel, T., Selzer, F., Riede, M. and Leo, K., 2014. Direct electrical evidence of plasmonic near-field enhancement in small molecule organic solar cells. *The Journal of Physical Chemistry C*, 118(28), pp.15128-15135.
58. Xu, M.F., Zhu, X.Z., Shi, X.B., Liang, J., Jin, Y., Wang, Z.K. and Liao, L.S., 2013. Plasmon resonance enhanced optical absorption in inverted polymer/fullerene solar cells with metal nanoparticle-doped solution-processable TiO₂ layer. *ACS applied materials & interfaces*, 5(8), pp.2935-2942.
59. MORFA, A. J., ROWLEN, K. L., REILLY III, T. H., ROMERO, M. J. & VAN DE LAGEMAAT, J. 2008. Plasmon-enhanced solar energy conversion in organic bulk heterojunction photovoltaics. *Applied Physics Letters*, 92, 013504
60. Cheng, P.P., Zhou, L., Li, J.A., Li, Y.Q., Lee, S.T. and Tang, J.X., 2013. Light trapping enhancement of inverted polymer solar cells with a nanostructured scattering rear electrode. *Organic Electronics*, 14(9), pp.2158-2163.

61. Jung, K., Song, H.J., Lee, G., Ko, Y., Ahn, K., Choi, H., Kim, J.Y., Ha, K., Song, J., Lee, J.K. and Lee, C., 2014. Plasmonic organic solar cells employing nanobump assembly via aerosol-derived nanoparticles. *ACS nano*, 8(3), pp.2590-2601.
62. Wang, D.H., Kim, J.K., Lim, G.H., Park, K.H., Park, O.O., Lim, B. and Park, J.H., 2012. Enhanced light harvesting in bulk heterojunction photovoltaic devices with shape-controlled Ag nanomaterials: Ag nanoparticles versus Ag nanoplates. *RSC Advances*, 2(18), pp.7268-7272.
63. Kim, C.H., Cha, S.H., Kim, S.C., Song, M., Lee, J., Shin, W.S., Moon, S.J., Bahng, J.H., Kotov, N.A. and Jin, S.H., 2011. Silver nanowire embedded in P3HT: PCBM for high-efficiency hybrid photovoltaic device applications. *ACS nano*, 5(4), pp.3319-3325.
64. Chen, H.C., Chou, S.W., Tseng, W.H., Chen, I.W.P., Liu, C.C., Liu, C., Liu, C.L., Chen, C.H., Wu, C.I. and Chou, P.T., 2012. Large AuAg Alloy Nanoparticles Synthesized in Organic Media Using a One-Pot Reaction: Their Applications for High-Performance Bulk Heterojunction Solar Cells. *Advanced Functional Materials*, 22(19), pp.3975-3984.
65. Li, X., Choy, W.C.H., Lu, H., Sha, W.E. and Ho, A.H.P., 2013. Efficiency Enhancement of Organic Solar Cells by Using Shape-Dependent Broadband Plasmonic Absorption in Metallic Nanoparticles. *Advanced Functional Materials*, 23(21), pp.2728-2735.
66. Jang, L.W., Park, H., Lee, S.H., Polyakov, A.Y., Khan, R., Yang, J.K. and Lee, I.H., 2015. Device performance of inverted polymer solar cells with AgSiO₂ nanoparticles in active layer. *Optics express*, 23(7), pp.A211-A218.
67. Yao, K., Salvador, M., Chueh, C.C., Xin, X.K., Xu, Y.X., Dequilettes, D.W., Hu, T., Chen, Y., Ginger, D.S. and Jen, A.K.Y., 2014. A general route to enhance polymer solar cell performance using plasmonic nanoprisms. *Advanced Energy Materials*, 4(9).

68. Shen, W., Tang, J., Wang, Y., Liu, J., Huang, L., Chen, W., Yang, L., Wang, W., Wang, Y., Yang, R. and Yun, J., 2017. Strong Enhancement of Photoelectric Conversion Efficiency of Co-hybridized Polymer Solar Cell by Silver Nanoplates and Core–Shell Nanoparticles. *ACS applied materials & interfaces*, 9(6), pp.5358-5365.
69. Li, X., Choy, W.C., Huo, L., Xie, F., Sha, W.E., Ding, B., Guo, X., Li, Y., Hou, J., You, J. and Yang, Y., 2012. Dual plasmonic nanostructures for high performance inverted organic solar cells. *Advanced Materials*, 24(22), pp.3046-3052.
70. Xue, M., Li, L., Tremolet de Villers, B.J., Shen, H., Zhu, J., Yu, Z., Stieg, A.Z., Pei, Q., Schwartz, B.J. and Wang, K.L., 2011. Charge-carrier dynamics in hybrid plasmonic organic solar cells with Ag nanoparticles. *Applied Physics Letters*, 98 (25), p.119.
71. Yoon, W.J., Jung, K.Y., Liu, J., Duraisamy, T., Revur, R., Teixeira, F.L., Sengupta, S. and Berger, P.R., 2010. Plasmon-enhanced optical absorption and photocurrent in organic bulk heterojunction photovoltaic devices using self-assembled layer of silver nanoparticles. *Solar Energy Materials and Solar Cells*, 94(2), pp.128-132.
72. Pei, J., Tao, J., Zhou, Y., Dong, Q., Liu, Z., Li, Z., Chen, F., Zhang, J., Xu, W. and Tian, W., 2011. Efficiency enhancement of polymer solar cells by incorporating a self-assembled layer of silver nanodisks. *Solar Energy Materials and Solar Cells*, 95(12), pp.3281-3286.
73. Wang, D.H., Park, K.H., Seo, J.H., Seifert, J., Jeon, J.H., Kim, J.K., Park, J.H., Park, O.O. and Heeger, A.J., 2011. Enhanced power conversion efficiency in PCDTBT/PC₇₀BM bulk heterojunction photovoltaic devices with embedded silver nanoparticle clusters. *Advanced Energy Materials*, 1(5), pp.766-770.
74. Zhang, D., Choy, W.C., Xie, F.X. and Li, X., 2012. Large-area, high-quality self-assembly electron transport layer for organic optoelectronic devices. *Organic Electronics*, 13(10), pp.2042-2046.
75. Anandan, S., Ikuma, Y. and Niwa, K., 2010. An overview of semi-conductor photocatalysis: modification of TiO₂ nanomaterials. In *Solid State Phenomena* (Vol. 162, pp. 239-260). Trans Tech Publications.

76. Kong, X., Hu, Y. and Pan, W., 2018. Enhancement of photocatalytic activity for fold-like ZnO via hybridisation with graphene. *Micro & Nano Letters*, 13(2), pp.232-236.
77. Hadipour, A., Müller, R. and Heremans, P., 2013. Room temperature solution-processed electron transport layer for organic solar cells. *Organic Electronics*, 14(10), pp.2379-2386.
78. Baek, W.H., Seo, I., Yoon, T.S., Lee, H.H., Yun, C.M. and Kim, Y.S., 2009. Hybrid inverted bulk heterojunction solar cells with nanoimprinted TiO₂ nanopores. *Solar Energy Materials and Solar Cells*, 93(9), pp.1587-1591.
79. Gopinath, K., Gowri, S., Karthika, V. and Arumugam, A., 2014. Green synthesis of gold nanoparticles from fruit extract of *Terminalia arjuna*, for the enhanced seed germination activity of *Gloriosa superba*. *Journal of Nanostructure in Chemistry*, 4(3), p.115.. .
80. Örnek, O., Kösemen, Z.A., Öztürk, S., Canımkuşbey, B., Fındık, Ş., Erkovan, M. and Kösemen, A., 2017. Performance enhancement of inverted type organic solar cells by using Eu doped TiO₂ thin film. *Surfaces and Interfaces*, 9, pp.64-69.
81. Xie, F.X., Choy, W.C., Wei, E.I., Zhang, D., Zhang, S., Li, X., Leung, C.W. and Hou, J., 2013. Enhanced charge extraction in organic solar cells through electron accumulation effects induced by metal nanoparticles. *Energy & Environmental Science*, 6(11), pp.3372-3379.
82. Lin, Y., Xie, J., Wang, H., Li, Y., Chavez, C., Lee, S., Foltyn, S.R., Crooker, S.A., Burrell, A.K., McCleskey, T.M. and Jia, Q.X., 2005. Green luminescent zinc oxide films prepared by polymer-assisted deposition with rapid thermal process. *Thin Solid Films*, 492(1-2), pp.101-104.
83. Wang, H., Patterson, B., Yang, J., Huang, D., Qin, Y. and Luo, H., 2017. Polymer-assisted deposition of SrTiO₃ film as cathode buffer layer in inverted polymer solar cells. *Applied Materials Today*, 9, pp.402-406.

84. Liao, W.P., Hsu, S.C., Lin, W.H. and Wu, J.J., 2012. Hierarchical TiO₂ nanostructured array/P3HT hybrid solar cells with interfacial modification. *The Journal of Physical Chemistry C*, 116(30), pp.15938-15945.
85. Yodyingyong, S., Zhou, X., Zhang, Q., Triampo, D., Xi, J., Park, K., Limketkai, B. and Cao, G., 2010. Enhanced photovoltaic performance of nanostructured hybrid solar cell using highly oriented TiO₂ nanotubes. *The Journal of Physical Chemistry C*, 114(49), pp.21851-21855.
86. Li, Y., Lu, P., Jiang, M., Dhakal, R., Thapaliya, P., Peng, Z., Jha, B. and Yan, X., 2012. Femtosecond time-resolved fluorescence study of TiO₂-coated ZnO nanorods/P3HT photovoltaic films. *The Journal of Physical Chemistry C*, 116(48), pp.25248-25256.
87. Yang, T., Cai, W., Qin, D., Wang, E., Lan, L., Gong, X., Peng, J. and Cao, Y., 2010. Solution-processed zinc oxide thin film as a buffer layer for polymer solar cells with an inverted device structure. *The Journal of Physical Chemistry C*, 114(14), pp.6849-6853.
88. Kline, R.J., McGehee, M.D., Kadnikova, E.N., Liu, J. and Frechet, J.M., 2003. Controlling the field-effect mobility of regioregular polythiophene by changing the molecular weight. *Advanced Materials*, 15(18), pp.1519-1522.
89. Wu, M.C., Lo, H.H., Liao, H.C., Chen, S., Lin, Y.Y., Yen, W.C., Zeng, T.W., Chen, Y.F., Chen, C.W. and Su, W.F., 2009. Using scanning probe microscopy to study the effect of molecular weight of poly (3-hexylthiophene) on the performance of poly (3-hexylthiophene): TiO₂ nanorod photovoltaic devices. *Solar Energy Materials and Solar Cells*, 93(6-7), pp.869-873.
90. Tai, Q., Zhao, X. and Yan, F., 2010. Hybrid solar cells based on poly (3-hexylthiophene) and electrospun TiO₂ nanofibers with effective interface modification. *Journal of Materials Chemistry*, 20(35), pp.7366-7371.

91. Tu, Y.C., Lim, H., Chang, C.Y., Shyue, J.J. and Su, W.F., 2015. Enhancing performance of P3HT: TiO₂ solar cells using doped and surface modified TiO₂ nanorods. *Journal of colloid and interface science*, 448, pp.315-319.
92. Kogo, A., Sanehira, Y., Numata, Y., Ikegami, M. and Miyasaka, T., 2018. Amorphous Metal Oxide Blocking Layers for Highly Efficient Low Temperature Brookite TiO₂-based Perovskite Solar Cells. *ACS Appl. Mater. Interfaces*, 10, pp 2224–2229.
93. Elumalai, N.K., Uddin, A., 2016. Open circuit voltage of organic solar cells: an in-depth review, *Energy Environ. Sci.*, 9, 391-410
94. Boroomandnia, A., Kasaeian, A.B., Nikfarjam, A., Akbarzadeh, A. and Mohammadpour, R., 2015. Effect of crystallinity and morphology of TiO₂ nanostructures on TiO₂: P3HT hybrid photovoltaic solar cells. *Applied Solar Energy*, 51(1), pp.34-40.
95. LIN, Y.Y., TSUNG, H.C., CHEN, C.W. and SU, W.F., 2007. Charge separation and transport in ZnO nanostructures. In *Proceedings of SPIE, the International Society for Optical Engineering* (pp. 66560B-1). Society of Photo-Optical Instrumentation Engineers.
96. Lim, S.L., Liu, Y., Liu, G., Xu, S.Y., Pan, H.Y., Kang, E.T. and Ong, C.K., 2011. Infiltrating P3HT polymer into ordered TiO₂ nanotube arrays. *physica status solidi (a)*, 208(3), pp.658-663.
97. Bartholomew, G.P. and Heeger, A.J., 2005. Infiltration of Regioregular Poly [2, 2'-(3-hexylthiophene)] into Random Nanocrystalline TiO₂ Networks. *Advanced Functional Materials*, 15(4), pp.677-682.
98. Coakley, K.M., Liu, Y., McGehee, M.D., Frindell, K.L. and Stucky, G.D., 2003. Infiltrating Semiconducting Polymers into Self-assembled Mesoporous Titania Films for Photovoltaic Applications. *Advanced Functional Materials*, 13(4), pp.301-306.
99. Shankar, K., Mor, G.K., Paulose, M., Varghese, O.K. and Grimes, C.A., 2008. Effect of device geometry on the performance of TiO₂ nanotube array-organic

- semiconductor double heterojunction solar cells. *Journal of Non-Crystalline Solids*, 354(19-25), pp.2767-2771.
100. Zhang, Q., Dandeneau, C.S., Zhou, X. and Cao, G., 2009. ZnO nanostructures for dye-sensitized solar cells. *Advanced Materials*, 21(41), pp.4087-4108.
101. The future of semiconductor oxide in the next generation solar cells. <https://doi.org/10.1016/b978-0-12-811165-9.00001-6>.
102. Stubhan, T., Litzov, I., Li, N., Salinas, M., Steidl, M., Sauer, G., Forberich, K., Matt, G.J., Halik, M. and Brabec, C.J., 2013. Overcoming interface losses in organic solar cells by applying low temperature, solution processed aluminum-doped zinc oxide electron extraction layers. *Journal of Materials Chemistry A*, 1(19), pp.6004-6009.
103. Pasquarelli, R.M., Ginley, D.S. and O'Hayre, R., 2011. Solution processing of transparent conductors: from flask to film. *Chemical Society Reviews*, 40(11), pp.5406-5441.
104. Chen, H.C., Lin, S.W., Jiang, J.M., Su, Y.W. and Wei, K.H., 2015. Solution-processed zinc oxide/polyethylenimine nanocomposites as tunable electron transport layers for highly efficient bulk heterojunction polymer solar cells. *ACS applied materials & interfaces*, 7(11), pp.6273-6281.
105. Woo, S.; Hyun Kim, W.; Kim, H.; Yi, Y.; Lyu, H.-K.; Kim, Y. 8.9% Single-Stack Inverted Polymer Solar Cells with Electron-Rich Polymer Nanolayer-Modified Inorganic Electron-Collecting Buffer Layers. *Adv. Energy Mater.* 2014, 4, 1301692
106. Tan, M.J., Zhong, S., Li, J., Chen, Z. and Chen, W., 2013. Air-stable efficient inverted polymer solar cells using solution-processed nanocrystalline ZnO interfacial layer. *ACS applied materials & interfaces*, 5(11), pp.4696-4701.
107. Ambade, S.B., Ambade, R.B., Bagde, S.S., Eom, S.H., Mane, R.S., Shin, W.S. and Lee, S.H., 2017. Low-Temperature Solution-Processed Thiophene-Sulfur-Doped Planar ZnO Nanorods as Electron-Transporting Layers for Enhanced Performance of Organic Solar Cells. *ACS applied materials & interfaces*, 9(4), pp.3831-3841.

108. Mohan, M., Nandal, V., Paramadam, S., Reddy, K.P., Ramkumar, S., Agarwal, S., Gopinath, C.S., Nair, P.R. and Namboothiry, M.A., 2017. Efficient Organic Photovoltaics with Improved Charge Extraction and High Short-Circuit Current. *The Journal of Physical Chemistry C*, 121(10), pp.5523-5530.
109. Tang, Z., Liu, B., Melianas, A., Bergqvist, J., Tress, W., Bao, Q., Qian, D., Inganäs, O. and Zhang, F., 2015. A New Fullerene-Free Bulk-Heterojunction System for Efficient High-Voltage and High-Fill Factor Solution-Processed Organic Photovoltaics. *Advanced Materials*, 27(11), pp.1900-1907.
110. Bartesaghi, D., del Carmen Pérez, I., Kniepert, J., Roland, S., Turbiez, M., Neher, D. and Koster, L.J.A., 2015. Competition between recombination and extraction of free charges determines the fill factor of organic solar cells. *Nature communications*, 6, p.7083.
111. Sharma, R., Lee, H., Borse, K., Gupta, V., Joshi, A.G., Yoo, S. and Gupta, D., 2017. Ga-doped ZnO as an electron transport layer for PffBT4T-2OD: PC70BM organic solar cells. *Organic Electronics*, 43, pp.207-
112. Wu, S., Li, J., Lo, S.C., Tai, Q. and Yan, F., 2012. Enhanced performance of hybrid solar cells based on ordered electrospun ZnO nanofibers modified with CdS on the surface. *Organic Electronics*, 13(9), pp.1569-1575.
113. Wu, S., Li, J., Tai, Q. and Yan, F., 2010. Investigation of high-performance air-processed poly (3-hexylthiophene)/methanofullerene bulk-heterojunction solar cells. *The Journal of Physical Chemistry C*, 114(49), pp.21873-21877.
114. Liu, Z. and Yan, F., 2011. Photovoltaic effect of BiFeO₃/poly (3-hexylthiophene) heterojunction. *physica status solidi (RRL)-Rapid Research Letters*, 5(10-11), pp.367-369.
115. Tai, Q., Li, J., Liu, Z., Sun, Z., Zhao, X. and Yan, F., 2011. Enhanced photovoltaic performance of polymer solar cells by adding fullerene end-capped polyethylene glycol. *Journal of Materials Chemistry*, 21(19), pp.6848-6853.

116. Lee, B.R., Choi, H., SunPark, J., Lee, H.J., Kim, S.O., Kim, J.Y. and Song, M.H., 2011. Surface modification of metal oxide using ionic liquid molecules in hybrid organic–inorganic optoelectronic devices. *Journal of Materials Chemistry*, 21(7), pp.2051-2053.
117. Chang, J.A., Rhee, J.H., Im, S.H., Lee, Y.H., Kim, H.J., Seok, S.I., Nazeeruddin, M.K. and Gratzel, M., 2010. High-performance nanostructured inorganic– organic heterojunction solar cells. *Nano letters*, 10(7), pp.2609-2612.
118. Seol, M., Kim, H., Tak, Y. and Yong, K., 2010. Novel nanowire array based highly efficient quantum dot sensitized solar cell. *Chemical Communications*, 46(30), pp.5521-5523.
119. Kim, I.D., Hong, J.M., Lee, B.H., Kim, D.Y., Jeon, E.K., Choi, D.K. and Yang, D.J., 2007. Dye-sensitized solar cells using network structure of electrospun ZnO nanofiber mats. *Applied Physics Letters*, 91(16), p.163109.
120. Zhang, W., Zhu, R., Liu, X., Liu, B. and Ramakrishna, S., 2009. Facile construction of nanofibrous ZnO photoelectrode for dye-sensitized solar cell applications. *Applied physics letters*, 95(4), p.203.
121. Wu, S., Tai, Q. and Yan, F., 2010. Hybrid photovoltaic devices based on poly (3-hexylthiophene) and ordered electrospun ZnO nanofibers. *The Journal of Physical Chemistry C*, 114(13), pp.6197-6200.
122. Spoerke, E.D., Lloyd, M.T., Lee, Y.J., Lambert, T.N., McKenzie, B.B., Jiang, Y.B., Olson, D.C., Sounart, T.L., Hsu, J.W. and Voigt, J.A., 2009. Nanocrystal layer deposition: surface-mediated templating of cadmium sulfide nanocrystals on zinc oxide architectures. *The Journal of Physical Chemistry C*, 113(37), pp.16329-16336.
123. Oh, S.H., Heo, S.J., Yang, J.S. and Kim, H.J., 2013. Effects of ZnO nanoparticles on P3HT:PCBM organic solar cells with DMF-modulated PEDOT: PSS buffer layers. *ACS applied materials & interfaces*, 5(22), pp.11530-11534.
124. Ajuria, J., Etxebarria, I., Azaceta, E., Tena-Zaera, R., Fernández-Montcada, N., Palomares, E. and Pacios, R., 2011. Novel ZnO nanostructured electrodes for higher

- power conversion efficiencies in polymeric solar cells. *Physical Chemistry Chemical Physics*, 13(46), pp.20871-20876.
125. Olson, D.C., Piris, J., Collins, R.T., Shaheen, S.E. and Ginley, D.S., 2006. Hybrid photovoltaic devices of polymer and ZnO nanofiber composites. *Thin solid films*, 496(1), pp.26-29.
126. Peiró, A.M., Ravirajan, P., Govender, K., Boyle, D.S., O'Brien, P., Bradley, D.D., Nelson, J. and Durrant, J.R., 2006. Hybrid polymer/metal oxide solar cells based on ZnO columnar structures. *Journal of Materials Chemistry*, 16(21), pp.2088-2096.
127. Ravirajan, P., Peiró, A.M., Nazeeruddin, M.K., Graetzel, M., Bradley, D.D., Durrant, J.R. and Nelson, J., 2006. Hybrid polymer/zinc oxide photovoltaic devices with vertically oriented ZnO nanorods and an amphiphilic molecular interface layer. *The Journal of Physical Chemistry B*, 110(15), pp.7635-7639.
128. Ravirajan, P., Haque, S.A., Durrant, J.R., Bradley, D.D. and Nelson, J., 2005. The effect of polymer optoelectronic properties on the performance of multilayer hybrid polymer/TiO₂ solar cells. *Advanced Functional Materials*, 15(4), pp.609-618.
129. Olson, D.C., Shaheen, S.E., Collins, R.T. and Ginley, D.S., 2007. The effect of atmosphere and ZnO morphology on the performance of hybrid poly (3-hexylthiophene)/ZnO nanofiber photovoltaic devices. *The Journal of Physical Chemistry C*, 111(44), pp.16670-16678.
130. Sung, Y.H., Liao, W.P., Chen, D.W., Wu, C.T., Chang, G.J. and Wu, J.J., 2012. Room-Temperature Tailoring of Vertical ZnO Nanoarchitecture Morphology for Efficient Hybrid Polymer Solar Cells. *Advanced Functional Materials*, 22(18), pp.3808-3814.
131. Lin, C.Y., Lai, Y.H., Chen, H.W., Chen, J.G., Kung, C.W., Vittal, R. and Ho, K.C., 2011. Highly efficient dye-sensitized solar cell with a ZnO nanosheet-based photoanode. *Energy & Environmental Science*, 4(9), pp.3448-3455.

132. Yun, D., Xia, X., Zhang, S., Bian, Z., Liu, R. and Huang, C., 2011. ZnO nanorod arrays with different densities in hybrid photovoltaic devices: Fabrication and the density effect on performance. *Chemical Physics Letters*, 516(1-3), pp.92-95.
133. Motaung, D.E., Malgas, G.F., Arendse, C.J., Mavundla, S.E., 2012. *Materials Chemistry and Physics* 135 (2–3), pp 401-410
134. Ibrahim, M.A., Wei, H.Y., Tsai, M.H., Ho, K.C., Shyue, J.J. and Chu, C.W., 2013. Solution-processed zinc oxide nanoparticles as interlayer materials for inverted organic solar cells. *Solar Energy Materials and Solar Cells*, 108, pp.156-163.
135. Wang, M. and Wang, X., 2008. Electrodeposition zinc-oxide inverse opal and its application in hybrid photovoltaics. *Solar Energy Materials and Solar Cells*, 92(3), pp.357-362.
136. Chou, C.Y., Huang, J.S., Wu, C.H., Lee, C.Y. and Lin, C.F., 2009. Lengthening the polymer solidification time to improve the performance of polymer/ZnO nanorod hybrid solar cells. *Solar Energy Materials and Solar Cells*, 93(9), pp.1608-1612.
137. Li, G., Shrotriya, V., Huang, J., Yao, Y., Moriarty, T., Emery, K. and Yang, Y., 2005. High-efficiency solution processable polymer photovoltaic cells by self-organization of polymer blends. *Nature materials*, 4(11), p.864.
138. Campoy-Quiles, M., Ferenczi, T., Agostinelli, T., Etchegoin, P.G., Kim, Y., Anthopoulos, T.D., Stavrinou, P.N., Bradley, D.D. and Nelson, J., 2008. Morphology evolution via self-organization and lateral and vertical diffusion in polymer: fullerene solar cell blends. *Nature materials*, 7(2), p.158.
139. Huang, J.S., Chou, C.Y. and Lin, C.F., 2010. Enhancing performance of organic–inorganic hybrid solar cells using a fullerene interlayer from all-solution processing. *Solar Energy Materials and Solar Cells*, 94(2), pp.182-186.
140. Musselman, K.P., Marin, A., Wisnet, A., Scheu, C., MacManus-Driscoll, J.L. and Schmidt-Mende, L., 2011. A Novel Buffering Technique for Aqueous Processing of Zinc Oxide Nanostructures and Interfaces, and Corresponding Improvement of

- Electrodeposited ZnO-Cu₂O Photovoltaics. *Advanced Functional Materials*, 21(3), pp.573-582.
141. Hameş, Y. and San, S.E., 2004. CdO/Cu₂O solar cells by chemical deposition. *Solar Energy*, 77(3), pp.291-294.
142. Marin, A.T., Muñoz-Rojas, D., Iza, D.C., Gershon, T., Musselman, K.P. and MacManus-Driscoll, J.L., 2013. Novel atmospheric growth technique to improve both light absorption and charge collection in ZnO/Cu₂O thin film solar cells. *Advanced Functional Materials*, 23(27), pp.3413-3419.
143. Kidowaki, H., Oku, T., Akiyama, T., Suzuki, A., Jeyadevan, B. and Cuya, J., 2012. Fabrication and characterization of CuO-based solar cells. *Journal of Materials Science Research*, 1(1), p.138.
144. Mittiga, A., Salza, E., Sarto, F., Tucci, M. and Vasanthi, R., 2006. Heterojunction solar cell with 2% efficiency based on a Cu₂O substrate. *Applied Physics Letters*, 88(16), p.163502.
145. Lin, M.Y., Lee, C.Y., Shiu, S.C., Wang, J., Sun, J.Y., Wu, W.H., Lin, Y.H., Huang, J.S. and Lin, C.F., 2010. Sol-gel processed CuO_x thin film as an anode interlayer for inverted polymer solar cells. *Organic Electronics*, 11(11), pp.1828-1834.
146. Dwivedi, S.K., Tiwari, D.C., Tripathi, S.K., Dwivedi, P.K., Dipak, P., Chandel, T. and Prasad, N.E., 2019. Fabrication and properties of P3HT: PCBM/Cu₂SnSe₃ (CTSe) nanocrystals based inverted hybrid solar cells. *Solar Energy*, 187, pp.167-174.
147. Xu, Q., Wang, F., Tan, Z.A., Li, L., Li, S., Hou, X., Sun, G., Tu, X., Hou, J. and Li, Y., 2013. High-Performance Polymer Solar Cells with Solution-Processed and Environmentally Friendly CuO_x Anode Buffer Layer. *ACS applied materials & interfaces*, 5(21), pp.10658-10664.
148. Kim, S., Hong, K., Kim, K., Lee, I. and Lee, J.L., 2012. Phase-controllable copper oxides for an efficient anode interfacial layer in organic light-emitting diodes. *Journal of Materials Chemistry*, 22(5), pp.2039-2044.

149. Frey, G.L., Reynolds, K.J., Friend, R.H., Cohen, H. and Feldman, Y., 2003. Solution-processed anodes from layer-structure materials for high-efficiency polymer light-emitting diodes. *Journal of the American Chemical Society*, 125(19), pp.5998-6007.
150. Kato, S., Ishikawa, R., Kubo, Y., Shirai, H. and Ueno, K., 2011. Efficient organic photovoltaic cells using hole-transporting MoO₃ buffer layers converted from solution-processed MoS₂ films. *Japanese Journal of Applied Physics*, 50(7R), p.071604.
151. Lien, H.T., Wong, D.P., Tsao, N.H., Huang, C.I., Su, C., Chen, K.H. and Chen, L.C., 2014. Effect of copper oxide oxidation state on the polymer-based solar cell buffer layers. *ACS applied materials & interfaces*, 6(24), pp.22445-22450.
152. Shen, W., Yang, C., Bao, X., Sun, L., Wang, N., Tang, J., Chen, W. and Yang, R., 2015. Simple solution-processed CuOX as anode buffer layer for efficient organic solar cells. *Materials Science and Engineering: B*, 200, pp.1-8.
153. Ruiz, E., Alvarez, S., Alemany, P. and Evarestov, R.A., 1997. Electronic structure and properties of Cu₂O. *Physical Review B*, 56(12), p.7189.
154. Tahir, D. and Tougaard, S., 2012. Electronic and optical properties of Cu, CuO and Cu₂O studied by electron spectroscopy. *Journal of physics: Condensed matter*, 24(17), p.175002.
155. Kidowaki, H., Oku, T. and Akiyama, T., 2012. Fabrication and characterization of CuO/ZnO solar cells. In *Journal of Physics: Conference Series* (Vol. 352, No. 1, p. 012022). IOP Publishing.
156. Wanninayake, A.P., Gunashekar, S., Li, S., Church, B.C. and Abu-Zahra, N., 2015. Performance enhancement of polymer solar cells using copper oxide nanoparticles. *Semiconductor Science and Technology*, 30(6), p.064004.
157. Wanninayake, A.P., Li, S., Church, B.C. and Abu-Zahra, N., 2015. Electrical and optical properties of hybrid polymer solar cells incorporating Au and CuO nanoparticles. *AIMS Materials Science*, 3(1), pp.35-50.

158. Wanninayake, A.P., Church, B.C. and Abu-Zahra, N., 2017. CuO NPs incorporated single and double junction polymer solar cells. *International Journal of Nanoelectronics & Materials*, 10(2).
159. Iqbal, M., Sial, M.A.Z.G., Shabbir, S., Siddiq, M. and Iqbal, A., 2017. Effect of Fe doping on the crystallinity of CuO nanotubes and the efficiency of the hybrid solar cells. *Journal of Photochemistry and Photobiology A: Chemistry*, 335, pp.112-118.
160. Lee, S., Kim, D.H. and Kim, T.W., 2013. Enhancement of the power conversion efficiency for inverted polymer solar cells due to an embedded Cu_xO interlayer formed by using Cu (I) acetate and Cu (II) acetate. *Journal of sol-gel science and technology*, 67(1), pp.105-111.
161. Ikram, M., Imran, M., Nunzi, J.M. and Ali, S., 2015. Efficient inverted hybrid solar cells using both CuO and P3HT as an electron donor material. *Journal of Materials Science: Materials in Electronics*, 26(9), pp.6478-6483.
162. Savva, A., Papadas, I.T., Tsikritzis, D., Armatas, G.S., Kennou, S. and Choulis, S.A., 2017. Room temperature nanoparticulate interfacial layers for perovskite solar cells via solvothermal synthesis. *Journal of Materials Chemistry A*, 5(38), pp.20381-20389.
163. Yu, Y.Y., Chien, W.C. and Wang, Y.J., 2016. Copper oxide hole transport materials for heterojunction solar cell applications. *Thin Solid Films*, 618, pp.134-140.
164. Sabri, N.S., Yap, C.C., Yahaya, M., Mat Salleh, M., Jumali, H. and Hafizuddin, M., 2017. Solution-dispersed CuO nanoparticles as anode buffer layer in inverted type hybrid organic solar cells. *physica status solidi (a)*, 214(1).
165. Sun, B., Zhou, D., Wang, C., Liu, P., Hao, Y., Han, D., Feng, L. and Zhou, Y., 2017. Copper (II) chloride doped graphene oxides as efficient hole transport layer for high-performance polymer solar cells. *Organic Electronics*, 44, pp.176-182.
166. Kim, S., Huang, Y.N., Ameena, F., Hoffman, D.W., Jin, M.H.C., Banger, K.K., Scheiman, D.A., McMillon, L.B. and McNatt, J.S., 2012, June. Semi-transparent photovoltaic devices for smart window applications. In *Photovoltaic Specialists Conference (PVSC), 2012 38th IEEE* (pp. 002807-002810). IEEE.

167. Reddy, N.L., Kumar, S., Krishnan, V., Sathish, M. and Shankar, M.V., 2017. Multifunctional Cu/Ag quantum dots on TiO₂ nanotubes as highly efficient photocatalysts for enhanced solar hydrogen evolution. *Journal of Catalysis*, 350, pp.226-239.
168. Qin, L., Si, G., Li, X. and Kang, S.Z., 2015. Synergetic effect of Cu–Pt bimetallic cocatalyst on SrTiO₃ for efficient photocatalytic hydrogen production from water. *RSC Advances*, 5(124), pp.102593-102598.
169. Tonui, P. and Mola, G.T., 2019. Improved charge extraction in polymer solar cell using metal nano-composite. *Physica E: Low-dimensional Systems and Nanostructures*, 107, pp.154-159.
170. Dlamini, M.W. and Mola, G.T., 2019. Near-field enhanced performance of organic photovoltaic cells. *Physica B: Condensed Matter*, 552, pp.78-83.
171. Sah, P.T., Chang, W.C., Chen, J.H., Wang, H.H. and Chan, L.H., 2018. Bimetallic Ag–Au–Ag nanorods used to enhance efficiency of polymer solar cells. *Electrochimica Acta*, 259, pp.293-302.
172. Arbab, E.A.A. and Mola, G.T., 2019. Metals decorated nanocomposite assisted charge transport in polymer solar cell. *Materials Science in Semiconductor Processing*, 91, pp.1-8.
173. Schulz P, Edri E, Kirmayer S, Hodes G, Cahen D, Kahn A. Interface energetics in organo-metal halide perovskite-based photovoltaic cells. *Energy Environ Sci* 2014;7:1377–81.
174. Lim KG, Ahn S, Kim YH, Qi Y, Lee TW. Universal energy level tailoring of self-organized hole extraction layers in organic solar cells and organic–inorganic hybrid perovskite solar cells. *Energy Environ Sci*. 2016;9:932–9.
175. Jeon NJ, Na H, Jung EH, Yang TY, Lee YG, Kim G, et al. A fluorene-terminated holetransporting material for highly efficient and stable perovskite solar cells. *Nature Energy* 2018;3:682–9.

176. Bakr ZH, Wali Q, Fakharuddin A, Schmidt-Mende L, Brown TM, Jose R. Advances in hole transport materials engineering for stable and efficient perovskite solar cells. *Nanomater Energy* 2017;34:271–305.
177. Calio L, Kazim S, Grätzel M, 2016. Ahmad S. Hole-transport materials for perovskite solar cells. *Angew Chem Int Ed*, 55, pp.14522–45.
178. Jeong, I., Jo, J.W., Bae, S., Son, H.J. and Ko, M.J., 2019. A fluorinated polythiophene hole-transport material for efficient and stable perovskite solar cells. *Dyes and Pigments*, 164: 1-6.
179. Yang, D., Löhrer, F.C., Körstgens, V., Schreiber, A., Bernstorff, S., Buriak, J.M. and Muller-Buschbaum, P., 2019. In-operando Study of the Effects of Solvent Additives on the Stability of Organic Solar Cells Based on PTB7-Th: PC₇₁BM. *ACS Energy Letters*.
180. Reeja-Jayan, B. and Manthiram, A., 2010. Influence of polymer–metal interface on the photovoltaic properties and long-term stability of nc-TiO₂-P3HT hybrid solar cells. *Solar Energy Materials and Solar Cells*, 94(5), pp.907-914.
181. Kadem, B.Y., Al-Hashimi, M., Hasan, A.S., Kadhim, R.G., Rahaq, Y. and Hassan, A.K., 2018. The effects of the PEDOT: PSS acidity on the performance and stability of P3HT: PCBM-based OSCs. *Journal of Materials Science: Materials in Electronics*, 29(22), pp.19287-19295.
182. Soultatia A., Verykios, A., Speliotis, T., Fakis, M., Sakellis, I., Jaouanid, H., Davazoglou, D., Argitis, P., Vasilopoulou, M., 2019. Organic solar cells of enhanced efficiency and stability using zinc oxide:zinc tungstate nanocomposite as electron extraction layer *Organic Electronics* 71 pp.227–237

CHAPTER FOUR

CHARACTERIZATION TECHNIQUES

4.1 INTRODUCTION

The principles and theories behind various characterization techniques such as X-ray diffraction, X-ray photoelectron spectroscopy, scanning electron microscope, Transmission electron microscope and gas sensing station used to determine the chemical, electrical, optical, morphological and structural properties of the synthesized materials are discussed in this chapter.

4.2 X-RAY DIFFRACTION

The use of X-ray diffraction (XRD) technique to define structural properties including crystallite size, crystalline structure, lattice strain, and lattice parameter of the synthesised materials was studied to acquire detailed information. XRD is an effective technique for identifying the crystalline structure of compound by their diffraction pattern as shown in figure 4.1. Each crystalline material provides a unique XRD pattern which identifies its crystal structure. The observed XRD patterns denotes the arrangement and orientation of a specific set acknowledged by Miller indices (h,k,l) [1]. Wherefore, production of the peaks must satisfy the Bragg's condition (equation 4.1).

$$n\lambda = 2d \sin\theta, \quad (4.1)$$

Where n is a positive integer equated to 1 and λ is a wavelength at 1.5418 Å corresponding to Cu K α emission. Fig 4.1 below shows the schematic diagram based on the conditions for Bragg's law [2].

This study used the PANalytical X'Pert Pro diffractometer fitted with CuK α monochromated radiation source. Fig 4.2 displays the schematic diagram for the XRD system, showing X-rays from the anode to sample set at desired angle to the incident beam and to measure the scattered rays by the detector.

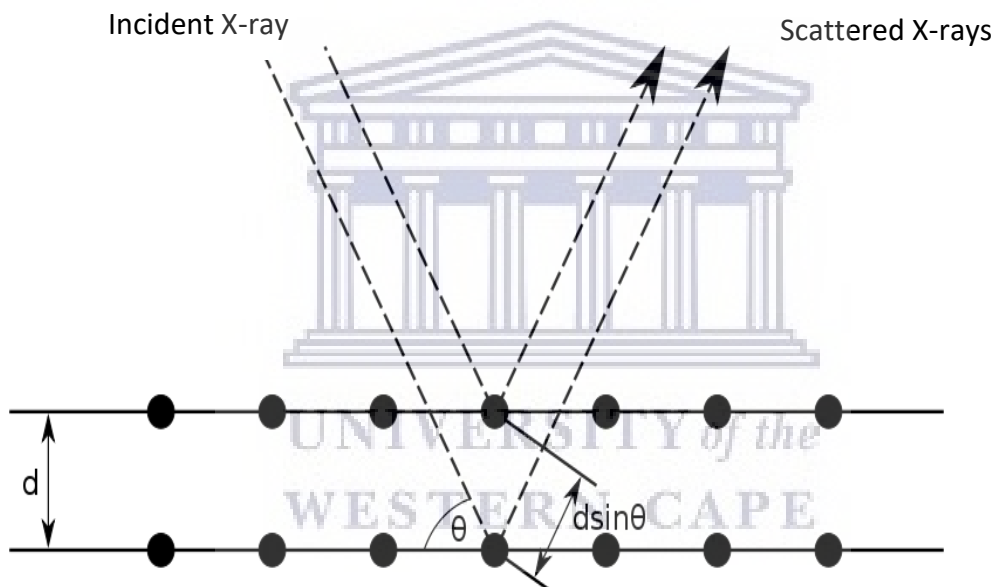


Fig. 4. 1: Schematic diagrams based on conditions for Bragg's law (cited from wikipedia).

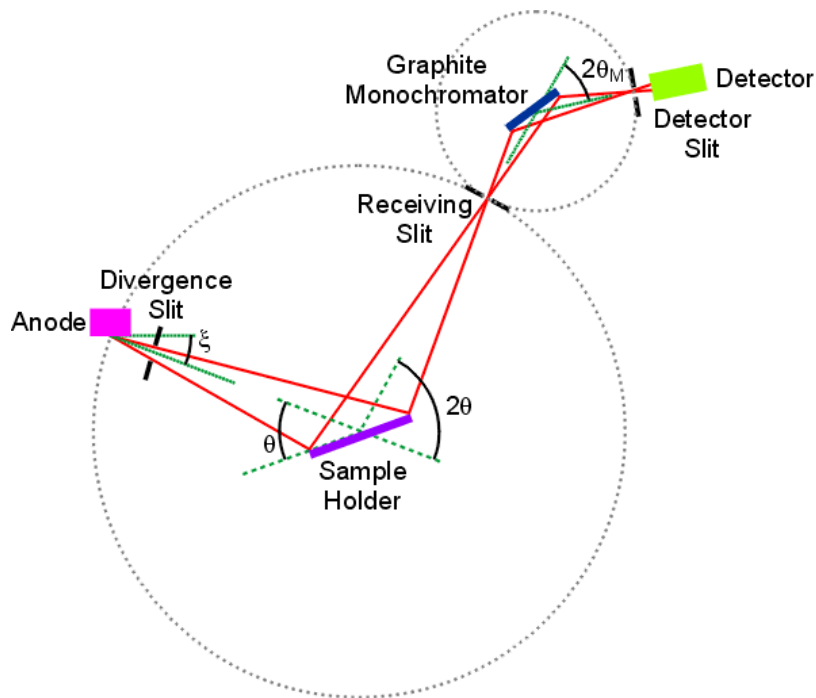


Fig. 4. 2: The schematic diagram for the XRD set-up [3].

4.3. ELECTRON MICROSCOPE

Electron microscopes are beneficial in this study due to beam of accelerated electrons used as probing source. The highly energetic electrons enable the microscope to operate at a high resolution and magnification to study surface morphology and topography using scanning electron microscope (SEM) and transmission electron microscope (TEM) [4].

4.3.1 Scanning Electron Microscope

SEM emits electrons from field-emitter into the electron gun located at the top column. Electrons are focused and directed by electromagnetic lenses using condenser, objective lenses and apertures. Then electrons are accelerated in vacuum at high voltage into fine probe, scanning the surface of material to release information from interaction between the beams of electron with the sample. The lost energy is converted into heat emitted as secondary or backscattered electrons and

the detector convert them into signals. Thus signals are directed to screen with intensity corresponding to the beam on samples [5]. Prepared samples on stubs are coated by conducting layer to obtain non-conductive image. SEM also gives information using the energy dispersive X-ray spectrometer to display the qualitative and quantitative elemental analyses of the material. In this study, Auriga ZEISS SEM was used to obtained images of TiO₂ powders. Fig 4.3 displays the schematic diagram of the SEM.

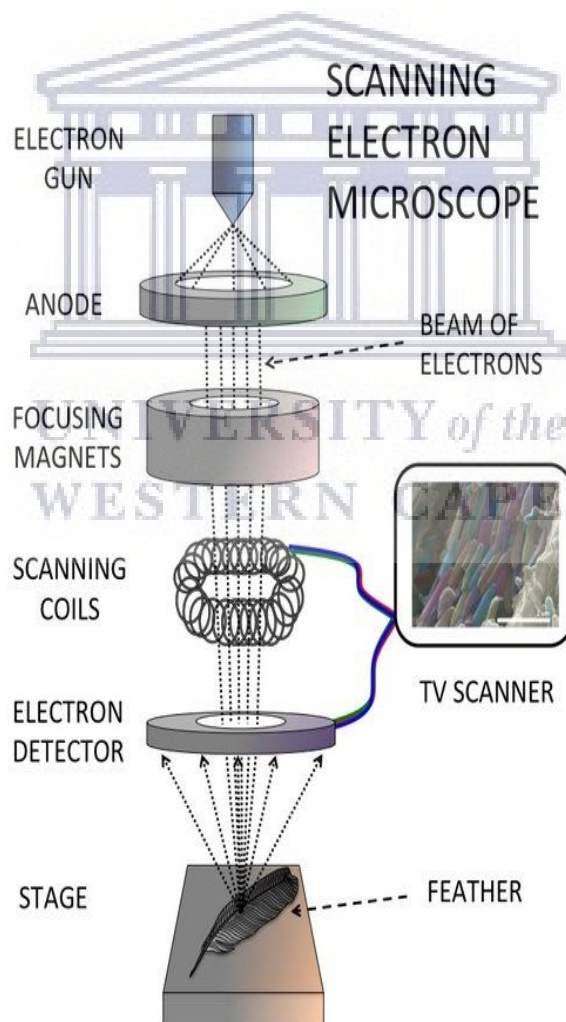


Fig. 4. 3: Schematic diagram of SEM [6].

4.3.2 Transmission Electron Microscope

Transmission electron microscope (TEM) is a vital tool used to characterize nanomaterials to obtain the size of particles, crystallinity and shapes. In TEM, the primary electron beam is transmitted through the sample unlike the backscattering of electron in SEM [4]. Excited beam of electron from Tungsten source is focused through the very thin sample to release information about the crystalline structure from interaction between the electrons and atoms. High accelerated electrons are emitted from the hot cathode in the electron gun through an anode. Electrons are then focused into a thin and coherent beam through a condenser lens to form parallel beam before passing through samples. While condenser aperture precludes high angle electrons from interrelating with sample. Information about samples is magnified by the objective lens in order to view image on the screen [5]. In this study, JEOL JEM 2100 transmission electron microscope (HR-TEM) of 200kV acceleration voltage was used. The powder samples were dispersed in ethanol and ultra-sonicated till completely dissolved. Then the solution was deposited on holey-carbon copper grid and dried in room temperature. The selected area electron diffraction patterns were obtained from TEM. Fig. 4.4 displays the schematic diagram of TEM.

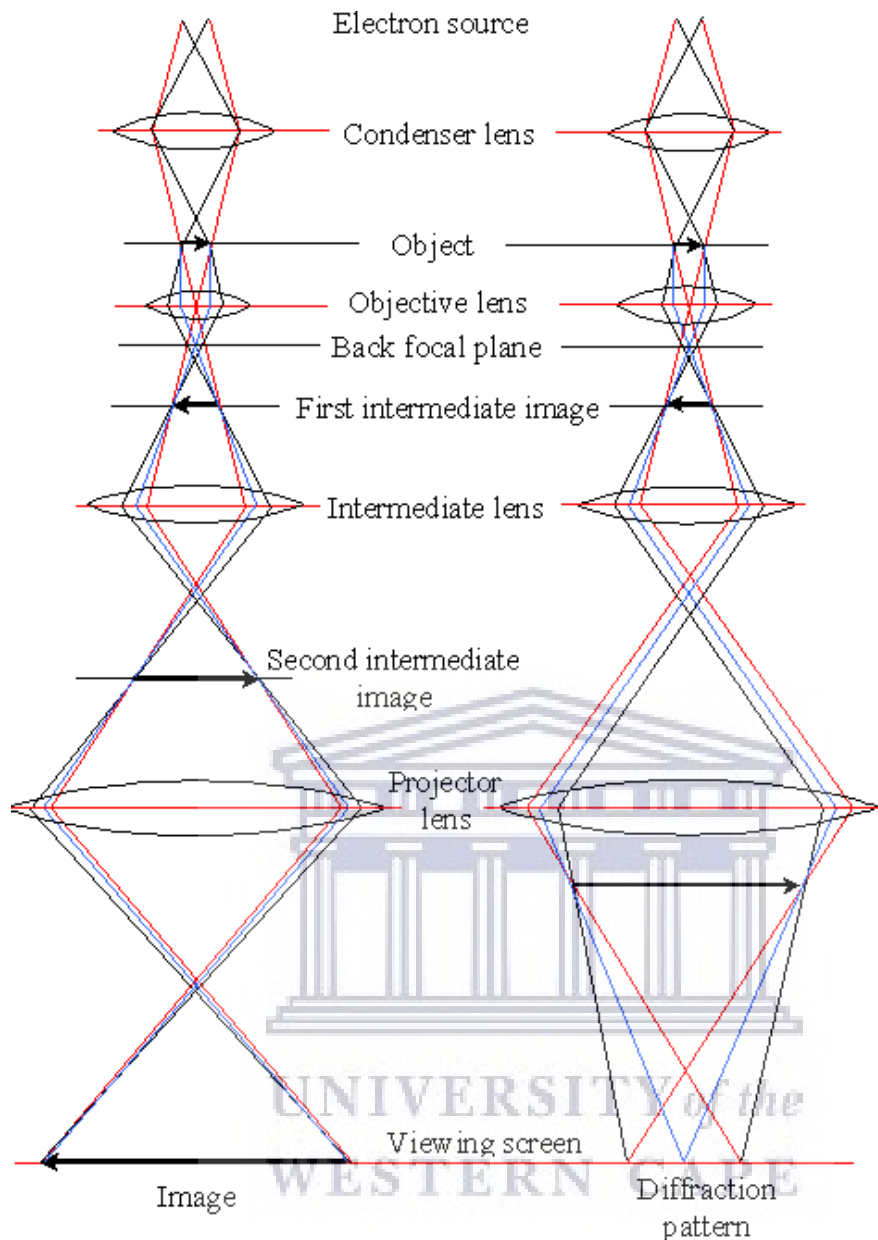


Fig. 4. 4: Schematic diagram displaying the TEM set-up [7].

4.4 PHOTOLUMINESCENCE SPECTROSCOPY

Photoluminescence spectroscopy technique is used to study the surface defects state of the material and induced states present within the band gap of the material. Photo-excitation process causes valence electrons within the material to transit to the conduction band. The excited electron returns back to the ground state with

excess energy emitted as photon in the form of radiation [8]. The excess energy can disintegrate through luminescence by the sample. This luminescence may occur due to recombination radiation of excitons. Horiba Jobin-Yvon IHR 320 nanolog spectrometer with symphony cryogenic detector using Xenon lamp as a continuous energy supply excited at 325 was used in this study. Fig.4.5 display the schematic diagram of PL spectrophotometer

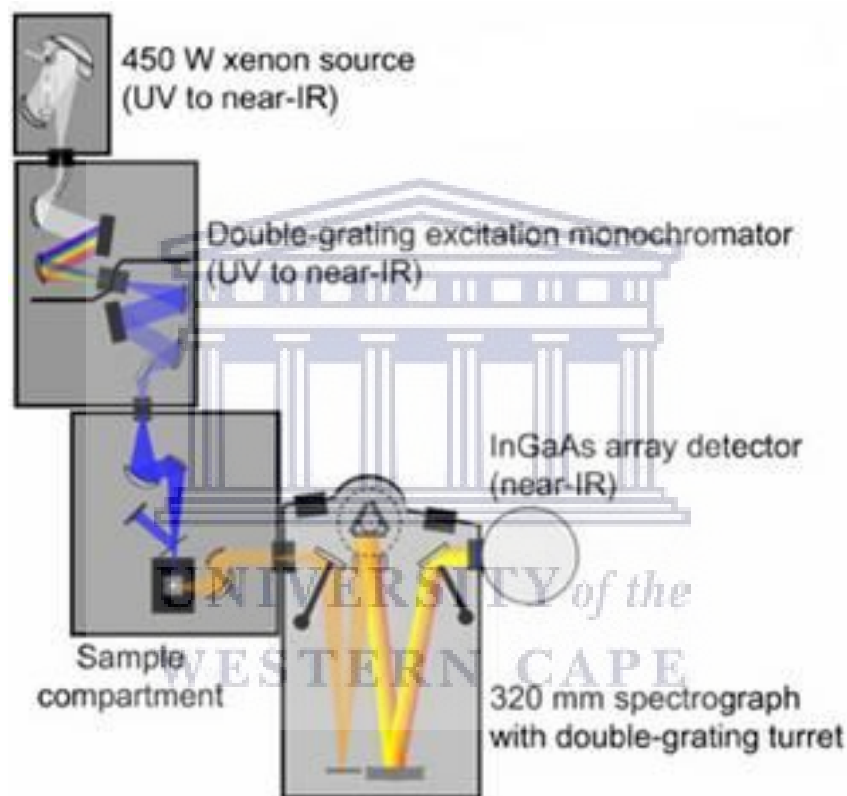


Fig. 4. 5: Schematic representation of Nanolog [9].

4.5 X-RAY PHOTOELECTRON SPECTROSCOPY (XPS)

X-ray photoelectron spectroscopy's usage is to study the chemical, electronic, elemental and surface state of elements in the material. The mechanism involves the photoelectric effect which refers to the ejection of electron from metal surface once is irradiated by light [10]. For ejection of an electron to occur, the photon energy must

be greater than the material work function (ϕ). If the energy is less, the electron will not be ejected. Hence, the photoelectric effect equation (4.2) is define as

$$E_{k(max)} = hv - \phi \quad (4.2)$$

where $E_{k,max}$ is the maximum kinetic energy of the electron ejected, h is the planck constant and v is the frequency. Once the electron is excited it advances from the core state into continuum resulting to form an ion (X^+). Wherefore the detector measures the kinetic energy of the electron ejected. XPS technique depends on photoemission because of X-ray. The binding energy from the ejected electron of a specific orbital can be evaluated by Einstein equation (4.3) of photoelectric effect:

$$BE = E_p - E_{k(max)} - \phi \quad (4.3)$$

where E_p is the X-ray photon irradiated energy of a material. The XPS detector measures only ejected electron that reach the detector. The excited electron can undergo recombination and loose kinetic energy resulting in less electron escaping within the material. The electronic configuration in the atoms correspond to the characteristic of spectral peaks on the XPS spectrum and each peak illustrate the amount of element contained [11]. PHI 500 Versaprobe-scanning ESCA microscopes with monochromatic Al-Ka X-ray source was used in this study to analyse the XPS measurements. Fig.4.6 shows a schematic diagram of XPS technique.

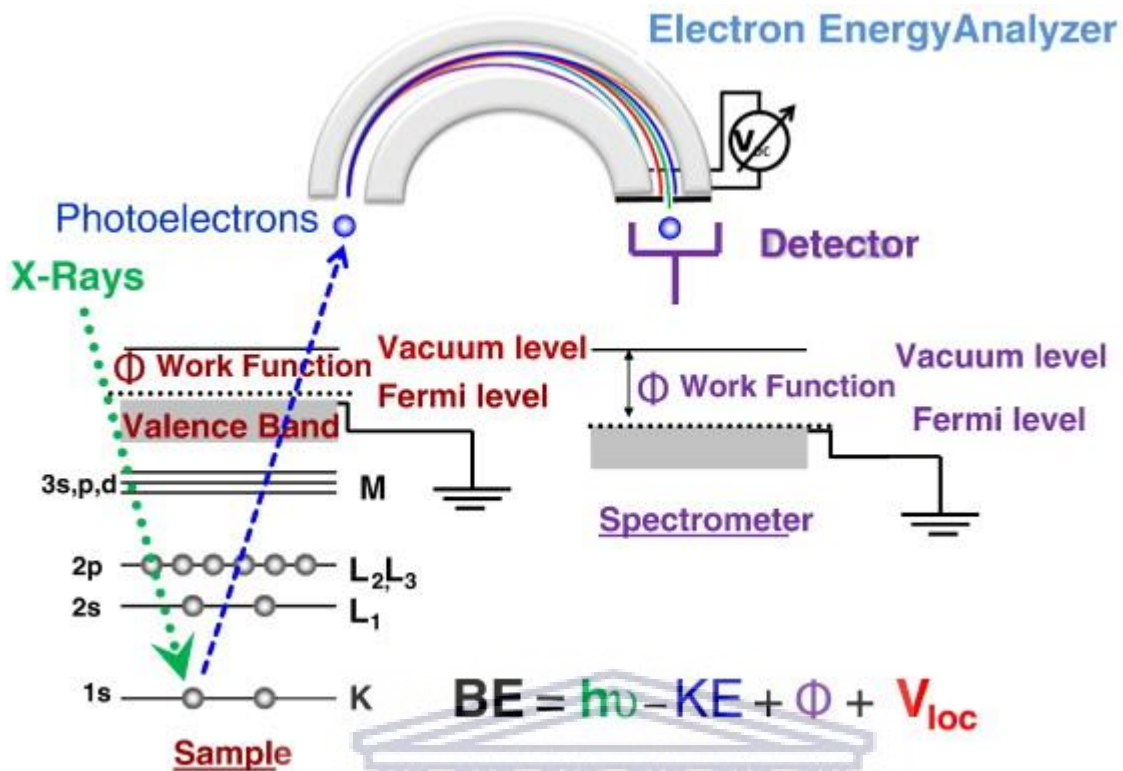


Fig. 4. 6: Schematic diagram of XPS technique [12].

4.6. BRUNAUER-EMMETT-TELLER

Brunauer-Emmett-Teller (BET) studies the adsorption of gas molecules on the surface of the material such as pore diameter and pore volume. The Langmuir theory presumed that the adsorbate behaves as an ideal gas at isothermal conditions and holds on each layer, while the BET theory denotes to infinite-layer adsorption with no interaction between each layers. BET adsorption isotherm equation 4.4 is:

$$\frac{V}{V(p_0 - p)} = \frac{1}{V_m c} + \frac{c - 1}{V_m c} \frac{p}{p_0} \quad (4.4)$$

where N is the adsorbed gas quantity, N_m is the monolayer adsorbed gas quantity, p is the partial vapour pressure of the adsorbate gas in equilibrium and p_0 is saturation

pressure of the adsorbate gas. Wherefore C is constant and related to enthalpy of the adsorption. The BET surface area is given by equation 4.5 which is:

$$S_{\text{bet}} = N_m N_a / V_A \quad (4.5)$$

where N_m is the monolayer adsorbed gas, N_a is the Avogadro's number and V_A is the molar volume [13,14]. BET surface area used in this study is the Micromeritics TRISTAR 3000 surface area analyser. Fig. 4.7 displays the schematic diagram of BET.

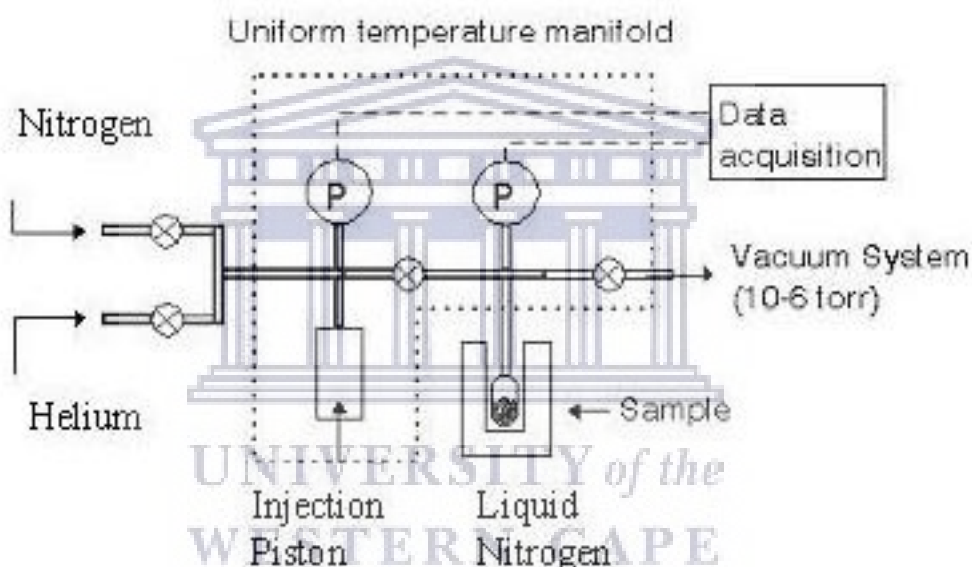


Fig. 4. 7: Schematic diagram of BET system [15].

4.7. ELECTRON PARAMAGNETIC RESONANCE (EPR)

Electron paramagnetic resonance (EPR) is an unpaired electron of an atom causing resonant absorption of microwave radiation when placed in the strong magnetic field. The technique is used to give information concerning paramagnetic centres on several oxide surfaces which includes diamagnetic oxides and transition metal ions among the list.

An unpaired electron of a compound, when involved in spin interaction with a strong magnetic field, the unpaired electrons spin permit alignment in two possible orientations. These two orientations result in different magnetic potential energy, thus inducing a lift in degeneracy of the state of electron spin. The spin of unpaired electron can be either in the direction similar to magnetic field with low energy state $m_s = -1/2$ or antiparallel to the magnetic field with high energy state $m_s = +1/2$. Fig 3.8 shows the energy level for the electron spin.

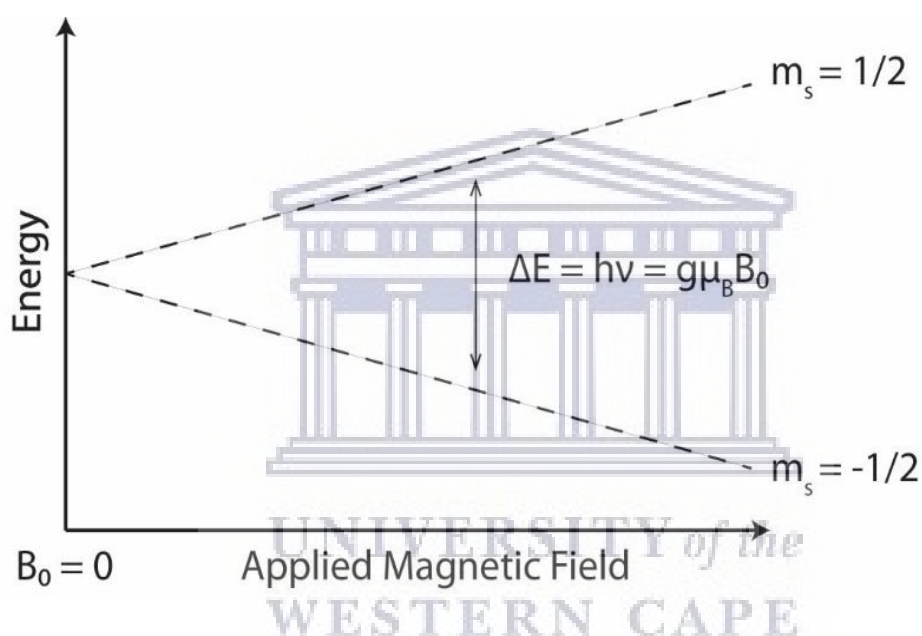


Fig. 4. 8: Energy level for an electron spin in applied magnetic field B [16].

Samples in EPR are exposed to fixed microwave irradiation which induces a change in orientation of some unpaired electrons at certain magnetic field which result in separation of energy state as shown in Fig 4.9. In this study the JEOL electron paramagnetic resonance spectrometer was used and operated at 9.4GHz X-band at room temperature.

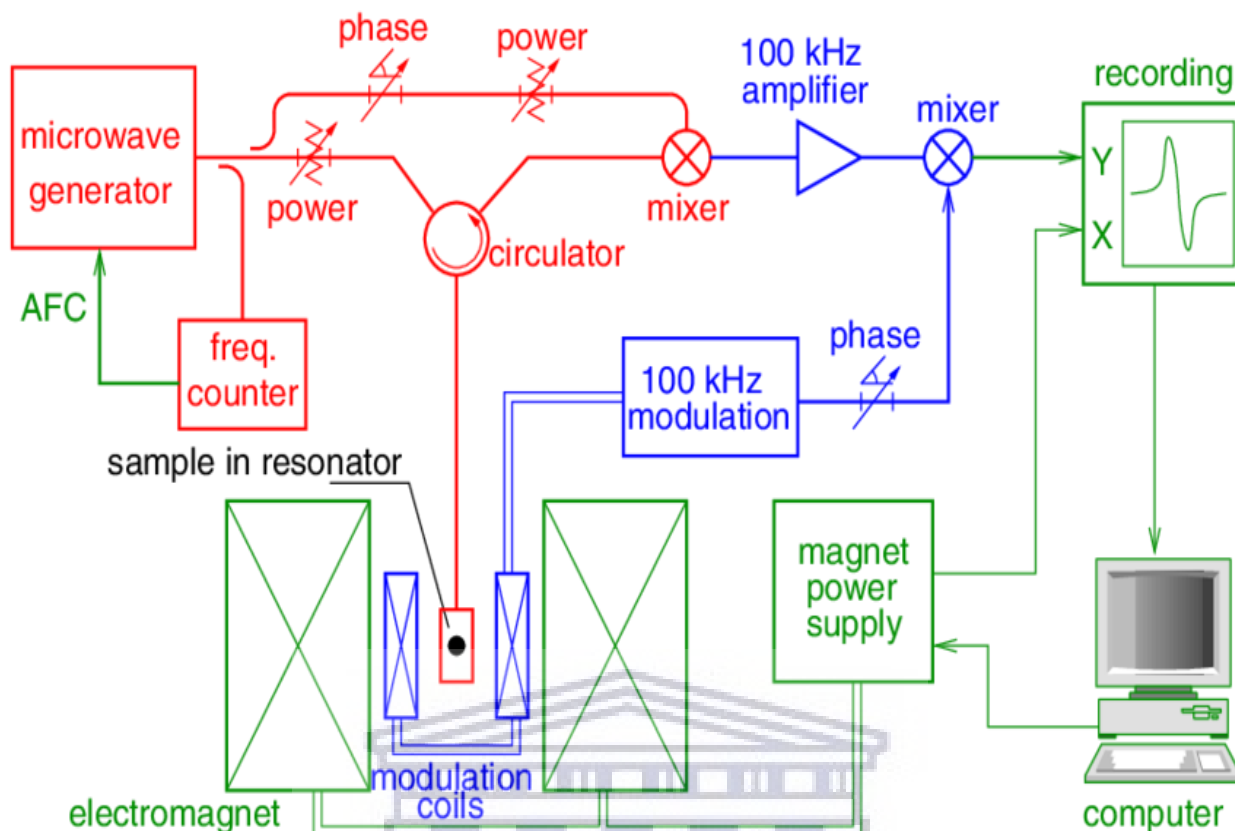


Fig. 4. 9: Schematic diagram of electron paramagnetic resonance [17].

4.8. GAS SENSING STATION

Gas sensing instrument detect and monitor different types of gases. In this study KENOSISTEC UHV gas sensing instrument was used for gas sensing experiments. The system comprises of sensing chamber with sample stage, an air mixer, and gas inlet for different test gases. There's two thermostatic bath which supplier wet air in the mixer for measuring humidity and the other one for measuring volatile air. And also includes six heaters and six KEITHLEY picoammeter.

The sensing films were conducted from homogenous paste at room temperature. Then drop-coated on aluminium substrate interdigitated with Au/Pt electrode and secured the sensing films on sample stage in the chamber. Samples were exposed to the gases and humidity in chamber and the picoammeters recorded the

concentration of gas and humidity. Figure 4.10 display the gas sensor station setup diagram [18].

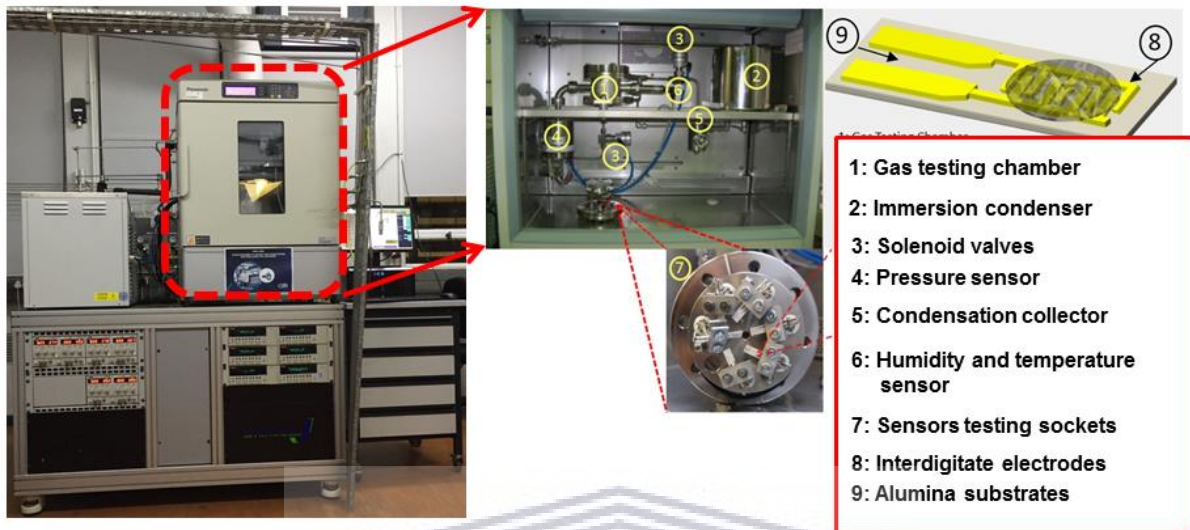
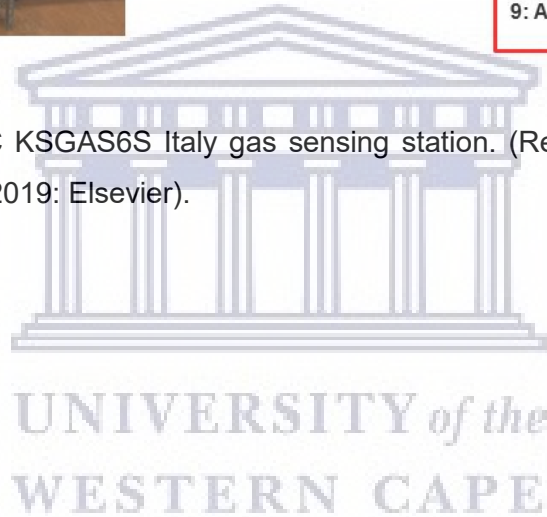


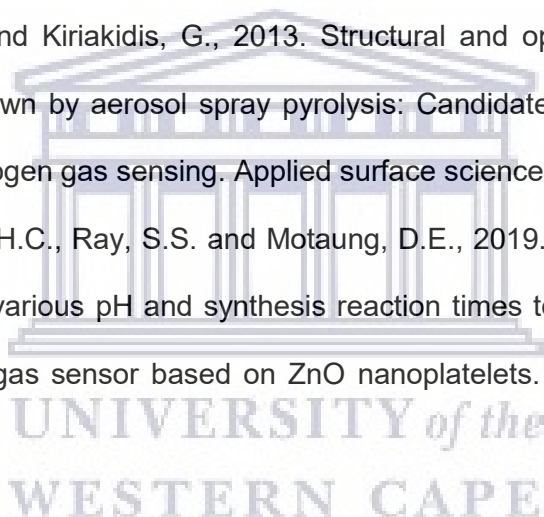
Fig. 4. 10: KENOSISTEC KSGAS6S Italy gas sensing station. (Reprinted with permission from Ref. [19]. Copyright 2019: Elsevier).



REFERENCES

1. Cullity, B.D., 1956. *Elements of X-ray Diffraction*. Addison-Wesley Publishing.
2. Xiaoming, J. and Ziqin, W., 1991. Bragg's law with refractive correction of low-angle x-ray diffraction for periodic multilayers. *Chinese Physics Letters*, 8(7), p.356.
3. <http://pd.chem.ucl.ac.uk/pdnn/inst1/optics1.htm> (accessed on the 10th Jan 2021).
4. Williams, D.B. and Carter, C.B., 2009. Scattering and diffraction. In *Transmission Electron Microscopy* (pp. 23-38). Springer, Boston, MA.
5. Egerton, R.F., 2005. The scanning electron microscope. In *Physical Principles of Electron Microscopy* (pp. 125-153). Springer, Boston, MA.
6. http://media.tumblr.com/fbdf3232a175493f1938e7abc08dc9c6/tumblr_inline_mojzcz8HJv1qz4rgp.jpg (accessed on the 10th Jan 2021).
7. <http://labs.mete.metu.edu.tr/tem/TEMtext/raydiagram.gif> (accessed on the 10th Jan 2021).
8. Laia, C.A. and Ruivo, A., 2019. Photoluminescent glasses and their applications. *Fluorescence in Industry*, pp.365-388.
9. https://www.horiba.com/typo3temp/processed/csm_nanolog_sch_04_d9a8f47b8d.jpg (accessed on the 10th Jan 2021).
10. Mokoena, P.P., 2014. Narrowband Ultraviolet B emission from gadolinium and praseodymium co-activated calcium phosphate phosphors for phototherapy lamps (Masters dissertation, University of the Free State).
11. Tshabalala, Z.P., 2016. Room temperature gas sensing characteristics of titanium dioxide nanostructures: effects of hydrochloric acid on the structure and magnetic properties (Doctoral dissertation, University of the Free State).
12. Shingange, K., 2016. Magnetic, luminescence and gas sensing properties of various zinc oxide nanostructures: The influence of surface modification by gold on the gas sensing properties (Doctoral dissertation, University of the Free State).
13. Anderson, R.B., 1946. Modifications of the Brunauer, Emmett and Teller equation. *Journal of the American Chemical Society*, 68(4), pp.686-691.

14. <https://particle.dk/methods-analytical-laboratory/surface-area-bet-2/> (accessed on the 10th Jan 2021).
15. <http://saf.chem.ox.ac.uk/operating-principles-3.aspx> (accessed on the 10th Jan 2021).
16. Weil, J.A. and Bolton, J.R., 2007. Electron paramagnetic resonance: elementary theory and practical applications. John Wiley & Sons.
17. https://www.researchgate.net/profile/Vit_Kudrle/publication/231038925/figure/fig2/AS:393478241570826@1470823931796/Arrangement-of-continuous-wave-cw-EPR-spectrometer-The-microwave-bridge-typically.png (accessed on the 10th Jan 2021).
18. Motaung, D.E., Mhlongo, G.H., Kortidis, I., Nkosi, S.S., Malgas, G.F., Mwakikunga, B.W., Ray, S.S. and Kiriakidis, G., 2013. Structural and optical properties of ZnO nanostructures grown by aerosol spray pyrolysis: Candidates for room temperature methane and hydrogen gas sensing. *Applied surface science*, 279, pp.142-149.
19. Kortidis, I., Swart, H.C., Ray, S.S. and Motaung, D.E., 2019. Detailed understanding on the relation of various pH and synthesis reaction times towards a prominent low temperature H₂S gas sensor based on ZnO nanoplatelets. *Results in Physics*, 12, pp.2189-2201



CHAPTER FIVE

Superior Open Circuit Voltage Induced by Metals Doping in TiO₂ as a Non-Fullerene Material Towards Organic Solar Cells Performance

5.1. INTRODUCTION

Polymer solar cells (PSCs) offer an economical and advantageous alternative as opposed to silicon based solar cells owing to its low cost of synthesis, low temperature preparations, etc. [1-9, 10]. However, the current efficiency of the state of the art materials, poly (3-hexylthiophene) (P3HT) and [6, 6]-phenyl-C₆₁-butyric acid methyl ester (PCBM), is limited around 6% [11, 12]. Most recent, an efficiency around 11 % has been reported [13, 14]. While an efficiency of approximately 13 % was disclosed by Raynergy Tek and Heliatek companies for tandem solar cells [15]. PSC's efficiency is influenced by charge carrier mobility of donor/acceptor (D/A) materials, illumination intensity, D/A energy gap, potent charge extraction in the photoactive layer and charge collection to their appropriate anode and cathode. Photoexcitation can be enhanced further by inclusion of hole transport layer (HTL) and electron transport layer (ETL) between photoactive layer and the electrodes [16-18].

Common application of zinc oxide (ZnO) nanoparticles as ETL is due to their thorough arranged band gap distribution and high electron mobility. Effective charge extraction obtained by incorporation of 3D structure in the ETL between the cathode and photoactive layer. The presences of ZnO nanoparticles in the blend of P3HT and

PC₇₁BM intensify surface roughness that effect light absorption in the active layer [19-22]. This surface roughness resulted from the deep band of ZnO, which enable the radiative recombination of electron-hole pair. The deep band is formed because of doping of ZnO nanoparticle that interferes with the arrangement of oxygen ion, hence, the formation of oxygen vacancy. The oxygen vacancy conducts itself as both shallow and deep trap state, thereby promoting diffusion of carriers and enhancing recombination of carriers respectively [23]. Incorporation of metal nanoparticles, such as silver (Ag), gold (Au) and copper (Cu) with ZnO nanoparticles impedes recombination of electron-hole pair and encourage electron-hole pair separation. These metal nanoparticles exhibit localized surface plasmon resonance (LPSR), which influences light absorption capability of organic photovoltaic devices within a broad spectrum range [24-27]. The particle size and shape of the metallic nanoparticles have been reported to have a significant role in the exciton-plasmon coupling and influence the performance parameters in OSC [28-30].

TiO₂ is desired in solar cells application due to its high electron mobility, lower density and low dielectric. Integration of TiO₂ nanoparticles in the blend of P3HT:PCBM reported to enhance stability and charge transfer owing to its excellent charge transport and highly stable properties thereby increase efficiency of the devise. Combination of TiO₂ and PCBM as electron acceptors in the active layer has shown preference of electron flowing to TiO₂ due to its wide band gap and high electron mobility. Nonetheless, the presence of PCBM acts as a surfactant thereby inhibiting segregation of TiO₂ nanoparticles. Previous studies displayed an enhanced absorption observed in rough surface of an active layer due to increase content of TiO₂ nanoparticles [31]. In this work, we report on the superior open circuit voltage (V_{oc}) induced by the incorporation of non-fullerene Au and Ag and Cu doped in TiO₂

nanoparticles on the polymer material matrix for improvement on the solar performance. The structural, optical and paramagnetic properties of the Au and Ag and Cu doped in TiO₂ nanoparticles are investigated in detail and correlated with the solar cells performance. We showed that the PCE and V_{OC} are dependent on the particular metal doping and its content.

5.2. EXPERIMENTAL

5.2.1. Materials

P3HT regioregular, indium tin oxide (ITO) coated glass on a 1 mm glass substrate (resistivity of 8-12 Ωsq⁻¹ and transmittance ≥ 83%) substrates were purchased from Sigma-Aldrich, while the 1, 2-Dichlorobenzene solution (purity 99.9 %) was purchased from Merck.

5.2.2. Synthesis of undoped and doped TiO₂ nanoparticles

All chemicals were purchased from Sigma Aldrich and used without any further purification. To synthesize TiO₂ and then doped with Ag, Au and ad Cu, about 1.0g of P25 Degusa titanium dissolved in 100 mL of deionized water. For doping, 0.1, 0.5, 1.0 and 2.0 mol.% of Au, Ag and Cu, respectively were added to the solutions. About 0.5 M of NaOH was added in the solution to reach the desired pH, and was continuously stirred for 5 h. The solutions were then placed in a 125 ml Teflon® liner made to fit inside a stainless steel acid digestion vessel (purchased Parr Instrument Company). The solutions were placed for 12 h in an oven at a temperature of 200 °C. After the synthesis, the vessels were allowed to cool to room temperature. The white precipitates were collected by filtration and washed 10 times with distilled water to remove impurities. The final products were dried in an oven at 90°C overnight to obtain undoped and doped TiO₂ nanoparticles.

5.2.3 Characterization

Structural analyses were carried out using the x-ray diffraction (Panalytical XPERT PRO PW 3040/60) equipped with Cu monochromatic radiation source and transmission electron microscopy (JEOL-2100) operated at 200 KeV. The surface morphology is investigated using the Auriga- Zeiss instrument, fitted with the energy dispersive spectroscopy. The optical properties of Au and Ag and Cu doped in TiO₂ nanoparticles were studied using UV-VIS Perkin Elmer Lambda 750 spectrometer in the wavelength range of 350-800 nm. The specific surface area and the pore volume of the samples were analyzed by nitrogen (N₂) physisorption using a Micromeritics TRISTAR 3000. The paramagnetic defects were probed using a JEOL X-band EPR spectrometer (JEOL, Japan) at room temperature.

5.2.4. Fabrication of Photovoltaic Solar Cell devices

The solar cell devices were devised using the ITO coated glass substrates employing the following configuration: ITO/PEDOT:PSS/P3HT:TiO₂-Au or Ag or Cu/MoO₃/Al. Prior to device fabrication, ITO was cleaned in boiled ethanol, then rinsed with deionised water and blow dried with nitrogen gas. A buffer layer (PEDOT:PSS) with a thickness of roughly 50 nm was spin-coated onto the ITO substrate at 2500 rpm for 30 s and annealed at 100 °C for 1 h. Active layers of P3HT blended in various concentrations of Au and Ag and Cu doped in TiO₂ nanoparticles (i.e. P3HT:TiO₂-Au, P3HT:TiO₂-Ag and P3HT:TiO₂-Cu) were weighed in 3 mg:3 mg (1:1 w/w) and dissolved in 1 mL solvent of 1, 2-dichlorobenzene with a boiling point of 180 °C and spin-coated ontop of the PEDOT layer. The developed films were afterwards annealed at 150 °C for 15 min to boost the polymer ordering. The hole transport layer containing molybdenum oxide (MoO₃) onto the photoactive layer was

deposited using a sputtering system (AJA international INC, USA). Lastly, an Al electrode was evaporated on the top of the MoO₃ layer by means of a shadow mask, producing an active area of 0.15 cm². Current density-voltage (I–V) analyses were carried out using a Keithley 4200 (USA) source measurement unit using Newport solar simulator at 100 mW/cm² (AM 1.5 G) irradiation. For reproducibility, three devices were measured.

5.3. RESULTS AND DISCUSSION

5.3.1. Structural properties of Au, Ag and Cu doped TiO₂ nanoparticles

The accomplishment of XRD measurements was to identify the effect of incorporation of noble and transitional metal on the TiO₂ structural properties. The diffraction peaks at crystal planes (101), (004), (111), (200), (105), (211) and (118), which can be indexed as relatively polycrystalline of TiO₂ phase anatase were observed. While, rutile crystal plane (110) was observed at $2\theta = 27.5^\circ$ in pristine TiO₂ patterns [32]. Upon doping, with Au, Ag and Cu, the XRD patterns showed no impurity peaks, revealing dopants were successfully inserted in the TiO₂ crystal lattice. Nonetheless, the rutile peak at 27.5° shifted slightly to higher angles (see the magnified spectra in Fig. 5.1b, d, f) and this behaviour is more visible for Cu doped TiO₂, which can be assigned to the closeness of ionic radius of Cu²⁺ and Ti⁴⁺. Moreover, the intensity is reduced at 0.5 and 1 % mol doping concentration, which further increased at 2.0 mol.% owing to saturation [31, 33]. From Table 5.1, it is very clear that the crystallite size decreased with an increase in doping concentration. This is clearer for the sample doped with Cu, especially at 0.5 and 1.0 % mol. However, an increase in lattice strain (ϵ) was observed upon doping TiO₂ with Au, Ag and Cu concentration.

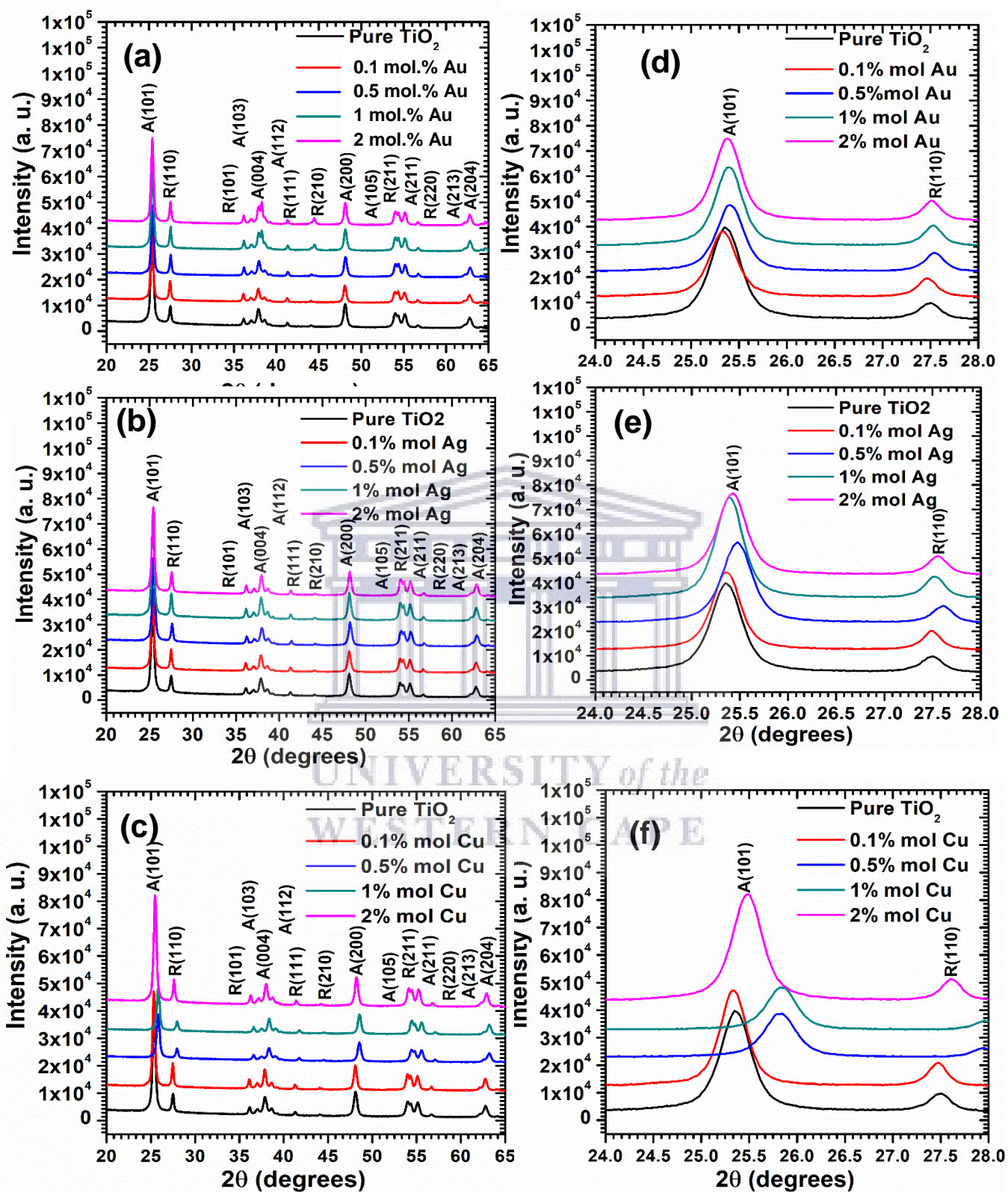


Fig. 5. 1: XRD patterns of (a) Au doped TiO_2 , (b) Ag doped TiO_2 and (c) Cu doped TiO_2 . Note (d-f) corresponds to magnified patterns of Fig. 5.1a-c, respectively.

Table 5. 1: Crystallite size and crystal lattice of Au, Ag and Cu doped TiO₂.

Doping concentration	Au		Ag		Cu	
	Lattice strain, ϵ ($\times 10^{-4}$)	Crystallite size (nm), L	Lattice strain, ϵ ($\times 10^{-4}$)	Crystallite size (nm), L	Lattice strain, ϵ ($\times 10^{-4}$)	Crystallite size (nm), L
Pure TiO ₂	0.003	16.3	0.003	16.1	0.0002	16.1
0.1% mol	0.002	18.84	0.008	18.88	0.00755	18.59
0.5% mol	0.002	16.55	0.765	16.27	0.003	16.52
1.0% mol	0.002	18.70	0.766	20.01	0.00988	17.00
2.0% mol	0.541	19.67	0.926	20.78	1.00	18.66

5.3.2. Morphology analyses of Au, Ag and Cu doped TiO₂ nanoparticles

Fig. 5.2 displays the detailed analyses on the surface morphology of various concentrations of Au, Ag and Cu doped TiO₂. SEM micrographs of pure TiO₂ illustrate small nanoparticles which upon incorporating the initial dopants concentration (i.e. 0.1 mol.%) in the TiO₂ matrix, the size of nanoparticle increases. This is probably due to the agglomeration as depicted in Fig. 5.1b, e and h. However, upon increasing the doping concentration, a slight decrease is witnessed and this confirmed by XRD analyses. At higher doping concentration, further agglomeration is noted, especially for the 2.0 mol.% Cu doped TiO₂ nanoparticles shown in Fig. 5.2j. Additionally, cracks or porous behaviour on the surface morphology is also noted to most of nanostructures, more specifically on the 2.0 mol.% Au and Ag. Larger porosity could be beneficial for gas sensing applications.

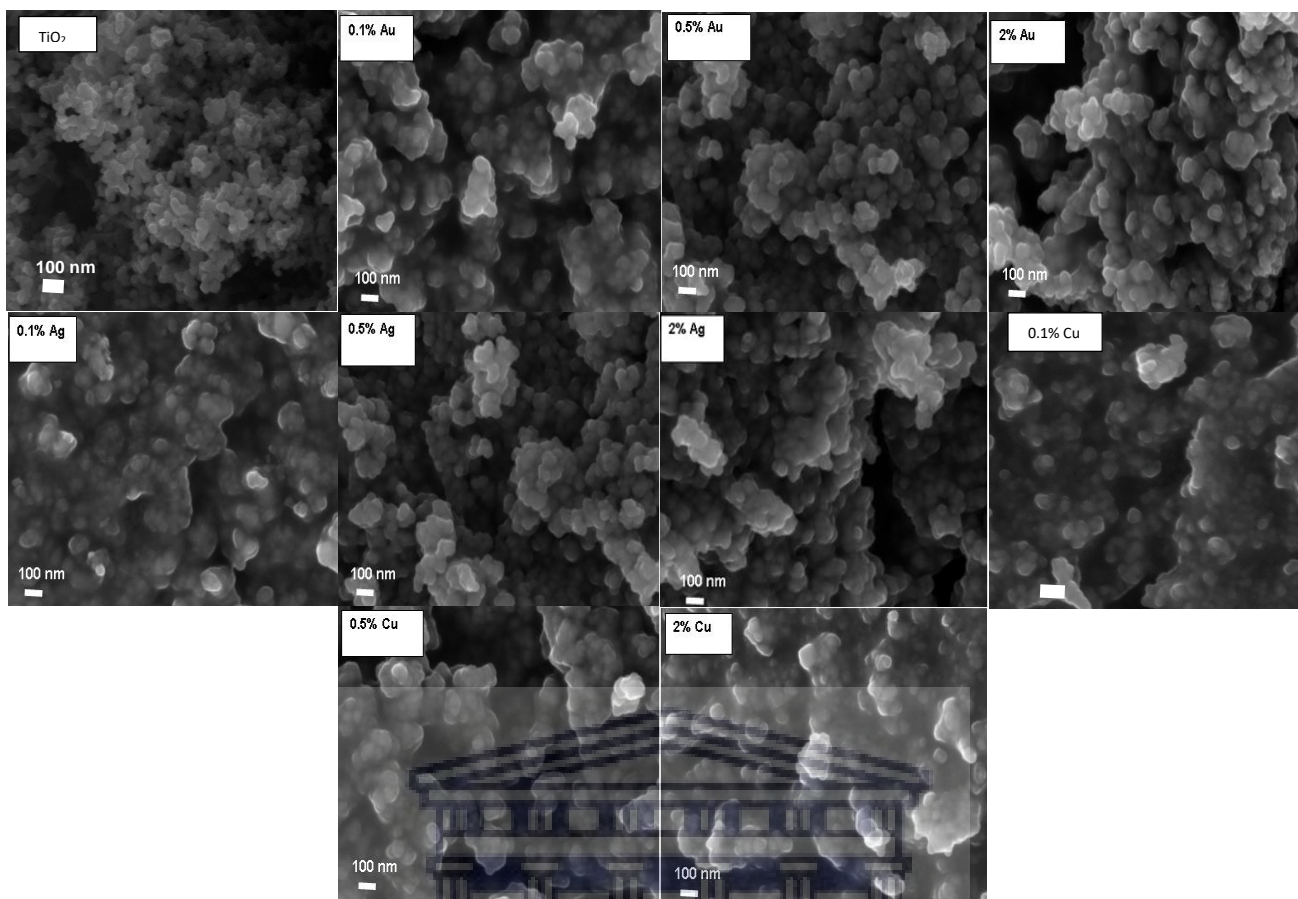


Fig. 5. 2: SEM images of various concentration of Ag, Au, Cu and pure TiO₂.

The internal structure of 0.5 mol.% Au, 0.5 mol.% Ag and 0.5 mol.% Cu doped TiO₂ nanostructures was probed using TEM, see Fig. 5.3. The low and high-resolution TEM analyses in Fig. 5.3a and b demonstrate that Au nanoparticles are homogeneously distributed across the TiO₂ matrix. The SAED patterns indicate that Au doped TiO₂ are highly crystalline. The interlayer spacing of 0.350 nm, which corresponds to (101) lattice planes of anatase TiO₂ is observed. Whereas, the d-spacing of 0.233 nm matched the (111) lattice planes of Au nanoparticles, which is consistent with the results reported by Zhu et al. [25]. The Ag doped TiO₂ displays lattice fringes with d-spacing of 0.351 nm corresponding to (101) plane of anatase phase. Whereas, The TEM image in Cu doped TiO₂ shows lattice fringes with d-spacing of 0.349 nm.

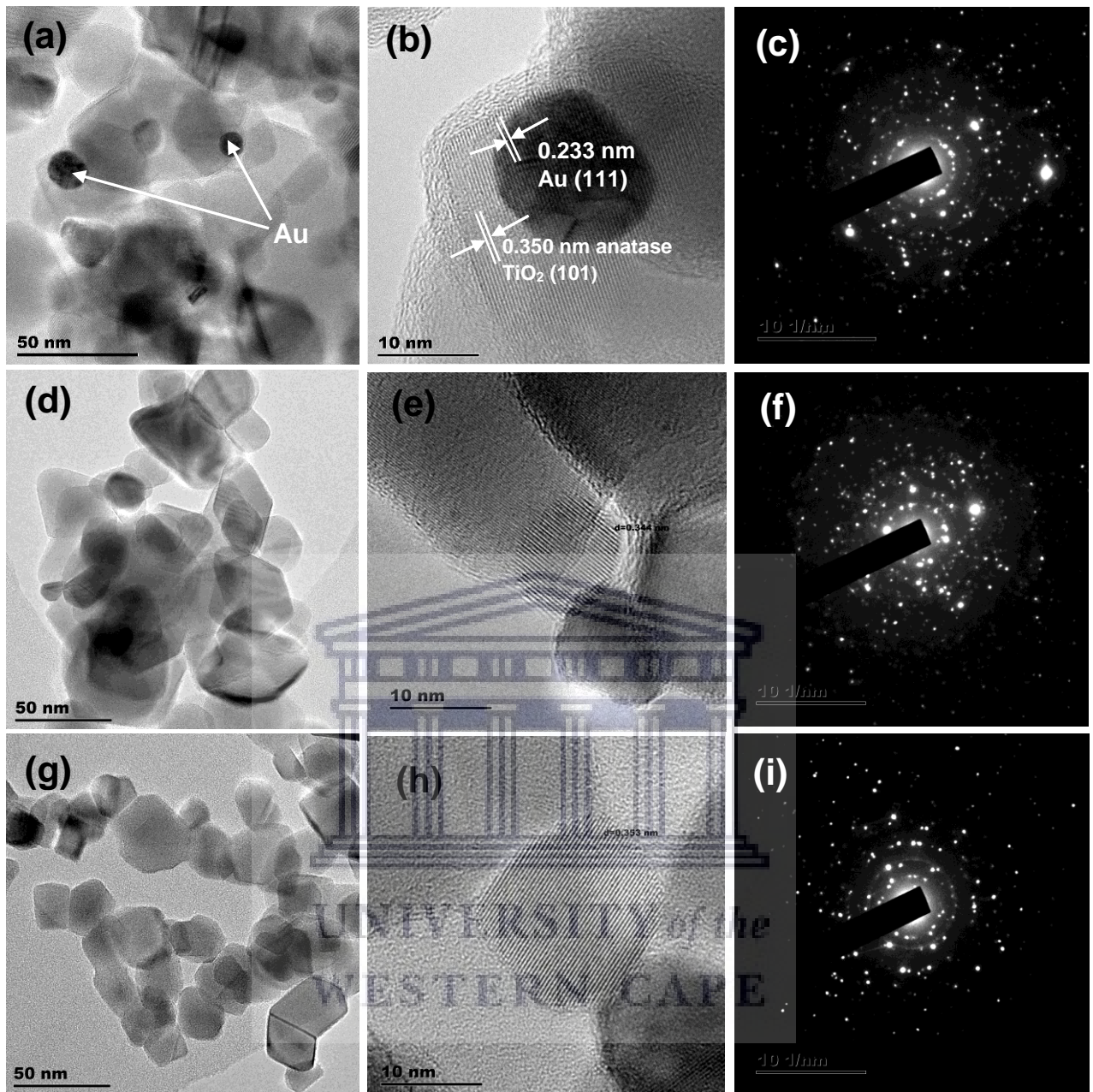


Fig. 5. 3: TEM micrographs of (a-b) 0.5 mol.% Au, (d-e) 0.5 mol. % Ag and (g-h) 0.5 mol.% Cu doped TiO₂ samples. Note: (c, f and i) correspond to SAED patterns of 0.5 mol.% Au, Ag and Cu doped TiO₂, respectively.

Fig. 5.4 displays the N₂ adsorption-desorption curves of TiO₂ doped with various concentrations of Au, Ag, and Cu. As shown in Fig. 5.4 the curves shift up upon incorporating the dopants within the TiO₂ matrix. Moreover, the BET surface area (S_{BET}) plot versus doping concentration shows that the S_{BET} increases with doping

concentration, disclosing a higher S_{BET} for 0.5 mol.% Cu compared to its counterparts. Such higher S_{BET} can be justified by smaller crystallite size and smaller particles observed from XRD and SEM analyses.

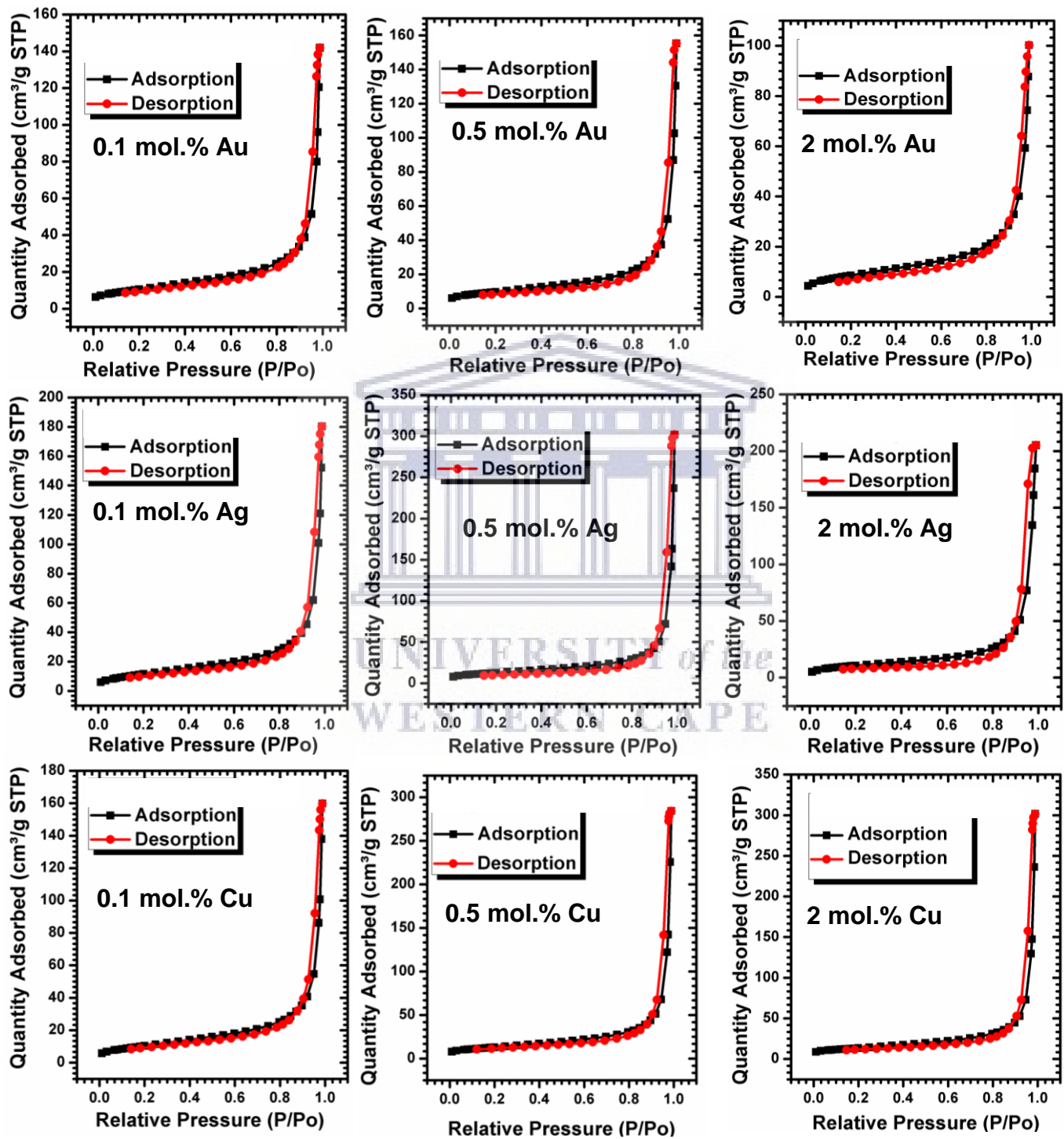


Fig. 5. 4: N_2 -adsorption-desorption isotherms of the pure and doped TiO_2 nanoparticles.

5.3.3. Chemical state analyses of Au, Ag and Cu doped TiO₂ nanoparticles

XPS analyses were conducted on evaluating the elemental composition and the oxidation state of TiO₂ doped with varies concentrations of Au, Ag and Cu interaction. The high resolution Ti2p of the 0.1 Au, Ag, and Cu doped is shown in the appendix A. The Ti 2p_{3/2} could be fitted into two peaks located at 458 and 461 eV. While the 2p_{1/2} of the 0.1 mol.% Au doped could be fitted into one peak centred at 466.3 eV. As for the 0.1 mol.% Ag doped, the Ti 2p_{3/2} could be fitted into one peak located at 458.9 eV. And the Ti 2p_{1/2} of the Ag doped TiO₂ maybe fitted into two peaks positioned at 463.8 and 464.5 eV. The Ti 2p_{3/2} and 2p_{1/2} of the Cu doped could be fitted into two peaks positioned at 457.6 and 458.4 eV and 463.9 and 464.7 eV [34].

The high resolution XPS spectra of the 0.1, 0.5 and 2 mol.% Au doped TiO₂ samples displayed the Au 4f spectrum in Fig. 5.5a-c containing two peaks owing to Au 4f_{7/2} and 4f_{5/2} levels. The Au 4f_{7/2} and 4f_{5/2} of the 0.1 mol.% are deconvoluted into one peak located at 85.4 eV and 88.8 eV. While, the Au 4f_{7/2} and 4f_{5/2} of the 0.5 mol.% doped Au is deconvoluted into one and two peaks located at 84.8 and 87.5 and 88.8 eV, respectively [35]. The intensity of the 2 mol. % increases in comparison to that of lower doping, where the peas related to Au 4f_{7/2} and 4f_{5/2} are more resolved, confirming the existence of AuNP on surface of TiO₂ [26, 35]. The XPS survey spectra of the 0.5 and 2 mol.% Ag doped TiO₂ samples exhibited the Ag 3d spectrum in Fig. 5.5d-f, which comprised two peaks due to Ag 3d_{5/2} and Ag 3d_{3/2} levels. Nonetheless, for the 0.1 mol.% Ag shown in Fig. 5.5d, no peaks related to Ag could be found. The peak assigned to Ag 3d_{5/2} is positioned at the binding energies of 367.9, and 367.9 eV for 0.5 and 2 mol.% Ag doped TiO₂, respectively. Likewise, peak assigned to Ag 3d_{3/2} is positioned at the binding energies of 375.5 and 373.9

eV for 0.5 and 2 mol. % Ag doped TiO₂, respectively [27]. The XPS survey spectra of the 0.1, 0.5 and 2 mol.% Cu doped TiO₂ samples in Fig. 5.5g-i, showed that the Cu (2p) spectrum is comprised of two individual peaks allocated to Cu (2p_{3/2}) and Cu (2p_{1/2}) levels, which are from Cu²⁺ ions. The peak assigned to Cu (2p_{3/2}) is positioned at binding energies of 932.51 and 932.36 eV and 932.9 for 0.1 and 0.5 and 2 mol.% Cu doped TiO₂ respectively. Similarly, the peak assigned to Cu (2p_{1/2}) is positioned at 952.16 and 952.12 eV for 0.1 and 0.5 mol. % mol Cu doped TiO₂, respectively. While that of the 2 mol.% could be fitted into peaks, which showed peaks of the Cu (2p_{3/2}) at 931.8 and 932.1 eV; whereas the Cu (2p_{1/2}) showed peaks at 951.7 and 952.3 eV. This sustenance the fact that doping of copper in TiO₂ was successful. The process of hydrothermal shows that Ti ions were substituted by Cu ions in TiO₂ lattice. While, formation of Cu-O bonds replaced the Ti-O bonds in TiO₂ [28].

Fig. 5.6g-i illustrates peaks position of O 1s core levels of 0.1, 0.5, 1 and 2 mol.% of Au, Ag and Cu doped TiO₂ nanoparticles. The peaks position of O 1s core level as Ag and Cu concentration increases, a shift to higher binding energy is noted. Nonetheless, Au concentration increased with a shift to lower binding energy. The O1s peaks of the Au can be fitted into three peaks located at 530.1, 532.3 and 533 eV associated to to O₂⁻ ions in the TiO₂ crystal lattice, hydroxyl groups absorbed on the surface [34]. It is noted that for the 0.5 mol.% Ag and Cu doped, the O1 peaks are very broad in comparison to their counterparts. Such broadness could be due higher amount of point defects in TiO₂.

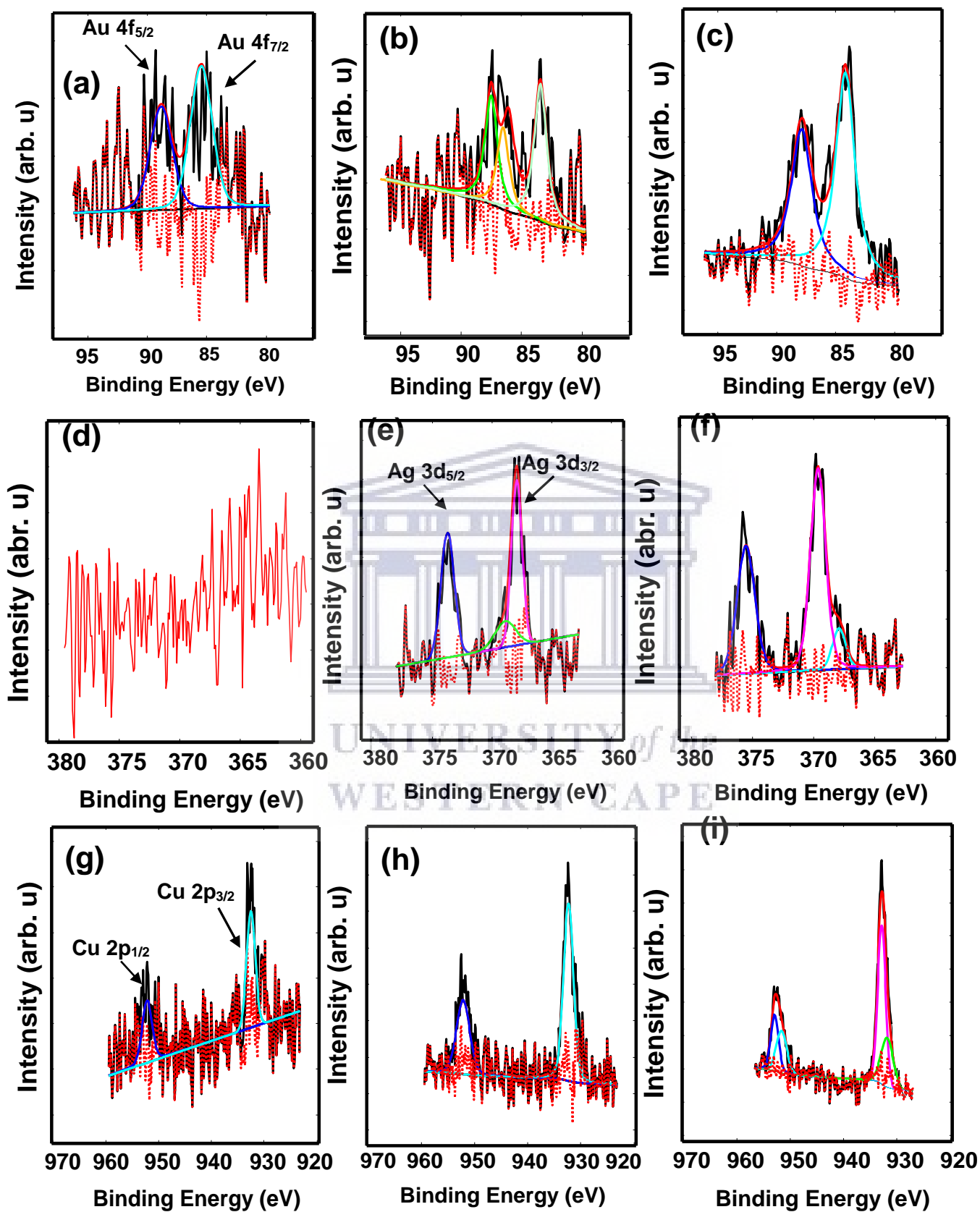


Fig. 5. 5: The XPS analyses of (a-c) 0.1, 0.5 and 2.0 mol.% Au, (d-f) 0.1, 0.5 and 2.0 mol.% Ag and (g-i) 0.1, 0.5 and 2.0 mol.% Cu doped TiO₂ samples.

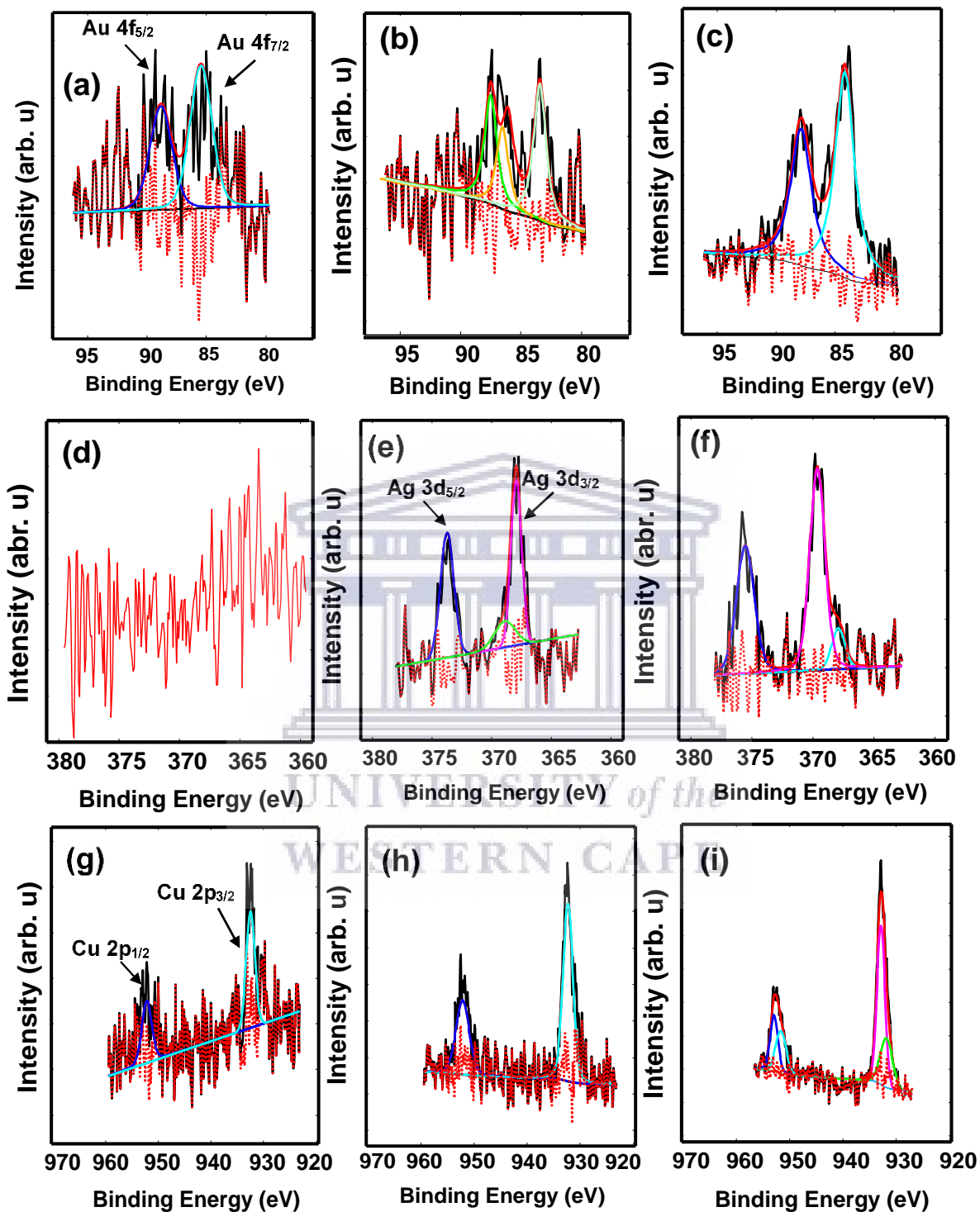


Fig. 5. 6: The XPS O 1s core levels of (a-c) 0.1, 0.5 and 2 mol.% Au, (d-f) 0.1, 0.5 and 2 mol.% Ag and (g-i) 0.1, 0.5 and 2 mol.% Cu doped TiO₂ samples.

5.3.4. Paramagnetic properties of Au, Ag and Cu doped TiO₂ nanoparticles

To investigate the paramagnetic properties of the pure and Au, Ag and Cu doped TiO₂ nanostructures, the EPR studies were performed as demonstrated in Fig. 5.7. The pure TiO₂ displays a single broad resonance peak related to ferromagnetism positioned at the magnetic fields of 100 and 350 mT. Which corresponds to a g-factor of 1.8706, corresponding to Ti³⁺ in rutile as shown in Table 5.2, which summarises all the g-factors and number of spins associated to the material. Upon doping with Au, a small shoulder is observed at 340 mT, and its intensity slightly improves with increased Au doping. Additionally, higher number of spins are witnessed for the 0.5 mol. % Au. By doping TiO₂ with 0.1 mol.% Ag, a signal transforms to sharper peak in comparison to that of the pure TiO₂, where the paramagnetic signal dominates the ferromagnetic signal. Such behaviour may be related to clustering of the metals on the TiO₂ surface. However, at 0.5 and 1 mol.% Ag, a broad signal is further observed, showing the g-values of 1.9582, 2.1084, 2.3826, corresponding to attributed to unpaired electrons trapped in singly ionized, superoxide radical O₂⁻ and associated with Ag²⁺ in TiO₂, respectively [36-38]. At higher doping of 2 mol.%, a sharper peak and hyperfine structures related to Ag are noted. The doped Cu TiO₂ nanoparticles in Fig. 5.7c also display sharper peaks and hyperfine structures that were previously observed for the 2 mol.% Ag.

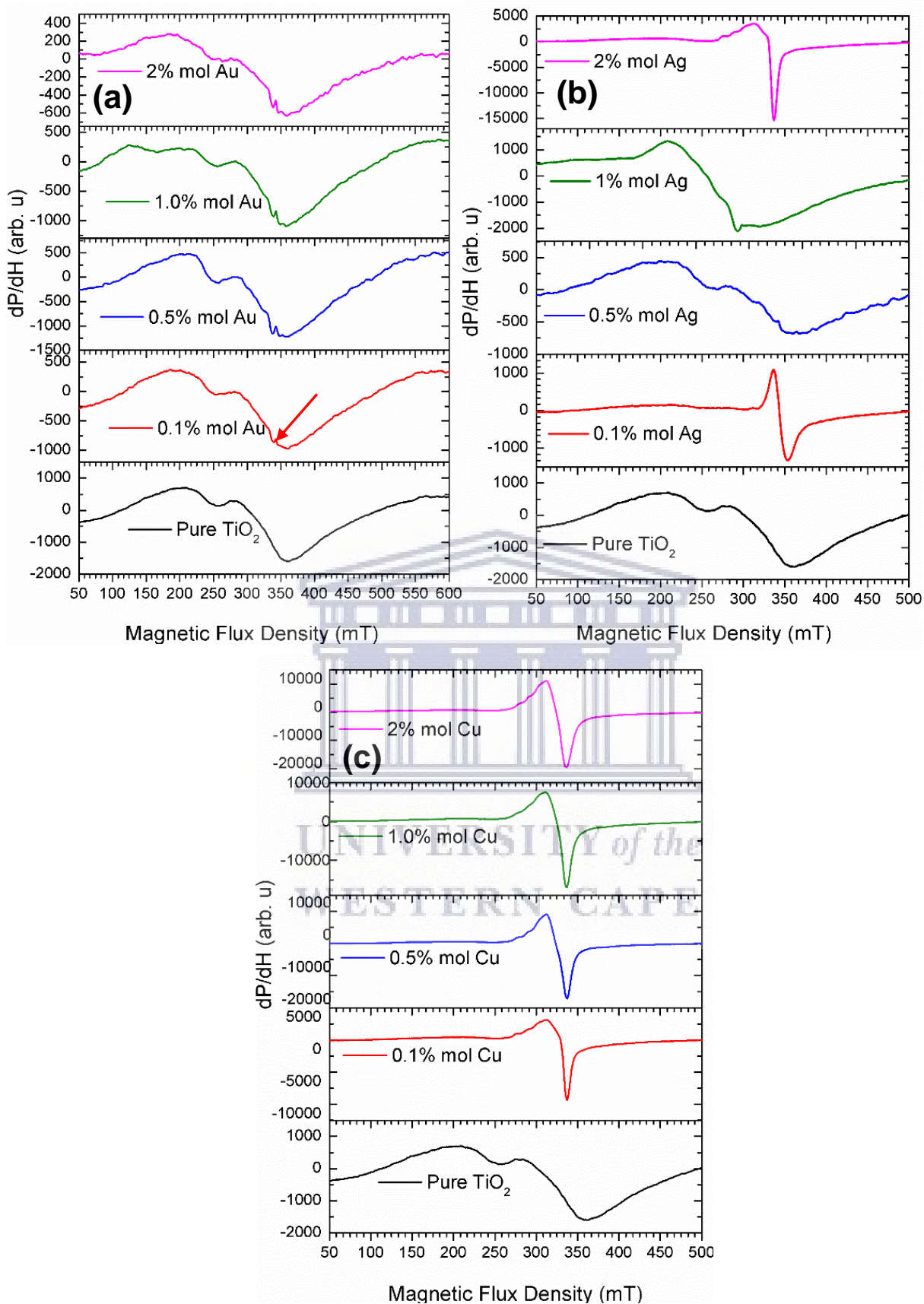


Fig. 5. 7: EPR measurement of TiO₂ doped with various concentration (0.1, 0.5, 1 and 2 mol.%) of (a) Au, (b) Ag and (c) taken at room temperature with microwave power of 5mW.

Table 5. 2: Summary of EPR data related to number of spins, g-factor and assignments of the peaks for the Au, Ag and Cu doped TiO₂ nanoparticles [39-41].

Sample	$N_s \times 10^5$	g-factor	Assigned to
Pure TiO ₂	14.87	1.8706	Surface Ti ³⁺ in colloidal TiO ₂
0.1% mol Au	6.62	2.3842	Associated with Ag ²⁺ in TiO ₂
		1.9595	Ti ³⁺ in rutile
0.5% mol Au	7.55	2.3944	Associated with Ag ²⁺ in TiO ₂
		1.9584	Ti ³⁺ in rutile
1.0% mol Au	7.01	2.3843	Octahedral distortion
		1.9596	Ti ³⁺ in rutile
2.0% mol Au	5.68	2.4412	Associated with Au ²⁺ in TiO ₂
		1.9581	Ti ³⁺ in rutile
0.1% mol Ag	3.5	2.4789	Associated with Ag ²⁺ in TiO ₂
		1.9904	Unpaired electrons trapped in V _o
0.5% mol Ag	8.06	2.3826	Associated with Ag ²⁺ in TiO ₂
		2.1084	superoxide radical O ₂ ⁻
		1.9582	Unpaired electrons trapped in V _o
1% mol Ag	3.1	2.4675	Associated with Ag ²⁺ in TiO ₂
		1.9911	Unpaired electrons trapped in V _o
2% mol Ag	3.7	2.3387	Rhombic distorted
		2.0070	Colloidal anatase TiO ₂
0.1% mol Cu	9.72	2.3390	Cu ²⁺ in octahedral
		2.0070	Colloidal anatase TiO ₂
0.5% mol Cu	2.1	2.4190	Cu ²⁺ in octahedral
		2.3171	Cu ²⁺ in octahedral
		1.9909	Unpaired electrons trapped in V _o
1% mol Cu	1.70	2.4186	Cu ²⁺ in octahedral
		2.3167	Cu ²⁺ in octahedral
		2.0070	Colloidal anatase TiO ₂
2% mol Cu	2.82	2.4303	Cu ²⁺ in octahedral
		2.3276	Cu ²⁺ in octahedral
		1.9986	Unpaired electrons trapped in V _o

5.3.5. Incorporation of Au, Ag and Cu TiO₂ blended in P3HT

3.5.1. Thermo-gravimetric analyses of Au, Ag and Cu doped TiO₂ blended in P3HT

To study the thermal stability and crystallization aspect during thermal processes of the gold, silver and copper TiO₂ blended in P3HT, the TGA profile was carried out from room temperature to 1000 °C (see Fig. 5.8). The TGA graph of P3HT polymer reveals a mass loss of 5% at temperature of 440 °C, which is ascribed to water removal and the last step that display crystallization phase was observed at a mass loss of 70% around temperature of 513 °C. However, upon addition of different concentrations of Au, Ag and Cu doped TiO₂, we observe crystallization phase taking place at a mass loss of 60-50% at temperature range of around 600 °C. The presence of metal oxides doped with TiO₂ enhanced the thermal stability of the P3HT polymer.

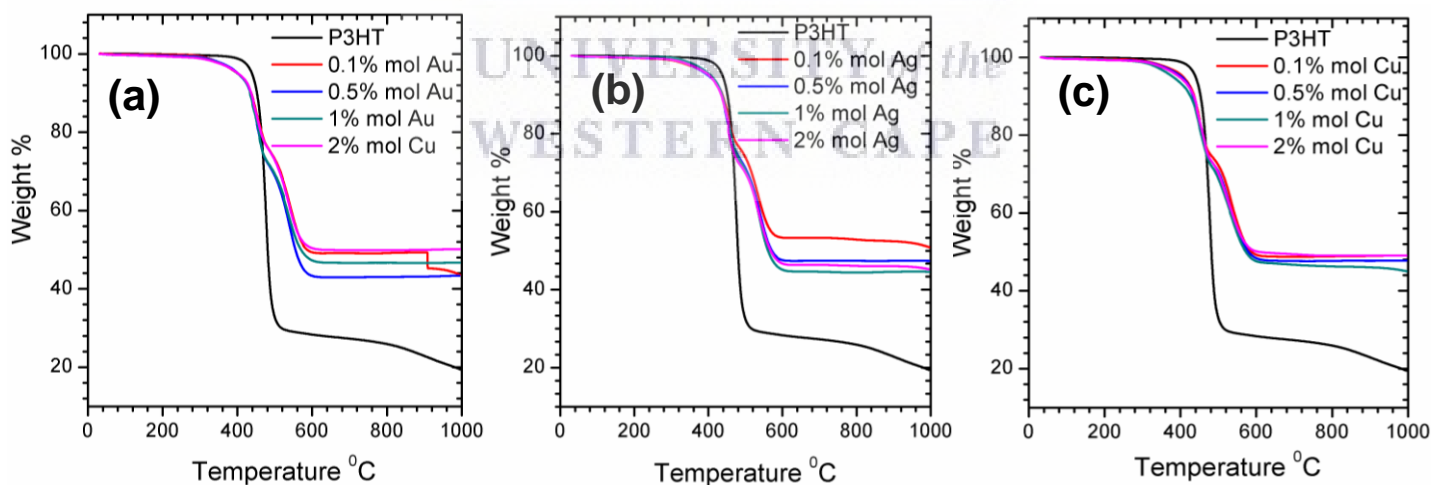


Fig. 5. 8: TGA graphs of Au, Ag, Cu doped TiO₂.

5.3.6. UV-VIS absorbance spectra of Au, Ag and Cu doped TiO₂ blended in P3HT

Fig. 5.9 displays the UV-VIS spectra of P3HT blended with TiO₂ doped with various concentrations of Au, Ag and Cu nanoparticles. For optimization, the TiO₂ with various weight ratios was blended in P3HT as shown in the appendix. From the Figure, the 1:1 wt. ratio display improved absorption. Thus, for P3HT blended with various concentrations of Au, Ag and Cu nanoparticles, the 1:1 wt. ratio was adopted, based on the findings of the P3HT:TiO₂ blend. Nonetheless, in comparison to the P3HT:TiO₂, the P3HT blended with various concentrations of Au, Ag and Cu nanoparticles show pronounced peaks at 520 and 563 nm and one shoulder at 612 nm. The first two bands are associated to the $\pi-\pi^*$ transition, while the shoulder at 612 nm is associated with the inter-chain interactions [42, 43]. The arrow pointed in at around 380 denotes absorption peaks of TiO₂, while the arrow positioned at around 450 nm displays peaks associated to either Au or Ag absorption. Their absorption increases with doping amount. It is evident from Fig. 5.9a that the 0.1 mol.% displays improved absorption for the Au, while for the Ag and Cu doped, the 0.5 mol.% is more dominating in terms of absorption.

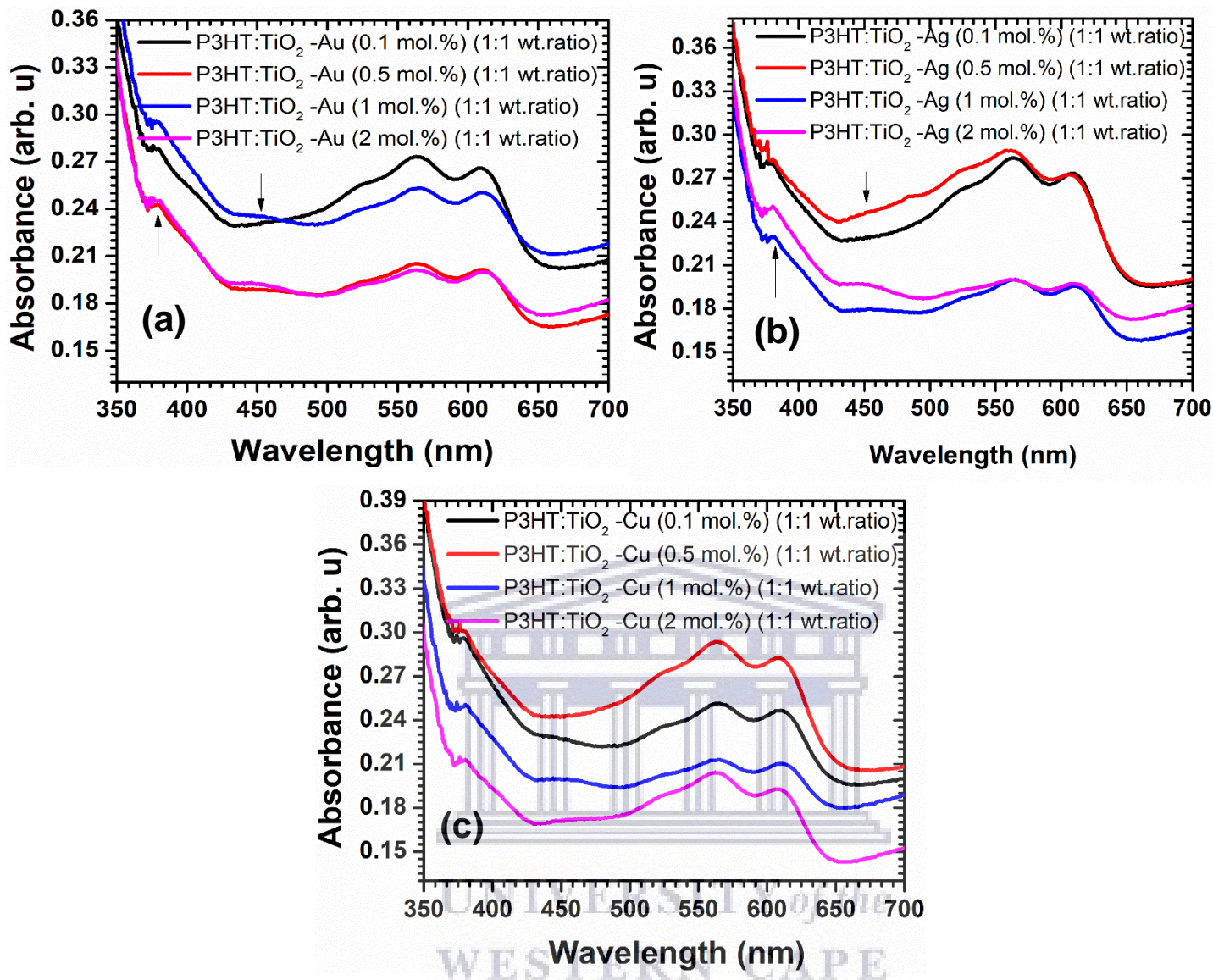


Fig. 5. 9: UV/vis absorbance spectra of (a) P3HT blended with various concentrations of (a) Au, (b) Ag and (c) doped in TiO_2 . The blended materials are prepared in a 1:1 wt. ratio of P3HT: TiO_2 -dopants (i.e Au, Ag and Cu)

3.7. Photovoltaic Solar Cells Devices

Fig 5.10 shows the short current density (J_{sc}), open circuit voltage (V_{oc}) curves of blended P3HT: TiO_2 doped with various concentration of Au, Ag and Cu. As shown in Fig. 5.10 and Table 3, the J_{sc} , V_{oc} of the P3HT: TiO_2 -Au (0.1 mol.%) devices enhanced from 4.01 mA/cm^2 and 0.58 V to 11.08 mA/cm^2 and 0.64 V for P3HT: TiO_2 -

Ag, respectively. While the power conversion efficiency (PCE) increased from 1.15 % for the P3HT:TiO₂-Au to 3.77 % for the P3HT:TiO₂-Ag. Nonetheless, when using the P3HT:TiO₂-Cu, the PCE efficiency increased drastically to about 0.07%. Such decrease could probably due to limited charge transport due possible recombination of charge carriers. More remarkably, upon increasing the loading of the Au (to 0.5 mol.%) in TiO₂ blended in P3HT, the PCE increased to 1.79%, while that of the 0.5 mol.% Ag loaded in TiO₂ increased to the higher PCE of 3.88 %. At higher doping concentration of 2 mol.% in TiO₂, blended in P3HT, the PCE reduced drastically in comparison to that of 0.5 mol.% as depicted in Table 5.3.

To comprehend the reason behind the improved PCE with increased doping of metals in TiO₂ blended in P3HT, the series resistance (R_s) and shunt resistance (R_{sh}) were estimated by fitting the J–V plots as recorded in Table 5.3 [44, 45]. The 0.5 mol.% Ag doped TiO₂ blended in P3HT displayed higher R_{sh} and smaller R_s in contrast to other solar cells [46, 47]. This could be justified by enhanced hole transport to the molybdenum oxide layer and reduced the carrier recombination in the absorption layer. It is further clear in Table 5.3 that the J_{sc} and V_{oc} are dependent on the metal doping and the content of the doping. This is due to the fact that both the J_{sc} , V_{oc} increase with particular doping level, more especially that of 0.5 mol.% Ag. It is well known that the V_{oc} is one of the main aspects towards facilitating improved PCE of the solar cells.

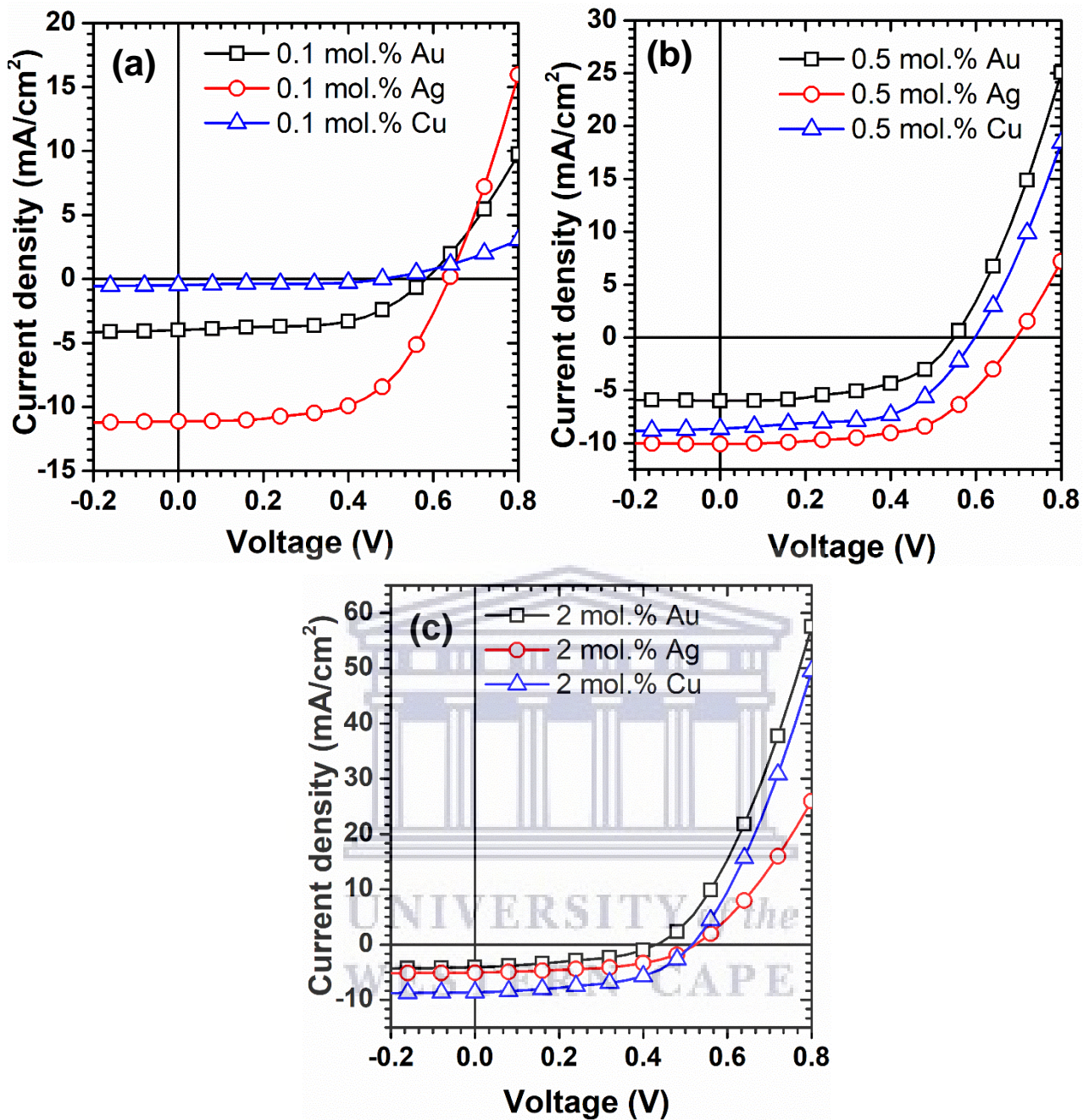


Fig. 5. 10: J-V curves of the doped TiO₂ blended in P3HT solar cells. (a) 0.1 mol.%, (b) 0.5 mol.% and (c) 2 mol.%.

We further compared the V_{oc} with the PCE and we found that for the Au doped TiO₂, the PCE is not dependent on the V_{oc} as depicted in Fig. 5.11. While for the Cu and Ag doped TiO₂, the PCE is highly dependent of the V_{oc} , as result, higher PCE was

observed. In over all, it was noted that the Ag doped possessed remarkable V_{oc} of 0.69 V, which result to higher efficiency of 3.88%.

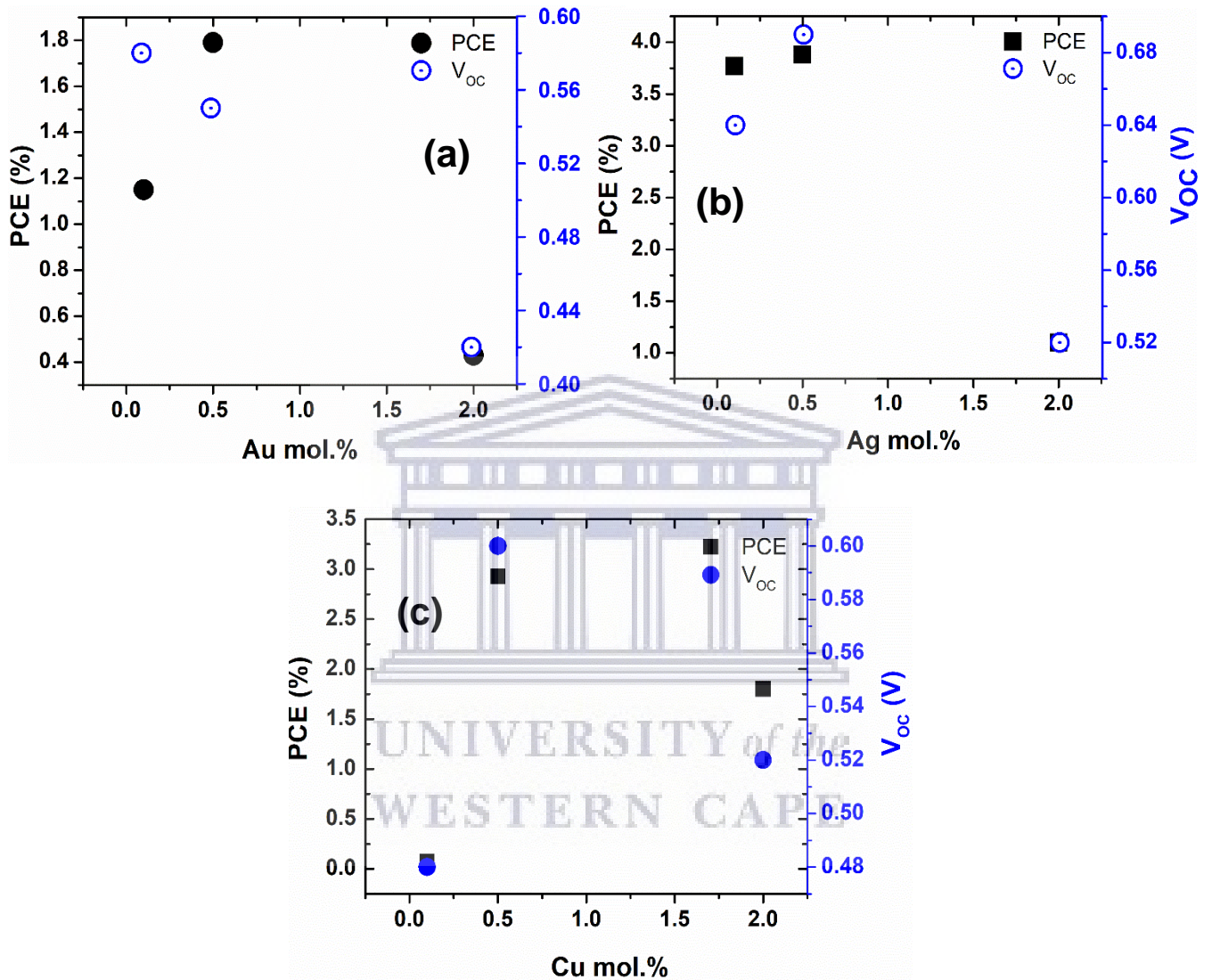


Fig. 5. 11: PCE and V_{oc} as a function of doping level of metals in TiO_2 blended in P3HT solar cells.

According to previous studies, the observed superior V_{oc} of the non-fullerene based solar cells devices in Fig. 5.11 and Table 5.3 is due to the existence of inferior interfacial traps in active layer. From our XPS and EPR results, we observed that the doping of Ag in TiO_2 surface for instance led to transformation of Ti^{3+} from Ti^{4+} ions,

producing oxygen vacancies (V_o). Commonly, the V_o behaves as both as shallow and deep trap states. Thus, studies have pointed out that the inherent features of shallow and deep trap states and their influence on the solar cells performance [48]. The shallow trap states activate the charge carriers' diffusion to the surface; while the deep trap states enhance the charge carriers' recombination [49]. The improved in Ag_x-TiO_2 light absorption was witnessed by Fakharan et al. [49], because of the increased content of Ag loading, induced by higher formation of V_o . As a result, from the UV-vis absorption spectra in Fig. 5.9b, the 0.5 mol.% Ag demonstrated enhanced absorption properties in comparison to its counterparts. As a result, the superior V_{oc} of 0.69 V for 0.5 mol.% Ag doped TiO_2 blended in P3HT solar cells support the positive influence of the plasmonic nanoparticles on the generation of exciton, dissociation of exciton and charge transport in active layers. This accomplished superior V_{oc} is linked to the enhanced ratio of shallow to deep traps of 0.5 mol.% Ag doped TiO_2 nanoparticles, motivating the carriers' diffusion to the surfaces and obstructing charge carrier recombination.

UNIVERSITY of the
WESTERN CAPE

Table 5. 3: Summary of the solar cells parameters.

Films		J _{sc} (mA/cm ²)	V _{oc} (V)	FF	R _s (Ωcm ²)	R _{sh} (Ω cm ²)	PCE (%)
0.1 mol. %	P3HT:TiO ₂ -Au	4.01	0.58	0.49	13.29	201.76	1.15 (0.38)*
	P3HT:TiO ₂ -Ag	11.08	0.64	0.53	6.54	134.04	3.77 (3.68)
	P3HT:TiO ₂ -Cu	0.43	0.48	0.33	15.66	28.45	0.07 (0.03)
0.5 mol. %	P3HT:TiO ₂ -Au	5.99	0.55	0.52	23.38	242.70	1.79(1.58)
	P3HT:TiO ₂ -Ag	10.08	0.69	0.56	11.44	266.40	3.88 (3.78)
	P3HT:TiO ₂ -Cu	8.64	0.60	0.57	11.73	168.96	2.93 (2.81)
2 mol. %	P3HT:TiO ₂ -Au	4.20	0.43	0.24	13.06	181.96	0.43(0.25)
	P3HT:TiO ₂ -Ag	5.03	0.52	0.43	4.33	99.92	1.10(0.88)
	P3HT:TiO ₂ -Cu	8.60	0.52	0.40	6.08	88.85	1.80 (1.44)

Note: the values in parentheses stand for the average efficiency extracted from over 3 solar cell devices.

5.4. CONCLUSION

In summary, we have synthesised undoped and Au, Ag and Cu doped TiO₂ nanoparticles using hydrothermal method and incorporated into P3HT matrix as to form a blend. The XRD showed that the peaks of the TiO₂ shift when the Au, Ag and Cu were inserted. The HR-TEM micrographs showed the Au, Ag and Cu inserted in the TiO₂ surface. The paramagnetic and XPS studies showed that incorporation of Au, Ag and Cu led to a formation V_O, which could be very beneficial for solar cells performance. EPR signals also transformed based on the doping level, which could

probably be due clustering of the metals on the TiO₂ surface. The solar cell performance and V_{OC} were dependent on the doping content and the level, showing higher efficiency performance and superior V_{OC} of 3.88% and 0.69 V, respectively for the 0.5 mol.% Ag doped TiO₂ blended in P3HT. Furthermore, the 0.5 mol.% Ag doped TiO₂ blended in P3HT displayed an internal series resistance (R_s) and shunt resistance (R_{sh}) values of 11.44 and 266.40 Ω cm², respectively.



REFERENCES

1. Bavel, S.S.V., Sourty, E., With, G.D. and Loos, J., 2008. Three-dimensional nanoscale organization of bulk heterojunction polymer solar cells. *Nano letters*, 9(2), pp.507-513.
2. Wu, J.L., Chen, F.C., Hsiao, Y.S., Chien, F.C., Chen, P., Kuo, C.H., Huang, M.H. and Hsu, C.S., 2011. Surface plasmonic effects of metallic nanoparticles on the performance of polymer bulk heterojunction solar cells. *ACS nano*, 5(2), pp.959-967.
3. Kim, K., Liu, J., Namboothiry, M.A. and Carroll, D.L., 2007. Roles of donor and acceptor nanodomains in 6% efficient thermally annealed polymer photovoltaics. *Applied Physics Letters*, 90(16), p.163511.
4. Moulé, A.J. and Meerholz, K., 2008. Controlling morphology in polymer–fullerene mixtures. *Advanced Materials*, 20(2), pp.240-245.
5. Green, M.A., Emery, K., Hishikawa, Y., Warta, W. and Dunlop, E.D. 2012, *Prog. Photovolt: Res. Appl.* 20, pp.12.
6. Hu, H., Jiang, K., Yang, G., Liu, J., Li, Z., Lin, H., Liu, Y., Zhao, J., Zhang, J., Huang, F. and Qu, Y., 2015. Terthiophene-based D–A polymer with an asymmetric arrangement of alkyl chains that enables efficient polymer solar cells. *Journal of the American Chemical Society*, 137(44), pp.14149-14157.
7. Pereira, M.S., Lima, F.A.S., Ribeiro, T.S., da Silva, M.R., Almeida, R.Q., Barros, E.B. and Vasconcelos, I.F., 2017. Application of Fe-doped SnO₂ nanoparticles in organic solar cells with enhanced stability. *Optical Materials*, 64, pp.548-556.
8. Guo, X., Zhou, N., Lou, S.J., Smith, J., Tice, D.B., Hennek, J.W., Ortiz, R.P., Navarrete, J.T.L., Li, S., Strzalka, J. and Chen, L.X., 2013. Polymer solar cells with enhanced fill factors. *Nature Photonics*, 7(10), pp. 825–833.
9. Huang, F., Chen, K.S., Yip, H.L., Hau, S.K., Acton, O., Zhang, Y., Luo, J. and Jen, A.K.Y., 2009. Development of new conjugated polymers with donor– π -bridge– acceptor side chains for high performance solar cells. *Journal of the American Chemical Society*, 131(39), pp.13886-13887.
10. Wang, M., Hu, X., Liu, P., Li, W., Gong, X., Huang, F. and Cao, Y., 2011. Donor–acceptor conjugated polymer based on naphtho [1, 2-c: 5, 6-c] bis [1, 2, 5] thiadiazole for high-performance polymer solar cells. *Journal of the American Chemical Society*, 133(25), pp.9638-9641.
11. Liu, D., Yang, J. and Kelly, T.L., 2014. Compact layer free perovskite solar cells with 13.5% efficiency. *Journal of the American Chemical Society*, 136(49), pp.17116-17122.
12. Talapin, D.V., Lee, J.S., Kovalenko, M.V. and Shevchenko, E.V., 2009. Prospects of colloidal nanocrystals for electronic and optoelectronic applications. *Chemical reviews*, 110(1), pp.389-458.
13. Zuo, L., Gu, Z., Ye, T., Fu, W., Wu, G., Li, H. and Chen, H., 2015. Enhanced photovoltaic performance of CH₃NH₃PbI₃ perovskite solar cells through interfacial engineering using self-assembling monolayer. *Journal of the American Chemical Society*, 137(7), pp.2674-2679.
14. Kim, B.H., Nam, S., Oh, N., Cho, S.Y., Yu, K.J., Lee, C.H., Zhang, J., Deshpande, K., Trefonas, P., Kim, J.H. and Lee, J., 2016. Multilayer transfer printing for pixelated, multicolor quantum dot light-emitting diodes. *ACS nano*, 10(5), pp.4920-4925.

15. Bilgaiyan, A., Dixit, T., Palani, I.A. and Singh, V., 2017. Performance improvement of ZnO/P3HT hybrid UV photo-detector by interfacial Au nanolayer. *Physica E: Low-dimensional Systems and Nanostructures*, 86, pp.136-141.
16. Oseni, S.O. and Mola, G.T., 2019. Bimetallic nanocomposites and the performance of inverted organic solar cell. *Composites Part B: Engineering*, 172, pp.660-665.
17. Gao, M., Zhu, L., Peh, C.K. and Ho, G.W., 2019. Solar absorber material and system designs for photothermal water vaporization towards clean water and energy production. *Energy & Environmental Science*, 12(3), pp.841-864.
18. Putnin, T., Lertvachirapaiboon, C., Ishikawa, R., Shinbo, K., Kato, K., Ekgasit, S., Ounnunkad, K. and Baba, A., 2019. Enhanced organic solar cell performance: Multiple surface plasmon resonance and incorporation of silver nanodisks into a grating-structure electrode. *Opto-Electronic Advances*, 2(07), p.190010.
19. Yao, K., Zhong, H., Liu, Z., Xiong, M., Leng, S., Zhang, J., Xu, Y.X., Wang, W., Zhou, L., Huang, H. and Jen, A.K.Y., 2019. Plasmonic Metal Nanoparticles with Core-Shell Structure for High-Performance Organic and Perovskite Solar Cells. *ACS nano*, 13, 5, pp.5397–5409
20. Shabaninezhad, M., Abuhagr, A., Sakthivel, N.A., Kumara, C., Dass, A., Kwak, K., Pyo, K., Lee, D. and Ramakrishna, G., 2019. Ultrafast Electron Dynamics in Thiolate-Protected Plasmonic Gold Clusters: Size and Ligand Effect. *The Journal of Physical Chemistry C*. 123, 21, pp.13344–13353.
21. Kuriakose, A.C., Nampoore, V.P.N. and Thomas, S., 2019. Facile synthesis of Au/CdS core-shell nanocomposites using laser ablation technique. *Materials Science in Semiconductor Processing*, 101, pp.124-130.
22. Paul, Kamal Kumar, P. K. Giri, H. Sugimoto, Minoru Fujii, and Biswajit Choudhury., 2019. Evidence for plasmonic hot electron injection induced superior visible light photocatalysis by g-C₃N₄ nanosheets decorated with Ag–TiO₂ (B) and Au–TiO₂ (B) nanorods. *Solar Energy Materials and Solar Cells* 201, pp.110053.
23. Fakharan, Z. and Naji, L., 2017. Fabrication of non-fullerene P3HT/Agx-TiO₂ based polymer solar cells with high open circuit voltage. *Journal of Alloys and Compounds*, 708, pp.1184-1194.
24. Fiorenza, R., Bellardita, M., Scirè, S. and Palmisano, L., 2018. Effect of the addition of different doping agents on visible light activity of porous TiO₂ photocatalysts. *Molecular Catalysis*, 455, pp.108-120.
25. Zhu, S., Liang, S., Gu, Q., Xie, L., Wang, J., Ding, Z. and Liu, P., 2012. Effect of Au supported TiO₂ with dominant exposed {001} facets on the visible-light photocatalytic activity. *Applied Catalysis B: Environmental*, 119, pp.146-155.
26. Yin, Y., Liu, E., Li, H., Wan, J., Fan, J., Hu, X., Li, J., Tang, C. and Pu, C., 2016. Fabrication of plasmonic Au/TiO₂ nanotube arrays with enhanced photoelectrocatalytic activities. *Ceramics International*, 42(8), pp.9387-9395.
27. Jasmina, J.-P., Miserque, F., Dumas E., Vickridge, I., Ganem, J.-J., Cannizzo, C., Chausséa, A., 2017. XPS and NRA investigations during the fabrication of gold nanostructured functionalized screen-printed sensors for the detection of metallic pollutants. *Applied Surface Science*, pp.159-166.
28. Tshabalala, Z.P., Motaung, D.E., Swart, H.C., 2018. Structural transformation and

enhanced gas sensing characteristics of TiO₂ nanostructures induced by annealing, *Physica B: Condensed Matter*, 535, 227-231

29. Naik, G.K., Majhi, S.M., Jeong, K.U., Lee, I.H. and Yu, Y.T., 2019. Nitrogen doping on the core-shell structured Au@ TiO₂ nanoparticles and its enhanced photocatalytic hydrogen evolution under visible light irradiation. *Journal of Alloys and Compounds*, 771, pp.505-512.
30. Dong, P., Yang, F., Cheng, X., Huang, Z., Nie, X., Xiao, Y. and Zhang, X., 2019. Plasmon enhanced photocatalytic and antimicrobial activities of Ag-TiO₂ nanocomposites under visible light irradiation prepared by DBD cold plasma treatment. *Materials Science and Engineering: C*, 96, pp.197-204.
31. Hu, H., Jiang, K., Yang, G., Liu, J., Li, Z., Lin, H., Liu, Y., Zhao, J., Zhang, J., Huang, F. and Qu, Y., 2015. Terthiophene-based D–A polymer with an asymmetric arrangement of alkyl chains that enables efficient polymer solar cells. *Journal of the American Chemical Society*, 137(44), pp.14149-14157.
32. Tshabalala, Z.P., Shingange, K., Cummings, F.R., Ntwaeaborwa, O.M., Mhlongo, G.H., Motaung, D.E., 2017. Ultra-sensitive and selective NH₃ room temperature gas sensing induced by manganese-doped titanium dioxide nanoparticles. *Journal of colloid and interface science*, 504, pp.371-386.
33. Monga, A., Bathla, A. and Pal, B., 2017. A Cu-Au bimetallic co-catalysis for the improved photocatalytic activity of TiO₂ under visible light radiation. *Solar Energy*, 155, pp.1403-1410.
34. Tshabalala, Z.P., Mokoena, T.P., Jozela, M., Tshilongo, J., Hillie, T.K., Swart, H.C. and Motaung, D.E., 2020. TiO₂ Nanowires for Humidity-Stable Gas Sensors for Toluene and Xylene. *ACS Applied Nano Materials*, 4 (1), 702–716.
35. Motsoeneng, R.G., 2019. Detailed Investigation on the Correlation Between Magnetization and Sensing Properties of the n-Type (SnO₂) and p-Type (NiO) and Mixed Oxides Heterostructures. University of Johannesburg (South Africa).
36. Liu, J.; Dai, M.; Wang, T.; Sun, P.; Liang, X.; Lu, G.; Shimanoe, K.; Yamazoe, N. 2016. Enhanced Gas Sensing Properties of SnO₂ Hollow Spheres Decorated with CeO₂ Nanoparticles Heterostructure Composite Materials. *ACS Appl. Mater. Interfaces*, 8, 6669– 6677.
37. Chetri, P.; Choudhury, B.; Choudhury, A. 2014. Room Temperature Ferromagnetism in SnO₂ Nanoparticles: An Experimental and Density Functional Study. *J. Mater. Chem. C*, 2, pp.9294–9302.
38. Acciarri, M.; Canevali, C.; Mari, C. M.; Mattoni, M.; Ruffo, R.; Scotti, R.; Morazzoni, F.; Barreca, D.; Armelao, L.; Tondello, E.; Bontempi, E.; Depero, L.E., 2003. Nanocrystalline SnO₂-Based Thin Films Obtained by Sol–Gel Route: A Morphological and Structural Investigation. *Chem. Mater.* 15, pp.2646–2650.
39. Kumar, C.P., Gopal, N.O., Wang, T.C., Wong, M.S. and Ke, S.C., 2006. EPR investigation of TiO₂ nanoparticles with temperature-dependent properties. *The Journal of Physical Chemistry B*, 110(11), pp.5223-5229.
40. Misra, S.K., Andronenko, S.I., Tipikin, D., Freed, J.H., Somani, V. and Prakash, O., 2016. Study of paramagnetic defect centers in as-grown and annealed TiO₂ anatase and rutile nanoparticles by a variable-temperature X-band and high-frequency (236 GHz) EPR. *Journal of magnetism and magnetic materials*, 401, pp.495-505.

41. Micic, O. I.; Zhang, Y.; Cromack, K. R.; Trifunac, A. D.; Thurnauer, M. C. J. Trapped holes on titania colloids studied by electron paramagnetic resonance. *Phys. Chem.* 1993, 97, pp. 7277–7283.
42. Motaung, D.E., Malgas, G.F., Nkosi, S.S., Mhlongo, G.H., Mwakikunga, B.W., Malwela, T., Arendse, C.J., Muller, T.F. and Cummings, F.R., 2013. Comparative study: the effect of annealing conditions on the properties of P3HT: PCBM blends. *Journal of materials Science*, 48(4), pp.1763-1778.
43. Motaung, D.E., Malgas, G.F., Arendse, C.J. and Mavundla, S.E., 2012. Determination of the structure, morphology and complex refractive index in ZnO-nanopencils/P3HT hybrid structures. *Materials Chemistry and Physics*, 135(2-3), pp.401-410.
44. Kim, M.S., Kim, B.G. and Kim, J., 2009. Effective variables to control the fill factor of organic photovoltaic cells. *ACS applied materials & interfaces*, 1(6), pp.1264-1269.
45. Pysch, D., Mette, A. and Glunz, S.W., 2007. A review and comparison of different methods to determine the series resistance of solar cells. *Solar Energy Materials and Solar Cells*, 91(18), pp.1698-1706.
46. Huang, H.L., Lee, C.T. and Lee, H.Y., 2015. Performance improvement mechanisms of P3HT: PCBM inverted polymer solar cells using extra PCBM and extra P3HT interfacial layers. *Organic Electronics*, 21, pp.126-131.
47. Das, S., Choi, J.Y. and Alford, T.L., 2015. P3HT: PC61BM based solar cells employing solution processed copper iodide as the hole transport layer. *Solar Energy Materials and Solar Cells*, 133, pp.255-259.
48. Wang, Q., Zhang, Z., Zakeeruddin, S.M. and Graetzel, M., 2008. Enhancement of the performance of dye-sensitized solar cell by formation of shallow transport levels under visible light illumination. *The Journal of Physical Chemistry C*, 112(17), pp.7084-7092.
49. Fakharan, Z., Naji, L., 2017. Fabrication of non-fullerene P3HT/Agx-TiO₂ based polymer solar cells with high open circuit voltage. *J. Alloys and Compds*, 708, pp.1184-1194.

UNIVERSITY OF
WESTERN CAPE

CHAPTER SIX

Fabrication of P-type Bimetallic Ag/Cu doped TiO₂ Nanoparticles for Dual Application for Selective Detection of Xylene Vapour and Their use in Organic Solar as Non-Fullerene

6.1. INTRODUCTION

The world today is facing serious health risks from global warming due to air pollutants such as carbon dioxide (CO₂) and hydrocarbons like benzene, toluene, xylene (BTX) gases emitted from industries and auto motive vehicles [1, 2]. These pollutants, if inhaled in high concentration cause neurotoxicity that result in fatality [1, 2]. Thus, timely detection of such pollutants is of immense important and requires gas-sensing devices that regulate air quality in industrial emission and combustible developments. The fundamental characteristics of gas sensors are better sensitivity and selectivity for specific type of gases which providing short response-recovery time at low temperature for early detection of gases to prevent fatality [3].

Amongst the semiconductor metal oxide (SMO), n-type titanium dioxide (TiO₂) possessing a wide optical band gap of ~3.6 eV at 300 K has attracted significant attention for possible commercial gas sensor applications, due to its superior sensitivity, low-cost, and low toxicity [4]. Nonetheless, the shortcomings of the pristine TiO₂ have fundamentally restricted their real-world applications in the market because of their limited selectivity and tall operational temperature. Studies have shown that doping of TiO₂ with noble metals (e.g. Pt, Au, Pd and Ag) or transitional metals (Cu, Zn, etc.) enhances the sensing characteristics, since they can regulate the morphology, enable surface reactions, transforms the space charge distribution,

and hence, advanced the gas sensing characteristics [5- 8]. Amongst the noble metals, Ag has appealed much attention for being considered as a perfect candidate for commercial purpose, because of its low cost.

Amongst different volatile organic compounds (VOCs), benzene, toluene, ethylene-benzene and xylene (BTEX) are exceedingly cancer-causing inherent features [9]. Since BTEX are natural components of coal and crude oil, they are released to air via vehicles exhaust and various industrial developments, such as paints, cosmetics, glue, etc. [10]. In risky situations, BTEX breath, oral intake and/or skin absorption could influence nervous and blood manufacture system [9, 10]. Furthermore, BTEX monitoring and detection could be profitable for agricultural since they are released from orange at various phases of maturity (or ripening) [11]. Therefore, appropriate and selective detection of BTEX vapours, predominantly in minimal concentrations, is very vital and efficient farming with capable conveyance and storage may be realized.

Up to now, the organic solar cells power conversion efficiencies (PCEs) have surpassed 14% in single junction cells [12-14]. While more than 17% of PCE in tandem solar cells have been realized [15], which is mostly attributed to the prompt advance of chemically tailored, vastly absorbing donor polymers and non-fullerene acceptors with improved optoelectronic features. Nevertheless, these pleasing findings are mostly established on expensive donor-acceptor copolymer, in comparison to the low cost synthesis state of the art poly(3-hexylthiophene) (P3HT) [16-18]. With respect to the non-fullerene acceptor in P3HT, studies have used TiO₂, replacing the fullerene derivative [6, 6]-phenyl-C₆₁-butyric acid (PCBM) [19]

However, due to its wide band gap and inability to harvest light in the visible region the use of metals, non-metals or co-doping of TiO₂ were reported by many researchers to enhance the visible light activity in the photovoltaic cells [20]. The use of monometallic nanostructure doping in the lattice of TiO₂ were reported by many, which included the likes of Abdel-Wahab et al. [21] that the rate of electron-hole recombination can be slowed down by electron trapping of Ag nanoparticles, which was ascribed to localized surface plasmon resonance (LSPR). Strong near field caused by LSPR that surround the Au nanoparticles to enhance the light absorption has been reported [22]. Hernandez et al. [23] made a comparative study of Cu doped TiO₂ to act as charge carrier traps in order to reduce recombination effect. While enhancement of electromagnetic field at the interface by Ag doped TiO₂ limit the process of recombination rate. Whereas, the presence of Eu dopant suppressed TiO₂ nanoparticles growth.

Further studies have been reported in the use of bimetallic nanostructure doping in the TiO₂ matrix, which exhibit better properties attributed to their interaction over their monometallic counterparts and were found useful in many applications. Their interaction not only displayed the properties related with the two individual metals but also brought in new properties owing to their cooperation [24]. Gao et al. [25] displayed a transformed morphology of mixed layer of Au:Ag having both small and large nanoparticles with a broader LSPR band compared to the Au counterpart, Whereas the Ag counterpart has lower fill factor, which limits its PCE compared to the mixed Au:Ag layer. Therefore, herein we report on the low temperature gas sensing characteristics of a p-type bimetallic Ag/Cu TiO₂ nanoparticles based sensor for detection of xylene vapour at a low operating temperature. We demonstrate that by increasing the loading of Cu and Ag, the material transforms from an n-type to a

p-type, which resulted to an improved xylene sensing performance. We further reveal the influence of LSPR in non-fullerene bulk heterojunction (BHJ) organic solar cells by infiltrating bimetallic Ag/Cu doped TiO₂ nanoparticles into the P3HT: ZnO layer. At a lower loading doping the bimetallic Ag/Cu in TiO₂ nanoparticles acted as an electron acceptor material in the fabrication of the BHJ, displaying a lower PCE, while at higher doping it acted as a donor, which illustrated an enhanced short circuit current density, superior open circuit voltage, and thus improved efficiency.

6.2. EXPERIMENTAL PROCEDURE

6.2.1 Materials

All chemicals, P3HT regioregular, copper nitrate, silver nitrate (≥ 99.0), TiO₂ P25 Degussa, indium tin oxide (ITO) coated glass on a 1 mm glass substrate (resistivity of 8-12 Ωsq^{-1} and transmittance $\geq 83\%$), 1, 2-Dichlorobenzene solution (purity 99.9%), sodium hydroxide (NaOH, purity 99%) were purchased from Sigma-Aldrich.

6.2.2. Synthesis of TiO₂ and ZnO nanoparticles

Synthesis of TiO₂ was done by dissolving about 2g of TiO₂ P25 Degussa in 100 ml distilled water and stirred for 2 h to achieve homogenous mixture. Then, a pH of 8 was maintained using an appropriate amount of NaOH solution. As for the ZnO nanoparticles, a precursor of zinc acetate dehydrate ($\text{Zn}(\text{CH}_3\text{COO})_2 \cdot 2\text{H}_2\text{O}$) was dissolved in distilled water and stirred for 2h. Then, an appropriate amount of NaOH was used to maintain the pH at 8. After stirring, both solutions were added into two separate Aton Parr autoclaves and heated at 200 °C for 12 h. After the autoclave reaction, the solutions were cooled down to room temperature, the precipitates were

collected and washed several times with distilled water and then dried at 90 °C for 15 h. The final products were calcined at 250 °C in air for 2 h.

6.2.3. Synthesis of bimetallic Ag/Cu doped TiO₂ nanoparticles

The bimetallic Ag/Cu doped TiO₂ nanoparticles were synthesized by dissolving an appropriate amount of TiO₂ P25 Degussa and different ratio of mixed 0.1 and 0.5 mol.% interchangeable of Ag and Cu nanoparticles and dissolved in 100 ml of distilled water and stirred for 2 h to achieve homogenous solution. Then, 0.5 M NaOH was added in the solution to reach a pH of 8 and continued stirring to a total of 5 h. The solutions were added in a Teflon liner made to fit inside the stainless steel pressure vessel for 12 h at 200°C. Before washing the solutions, they were permitted to cool to 25 °C. Then, the filtrates were thoroughly washed with distilled water to eliminate impurities. Final products were dried at 90 °C for 12 h, then calcined at 250 °C in air for 2 h.

6.2.4. Characterization

The X-ray diffraction (Panalytical XPERT PRO PW 3040/60) equipped with a Cu monochromatic radiation source was used to analyse the structures. The surface morphology was determined using the Auriga Zeiss scanning electron microscopy (Zeiss). The internal structure was probed using the JEOL, 2100 transmission electron microscopy (TEM) operated at 200 keV. The optical characteristics were probed using a UV-VIS Perkin Elmer Lambda 750 and Nanolog photoluminescence (PL) spectrometer (Jobin Yvon, Horiba). The surface area and N₂ adsorption/desorption isotherms were probed using a Brunauer-Emmett-Teller (BET)

(Micromeritics TRISTAR 3000). A PHI 5000Versaprobe-Scanning ESCA Microprobe was used to carry out X-ray photo-electron spectroscopy (XPS) analyses.

6.2.5. Fabrication of Photovoltaic Devices and Characterization

The organic solar cell devices were constructed based on the following configuration: ITO/PEDOT: PSS- buffer layer/P3HT:TiO₂ (or Cu/Ag doped TiO₂) active layer/ZnO/MoO₃ hole transporting layer/Al. Before the deposition, ITO substrates were washed carefully in organic solvents and dried using a pure nitrogen gas (purity, 99.99%). A buffer layer (PEDOT:PSS) with a thickness of roughly 50 nm was spin-coated onto the ITO substrate at 2500 rpm for 30 s and annealed at 100 °C for 1 h. Then, active layers fabricated from 0.1 mol. % Cu/Ag, 0.5 mol. % Cu/Ag, 0.1 mol. % Cu/0.5 mol.% Ag, 0.5 mol. %Cu/0.1 mol.% Ag doped TiO₂ nanostructures were mixed with P3HT:ZnO and dissolved in 1,2 dichlorobenzene in an enhanced wt. ratio of 1:1:1 ternary structure and spin-coated on top of the PEDOT:PSS layer. It basically consisted out of four types of Ag/Cu- TiO₂ nanoparticles with different Ag and Cu contents. At higher Ag/Cu loading in TiO₂, the structure transformed to p-type, while at lower Ag/Cu loading, it remained as an n-type, which was used as an electron donor and acceptor, respectively in fabrication of the BHJ P3HT: ZnO devices. The developed films were subsequently annealed at 150 °C for 15 min to improve the polymer blends ordering. The hole transport layer containing molybdenum oxide (MoO₃) onto the photoactive layer was deposited using an ATC Orion 8-T sputtering system (AJA international INC, USA). Finally, an Al electrode was evaporated on the top of the MoO₃ layer using a shadow mask, causing an active area of 0.15 cm². Current density-voltage (I–V) analyses were carried out using a Keithley 4200 (USA) source measurement unit using Newport solar simulator

at 100 mW/cm² (AM 1.5 G) irradiation. For reproducibility, three devices were measured.

6.2.6. Fabrication of Gas Sensor Devices and Characterization

The fabrication of TiO₂ gas sensors were done according to ref. [26]. Pure TiO₂ and bimetallic nanostructures were rinsed and ultrasonically dispersed in ethanol (Analytical Reagent) to attain a 2.5 mol/L TiO₂ suspension. The suspension was sonicated for 30 min to achieve a uniform paste or slurry. The paste was carefully coated onto platinum (Pt) inter digital pattern designed in an area on an alumina substrate. The sensor resistance was measured by using a KSGAS6S KENOSISTEC gas testing station. The fabricated sensors were placed in an airtight chamber and exposed to several volatile organic compounds (VOCs), such as benzene, ethylene-benzene, toluene, xylene (BTEX), and acetone. The analyses were carried at various operating temperatures, ranging from 25, 100 and 150 °C.

6.3. RESULTS AND DISCUSSION

6.3.1. Structural properties and surface morphology

6.3.1.1. Incorporation of bimetallic of Cu and Ag nanoparticles doped TiO₂

Fig. 6.1 displays the XRD patterns of the bimetallic Ag/Cu doped TiO₂ nanoparticles. As seen in Fig. 6.1, upon adding 0.1 mol.% of Ag and Cu, the peaks shifted to higher angles. Peak intensities increased with increasing concentration of bimetallic Ag/Cu doped TiO₂. This behaviour was also witnessed by Reddy et al. [27]. At the doping level of 0.1 mol.% Ag/0.5 mol.% Cu bimetallic, no peak shifting was noted, instead

the peaks intensity reduced strongly. Such behaviour was also witnessed for the 0.5 mol.% Ag and 0.1 mol.% Cu. When increasing the concentration of Cu, the peaks marginally enlarged and the crystallite sizes decreased (see Table 6.1), representing an alteration in the crystal structure. The creation of point defects because of the substitution of Ti^{4+} by Ag^{2+} and Cu^{2+} result to the decreased intensity when increasing the Ag and Cu content.

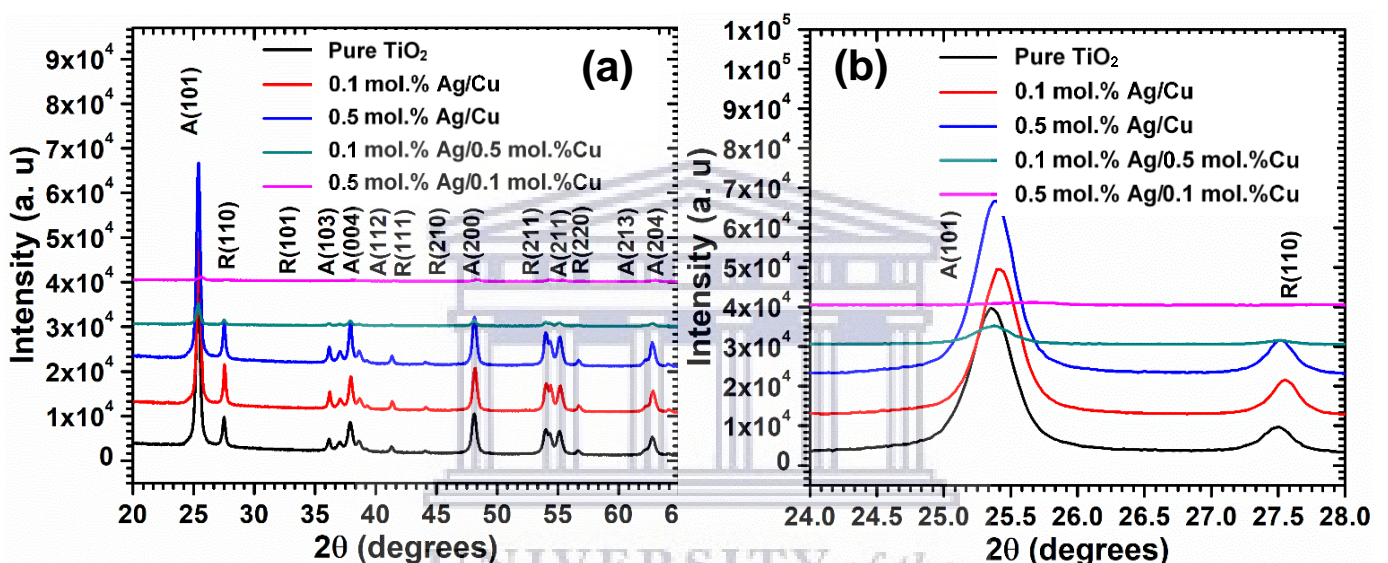


Fig. 6. 1: (a) XRD patterns of bimetallic Ag/Cu doped TiO_2 nanoparticles and (b) magnified patterns showing (101) and (110) peaks.

Table 6. 1: Summary of the crystallite size and lattice strain of bimetallic Ag/Cu doped TiO_2

Materials	Lattice strain, ϵ ($\times 10^{-4}$)	Crystallite size (nm), L
Pure TiO_2	0.0002	16.1
0.1% mol Ag/Cu	0.0005	13.1
0.5% mol. Ag/Cu	0.0004	17.2
0.5% mol Ag/0.1% mol Cu	0.0009	8.5
0.1% mol Ag /0.5% mol Cu	0.0053	9.8

The surface morphology of the pure TiO₂ and bimetallic Ag/Cu doped TiO₂ was investigated using the scanning electron microscopy, as presented in Fig. 6.2. The SEM micrograph of the pure TiO₂ shows nanoparticles. Upon doping with the 0.1 mol.% Ag/Cu in TiO₂ surface, revealed that the nanoparticles size decreased. At 0.5 mol.% with increased concentration from 0.1 mol.% Ag/Cu bimetallic content to 0.5 mol.% Ag/Cu. This observation is consistent with the XRD analyses, showing smaller crystalline sizes for the 0.5 mol.% Ag/0.1 mol.% Cu bimetallic. The EDX spectrum of 0.1 mol.% Ag/Cu shown in the appendix B indicated that only Ti, O, Ag and Cu existed on the surface. The elemental mapping also showed that the Ag and Cu are evenly dispersed on the TiO₂ surface.



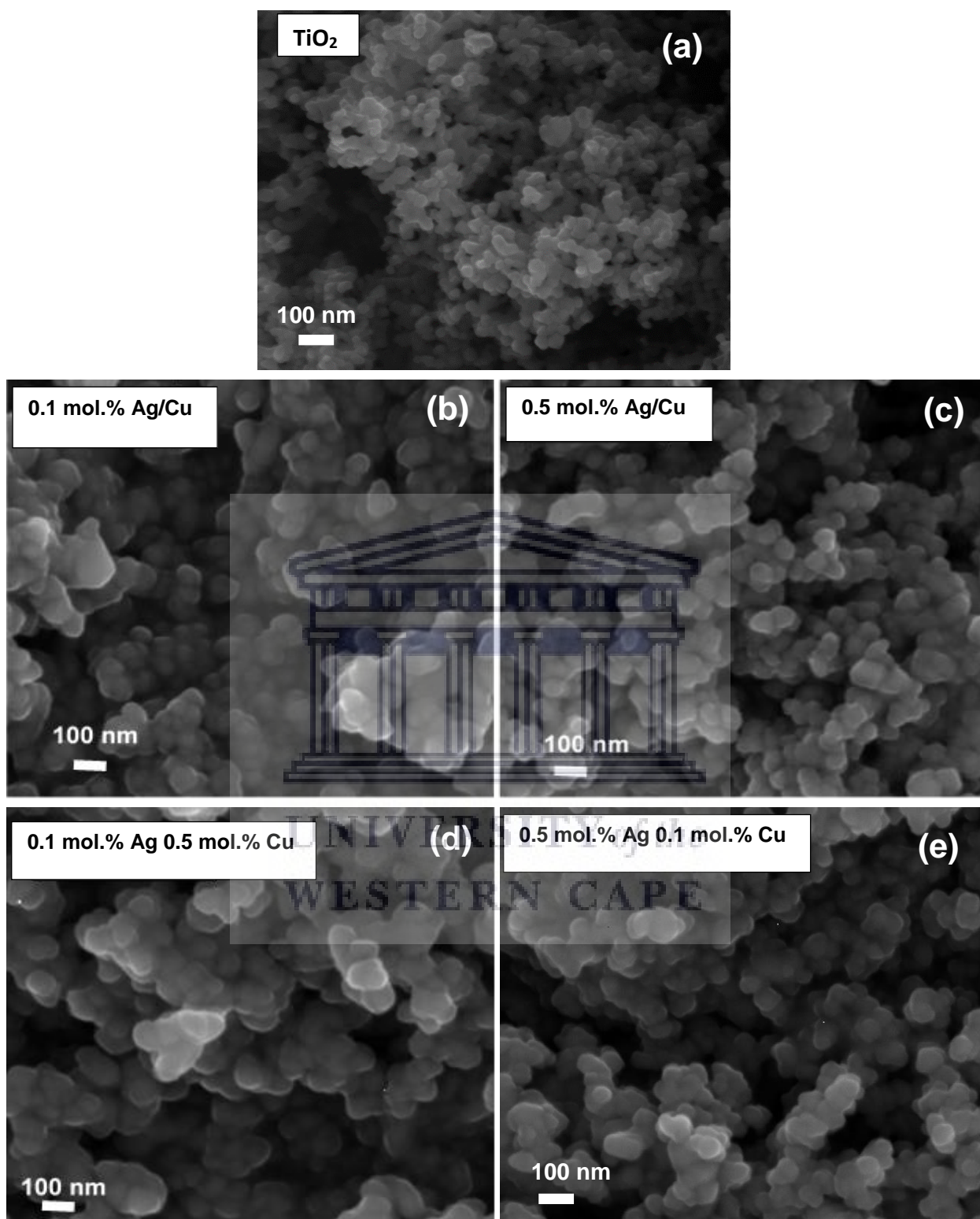


Fig. 6. 2: SEM micrographs of the (a) pure TiO₂, bimetallic Ag/Cu doped TiO₂ nanoparticles (b) 0.1 mol.% Ag/Cu, (c) 0.5 mol.% Ag/Cu, (d) 0.1 mol.% Ag /0.5 mol.% Cu and (e) 0.5 mol.% Ag/ 0.1 mol.% Cu.

It is recognized that the operational temperature has a pronounced effect on the gas sensing characteristics [28]. Fig. 6.3a shows the sensor electrical resistance in air (R_a) versus the operating temperature (25–150 °C). The R_a of all the sensing materials declined when the operational temperature increased. The plot basically displays a behavior of negative temperature coefficient of the electrical resistance, this is in-line with an n-type semiconductor manner. This behaviour follows exponent law approximately, which is due to the ionization of donor impurity and defects. Basically, movement of electrons from the valence band to the conduction band of the sensing material occurs and consequently further electrons are accessible for transporting the current, leading in a decrease in the sensor resistance. As noted in Fig. 6.3, the R_a increased with addition of either Ag or Cu. More interesting, at higher loading of Ag and Cu (i.e. 0.5 mol. % AuCu), a higher R_a was observed. This behaviour was also witnessed by Motsoeneng et al. [29] at higher Au loading in SnO₂/NiO/Au (2.5wt.%), because of the nanoscale formation of p-n nanojunctions in NiO and SnO₂ phases.

UNIVERSITY of the
WESTERN CAPE

Fig. 6.3b presents the response of the various sensors versus the operational temperature towards BTEX and acetone vapour. As demonstrated in Fig. 6.3b, as the the sensors were exposed to benzene vapour, the bimetallic 0.5 mol.% Ag/Cu doped TiO₂ nanoparticles based sensor displayed higher response at 100 °C, which decreased at 150 °C operational temperature. Such behaviour was also noted for the toluene vapour, where the bimetallic 0.5 mol.% Ag/Cu doped TiO₂ nanoparticles displayed higher response at 100 °C. Upon exposing the sensors to ethylene-benzene and toluene vapours, the the bimetallic 0.5 mol.% Ag/Cu doped TiO₂ nanoparticles based sensor still showed better response. It is interesting to point out

that when the sensors were exposed to xylene vapour, the bimetallic 0.5 mol.% Ag/Cu doped TiO₂ nanoparticles displayed a response of 21.2, which is almost twice times higher than other gases at 100 °C. Nonetheless, at higher operational temperature, the sensor revealed a remarkable response of 33.2, which is about three times, higher than other gases. Since the TiO₂ is know as an n-type semiconductor, thus the higher sensing response could be justified by the formation of a p type behaviour observed for the bimetallic 0.5 mol.% Ag/Cu doped TiO₂ nanoparticles. This behaviour is witnessed on the real time resistance plots shown in Fig. 6.4a and b. As noted in Fig. 6.4a and b, as the loading concentration of Ag was increased to 0.5 mol.%, while that of Cu was kept at 0.1 mol.%, the TiO₂ strucutre transformed to p-type. Such beaviour was noted when the sensor was tested in both operational temperatures of 100 and 150 °C towards xylene. Furthermore, when increasing the concentration of Ag and Cu to 0.5 mol.% in TiO₂ (i.e. bimetallic 0.5 mol.% Ag/Cu), p-type behaviour was still observed, though the change in resistance improved more in comparison to that of 0.5 mol.% Ag /0.1 mol.% Cu based sensor. It is worthy to point out that this behaviour was also witnessed to other target gases, such as benzene, toluene and ethylene-benzene, see Fig. 6.S1 of the supporting information.

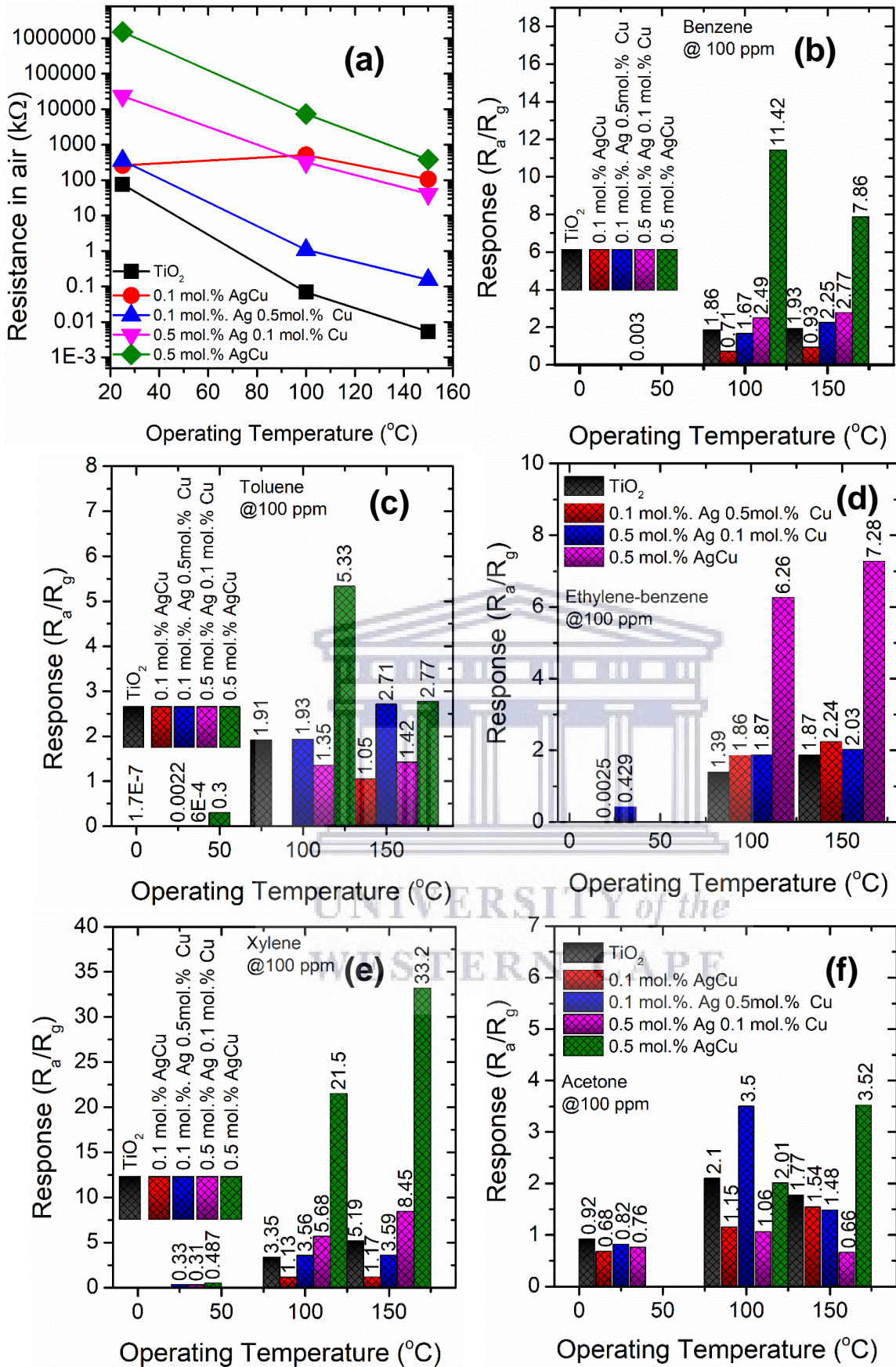


Fig. 6. 3: (a) Resistance in air of various bimetallic Ag/Cu doped TiO_2 nanoparticless ensors at various operational temperature, (b) benzene, (c) toluene, (d) ethylene-enzene, (e) xylene and (f) acetone.

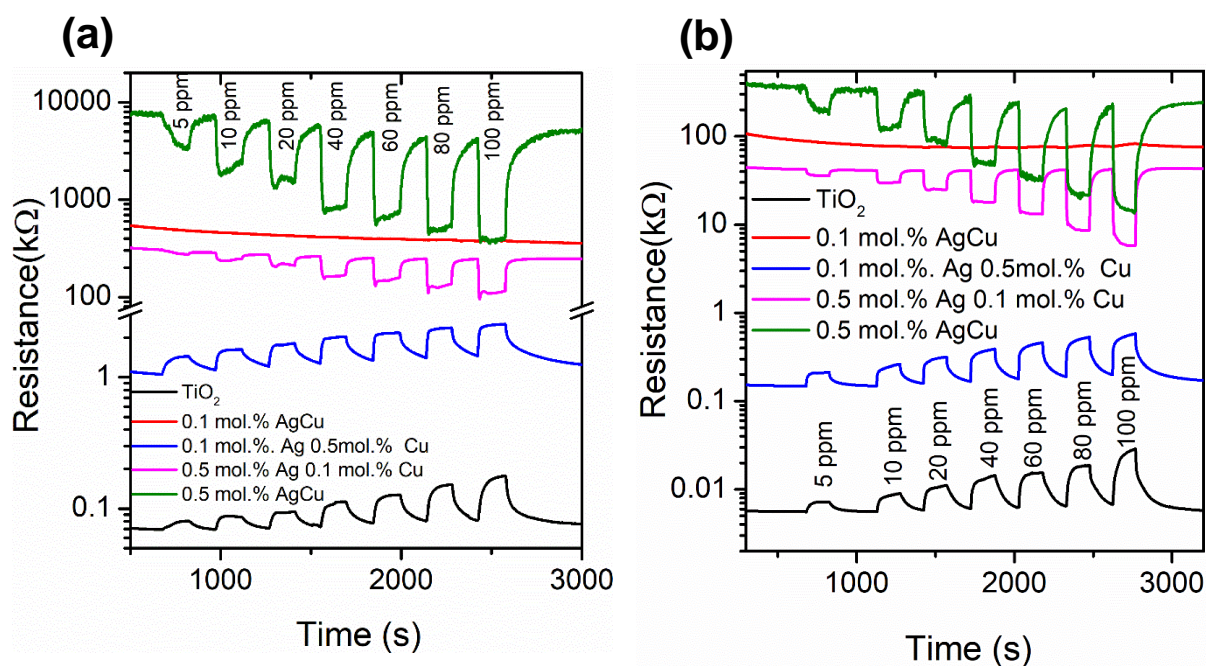


Fig. 6. 4: Real-time resistance plot of various sensors tested to xylene vapour at (a) 100 and (b) 150 °C.

The responses of the various bimetallic AgCu doped TiO₂ based sensors tested towards different concentrations of BTEX and acetone vapours ranging from 5 ppm to 100 ppm at 150 °C are displayed in Fig. 6.5. As noted in Fig. 6.5, among all the sensors tested to all these target gases, the bimetallic 0.5 mol.% Ag/Cu doped TiO₂ nanoparticles displayed improved response in all the gases. Additionally, among all the tested gases, the bimetallic 0.5 mol.% Ag/Cu doped TiO₂ nanoparticles displayed improved response towards xylene, see Fig. 6.5d. Its response increased exponential without disclosing any point of saturation, and at 100 ppm, its response was about 33, which is almost three times higher than that of other gases. The exponential behaviour with the gas concentration is clearly observed in the real time response plot in Fig. 6.5f. In this plot, the sensor indeed responded when the xylene was introduced in the chamber and further recovered when the xylene was released.

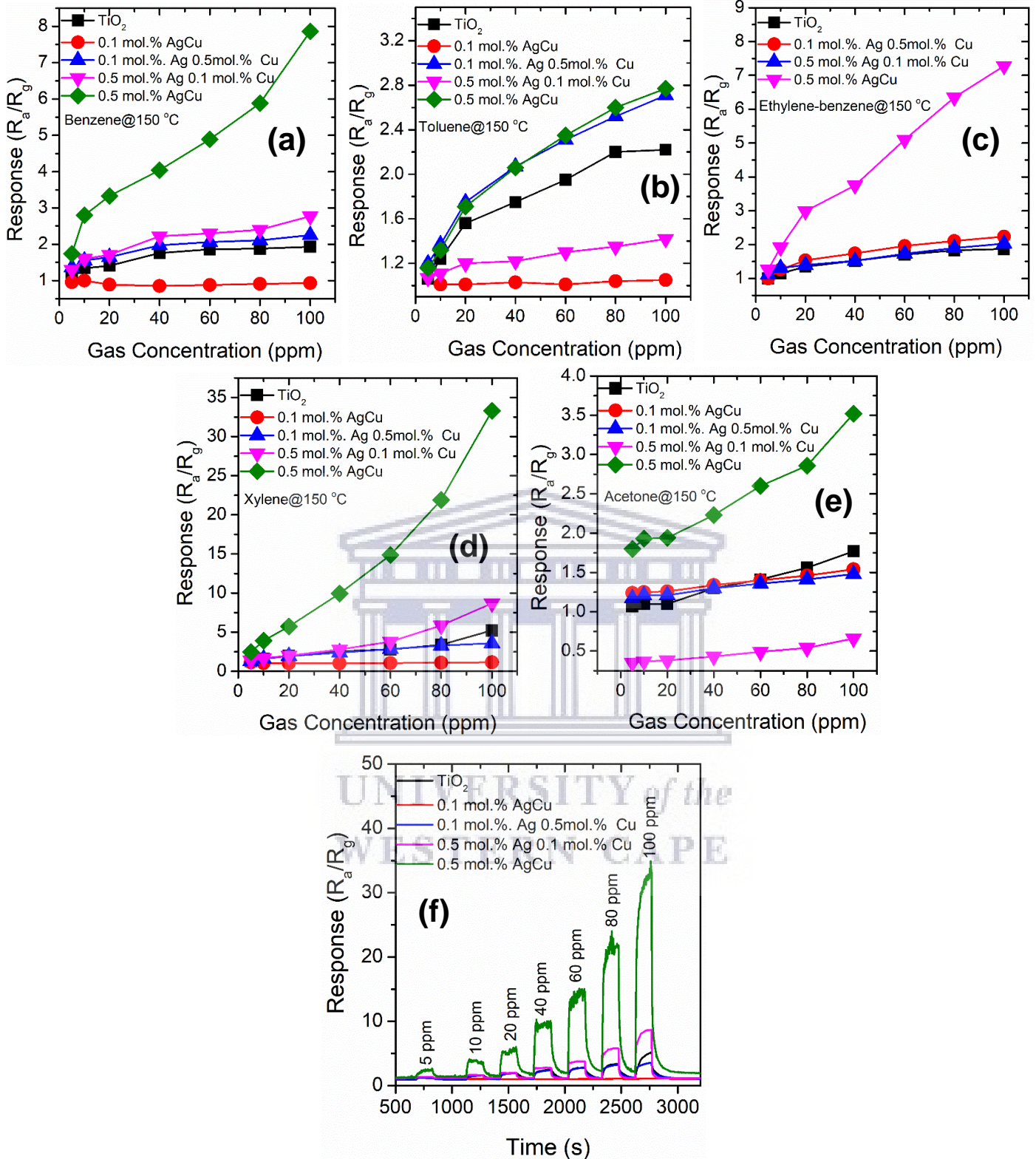


Fig. 6. 5: Response curves for pure TiO_2 and bimetallic Ag/Cu nanoparticles based sensors tested towards (a) benzene, (b) toluene, (c) ethylene-benzene, (d) xylene and (e) acetone. Note (f) corresponds to real-time response curve of bimetallic 0.5 mol.% AgCu doped TiO_2 based sensor towards xylene.

Apart from an excellent response to the xylene vapour, the gas selectivity is also another vital parameter to be considered for practical application of gas sensors. As a result, gas selectivity of the undoped and bimetallic Ag/Cu doped TiO₂ nanoparticles based sensors were performed towards five different vapours, which include the BTEX and acetone (i.e. is letter A in the radar plot) vapour at 100 ppm and an operational temperature of 150 °C. Fig. 6.6 demonstrates that among the sensors bimetallic 0.5 mol.% Ag/Cu doped TiO₂ nanoparticles based sensor was extremely selectivity towards xylene among other gases and sensors. The sensor displayed a response of 33.2, which was almost three times higher than that of other gases in the same conditions. As known, xylene is a harmful indoor aromatic hydrocarbon vapour, which is found in several domestic products. Thus, the breathing of xylene causes different symptoms, like headache, dizziness, nausea, serious diseases in the memory and nervous systems, etc. As a result, the current selectivity could be useful for its timely detection.

Constant gas detection for a sensor is essential to assess its reproducibility, linearity and stability. Fig. 6.6b exhibits five cycles of the reproducibility plot of the sensor on successive exposure to 80 and 100 ppm xylene gas and air. The sensor was exposed to five cycles at 80 ppm, then 100 ppm and then 80 ppm xylene for 30 days as to observe their stability too. As noted in Fig. 6.6a, the sensor shows a clear response and recovery characteristics (i.e. repeatability) towards xylene and air from day 1 to day 30 without collapsing or showing any poisoning, it only reduced by 15%. This behaviour denotes that the sensor was indeed stable and this is validated by the response versus number of days' plot in Fig. 6.6b. Thus, in summary, these findings demonstrate that the bimetallic 0.5 mol.% Ag/Cu doped TiO₂ nanoparticle based sensor presents a good reproducibility and stability towards xylene vapour.

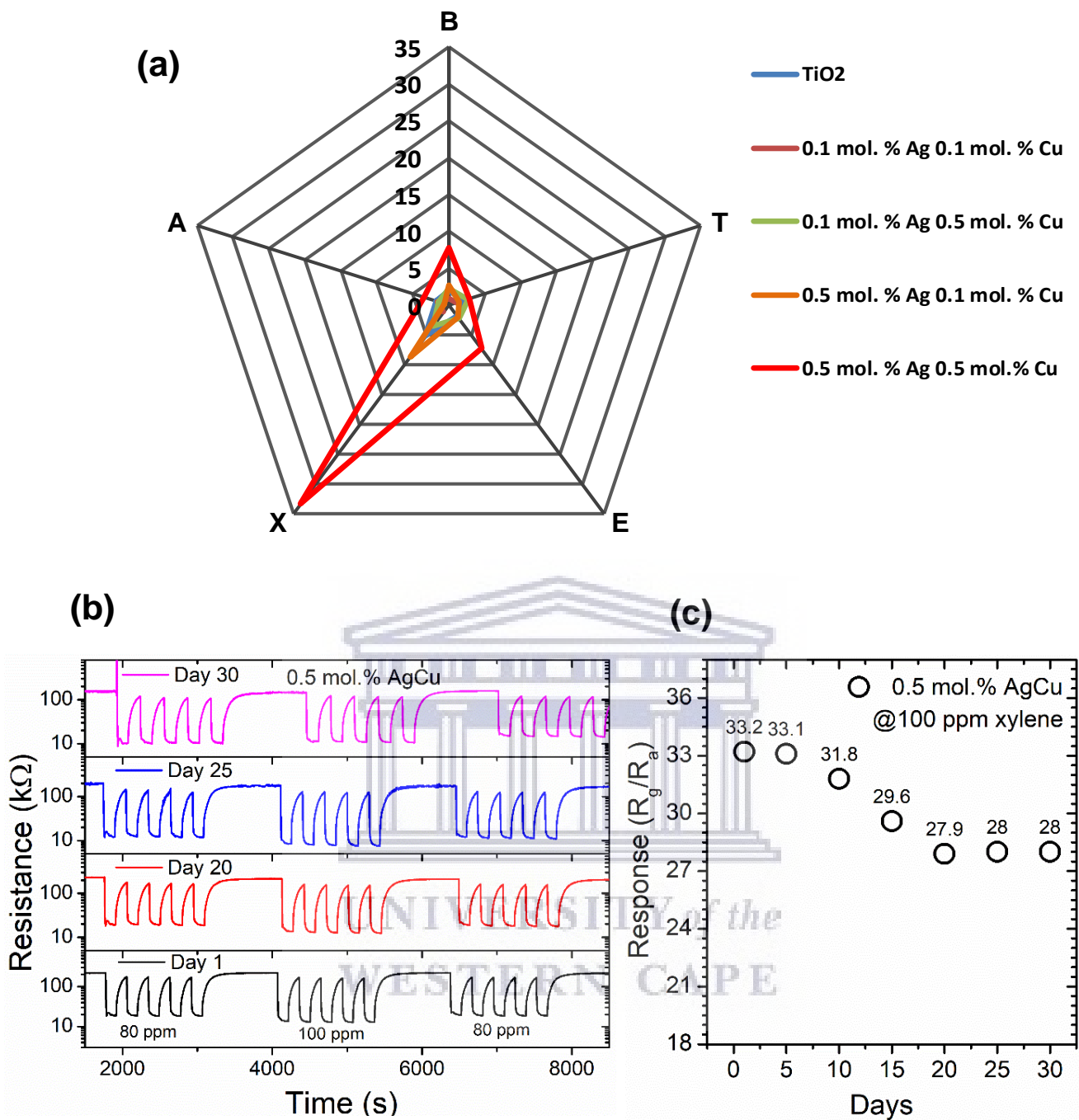


Fig. 6. 6: (a) Radar selectivity plot (a-b) repeatability and stability plot of bimetallic 0.5 mol.% Ag/Cu doped TiO₂ nanoparticle based sensor towards 80 and 100 ppm xylene over seven days at 150 °C and (c) Response versus number of days (i.e. stability) plot of bimetallic 0.5 mol.% Ag/Cu doped TiO₂ nanoparticle based sensor towards 100 ppm xylene vapour at 150 °C. Note letter A correspond to acetone, while others are BTEX in radar plot, i.e Fig. 6.6a.

The gas sensing characteristics comparison of bimetallic p-type 0.5 mol.% Ag/Cu doped TiO₂ nanoparticle based sensor in the current study and other p-type and n-

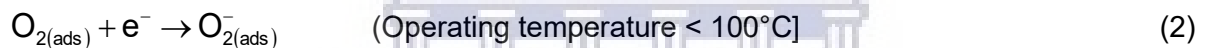
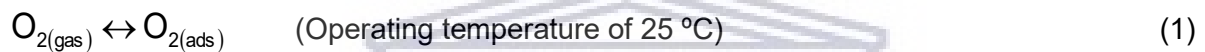
type sensing materials in literatures are listed in Table 6.2. Matched to xylene gas sensing characteristics of Ni-TiO₂ submicron [32], 0.5 at. % Ag/TiO₂ [30], Co₃O₄-TiO₂ [33], Co₃O₄-TiO₂ [34], SDBS-TiO₂ [35], TiO₂/ α-Fe₂O₃ [36], In-TiO₂ [37], our current sensor, i.e. the bimetallic p-type 0.5 mol.% Ag/Cu doped TiO₂ displays a competitive response and timely selectivity towards xylene, more especially when it compared those operated at higher temperature.

Table 6. 2: Summary of pure, doped and heterostructure derived from TiO₂ sensors for detection of xylene vapour.

Sensing element	Conc (ppm)	T _{res} /T _{rec} (s)	Response	Temp (°C)	Refs.
TiO ₂ NPs	0.1	20/14	-	75	[30]
0.5 at% Ag/TiO ₂	100	5/2	6.49	375	[31]
Ni-TiO ₂ submicron	100	9/12	2	302	[32]
Co ₃ O ₄ -TiO ₂	50	-	113	115	[33]
Co ₃ O ₄ -TiO ₂	50	<23/-	6.21	120	[34]
SDBS-TiO ₂	0.001	4/61	-	R/T	[35]
TiO ₂ / α-Fe ₂ O ₃	100	4/3	27.5	370	[36]
In-TiO ₂	50	2.2/3	127.2	200	[37]
0.5 mol.% Ag/Cu-TiO ₂	100		33.2	150	Current work

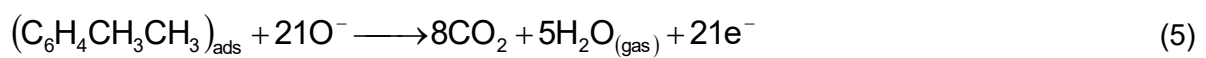
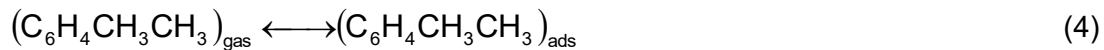
6.3.2. Xylene gas sensing mechanism

A bimetallic 0.5 mol.% Ag/Cu doped TiO₂ based sensor as a p-type semiconductor metal oxide (SMO), the sensing mechanism is established on the resistance variation when exposed to the target gas. The adsorption-desorption mechanism is associated with the oxygen species (O²⁻, O⁻, and O₂⁻) that become adsorbed on the metal oxide surface [38, 39]. The p-type surface, such as bimetallic 0.5 mol.% Ag/Cu doped TiO₂ based sensor adsorbs the ionized oxygen molecules by conduction band electrons, resulting in increased charge carriers in the hole (h⁺) accumulation layer (HAL), and consequently forms lower sensor resistance.



When bimetallic 0.5 mol.% Ag/Cu doped TiO₂ based sensor is exposed to VOCs, such as BTEX vapours, they interact with the chemisorbed oxygen ions (O₂⁻ and O⁻ at 100 and 150 °C, respectively), resulting to releasing of electrons, which in turn increases the sensor resistance, because of the decreased holes concentration in the HAL caused by the electron-hole recombination. Thus, the improved performance of BTEX, more especially xylene vapour, could result from the possible speculations. Generally, the n-type SMO responses to a lesser amount of responsive BTEX vapours are inferior in-line to those that are highly reactive, such as ethanol or formaldehyde [40]. Contradictorily, p-type SMO tend to produce superior catalytic activity to enable and speed up the BTEX vapour oxidation due to their plentiful oxygen adsorption and multi-valent features [41]. Even though BTEX retain

comparable structures, they are dissimilar by the total of methyl groups. For instance, xylene contains one and two more methyl group in comparison to toluene and benzene respectively, causing to be more reactive with a greater oxidation, hence superior sensing was observed for xylene vapour towards p-type [42- 45].



To complement the sensing results, the XPS, BET and in-situ PL measurements were conducted. For a clear association, in-situ PL analyses were conducted at the temperatures matching to the operational sensor temperatures ranging from 30-150 °C at an excitation wavelength of 320 nm. Fig. 6.7 demonstrates the PL spectra of the pure and bimetallic AgCu doped TiO₂ nanoparticles. A broad emission ranging from 1.5 to 3.5 eV and a broadening, and as well as a shift of the peaks to higher energy when increasing the concentration of Ag to 0.5 mol.% are observed. The significant in the PL energy is probably due to increased relative concentration of defects such as oxygen vacancies and Ti³⁺ ions. It is clear that the shift is mostly dependent on Ag concentration, while the intensity (i.e. at 2.5 eV) is dependent on the Cu concentration. It is further observed in Fig. 6.7b-c the intensity of the peaks decreased with the PL temperature from 100 to 150 °C. Such decrease was more significant for the samples doped with low concentration of Ag. Additionally, the width of peaks becomes narrower with operational temperature. The deconvoluted graphs using Gaussian fit illustrated four peaks centred at 3.42, 3.24, 2.99, 2.72, 2.42 and 2.0 eV for pure TiO₂. The peaks located between 3.4 and 3.0 eV ascribed to direct

electronic evolution from the bottom of the conduction band to the top of the valence band were witnessed for all the samples [46]. The broad visible PL emission was related to an increase in the point defects, such as oxygen vacancies. Electronic transitions from defects levels within the band gap led to in further peaks located at 2.7 eV, which were associated to self-trapped excitons in the octahedral [46-48]. The peaks at approximately 2.6 eV and 2.4 eV are related to shallow and deep oxygen vacancy correlated trap states (i.e. Ti^{3+} and F^+ centres, respectively) [47- 49].

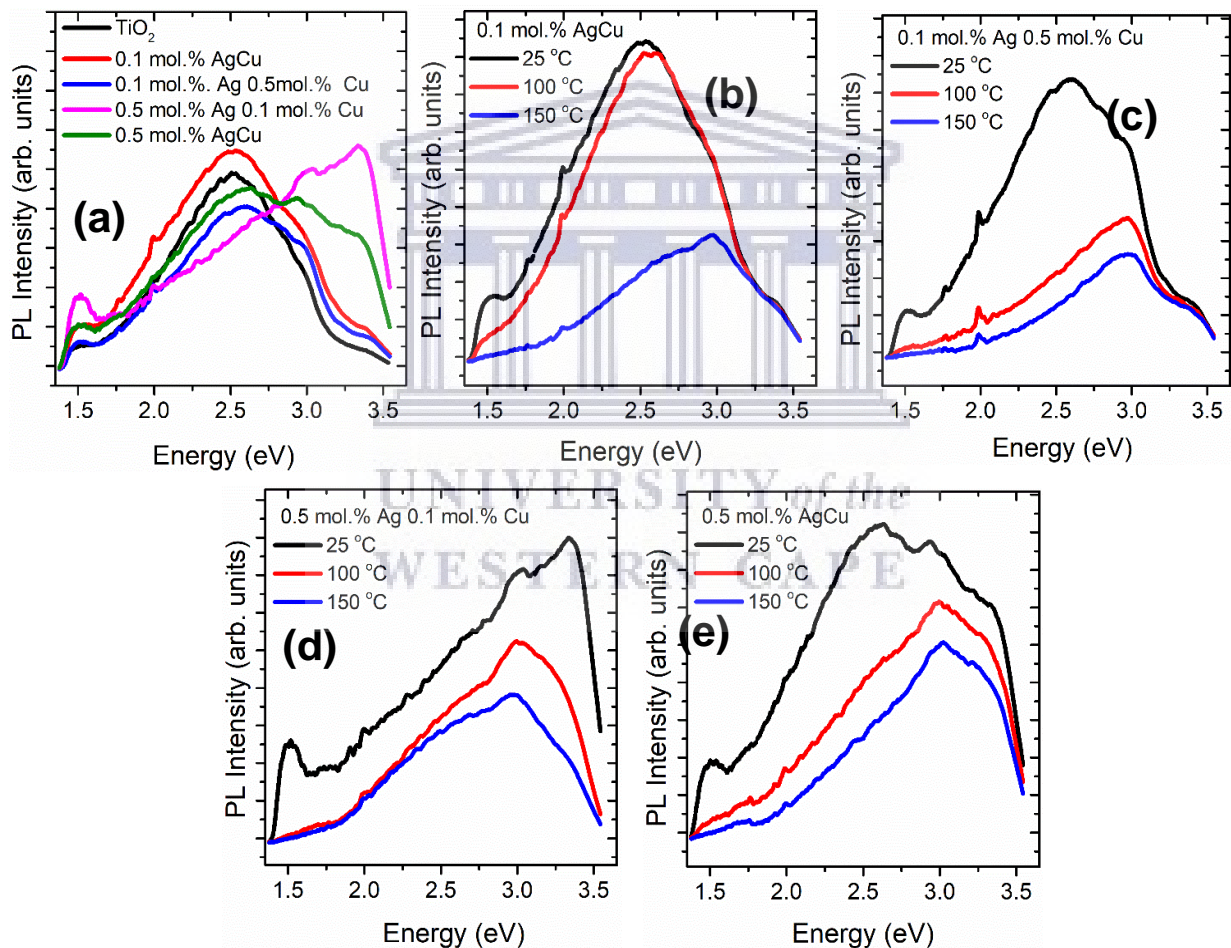


Fig. 6. 7: Room temperature PL spectra of (a) undoped and bimetallic AgCu doped TiO₂ nanoparticles, and (b-e) In-situ PL spectra of bimetallic AgCu doped TiO₂ nanoparticles conducted from 25 to 150 °C.

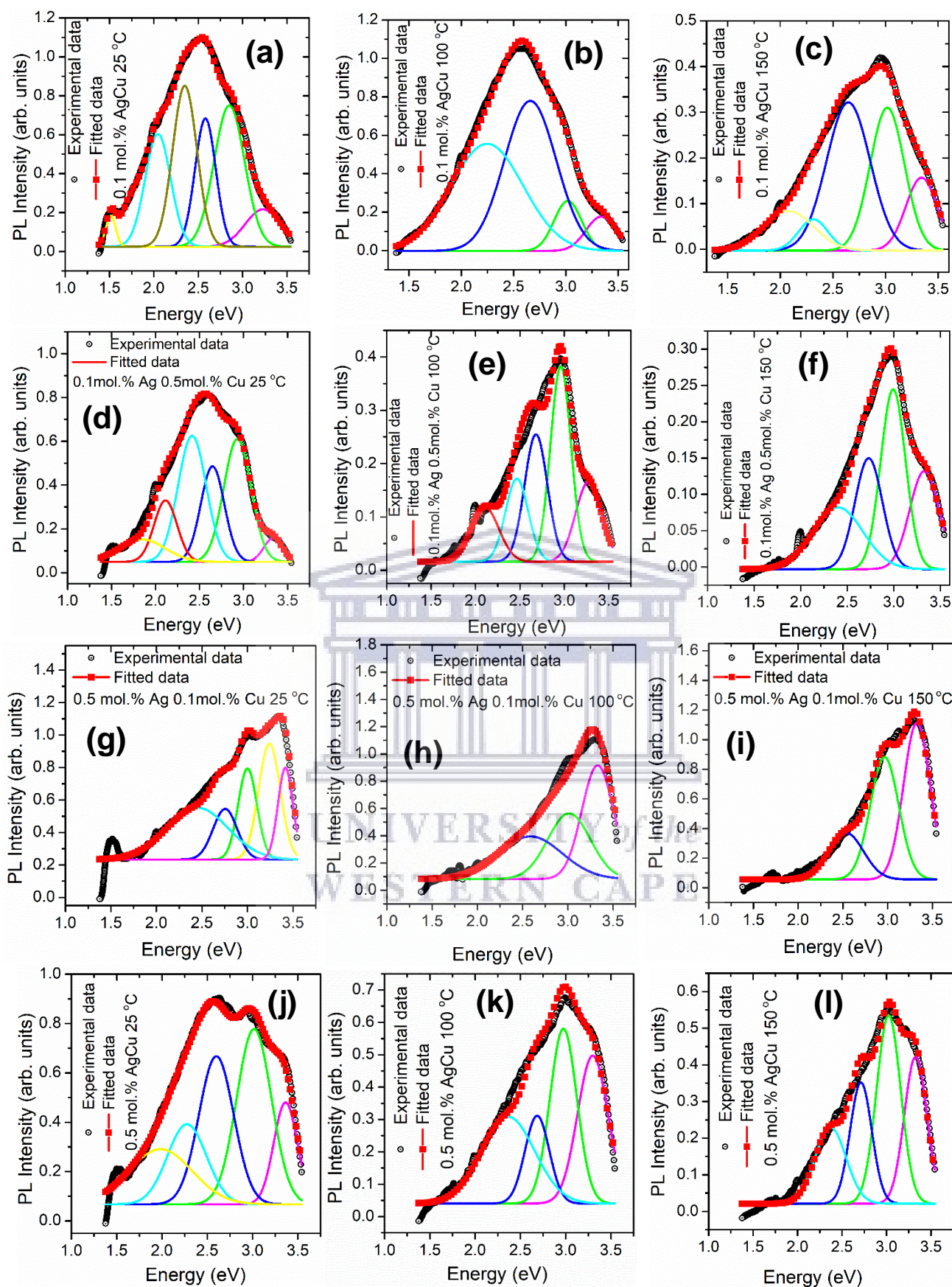


Fig. 6. 8: In-situ PL fitted spectra of at different temperatures (a-c) 0.1 % mol. Ag/Cu (d-f) 0.1 mol. Ag/0.5 mol.% Cu, (g-i) 0.5% Ag /0.1% mol. Cu and (j-l) 0.5 % mol. Ag/Cu of at 25, 100 and 150 °C, respectively.

Fig. 6.9. presents the high resolution XPS spectra of O 1s of bimetallic AgCu doped TiO₂ nanoparticles. The deconvoluted spectra of the bimetallic 0.1 mol.% Ag/Cu, 0.1 mol.% Ag/ 0.5 mol.% Cu, and 0.5 mol.% Ag/ 0.1 mol.% Cu doped TiO₂ nanoparticles in Fig. 6.9a-c show three peaks O₁ and O₂ and O₃ centred at 529.80, 530 and 531.30 eV ascribed to Ti⁴⁺, O²⁻-ions in the TiO₂ crystal lattice [50-52] and Ti³⁺ oxygen vacancies on the surface. It is remarkable to point out that the bimetallic 0.5 mol.% Ag/Cu doped TiO₂ nanoparticles shows a broad peak, with a tail (shoulder) extending towards higher energies in comparison to its counterparts, which displays three deconvoluted peaks at 528.5, 530.6 and 531.8 eV. In general, O²⁻ is deliberated to be stable, which may not contribute to the gas performance, while the O⁻ and Ti³⁺ oxygen vacancies components contain a considerable influence in the gas sensing characteristics [53, 54]. Thus, the relative concentration of the Ti³⁺ oxygen vacancies constituent for the bimetallic 0.5 mol.% Ag/Cu doped TiO₂ nanoparticles shows a maximum value of 63.9 %, as listed in Table S1, validating the reduction of Ti⁴⁺ to Ti³⁺.

Fig. 6.9a-d illustrates the XPS spectra of Ti2p peaks of the bimetallic AgCu doped TiO₂ nanoparticles. The deconvoluted spectra of the 0.1 mol.% AgCu and 0.1 mol.% Ag 0.5 mol.% Cu were fitted into four peaks. For the 0.1 mol.% AgCu, the peaks were located at 457.8, 458.9, 464.3 and 465.2 eV, while for the 0.1 mol.% Ag 0.5 mol.% Cu, the peaks were located at 456.1, 458.1, 461.3, 464.1 eV. The peaks around 458 eV and 463 eV are associated to Ti⁴⁺ 2p_{3/2} and Ti³⁺ 2p_{1/2} [55, 56]. Whereas, for the 0.5 mol.% Ag 0.1 mol.% Cu and 0.5 mol.% AgCu, the spectra were fitted into five peaks. It is further observed that the 0.5 mol.% AgCu spectrum shows a strong shoulder at lower binding energy, probably induced by higher doping concentration of Ag and Cu, resulting to defects, such as Ti³⁺ and this is consistent

with the PL analyses. Such behaviour was previously reported by Tshabalala et al. [56] associating it to Ti^{3+} .

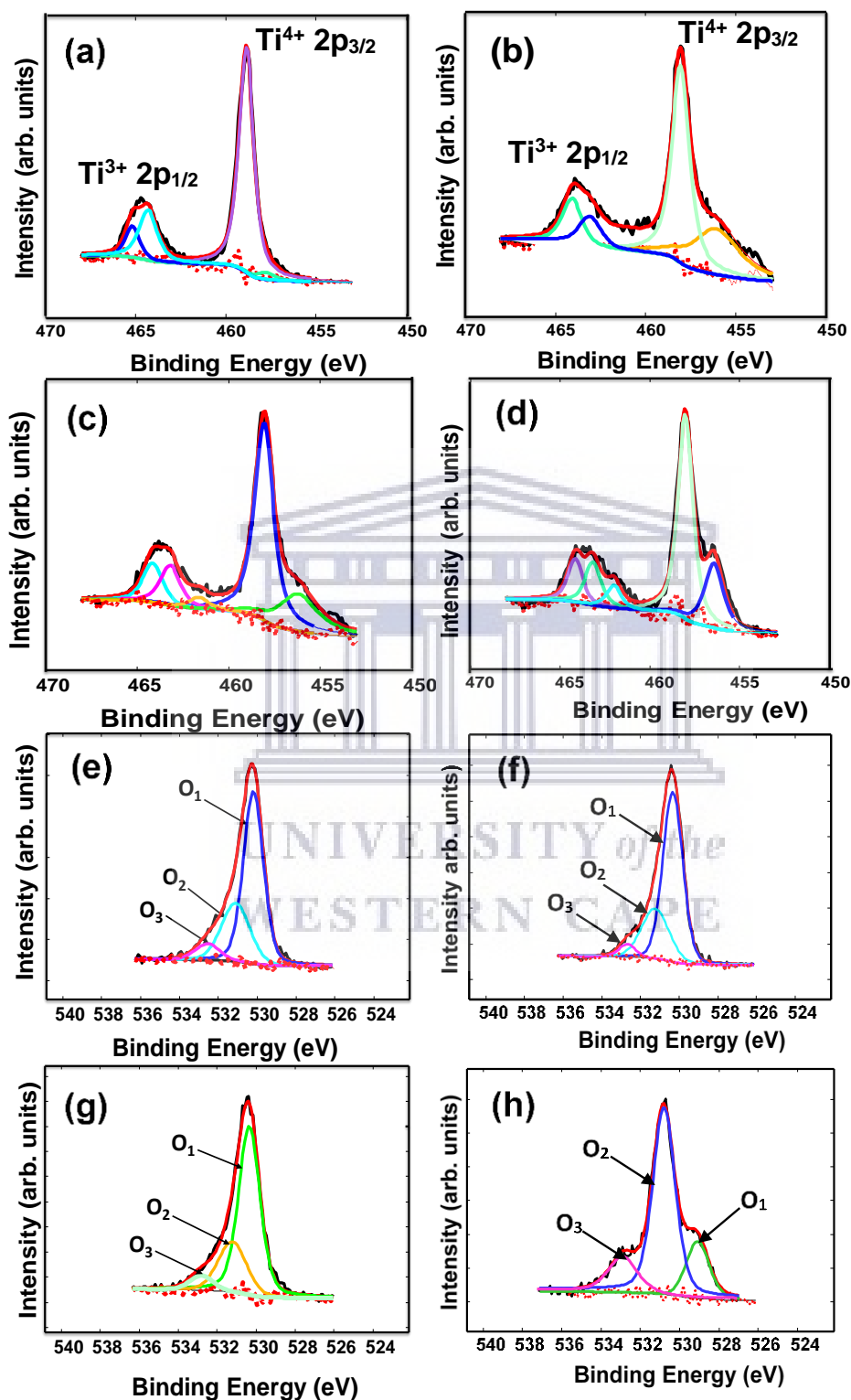


Fig. 6. 9: Ti2p XPS spectra of (a) 0.1 mol.% Ag/Cu, (b) 0.1 mol.% Ag/0.5 mol.% Cu, (c) 0.5 mol.% Ag/ 0.1 mol.% Cu ad (d) 0.5 mol.% Ag/Cu. Note (e-h) correspond to O 1s spectra of (e) 0.1 mol. % Ag/Cu, (f) 0.1 mol.% Ag /0.5 mol.% Cu, (g) 0.5 mol.% Ag/ 0.1 mol.% Cu and 0.5 mol.% Ag/Cu bimetallic doped TiO_2 nanoparticles.

The peaks in XPS spectra of Cu2p were fitted using Gaussian function as shown in Fig. 6.10a-d. The Cu 2p_{3/2} profiles of the 0.1 mol.% Ag/Cu and 0.5 mol.% Ag/0.1 mol.%Cu of the bimetallic Ag/Cu doped TiO₂ nanoparticles in Fig. 6.10a and b display minimal peaks located at 952.6 eV and 952.9 eV, respectively. While that of the Cu 2p_{1/2} peak for both samples displays peaks at 932.6 eV and 933.1 eV, respectively. At higher doping concentration of Cu (i.e. 0.1 mol.% Ag/0.5 mol.% Cu and 0.5 mol.% AgCu doped TiO₂ nanoparticles), the intensity of both Cu 2p peaks increased.

The XPS Ag 3d peaks of the bimetallic Ag/Cu doped TiO₂ nanoparticles are illustrated in Fig. 6.10e-h. While the high resolution XPS clear confirms that the incorporation of Ag in the TiO₂ surface. However, at lower doping the intensity of peaks related Ag 3d_{3/2} and Ag 3d_{5/2} is very minimal and this observation is similar to that of Cu in Fig. 6.10a and b at lower doping concentration.



UNIVERSITY of the
WESTERN CAPE

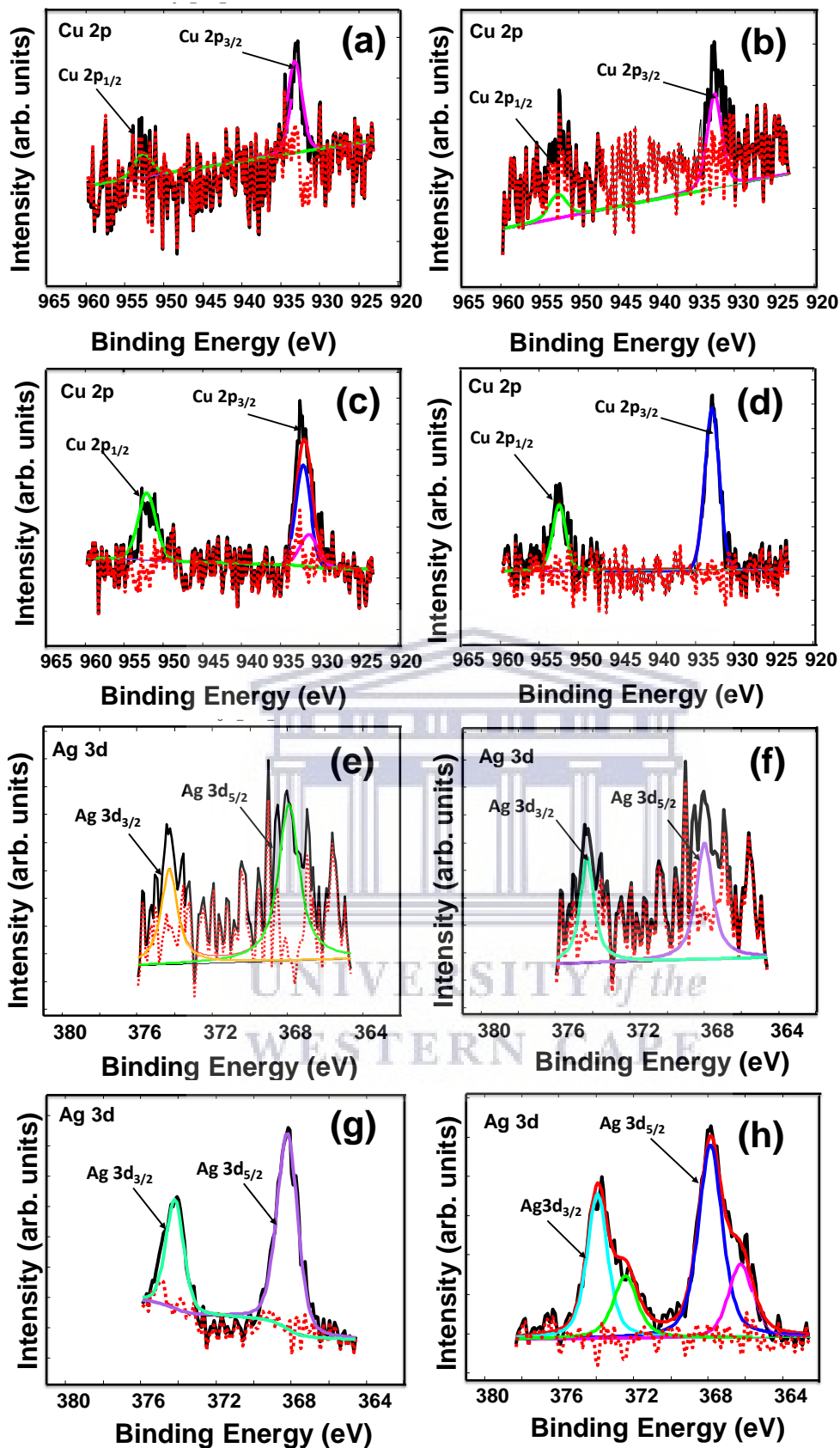


Fig. 6. 10: (a-d) Cu2p (a) 0.1 % mol. Ag/Cu, (b) 0.1% mol. Ag/0.5 mol.%Cu, (c) 0.5% Ag /0.1 mol.% Cu and (d) 0.5 mol.% Ag/Cu, and (e-h) Ag 3d of (e) 0.1 % mol. Ag/Cu, (f) 0.1% mol. Ag/0.5 mol.%Cu, (g) 0.5% Ag /0.1 mol.% Cu and (h) 0.5 mol.% of the bimetallic Ag/Cu doped TiO₂ nanoparticles.

To understand the sensing performance, we conducted the nitrogen adsorption measurements as depicted in Fig. 6.11. The N₂ adsorption/desorption isotherms of NiO structures exposed that materials are mesoporous and macroporous based on IUPAC classification type V. The NiO nanostructures showed H3 type hysteresis loop associated with slit-shaped pores. The surface areas of the bimetallic nanoparticles are 34.9736 ± 0.0458 m²/g for 0.1 mol.% Ag/Cu, 34.2224 ± 0.1629 m²/g for 0.1 mol.% Ag 0.5 mol.% Cu, 36.1635 ± 0.1917 m²/g for 0.5 mol.% Ag 0.1 mol.% Cu, 32.0335 ± 0.3842 m²/g 0.5 mol.% Ag Cu. Additionally, the pore volume of different contents calculated by Barret–Joyner–Halenda (BJH) method were 0.243931 cm³/g for 0.1 mol.% Ag/Cu, 0.295374 cm³/g for 0.1 mol.% Ag 0.5 mol.% Cu, 0.245314 cm³/g for 0.5 mol.% Ag 0.1 mol.% Cu, 0.291393 cm³/g 0.5 mol.% Ag Cu, respectively. It is well adopted that the large surface area can deliver more active sites that are beneficial to enhancing the gas sensing performance [57]. Since the structures displayed almost similar surface areas and pore volumes, thus it is very clear that the surface area plays a minimal different in the current sensing performance of the bimetallic structures. Such similar surface area could be justified by minimal difference in crystallite sizes as witnessed on the XRD analyses.

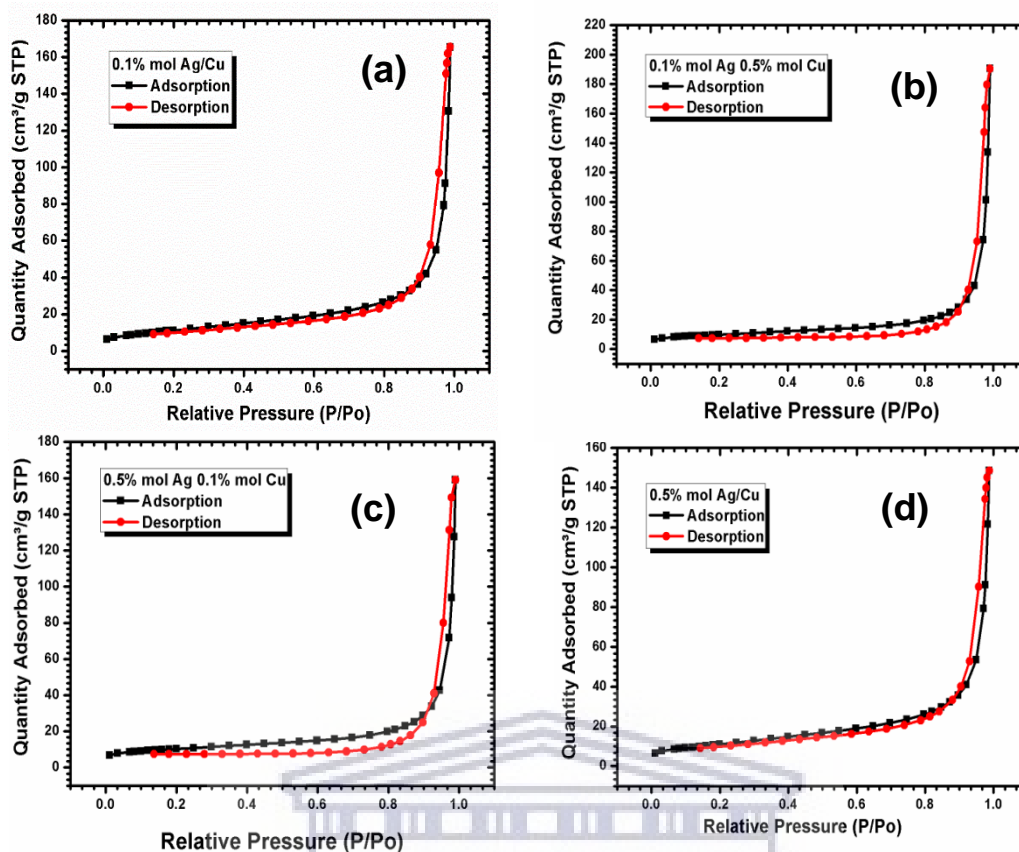


Fig. 6. 11: N₂ adsorption-desorption isotherms of the (a) 0.1 mol. % AgCu, 0.1 mol.% Ag0.5 mol.%Cu, (c) 0.5 mol.% Ag /0.1 mol.% Cu and (d) 0.5 mol.% Ag/Cu of the bimetallic Ag/Cu doped TiO₂ nanoparticles

6.3.3. Characterization of Solar Cells Devices

The current-voltage (J-V) features of the fabricated P3HT: bimetallic AgCu doped TiO₂ solar cells and photovoltaic parameters are displayed in Fig. 6.12 and Table 6.3, respectively. The short current density (J_{sc}), open circuit voltage (V_{oc}), and PCE of the devices enhanced from 0.45 % to 2.26 % upon loading 0.1 mol. % Ag/Cu bimetallic doped TiO₂ nanoparticles on polymer matrix. When increasing the loading of Cu to 0.1 mol.% Ag/ 0.5 mol.%Cu, the PCE efficiency further increased to 3.30 %. Nonetheless, at Ag loading of 0.5 mol.% Ag /0.1 mol.% Cu, highest PCE of 4.11 % was witnessed and this value is almost comparable to that of the 0.5 mol.% Ag/Cu, which was 4.01%. Clearly the increased loadings of Ag and Cu have significant

influence on the solar cell performance of the bimetallic Ag/Cu doped TiO₂ nanoparticles. Such increase could be due to a transformation of p-type bimetallic 0.5 mol.% Ag 0.1 mol.% Cu or 0.1 mol.% Ag 0.5 mol.% Cu doped TiO₂ nanoparticles incorporated in P3HT matrix, which acts now as a donor instead of an acceptor, since at the low bimetallic loading the material acts as an acceptor. Siddiqui et al. [58] have reported improved efficiency upon introducing a p-type CuO in the matrix, which also acted as donor. Their solar cell photocurrent density enhanced from 9.43 mA/cm² to 11.32 mA/cm² and the external quantum efficiency also increased. While the PCE increased from 2.85% to 3.82%.

To understand the increased PCE with increased loading of the bimetallic Ag /Cu doped TiO₂ on the P3HT:TiO₂-AgCu, we estimated the series resistance (R_s) and shunt resistance (R_{sh}) by fitting the J–V plots as listed in Table 6.3 [59, 60]. It was observed that the 0.5 mol.% Ag/ 0.1 mol.% Cu and 0.5 mol.% Ag/Cu displayed higher R_{sh} and smaller R_s in comparison to other solar cells [61, 62]. This was due to improved hole transport to the molybdenum oxide layer and decreased the carrier recombination in the absorption layer.

Furthermore, we compared the deviation of V_{OC} and I_{SC} of devices versus the Ag and Cu content of the bimetallic doped TiO₂ incorporated in P3HT matrix. As demonstrated in Fig. 6.13b, the J_{SC} and V_{OC} can be tweaked by varying the content of Ag and Cu in TiO₂. It is well known that the V_{OC} is one of the main aspects towards facilitating improved PCE of the solar cells. Studies have reported that the V_{OC} of bulk-heterostructure solar cells relies on the donor/acceptor energy band gap; charge-carrier recombination rates; the extent of energetic disorder, etc. [63, 64]. Blakesley et al. [62] have reported that a great amount of active disrupt, or a high density of traps, induces substantial drops in V_{OC}. Street et al. [65] have suggested a

Shockley Read-Hall (SRH) recombination at the interfacial traps as the prevailing mechanism. Furthermore, Cowan et al. [66] also pointed out that impurities that may exist in the polymer or fullerene and partial phase-separation, i.e. interfacial defects which act as traps are expected to play a role to a trap-based recombination.

As a result, the perceived superior V_{oc} of the non-fullerene based solar cells devices in Fig. 6.12 and Table 6.3 may be associated to the existence of inferior interfacial traps in active layer. PL and XPS analyses showed that the doping of Ag and Cu in TiO_2 surface resulted to Ti^{3+} from Ti^{4+} ions, releasing oxygen vacancies (V_o). Generally, the V_o act both as shallow and deep trap states. Hence, Wang et al. [67] have reported the inherent features of shallow and deep trap states and their influence on the solar cells performance. The shallow trap states stimulate carriers' diffusion to the surface; whereas the deep trap states improve the carriers' recombination [19, 67, 68]. Most recent study by Fakharan et al. [19] have reported that the Ag_x-TiO_2 light absorption was improved due to increased Ag loading, because of the creation of higher V_o . Such behaviour was witnessed in our UV-vis absorption spectra in Fig. 6.12c, where the 0.5 mol.% Ag/0.2 mol.% Cu and 0.5 mol.% Ag/Cu nanoparticles displayed improved absorption. The bimetallic Ag/Cu displayed excellent properties compared to the monometallic due to the LSPR influence of Ag and the co-catalytic role of Cu. The synergy between Ag and Cu results to metal sites, by acting as electron traps, moreover facilitates electron-hole separation resulting in successful utilization of wide range absorption.

This observation was further witnessed by Choudhury et al. [68] by noting that increased Ag content resulted to a variation in the ratio of shallow to deep traps. Thus, the increased V_{oc} of 0.5 mol.% Ag/0.1 mol.% Cu and 0.5 mol.% Ag/Cu based solar cells advocates the positive impact of the plasmonic nanostructures on the

generation of exciton, dissociation of exciton and charge transport in active layers. This attained superior V_{oc} is associated to the increased in the ratio of shallow to deep traps of 0.5 mol.% Ag/0.1 mol.% Cu and 0.5 mol.% Ag/Cu doped TiO_2 nanoparticles, stimulating the carriers' diffusion to the surfaces and hindering charge carrier recombination.

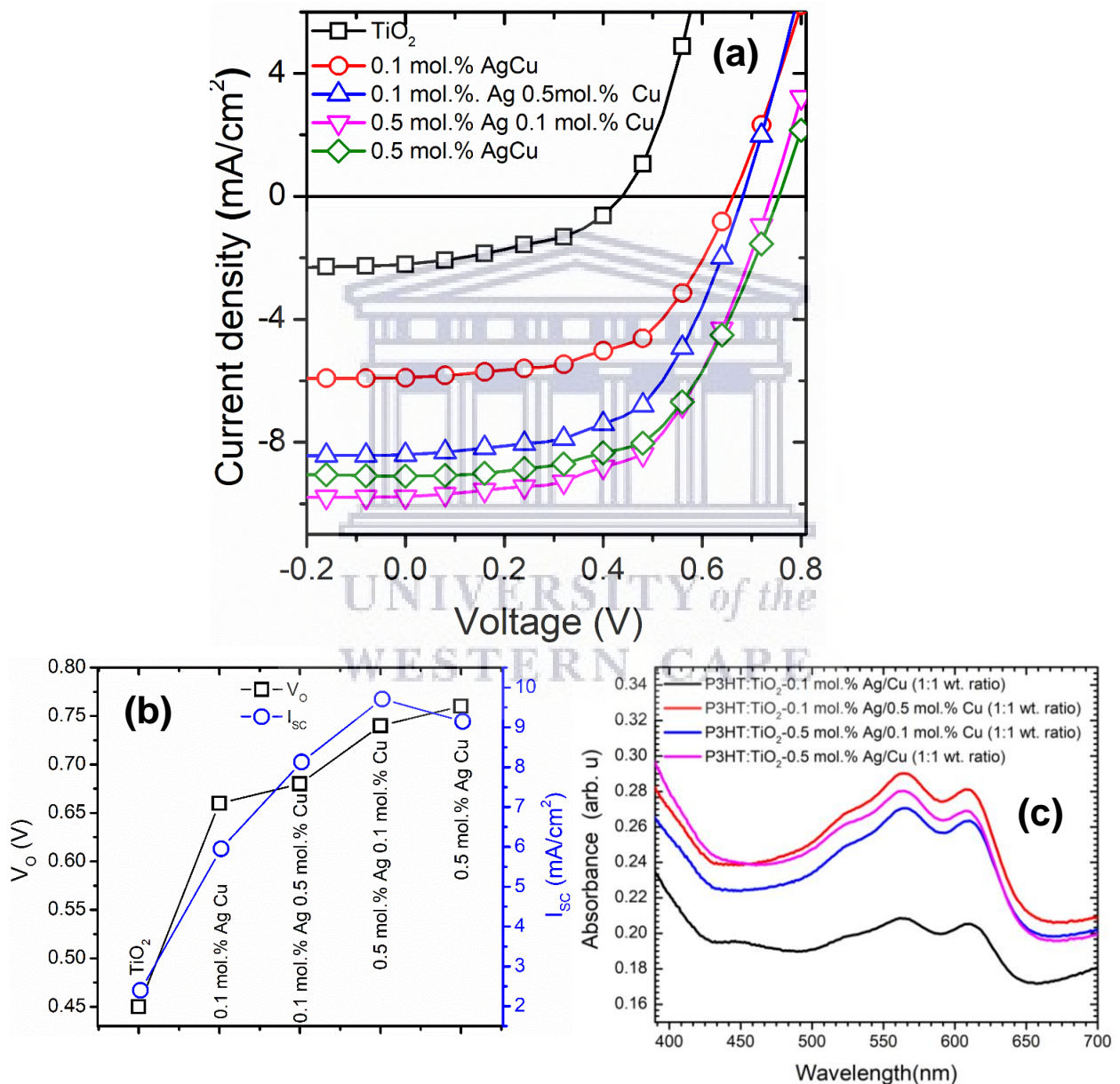


Fig. 6. 12: I-V characteristics of the P3HT blended with 0.1 mol. % Ag/0.5 mol.%Cu, (c) 0.5 mol.% Ag /0.1 mol.% Cu and (d) 0.5 mol.% Ag/Cu of the bimetallic Ag/Cu doped TiO_2 nanoparticles recorded under illumination (AM1.5G), (b) I_{sc} and V_{oc} as a function of Ag and Cu contents, and (c) UV-Vis spectra of P3HT incorporated with TiO_2 doped with Ag/Cu concentrations.

Table 6. 3: Summary of photovoltaic properties extracted under illumination (AM1.5G).

Films	J _{sc} (mA/cm ²)	V _{oc} (V)	FF	R _s (Ω cm ²)	R _{sh} (Ω cm ²)	PCE (%)
TiO ₂	2.40	0.45	0.42	4.41	70.68	0.46 (0.38)*
0.1 mol. % Ag/Cu	5.95	0.66	0.57	8.42	73.40	2.26 (2.18)
0.1 mol. % Ag/0.5 mol.%Cu	8.13	0.68	0.60	12.55	138.82	3.30(3.03)
0.5 mol.% Ag /0.1 mol.% Cu	9.56	0.74	0.58	14.29	947.04	4.11(3.98)
0.5 mol.% Ag/Cu	9.11	0.76	0.58	13.86	801.66	4.01(3.88)

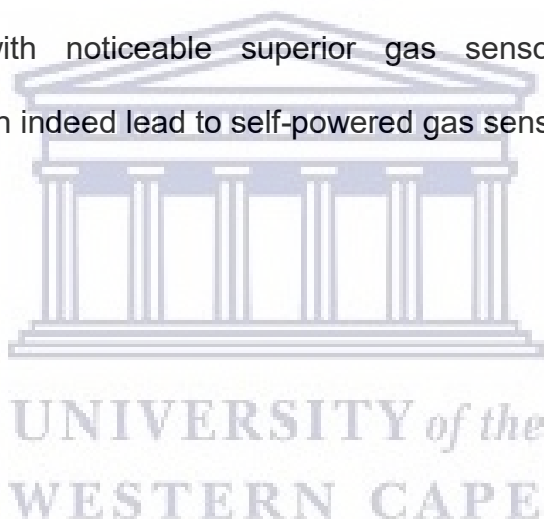
Note: the values in parentheses stand for the average efficiency extracted from over 3 solar cell devices.

6.4. CONCLUSION AND REMARKS

In summary, we have successfully synthesized n-type and p-type bimetallic Ag/Cu doped TiO₂ nanostructures via the hydrothermal method. The structural and surface analyses validated that the bimetallic Ag/Cu were inserted in the TiO₂ surface. The real-time resistance analyses confirmed that at lower loading, the nanostructures were n-type and at higher loading they transformed to p-type behaviour. The sensing analyses further demonstrated improved response towards xylene vapour at 150 °C for the p-type 0.5% bimetallic Ag/Cu doped TiO₂. The sensor further disclosed excellent repeatability and stability towards xylene. These findings validate that depending on the doping degree, appropriate selectivity can be realized. More precisely, xylene was selectively detected through doping of bimetallic p-type 0.5 mol.% Au/Cu doped TiO₂, denoting that bimetallic doping is yet additional

methodology not only to improve their sensing response, nonetheless also to adjust selectivity.

The findings further revealed the influence of LSPR in a non-fullerene BHJ solar cells by adding bimetallic p-type Ag/Cu doped TiO₂ nanoparticles into the P3HT:ZnO layer. It was observed that at lower doping of bimetallic Ag/Cu in TiO₂ nanoparticles, they behaved as electron acceptor material in the fabrication of BHJ, displaying lower PCE, while at higher doping, they acted as donor and illustrated superior short circuit current density and open circuit voltage, which resulted in improved efficiency of 4.1%. These remarks suggest new prospects in the design of innovative multi-functional materials with noticeable superior gas sensors and photovoltaic performances, which can indeed lead to self-powered gas sensors devices.



REFERENCES

1. Tshabalala, Z.P., Motaung, D.E., Mhlongo, G.H. and Ntwaeaborwa, O.M., 2016. Facile synthesis of improved room temperature gas sensing properties of TiO₂ nanostructures: Effect of acid treatment. *Sensors and Actuators B: Chemical*, 224, pp.841-856.
2. Dutta, K., Chattopadhyay, P.P., Lu, C.W., Ho, M.S. and Bhattacharyya, P., 2015. A highly sensitive BTX sensor based on electrochemically derived wall connected TiO₂ nanotubes. *Applied Surface Science*, 354, pp.353-361.
3. Tshabalala, Z.P., Shingange, K., Dhonge, B.P., Ntwaeaborwa, O.M., Mhlongo, G.H. and Motaung, D.E., 2017. Fabrication of ultra-high sensitive and selective CH₄ room temperature gas sensing of TiO₂ nanorods: Detailed study on the annealing temperature. *Sensors and Actuators B: Chemical*, 238, pp.402-419
4. Haidry, A.A., Sun, L., Saruhan, B., Plecenik, A., Plecenik, T., Shen, H. and Yao, Z., 2018. Cost-effective fabrication of polycrystalline TiO₂ with tunable n/p response for selective hydrogen monitoring. *Sensors and Actuators B: Chemical*, 274, pp.10-21.
5. Gao, X., Li, Y., Zeng, W., Zhang, C. and Wei, Y., 2017. Hydrothermal synthesis of agglomerating TiO₂ nanoflowers and its gas sensing. *Journal of Materials Science: Materials in Electronics*, 28(24), pp.18781-18786.
6. Xing, X., Chen, N., Yang, Y., Zhao, R., Wang, Z., Wang, Z., Zou, T. and Wang, Y., 2018. Pt-functionalized nanoporous TiO₂ nanoparticles with enhanced gas sensing performances toward acetone. *physica status solidi (a)*, 215(14), p.1800100.
7. Naik, G.K., Majhi, S.M., Jeong, K.U., Lee, I.H. and Yu, Y.T., 2019. Nitrogen doping on the core-shell structured Au@ TiO₂ nanoparticles and its enhanced photocatalytic hydrogen evolution under visible light irradiation. *Journal of Alloys and Compounds*, 771, pp.505-512.
8. Mao, S., Zhou, H., Wu, S., Yang, J., Li, Z., Wei, X., Wang, X., Wang, Z. and Li, J., 2018. High performance hydrogen sensor based on Pd/TiO₂ composite film. *International Journal of Hydrogen Energy*, 43(50), pp.22727-22732.
9. Endo, T., Yanagida, Y. and Hatsuzawa, T., 2007. Colorimetric detection of volatile organic compounds using a colloidal crystal-based chemical sensor for environmental applications. *Sensors and Actuators B: Chemical*, 125(2), pp.589-595.

10. Leusch, F. and Bartkow, M., 2010. A Short Primer on Benzene, Toluene, Ethylbenzene and Zylenes (BTEX) in the Environment and in Hydraulic Fracturing Fluids. Griffith University.
11. Fleming-Jones, M.E. and Smith, R.E., 2003. Volatile organic compounds in foods: a five year study. *Journal of agricultural and food chemistry*, 51(27), pp.8120-8127.
12. Zhang, S., Qin, Y., Zhu, J. and Hou, J., 2018. Over 14% efficiency in polymer solar cells enabled by a chlorinated polymer donor. *Advanced Materials*, 30(20), p.1800868.
13. Li, S., Ye, L., Zhao, W., Yan, H., Yang, B., Liu, D., Li, W., Ade, H. and Hou, J., 2018. A wide band gap polymer with a deep highest occupied molecular orbital level enables 14.2% efficiency in polymer solar cells. *Journal of the American Chemical Society*, 140(23), pp.7159-7167.
14. Zheng, Z., Hu, Q., Zhang, S., Zhang, D., Wang, J., Xie, S., Wang, R., Qin, Y., Li, W., Hong, L. and Liang, N., 2018. A Highly Efficient Non-Fullerene Organic Solar Cell with a Fill Factor over 0.80 Enabled by a Fine-Tuned Hole-Transporting Layer. *Advanced materials*, 30(34), p.1801801.
15. Meng, L., Zhang, Y., Wan, X., Li, C., Zhang, X., Wang, Y., Ke, X., Xiao, Z., Ding, L., Xia, R. and Yip, H.L., 2018. Organic and solution-processed tandem solar cells with 17.3% efficiency. *Science*, 361(6407), pp.1094-1098.
16. Dang, M.T., Hirsch, L. and Wantz, G., 2011. P3HT: PCBM, best seller in polymer photovoltaic research. *Adv Mater*, 16;23(31), pp.3597-3602
17. Po, R., Bernardi, A., Calabrese, A., Carbonera, C., Corso, G. and Pellegrino, A., 2014. From lab to fab: how must the polymer solar cell materials design change?—an industrial perspective. *Energy & Environmental Science*, 7(3), pp.925-943.
18. Holliday, S., Ashraf, R.S., Wadsworth, A., Baran, D., Yousaf, S.A., Nielsen, C.B., Tan, C.H., Dimitrov, S.D., Shang, Z., Gasparini, N. and Alamoudi, M., 2016. High-efficiency and air-stable P3HT-based polymer solar cells with a new non-fullerene acceptor. *Nature communications*, 7(1), pp.1-11.
19. Fakharan, Z. and Naji, L., 2017. Fabrication of non-fullerene P3HT/Agx-TiO₂ based polymer solar cells with high open circuit voltage. *Journal of Alloys and Compounds*, 708, pp.1184-1194.

20. Barakat, M.A. and Kumar, R., 2016. Photocatalytic activity enhancement of titanium dioxide nanoparticles. In *Photocatalytic Activity Enhancement of Titanium Dioxide Nanoparticles* (pp. 1-29). Springer, Cham.
21. Abdel-Wahab, A.M.A., Mohamed, O.S., Ahmed, S.A. and Mostafa, M.F., 2012. Ag-doped TiO₂ enhanced photocatalytic oxidation of 1, 2-cyclohexanediol. *Journal of Physical Organic Chemistry*, 25(12), pp.1418-1421.
22. Maake, P.J., Bolokang, A.S., Arendse, C.J., Vohra, V., Iwuoha, E.I. and Motaung, D.E., 2020. Metal oxides and noble metals application in organic solar cells. *Solar Energy*, 207, pp.347-366.
23. Hernández, J.V., Coste, S., Murillo, A.G., Romo, F.C. and Kassiba, A., 2017. Effects of metal doping (Cu, Ag, Eu) on the electronic and optical behavior of nanostructured TiO₂. *Journal of Alloys and Compounds*, 710, pp.355-363.
24. Kumar, D.P., Reddy, N.L., Srinivas, B., Durgakumari, V., Roddatis, V., Bondarchuk, O., Karthik, M., Ikuma, Y. and Shankar, M.V., 2016. Stable and active Cu_xO/TiO₂ nanostructured catalyst for proficient hydrogen production under solar light irradiation. *Solar Energy Materials and Solar Cells*, 146, pp.63-71.
25. Gao, Y., Jin, F., Su, Z., Zhao, H., Luo, Y., Chu, B. and Li, W., 2017. Cooperative plasmon enhanced organic solar cells with thermal coevaporated Au and Ag nanoparticles. *Organic Electronics*, 48, pp.336-341.
26. Mokoena, T.P., Tshabalala, Z.P., Hillie, K.T., Swart, H.C. and Motaung, D.E., 2020. The blue luminescence of p-type NiO nanostructured material induced by defects: H₂S gas sensing characteristics at a relatively low operating temperature. *Applied Surface Science*, 525, p.146002.
27. Reddy, N.L., Kumar, S., Krishnan, V., Sathish, M. and Shankar, M.V., 2017. Multifunctional Cu/Ag quantum dots on TiO₂ nanotubes as highly efficient photocatalysts for enhanced solar hydrogen evolution. *Journal of Catalysis*, 350, pp.226-239.
28. Xia, S., Zhu, H., Cai, H., Zhang, J. and Yu, J., 2014. Hydrothermally synthesized CuO based volatile organic compound gas sensor. *RSC Advances*, 4(101), pp.57975-57982.
29. Motsoeneng, R.G., Kortidis, I., Rikhotso, R., Swart, H.C., Ray, S.S. and Motaung, D.E., 2020. Temperature-dependent response to C₃H₇OH and C₂H₅OH vapors induced by deposition of Au nanoparticles on SnO₂/NiO hollow sphere-based conductometric sensors. *Sensors and Actuators B: Chemical*, 316, p.128041.

30. Dutta, K., Bhowmik, B., Hazra, A., Chattopadhyay, P.P. and Bhattacharyya, P., 2015. An efficient BTX sensor based on p-type nanoporous titania thin films. *Microelectronics Reliability*, 55(3-4), pp.558-564.
31. Zhang, Y., Bai, J., Zhou, L., Liu, D., Liu, F., Liang, X., Gao, Y., Liu, F., Yan, X. and Lu, G., 2019. Preparation of silver-loaded titanium dioxide hedgehog-like architecture composed of hundreds of nanorods and its fast response to xylene. *Journal of colloid and interface science*, 536, pp.215-223.
32. Zhu, L., Zhang, D., Wang, Y., Feng, C., Zhou, J., Liu, C. and Ruan, S., 2015. Xylene gas sensor based on Ni doped TiO₂ bowl-like submicron particles with enhanced sensing performance. *RSC Advances*, 5(36), pp.28105-28110.
33. Zhang, J., Tang, P., Liu, T., Feng, Y., Blackman, C. and Li, D., 2017. Facile synthesis of mesoporous hierarchical Co₃O₄-TiO₂ p-n heterojunctions with greatly enhanced gas sensing performance. *Journal of Materials Chemistry A*, 5(21), pp.10387-10397.
34. Bai, S., Tian, K., Tian, Y., Guo, J., Feng, Y., Luo, R., Li, D., Chen, A. and Liu, C.C., 2018. Synthesis of Co₃O₄/TiO₂ composite by pyrolyzing ZIF-67 for detection of xylene. *Applied Surface Science*, 435, pp.384-392.
35. Zhang, Y., Nizamidin, P., Abudukeremu, H. and Yimit, A., 2020. Optical waveguide xylene gas sensor based on sodium dodecylbenzene sulfonate (SDBS)-TiO₂ film for detection at room temperature. *Optical Materials Express*, 10(9), pp.2212-2226.
36. Wang, Y., Wang, S., Zhang, H., Gao, X., Yang, J. and Wang, L., 2014. Brookite TiO₂ decorated α -Fe₂O₃ nanoheterostructures with rod morphologies for gas sensor application. *Journal of Materials Chemistry A*, 2(21), pp.7935-7943.
37. Malik, R., Tomer, V.K., Chaudhary, V., Dahiya, M.S., Nehra, S.P., Rana, P.S. and Duhan, S., 2017. Ordered mesoporous In-(TiO₂/WO₃) nanohybrid: An ultrasensitive n-butanol sensor. *Sensors and Actuators B: Chemical*, 239, pp.364-373.
38. Mokoena, T.P., Hillie, K.T., Swart, H.C., Leshabane, N., Tshilongo, J. and Motaung, D.E., 2020. Fabrication of a propanol gas sensor using p-type nickel oxide nanostructures: The effect of ramping rate towards luminescence and gas sensing characteristics. *Materials Chemistry and Physics*, 253, p.123316.
39. Oosthuizen, D.N., Motaung, D.E. and Swart, H.C., 2019. Selective detection of CO at room temperature with CuO nanoplatelets sensor for indoor air quality monitoring manifested by crystallinity. *Applied Surface Science*, 466, pp.545-553.

40. Kim, B.Y., Ahn, J.H., Yoon, J.W., Lee, C.S., Kang, Y.C., Abdel-Hady, F., Wazzan, A.A. and Lee, J.H., 2016. Highly selective xylene sensor based on NiO/NiMoO₄ nanocomposite hierarchical spheres for indoor air monitoring. *ACS applied materials & interfaces*, 8(50), pp.34603-34611.
41. Woo, H.S., Kwak, C.H., Chung, J.H. and Lee, J.H., 2015. Highly selective and sensitive xylene sensors using Ni-doped branched ZnO nanowire networks. *Sensors and Actuators B: Chemical*, 216, pp.358-366.
42. Woo, H.S., Kwak, C.H., Chung, J.H. and Lee, J.H., 2014. Co-doped branched ZnO nanowires for ultrasensitive and sensitive detection of xylene. *ACS applied materials & interfaces*, 6(24), pp.22553-22560. *Appl. Mater. Interfaces* 6 (2014) 22553–22560.
43. Mirzaei, A., Kim, J.H., Kim, H.W. and Kim, S.S., 2018. Resistive-based gas sensors for detection of benzene, toluene and xylene (BTX) gases: a review. *Journal of Materials Chemistry C*, 6(16), pp.4342-4370.
44. Qu, F., Jiang, H. and Yang, M., 2016. Designed formation through a metal organic framework route of ZnO/ZnCo₂O₄ hollow core-shell nanocages with enhanced gas sensing properties. *Nanoscale*, 8(36), pp.16349-16356.
45. Sui, L., Zhang, X., Cheng, X., Wang, P., Xu, Y., Gao, S., Zhao, H. and Huo, L., 2017. Au-loaded hierarchical MoO₃ hollow spheres with enhanced gas-sensing performance for the detection of BTX (benzene, toluene, and xylene) and the sensing mechanism. *ACS applied materials & interfaces*, 9(2), pp.1661-1670.
46. Yang, M., Liu, W., Sun, J.L. and Zhu, J.L., 2012. High magnetic field annealing effect on visible photoluminescence enhancement of TiO₂ nanotube arrays. *Applied Physics Letters*, 100(4), p.043106.
47. Shi, J., Chen, J., Feng, Z., Chen, T., Lian, Y., Wang, X. and Li, C., 2007. Photoluminescence characteristics of TiO₂ and their relationship to the photoassisted reaction of water/methanol mixture. *The journal of physical chemistry C*, 111(2), pp.693-699.
48. Santara, B., Giri, P.K., Imakita, K. and Fujii, M., 2013. Evidence of oxygen vacancy induced room temperature ferromagnetism in solvothermally synthesized undoped TiO₂ nanoribbons. *Nanoscale*, 5(12), pp.5476-5488.
49. Mercado, C., Seeley, Z., Bandyopadhyay, A., Bose, S. and McHale, J.L., 2011. Photoluminescence of dense nanocrystalline titanium dioxide thin films: effect of doping and thickness and relation to gas sensing. *ACS applied materials & interfaces*, 3(7), pp.2281-2288.

50. Santara, B.; Giri, P.K.; Imakita, K.; Fujii, M. Evidence for Ti Interstitial Induced Extended Visible Absorption and Near Infrared Photoluminescence from Undoped TiO₂ Nanoribbons: An In Situ Photoluminescence Study. *J. Phys. Chem. C* 2013, 117, 23402–23411.
51. Santara, B., Giri, P.K., Dhara, S., Imakita, K. and Fujii, M., 2014. Oxygen vacancy-mediated enhanced ferromagnetism in undoped and Fe-doped TiO₂ nanoribbons. *Journal of Physics D: Applied Physics*, 47(23), p.235304.
52. Prokes, S.M.; Gole, J.L.; Chen, X.; Burda, C.; Carlos, W.E. Defect-Related Optical Behavior in Surface-Modified TiO₂ Nanostructures. *Adv. Funct. Mater.* 2005, 15(1), 161-167.
53. Tshabalala, Z.P., Mokoena, T.P., Hillie, K.T., Swart, H.C., Motaung, D.E., 2021. Improved BTEX gas sensing characteristics of thermally treated TiO₂ hierarchical spheres manifested by high-energy {001} crystal facets, *Sensors and Actuators B: Chemical*, 338, 129774
54. Ding, M., Xie, N., Wang, C., Kou, X., Zhang, H., Guo, L., Sun, Y., Chuai, X., Gao, Y., Liu, F. and Sun, P., 2017. Enhanced NO₂ gas sensing properties by Ag-doped hollow urchin-like In₂O₃ hierarchical nanostructures. *Sensors and Actuators B: Chemical*, 252, pp.418-427.
55. Santara, B., Imakita, K., Fujii, M. and Giri, P.K., 2016. Mechanism of defect induced ferromagnetism in undoped and Cr doped TiO₂ nanorods/nanoribbons. *Journal of Alloys and Compounds*, 661, pp.331-344.
56. Tshabalala, Z.P., Motaung, D.E. and Swart, H.C., 2018. Structural transformation and enhanced gas sensing characteristics of TiO₂ nanostructures induced by annealing. *Physica B: Condensed Matter*, 535, pp.227-231.4 (2016) 841-856
57. Kortidis, I., Swart, H.C., Ray, S.S. and Motaung, D.E., 2019. Detailed understanding on the relation of various pH and synthesis reaction times towards a prominent low temperature H₂S gas sensor based on ZnO nanoplatelets. *Results in Physics*, 12, pp.2189-2201.
58. Siddiqui, H., Parra, M.R., Pandey, P., Qureshi, M.S. and Haque, F.Z., 2020. Utility of copper oxide nanoparticles (CuO-NPs) as efficient electron donor material in bulk-heterojunction solar cells with enhanced power conversion efficiency. *Journal of Science: Advanced Materials and Devices*, 5(1), pp.104-110.
59. Kim, M.S., Kim, B.G. and Kim, J., 2009. Effective variables to control the fill factor of organic photovoltaic cells. *ACS applied materials & interfaces*, 1(6), pp.1264-1269.

60. Pysch, D., Mette, A. and Glunz, S.W., 2007. A review and comparison of different methods to determine the series resistance of solar cells. *Solar Energy Materials and Solar Cells*, 91(18), pp.1698-1706.
61. Huang, H.L., Lee, C.T. and Lee, H.Y., 2015. Performance improvement mechanisms of P3HT: PCBM inverted polymer solar cells using extra PCBM and extra P3HT interfacial layers. *Organic Electronics*, 21, pp.126-131.
62. Das, S., Choi, J.Y. and Alford, T.L., 2015. P3HT: PC61BM based solar cells employing solution processed copper iodide as the hole transport layer. *Solar Energy Materials and Solar Cells*, 133, pp.255-259.
63. Blakesley, J.C. and Neher, D., 2011. Relationship between energetic disorder and open-circuit voltage in bulk heterojunction organic solar cells. *Physical Review B*, 84(7), p.075210.
64. Krebs, F.C., 2008. *Polymer photovoltaics: a practical approach*. SPIE-International Society for Optical Engineering.
65. Street, R.A., Schoendorf, M., Roy, A. and Lee, J.H., 2010. Interface state recombination in organic solar cells. *Physical Review B*, 81(20), p.205307.
66. Cowan, S.R., Roy, A. and Heeger, A.J., 2010. Recombination in polymer-fullerene bulk heterojunction solar cells. *Physical Review B*, 82(24), p.245207.
67. Wang, Q., Zhang, Z., Zakeeruddin, S.M. and Graetzel, M., 2008. Enhancement of the performance of dye-sensitized solar cell by formation of shallow transport levels under visible light illumination. *The Journal of Physical Chemistry C*, 112(17), pp.7084-7092.
68. Choudhury, B., Dey, M. and Choudhury, A., 2014. Shallow and deep trap emission and luminescence quenching of TiO₂ nanoparticles on Cu doping. *Applied Nanoscience*, 4(4), pp.499-506.

CHAPTER SEVEN

SUMMARY/CONCLUSION AND FUTURE WORK

In final remarks, undoped and Au, Ag, Cu and bimetallic Ag/Cu doped TiO₂ nanoparticles were successfully prepared. Au, Ag, Cu doped TiO₂ nanoparticles were incorporated in P3HT matrix and tested for solar cell performances. Among the fabricated devices, the 0.5 mol.% Ag doped TiO₂ displayed remarkable efficiency of 3.88 % under 1.5. G due to higher V_{oc} of 0.69 V. While the 0.5 mol.% Cu displayed an efficiency of 2.93%.

With respect to the bimetallic Ag/Cu doped TiO₂ nanoparticles, the nanostructured displayed unique properties, by switching from n-type to p-type at higher plasmonic doping of Ag/Cu bimetallic. Such switching played vital role in solar cells and gas sensing performance. The p-type Ag/Cu bimetallic displayed improved solar cell performance in comparison to n-type. Such behaviour was also noted for the gas sensing properties of these materials. Though for gas sensing, the p-type bimetallic 0.5 mol.% Ag/Cu doped TiO₂ nanoparticles based sensor displayed a timely selective detection of xylene vapour among the BTEX (benzene, toluene, ethylene-benzene and xylene) and acetone vapours at low operating temperature. The improved xylene gas sensing behaviour was justified by the catalytic activity and point defects induced by the loading of the bimetallic Ag/Cu in the p-type TiO₂. While for the solar cell performance, 0.5 mol.% Ag /0.1 mol.% Cu doped TiO₂ blended in P3HT displayed improved solar cell performance, revealing an efficiency of 4.11 %. Besides, the higher plasmonic Ag/Cu loading -TiO₂ in P3HT: ZnO displayed a superior V_{oc} of 0.76 V. The fundamental mechanism to the rationalization of

improved PCE can be chiefly attributed to the strong synergistic effect of superior light scattering, light harvesting and charge generation and separation efficiency capability and the plasmonic-enhanced effect persuaded by the loading of p-type Ag/Cu-TiO₂ nanoparticles.

FUTURE WORK

Therefore, the future work ought to intensely endeavour to improve the efficiency of the non-fullerene materials. And focus on investigating the stability of the non-fullerene acceptor materials. The work should further try to enhance the sensing parameters of these materials, by reducing the operating to 25 °C, while maintaining the sensing performance. The long-term stability of these materials should also be investigated in the presence of relative humidity in order to reach commercialization. The approach of intergrating these materials into self-powered sensors should be investigated in detail. The influence of the applied bias voltage, and various exposure times (short and/or long term) should also be considered in order to minimize the drift in response curves on the sensing performance. This might benefit to close the breach between the research and practical exploitation.

APPENDIX SECTION

APPENDIX A: Corresponding to Chapter 5:

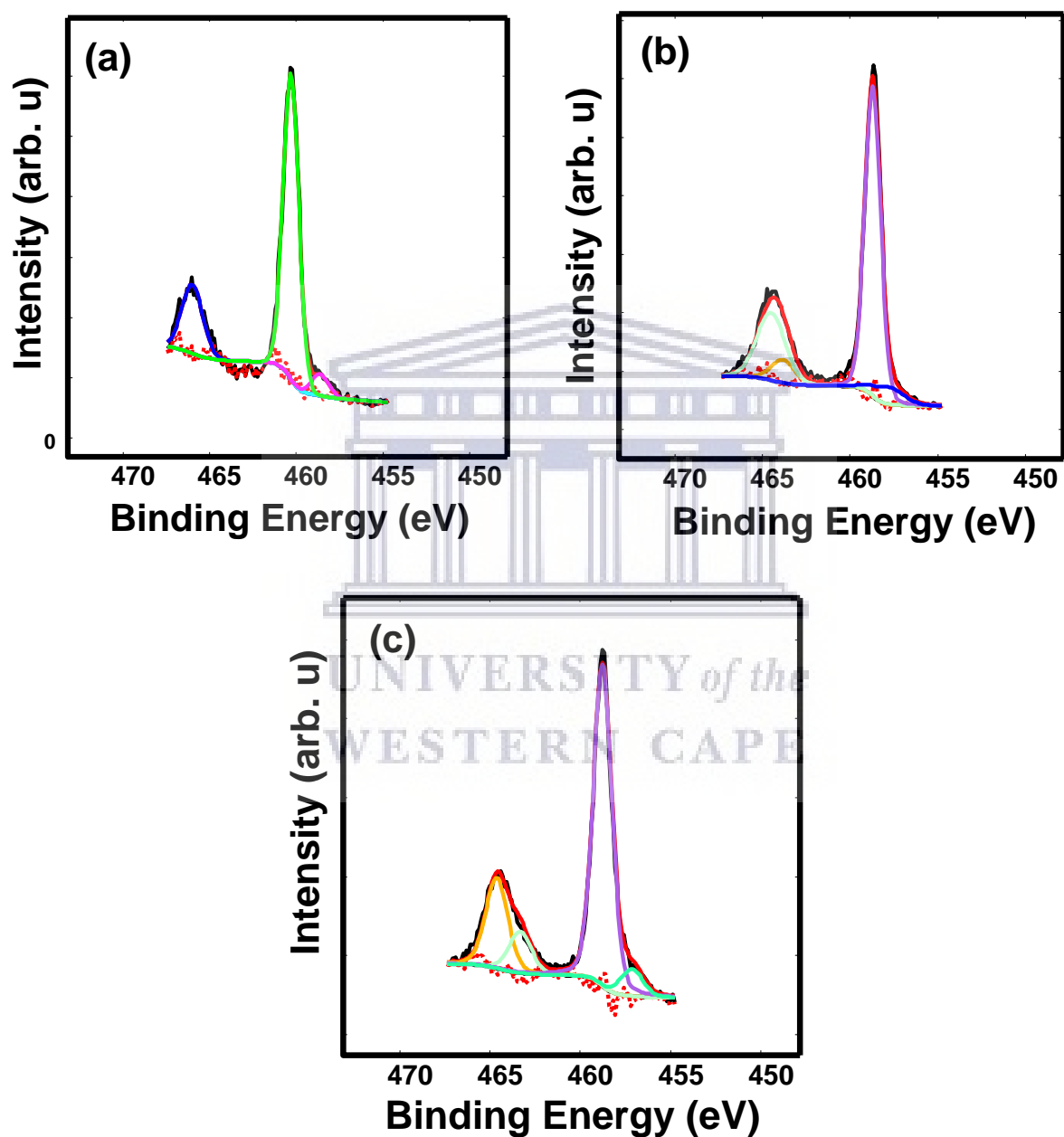


Fig. A1: XPS analyses of Ti2p of (a) 0.1 mol.% Au, (b) 0.1 mol.% Ag and (c) 0.1 mol.% Cu.

APPENDIX B: Corresponding to Chapter 6:

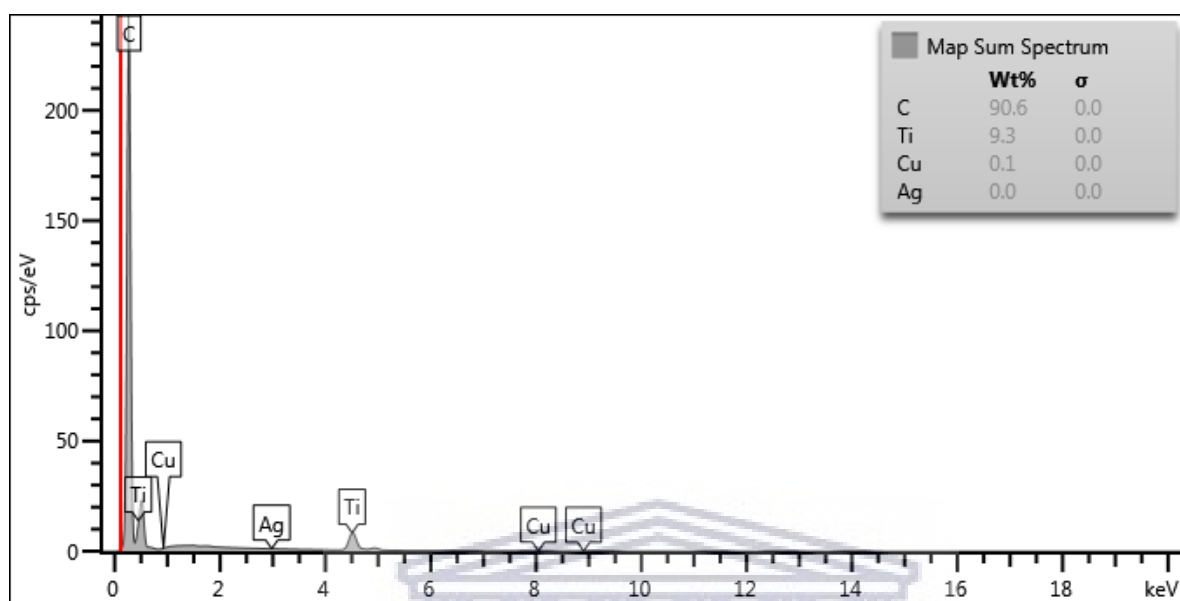


Figure B1: EDX spectra of NiO nanostructured material.

UNIVERSITY of the
WESTERN CAPE

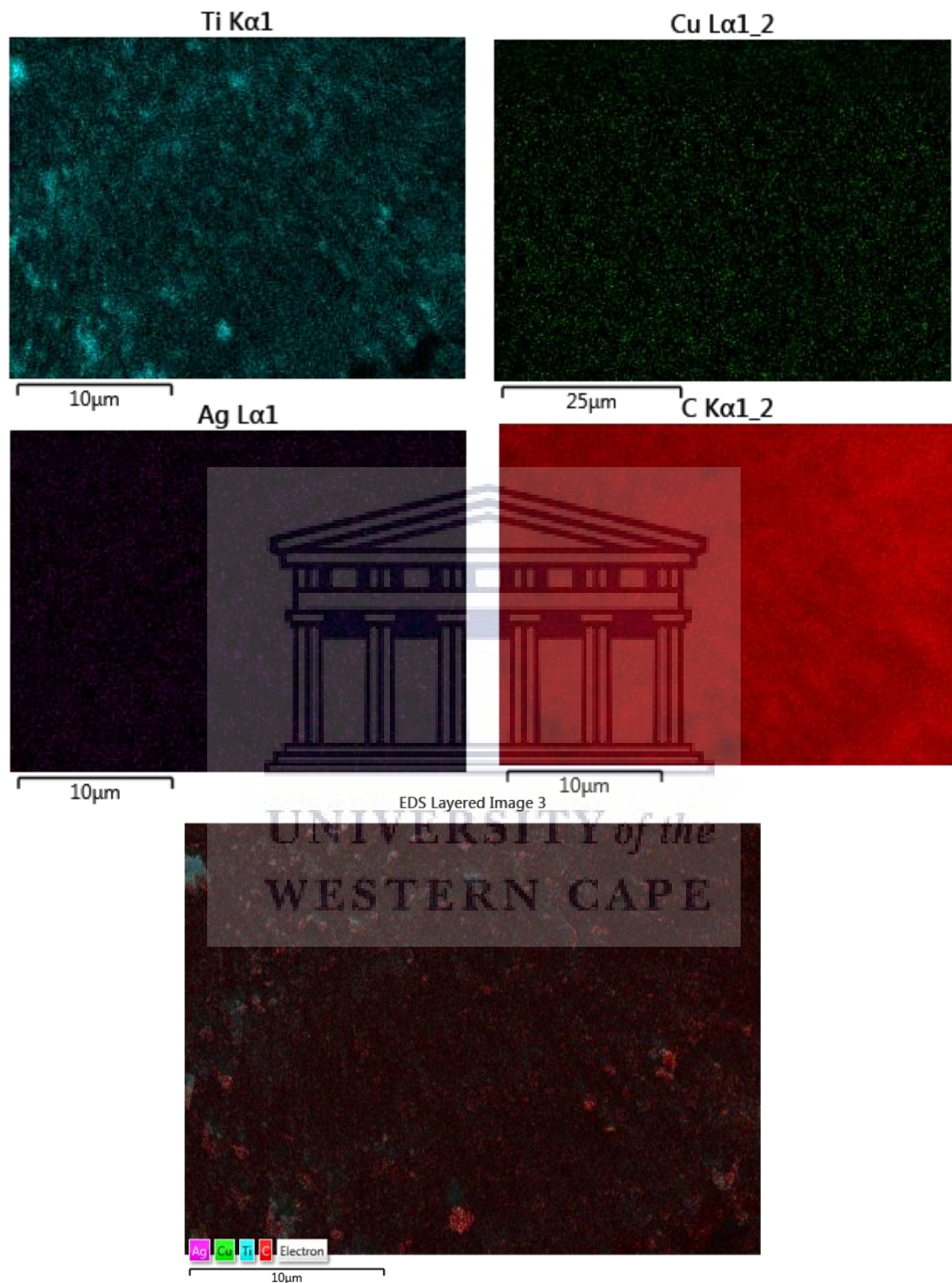


Fig. B2: EDS elemental mapping of 0.1 mol.% Ag/Cu doped TiO₂ nanoparticles.

Table S1:

Materials	529 eV	530 eV	531 eV	532 eV
	%	%	%	%
Pure TiO₂		65.5	11.1	23.4
0.1 mol.% Ag/Cu		64.0	28.9	7.1
0.1 mol.% Ag /0.5 mol.% Cu		68.0	27.7	4.3
0.5 mol.% Ag/0.1 mol.% Cu		83.2	12.0	4.8
0.5 mol.% Ag/Cu	20.0		63.9	16.1



UNIVERSITY *of the*
WESTERN CAPE